Electrode Effects on the Ferroelectric Properties of $Hf_{1-x}Zr_xO_2$

A

Dissertation

Presented to

The faculty of the School of Engineering and Applied Science

University of Virginia

---

in partial fulfillment

of the requirements for the degree

Doctor of Philosophy

by

Shelby Sutton Fields

February 17th, 2022

Approval Sheet

This

Dissertation

is submitted in partial fulfillment of the requirements

for the degree of

Doctor of Philosophy

Author: Shelby Sutton Fields

Advisor: Dr. Jon F. Ihlefeld

Committee Member: Dr. Stephen J. McDonnell

Committee Member: Dr. Patrick E. Hopkins

Committee Member: Dr. Nikhil Shukla

Committee Member: Dr. Sean W. Smith

Accepted for the School of Engineering and Applied Science:

Jennifer L. West, School of Engineering and Applied Science

Abstract

Research constituting this dissertation began in the middle of December, in 2017. At its outset, a number of projects on various thin film research topics presented potential candidates for its subject. However, a clear need for immediate work on electrode effects on the ferroelectric properties of hafnium zirconium oxide (HZO), through collaboration with Sandia National Laboratories, provided an initial deterministic push, which precipitated this study. As of 2017, the ferroelectric properties of hafnium oxide-based ferroelectric thin films, including HZO, had been readily published upon in open literature since their first reporting in 2011 by Böske *et al.*[1] and Müller *et al.*[2,3] Led mostly by electrical and device engineering research groups, much of the early work was devoted to understanding how polarization wake-up and fatigue in this silicon-compatible ferroelectric material could be optimized for scalable memory applications. Such research mostly utilized TiN electrode materials, given their promising behavior when incorporated into HfO_2-based devices and ready use in silicon technology. This work had identified that a favorable surface energy facilitated the stabilization of the ferroelectric orthorhombic phase in polycrystalline films grown to a thickness of < 40 nm, showed that oxygen vacancy content in the HfO_2-based layer played an important role in the stabilization of this ferroelectric phase, demonstrated superior thickness and lateral scalability in the ferroelectric properties of HfO_2-based films compared to conventional perovskites, and revealed that ferroelectric domain pinning and depinning, at least partially, drives the polarization instabilities that accompany field cycling of HfO_2-based devices. Research produced by materials science-focused research groups had also shown important effects of stress on the orthorhombic phase content and ferroelectric domain structure, and had observed localized phase transformations occurring during field cycling.

However, by 2017, a number of knowledge gaps pertaining to the interactions between electrodes and HfO_2-based layers remained. While the role of electrodes on the orthorhombic phase stabilization had been investigated, such findings mostly comprised observations on different behavior based upon which electrodes were utilized, and the various potential interactions that drive these different behaviors were largely unexplored. Comparisons between TaN and TiN electrodes revealed different ferroelectric orthorhombic phase compositions in processed HfO_2-based films and strongly different polarization wake-up and fatigue behavior. Separately, the field-

cycling behavior of devices processed with metallic electrodes had been sparsely investigated compared to binary nitrides. Electrode reactivity had been suggested as the cause of such different behaviors, however examinations involving specifically varying the electrode material to induce changes in the neighboring HfO_2-based layers had not yet been widely undertaken, and a device-scale understanding of the effects of field cycling on the phase constitutions of HfO_2-based devices remained elusive. Further, the field cycling behaviors of common binary nitride and metallic electrodes had only been briefly compared, and oxide electrodes, which aided in mitigating deleterious polarization fatigue during field cycling of conventional ferroelectric oxides, had not been explicitly investigated.

Separately, while stress effects on the ferroelectric properties of HfO_2-based films had been experimentally revealed, the electrode contributions to these effects had not been investigated. For example, nearly every investigation of HfO_2-based ferroelectrics observed that the presence of the top electrode during thermal processing resulted in enhanced contents of the orthorhombic phase. This enhancement was regularly attributed to mechanical stress imparted by the top electrode. However, the exact physical mechanism by which this stress was imparted by the top electrode, and the quantities of such stresses, had not been directly investigated. Such a gap stemmed, partially, from a dearth of knowledge about the elastic properties of HfO_2-based ferroelectrics, and alluded to the need for adaptation and application of diffraction-based stress analysis techniques for these systems.

Within this dissertation, the interactions between binary nitride, metallic, and conductive oxide electrodes and HZO will be investigated. These interactions will be shown to be both chemical and physical in nature. Different field-cycling behaviors of HZO will be shown to be related to the manner in which the electrode and ferroelectric layers exchange oxygen, oxygen vacancies, and injected electrons. It will also be shown that the specific interface with the top electrode is responsible for influencing the stress of the HZO layer and stabilizing the orthorhombic phase. Such observations will be made through application of adapted diffraction and electrical characterization techniques, and will facilitate the future engineering of HfO_2-based ferroelectric devices through tailoring their interactions with their neighboring electrode layers.

Acknowledgement

Completion of a doctorate of philosophy is oft described as a journey akin to a marathon. While there are parallels between these journeys, a real marathon occurs through the efforts of a single runner over the course of several hours during a single day, whereas this journey occurs through the combined efforts of many participants over several years. While it may seem that a dissertation defense is simply the testimony of a single researcher as they cross their finish line, in reality, the credibility of their effort, immortality of their findings, and strength of their continued resolve are the product of a community of support, which should take similar pride in the end of this race.

As the end of this journey approaches, I am compelled to reflect on those who have supported me throughout, and propelled me to learn and explore well beyond what I had originally envisioned. I have had the honor of calling number of wonderful people, well outside Charlottesville, Virginia, part of this network. My family, Julia, William, Mattson, and Jason Fields have provided a steady force of assurance since long before I began my academic journey, and encourage me every day to pursue my scientific interests. My longtime friends, Thomas McKinless, Daniel Shinners, Alan Gordon, Patrick Dwyer, Addison Janney, Greg Jacks, Johnny Nelson, Jake Ford, Theo Kelley, Bayard Roberts, Katie Menoche, Jonathan Bloom, and Lyle Henderson have always been and will forever be a source of warmth and happiness, who present constant reminders of what truly matters in life and in love. These people raised me, and any curiosity, work ethic, or optimism that I have displayed throughout my time at UVA can be traced to time spent with them.

Since I began this academic journey, a major part of my community of support has been my advisor, Dr. Jon Ihlefeld. Hiring the first member of any research group is an important, deterministic decision, and, on paper, Jon took a risk in selecting me. I was connected with him by Dr. Elizabeth Opila, who has been a simultaneous friend and indispensable source of research and professional guidance throughout my work in undergraduate and graduate school. Jon hired me in spite of my comparatively weak GPA, average test scores, and lack of background in materials science, asking only that I set an example to the future group and publish my work. His intellectual feedback and guidance have since been instrumental in helping me grow as a researcher and

assemble this dissertation. He has also demonstrated, from day one, that he would never ask me to work harder than he would. Should I ever find myself in a leadership role, I hope to also have this quality. I also benefitted heavily from his relationships with researchers at Sandia National Laboratories, including Drs. Sean Smith, David Henry, Giovanni Esteves, and Paul Davids, who taught me a great deal about the field of materials science, and helped me to become a better researcher and communicator through their collaboration. Dr. Henry, in particular, has been a great outside help in my navigation toward my future as a researcher.

Since my joining of the Ihlefeld Multifunctional Thin Films Research Group in December of 2017, this support network has steadily grown. Samantha Jaszewski, Ian Brummel, and Alejandro Salanova were some of the earliest additions to this film family, and it is impossible to imagine being in graduate school without them. Their talent, mindset, focus, sense of mischief, and strong work ethic are inspiring, and laid the foundation upon which the entire group has been constructed. More recent additions to the group, including Dr. Takanori Mimura, Liron Shvilberg, Lauren Askew, and Megan Lenox have continued the strong traditions of hard work, and raise the caliber of research every day. There are many other professors, staff, and students throughout the department who I have relied on for counsel and encouragement, however the production of such a list would be a dissertation chapter in itself, because on this subject, UVA materials science truly sets the standard for a collaborative and welcoming institution.

Outside of research, my support network has extended deep into the UVA and Charlottesville communities through this journey. Marcel Mibus, Colin Tattersall, Rob Golden, Erin Adonnino, Gerard Rodriguez-Lopez, Jane Muir, and Lucas Herweyer are a few of the many Charlottesvillians who I have been privileged enough to call friends. Their companionship during our various trips, concerts, sporting events, fitness classes, bar trivias, nights out, and nights in was never taken for granted, and I count my lucky stars every time I reflect on the fun that we have had together so far. Marcel, in particular, regularly provided guidance and support essential for the navigation of a naïve graduate student through the doctoral program.

A key member of this support group through this journey, who closely followed its every twist and turn, is my partner, Madeleine Gates. She, and her wonderful family, Gary, Laura, Luke, and Nathan Gates, have welcomed me countless times with open arms, genuine interest, and hearty laughs. With her, I have shared the highest highs and the lowest lows. From near and afar, she

showed incredible strength during difficult times, and grace when times were good. She is an everyday reminder to remain optimistic, irrespective of whatever else was going on in life. *Sine qua non*.

Table of Contents

Chapter 1: Conventional Perovskite Ferroelectrics and Their Polarization and Field Cycling Properties 26

1.1 Introduction 26

1.2 Conventional Ferroelectric Materials, Applications, and Concepts 26

1.3 Field Cycling Behavior of Conventional Perovskite Ferroelectrics 33

1.4 Common Applications of Conventional Perovskite Ferroelectric Materials 35

1.5 Factors Preventing Direct Integration of Perovskite Ferroelectrics into Silicon CMOS Technology 36

1.6 Summary 37

Chapter 2: Factors Affecting the Ferroelectric and Field Cycling Properties of Hafnium Oxide-Based Thin Films 39

2.1 Introduction 39

2.2 Ferroelectric Hafnium Oxide 39

2.3 Stabilization of the Ferroelectric Orthorhombic Phase in HfO_2-Based Thin Films 41

2.4 Overview of Electrode Interactions with HZO and HfO_2-based Thin Films 45

2.5 Field Cycling Properties of HZO and HfO_2-Based Thin Films 47

2.6 Summary 51

Chapter 3: Development of Deposition Processes and Characterization Techniques for Investigations of Ferroelectric Hafnium Zirconium Oxide 52

3.1 Introduction 52

3.2 Development of ALD, Sputtering, Annealing, and Etching Processes for HZO Devices.. 52

3.3 Quantifying Biaxial Stress in HZO Devices 66

3.4 Pyroelectric Measurements of HZO 76

3.5 Summary 80

Chapter 4: Phase-Transformation-Driven Wake-Up and Fatigue in Ferroelectric Hafnium Zirconium Oxide Films 81

4.1 Motivation 81

4.2 Abstract 82

4.3 Introduction 82

4.4 Experimental Procedures 86

4.5 Results and Discussion 88

4.6 Conclusions 102
4.7 Acknowledgement 103
Chapter 5: Compositional and Phase Dependence of Elastic Modulus of Crystalline and Amorphous $Hf_{1-x}Zr_xO_2$ Thin Films 105
5.1 Motivation 105
5.2 Abstract 106
5.3 Introduction 106
5.4 Experimental Procedures 108
5.5 Results and Discussion 109
5.6 Conclusions 126
5.7 Acknowledgement 127
Chapter 6: Metal Nitride Electrode Stress and Chemistry Effects on Phase and Polarization Response in Ferroelectric $Hf_{0.5}Zr_{0.5}O_2$ Thin Films 128
6.1 Motivation 128
6.2 Abstract 129
6.3 Introduction 129
6.4 Experimental Procedures 132
6.5 Results and Discussion 134
6.6 Conclusions 153
6.7 Acknowledgement 154
Chapter 7: Wake-up and Fatigue Mechanisms in Ferroelectric $Hf_{0.5}Zr_{0.5}O_2$ Films with Symmetric RuO_2 Electrodes 156
7.1 Motivation 156
7.2 Abstract 157
7.3 Introduction 157
7.4 Experimental Procedures 160
7.5 Results and Discussion 163
7.6 Conclusions 177
7.7 Acknowledgments 177
Chapter 8: Investigation of the Stresses Due to the Clamping Effect in Ferroelectric $Hf_{0.5}Zr_{0.5}O_2$ Thin Films with TaN Electrodes 179
8.1 Motivation 179
8.2 Abstract 180

8.3 Introduction 180
8.4 Experimental Procedures 183
8.5 Results and Discussion 186
8.6 Conclusions 215
8.7 Acknowledgements 217
Chapter 9: Conclusions 218
Chapter 10: Future Work 220
Chapter 11: Appendix 224

List of Figures

Figure 1.1. Diagram of conventional perovskite oxide ferroelectric switching. The orange spheres represent the oxygen atoms, whereas the red and blue spheres represent different cation species. The dipole orientation is indicated adjacent to each structure, and the orientation of the cation about the oxygen tetrahedra is indicated by green and red. 27

Figure 1.2. (a) Diagram of domains and domain wall in a generic ferroelectric material. The location of the domain wall, wall width, and polarization directions are indicated in black, whereas the shift of polarization orientation is indicated with a green dotted line. Plan view diagram of (b) unpoled and (c) poled ferroelectric surface. Positively and negatively oriented regions are indicated in orange and blue, respectively.. 29

Figure 1.3. Diagrams of (a) negatively poled domain structure, (b) domain structure switching during the application of a positive field, and (c) positively poled domain structure. The locations of the nucleation sites at the interfaces are indicated with red dotted lines, and the regions comprising the positively and negatively oriented domains are indicated by orange and blue, respectively. 30

Figure 1.4. (a) Electric field pulse shape and polarization response associated with an (b) ideal ferroelectric hysteresis loop and (c) a hysteresis loop with substantial leakage current contributions. Blue and green dots represent the beginning/end and middle of a typical measurement, respectively. Relevant characteristics which can be easily extracted from a hysteresis loop, including P_r, E_c, P_{sw}, and εr estimate, are indicated in red on diagram (b). In diagram (c), the blue line represents the total $P(E)$ response, including the film polarization and leakage current contribution. 31

Figure 1.5. (a) Pulse train utilized for PUND measurement. (b) Polarizations associated with each phase of measurement (orange solid line) with the corresponding electric field pulses (blue dotted line). Positive and negative maximum with switching contribution (P_*), remanent with switching contribution (P_{r*}), maximum without switching contribution ($P_\wedge$) and remanent without switching contribution ($P_{r\wedge}$) polarizations are indicated along with mathematical relationships between these quantities and the reported P_r and P_{sw} magnitudes (upper right).. 32

Figure 1.6. (a) Decrease in switchable polarization with field cycling due to fatigue. Domain structure experiencing (b) bulk domain wall pinning and (c) nanodomain nucleation inhibition following field cycling. Defect positions are indicated with red circles, whereas pinned nanodomains and domains are shown as solid red lines. 34

Figure 2.1. Crystal structures of (a) $P2_1/c$ monoclinic, (b) $P4_2nmc$ tetragonal, and (c) ferroelectric $Pca2_1$ orthorhombic phases of hafnium oxide. The arrow denotes the spontaneous polarization direction of the orthorhombic phase. 40

Figure 2.2. Diagrams of $P(E)$ responses for HZO thin films with compositions varying between pure HfO_2 and pure ZrO_2. Approximate film compositions and qualitative descriptions of responses are shown below each diagram. 44

Figure 2.3. Diagram of orthorhombic phase stabilization model showing effects of increasing grain surface area to volume ratio (SA:V) through decreasing film thickness and subsequent polarization enhancement with the addition of dopants, application of biaxial stress, and incorporation of oxygen vacancies. 45

Figure 2.4. Diagram of the interface between a HfO_2-based thin film (blue), TiN or TaN top electrode (gray) and oxide/oxynitride (orange) in the (a) as-deposited and (b) following processing states. The locations of oxygen (O), oxygen vacancies (Vo..), and metal-nitride (MN) species as well as oxide/oxynitride layers (MO_xN_y/MO_x) are indicated. 46

Figure 2.5. Diagram of typical field cycling behavior of a HfO_2-based ferroelectric. The oxygen vacancy behaviors are indicated in green, the resulting effects on the film properties are indicated in blue, the film polarization and separation between the wake-up and fatigue regimes are shown as red and gray dotted lines, respectively, and the qualitative regime descriptions are indicated in their respective regions. 48

Figure 2.6. Diagram comparing oxygen vacancy behavior before (Pristine) and following field cycling of HfO_2-based ferroelectric thin films processed with (a) Pt and (b) binary nitride electrodes. The layers are indicated on the left, and the general positions of the oxygen atoms (O) and oxygen vacancies (Vo..) are identified. 50

Figure 3.1. (a) GIXRD pattern measured on a 100 nm-thick as-deposited TaN film on a silicon substrate with associated (b) XRR pattern (blue) and fit (orange). (c) XPS spectra measured in the

N 1*s* and Ta 4*f* regions with associated fits. (d) Dark Field STEM micrograph measured on thermally processed TaN/HZO/TaN film stack. 54

Figure 3.2. Diagram of typical ALD process in which the (a) bare substrate is (b) exposed to precursor molecules, which (c) half-react with the substrate and remain on the surface. The precursor gas is then (d) purged from the atmosphere and (e) replaced with an oxidant (or second precursor species). This oxidant (f) fully reacts with the half-reacted precursor to form the near-monolayer of deposited species, followed by another (g) purge step, after which the substrate is then (h) re-exposed to precursor molecules which (i) half-react with this new layer. 55

Figure 3.3. Diagram of setup utilized to remove TaN layers with SC-1 etch procedures. 60

Figure 3.4. The standard MIM device used for investigations utilizing films prepared at the University of Virginia. The layer species are indicated on their respective locations, and the layer thicknesses are indicated on the right. 61

Figure 3.5. GIXRD patterns measured on (a) 20 and (b) 10 nm-thick HZO films with compositions ranging from pure HfO_2 (bottom) to pure ZrO_2 (top). The compositions of the films are indicated to the left of each respective pattern, and indexing for each of the observed reflections are indicated above each panel by grey dotted lines. 62

Figure 3.6. $P(E)$ responses measured before (orange) and after (blue) field cycling on (a-e) 20 and (f-j) 10 nm-thick HZO films with compositions spanning from pure HfO_2 to pure ZrO_2, as indicated above. 64

Figure 3.7. Remanent polarization magnitudes extracted from PUND measurements made on (a) 20 and (b) 10 nm-thick HZO films before (orange) and after (blue) field cycling as a function of composition. 65

Figure 3.8. CV profiles (orange line, left axis) and associated loss tangents (open points, right axis) measured on (a-e) 20 and (f-j) 10 nm-thick HZO films with varying composition, as indicated above the plots. 66

Figure 3.9. Area detector X-ray diffraction measurement setup utilized to collect patterns for $\sin^2(\psi)$ analyses. The programmable sample orientations, including incident angle (ω), sample tilt (χ), and sample rotation (ϕ), are indicated with green dotted lines and arrows, whereas the measurement frame angles, including angle from film normal (ψ), angle from detector normal (γ),

and diffraction angle (θ) are indicated with red dotted arrows. The location of the MgO powder standard is indicated with a black dotted arrow, whereas the X-ray path is indicated with blue arrows. 70

Figure 3.10. (a) Area detector diffraction pattern measured on a processed TaN/20 nm HZO/TaN film stack with indexing for HZO, silicon, and MgO reflections indicated with white arrows. (b) Unwarped area detector diffraction pattern with MgO diffraction lines indicated by white dotted lines and above panel. (c) Line scans extracted at various ψ angles, as indicated by the legend, with indexing for the HZO t + o reflection indicated with a blue dotted line. (d) Change in d-spacing (filled circles, left axis) and normalized t + o peak area (open circles, right axis) with ψ angle, along with linear fit of d-spacing data (red dotted line), calculated film biaxial stress (upper left), and XPS-measured film composition (upper left). 72

Figure 3.11. (a) Diagram of stylus profilometer measurement with substrate and profilometer tip labeled and scan profile direction indicated with a red dotted arrow. (b) Example height profile (blue) and associated 2d polynomial fit (orange) measured following HZO deposition on a TaN bottom electrode on a silicon substrate. 75

Figure 3.12. Diagram of pyroelectric measurement apparatus based on Sharp and Garn[226] method. Electrometer, thermocouple, Peltier cooler, sample, thermal mass, and AC drive components are indicated in black. 78

Figure 3.13. Sinusoidal temperature oscillation (red line, right axis) and resulting pyroelectric current (blue line, left axis) generated by a TaN/20 nm HZO/TaN device (a) before and (b) after poling with a single $P(E)$ measurement. The pyroelectric coefficients, calculated using the temperature and current profiles, are indicated in the lower left of each respective plot. 79

Figure 4.1. $P(E)$ response measured on symmetric MIM devices with (a) platinum (Pt), (b) TaN, and (c) tungsten (W) electrodes. (d) shows measured P_r and intrinsic ε_r for each structure in the pristine condition. 88

Figure 4.2. Rayleigh measurements at 10 kHz on symmetric MIM devices with (a) Pt, (b) TaN, and (c) W electrodes as a function of oscillator voltage. 89

Figure 4.3. X-ray diffraction patterns measured on each MIM device structure, TaN (top), Pt (middle), and W (bottom) with fits (solid lines) to each of the peaks shown. An X-ray wavelength of 1.3776 Å was utilized for diffraction measurements. 90

Figure 4.4. (a) Relative P_r, (b) relative t + o phase fraction, (c) relative permittivity, and (d) FWHM of the tetragonal/orthorhombic peak as a function of the number of 2.0 MV cm^{-1}, 1 kHz square wave cycles for symmetric MIM structures with Pt (grey triangles), TaN (blue squares), and W (orange circles) electrodes. 92

Figure 4.5. Diffraction patterns measured on each cycling interval pad for symmetric MIM devices with (a) Pt, (b) TaN, and (c) W electrodes. The number of 2.0 MV cm^{-1}, 1 kHz square wave cycles is indicated to the left of each pattern. The corresponding 2.5 MV cm^{-1}, 100 ms (Pt) or 1 ms (TaN, W) $P(E)$ response is plotted to the right of each pattern. An X-ray wavelength of 1.3776 Å was utilized for diffraction measurements. The magnitudes for the inset polarization and electric field axes are ± 25 μC cm^{-2} and ± 3.0 MV cm^{-1}, respectively. 93

Figure 4.6. Normalized integrated intensities for the (111) monoclinic, (111) monoclinic, and (101) tetragonal/(111) orthorhombic diffraction peaks measured on devices with platinum electrodes cycled at various intervals of 2.0 MV cm^{-1}, 1 kHz square waves. 94

Figure 4.7. Dielectric displacement dependence measured at each square wave interval for MIM devices with TaN (blue) and W (orange) electrodes (a, c, respectively), and corresponding $P(E)$ response with linear dielectric displacement subtracted (b, d, respectively). (e) Corresponding variable polarizations (P_v) for each square wave interval for devices constructed with TaN (blue) and W (orange) electrodes. 96

Figure 4.8. Relative permittivity versus electric field measurements on symmetric MIM devices with (a) TaN and (b) W electrodes cycled with 2.0 MV/cm, 1 kHz square waves at various intervals. 98

Figure 4.9. Switching current responses (a, b) derived from $P(E)$ response shown in Figure 4.7(a, c). Associated average $P(E)$ slope at the coercive field (c, d) measured on devices with TaN (blue) and W (orange) electrodes for P_v analysis in Figure 4.7(a-e). 100

Figure 4.10. Interplanar spacings of the (101) tetragonal/(111) orthorhombic, (111) monoclinic, and (111) monoclinic planes from symmetric MIM devices with (a) Pt, (b) TaN, and (c) W electrodes cycled at various intervals with 2.0 MV/cm, 1 kHz square waves. 101

Figure 5.1. (a) $P(E)$ measurements of HfO_2 (grey), $Hf_{0.69}Zr_{0.31}O_2$ (blue), $Hf_{0.54}Zr_{0.46}O_2$ (orange), $Hf_{0.21}Zr_{0.79}O_2$ (purple), and ZrO_2 (green) films. (b) P_r extracted from PUND measurements. .. 110

Figure 5.2. Current loops measured on HfO_2 (grey), $Hf_{0.69}Zr_{0.31}O_2$ (blue), $Hf_{0.54}Zr_{0.46}O_2$ (orange), $Hf_{0.21}Zr_{0.79}O_2$ (purple), and ZrO_2 (green) films. 110

Figure 5.3. GIXRD patterns measured on HfO_2 (grey), $Hf_{0.69}Zr_{0.31}O_2$ (blue), $Hf_{0.54}Zr_{0.46}O_2$ (orange), $Hf_{0.21}Zr_{0.79}O_2$ (purple), and ZrO_2 (green) films. 112

Figure 5.4. GIXRD patterns measured on amorphous HfO_2 (grey), $Hf_{0.69}Zr_{0.31}O_2$ (blue), $Hf_{0.54}Zr_{0.46}O_2$ (orange), $Hf_{0.21}Zr_{0.79}O_2$ (purple), and ZrO_2 (green) films. 112

Figure 5.5. Relative permittivity (lines, left axis) and loss tangent (open points, right axis) measured on (a) HfO_2, (b) $Hf_{0.69}Zr_{0.31}O_2$, (c) $Hf_{0.54}Zr_{0.46}O_2$, (d) $Hf_{0.21}Zr_{0.79}O_2$, and (e) ZrO_2 films. 113

Figure 5.6. XRR patterns (blue line) and associated fits (orange line) corresponding to crystalline (a) HfO_2, (b) $Hf_{0.69}Zr_{0.31}O_2$, (c) $Hf_{0.54}Zr_{0.46}O_2$, (d) $Hf_{0.21}Zr_{0.79}O_2$, and (e) ZrO_2 samples. 114

Figure 5.7. XRR patterns (blue line) and associated fits (orange line) corresponding to amorphous (a) HfO_2, (b) $Hf_{0.69}Zr_{0.31}O_2$, (c) $Hf_{0.54}Zr_{0.46}O_2$, (d) $Hf_{0.21}Zr_{0.79}O_2$, and (e) ZrO_2 samples. 114

Figure 5.8. Film density (orange, left axis) and thickness (blue, right axis) extracted from XRR patterns for crystallized (filled in circles) and amorphous (open squares) films with each composition. 115

Figure 5.9. (a) Acoustic responses measured on crystallized HfO_2 (grey), $Hf_{0.69}Zr_{0.31}O_2$ (blue), $Hf_{0.54}Zr_{0.46}O_2$ (orange), $Hf_{0.21}Zr_{0.79}O_2$ (purple), and ZrO_2 (green) films, with signatures corresponding to the Al/HZO and HZO/TaN interfaces indicated. (b) Elastic moduli calculated for crystallized (orange circles) and amorphous (blue squares) HZO films. 118

Figure 5.10. Acoustic responses measured on amorphous HfO_2 (grey), $Hf_{0.69}Zr_{0.31}O_2$ (blue), $Hf_{0.54}Zr_{0.46}O_2$ (orange), $Hf_{0.21}Zr_{0.79}O_2$ (purple), and ZrO_2 (green) films, with signatures corresponding to the Al/HZO and HZO/TaN interfaces indicated. 119

Figure 5.11. Schematic of picosecond acoustic wave propagation through sample. 119

Figure 5.12. Picosecond acoustic data (grey) and associated fitted background (blue), summed calculated fit (orange), Al/HZO signature gaussian fit (purple), and HZO/TaN signature gaussian fit (green) for the crystallized $Hf_{0.54}Zr_{0.46}O_2$ film. The positions of the acoustic signatures of the two interfaces (red lines) separated by a delay time, τ are indicated below. The composition of the film is indicated in the upper left of the panel. 120

Figure 5.13. (a) 2D XRD pattern measured on the $Hf_{0.69}Zr_{0.31}O_2$ sample with indexed m, t + o and MgO Debye rings indicated. (b) Change in t + o d-spacing with ψ angle relative to film normal (filled blue circles, left axis) with associated linear fit (red dotted line) used to calculate biaxial stress magnitude and normalized peak intensities (open blue circles, right axis) for the $Hf_{0.69}Zr_{0.31}O_2$ film. 122

Figure 5.14. (a) 2D XRD pattern measured on the $Hf_{0.21}Zr_{0.79}O_2$ sample with indexed HZO and MgO Debye rings indicated along (b) the associated unwarped pattern with intensity line scan profiles indicated as dotted lines. Intensity line scans are shown for the (c) HZO t/o diffraction peak used for $\sin^2(\psi)$ analysis and (d) (111), (e) (200), and (f) (022) MgO diffraction peaks used for pattern unwarping, with the associated ψ angle colorations identified in the legend in panel (c). Dashed lines represent the indexing for each diffraction peak. 123

Figure 5.15. 2D XRD patterns measured on (a) HfO_2, (b) $Hf_{0.54}Zr_{0.46}O_2$, (c) $Hf_{0.21}Zr_{0.79}O_2$, and (d) ZrO_2 samples with indexed monoclinic, tetragonal, and orthorhombic Debye rings indicated. The Debye rings from the stress-free MgO powder standard are also indicated. 124

Figure 5.16. Change in d-spacing with ψ angle relative to film normal (filled circles, left axis) with associated linear fit (red dotted line) and normalized peak intensities (open circles, right axis) for the (200) diffraction peak of the MgO stress-free standard adhered to the (a) HfO_2, (b) $Hf_{0.69}Zr_{0.31}O_2$, (c) $Hf_{0.54}Zr_{0.46}O_2$, (d) $Hf_{0.21}Zr_{0.79}O_2$, and (e) ZrO_2 samples. 124

Figure 5.17. Change in t + o d-spacings with ψ angle relative to film surface normal (filled circles, left axis) with associated linear fits (red dotted line) used to calculate biaxial stress magnitudes and normalized peak intensities (open circles, right axis) for the (a-b) HfO_2 ((111) and (111) reflections, respectively), (c) $Hf_{0.54}Zr_{0.46}O_2$, (d) $Hf_{0.21}Zr_{0.79}O_2$, and (e) ZrO_2 films. The calculated

biaxial stress magnitudes are tabulated in the upper left of each panel along with the HZO composition. 126

Figure 6.1. (a) Diagram of device structure with layer materials, thicknesses, and as-deposited biaxial stress states indicated (where applicable). (b) Variation in as-deposited biaxial stress of the TaN electrodes with argon background pressure utilized during sputter deposition. 135

Figure 6.2. (a) Unwarped XRD area detector data from the Bottom Varied sample with the 6.7 mTorr background pressure TaN sputtering condition following processing with indexed Debye rings indicated. (b) Diffraction line scans extracted from the area detector data at specific ψ angles (indicated to the left of corresponding patterns) with indexing (grey dashed lines) indicated across the top of the panel. 137

Figure 6.3. Grazing Incidence XRD patterns measured on (a) Top Varied and (b) Bottom Varied Sample series. Indexing for each of the observed peaks is indicated above the panels and the sputtering background pressure of the condition-varied TaN electrode is indicated to the left of each pattern. 138

Figure 6.4. t + o *d*-spacing (filled in points, left axis) and normalized t/o intensity (open points, right axis) dependence on ψ angle and associated linear fit (red lines) used to calculate the post-processing biaxial stress states for the (a) 6.7, (b) 7.7, (c) 8.3, (d) 9.4, and (e) 10.1 mTorr background pressure TaN sputtering conditions in the Bottom Varied sample series. The utilized background pressures during stress-varied electrode sputtering and calculated post processing HZO biaxial stress states are indicated in the lower left of each panel. (f) Comparison between as-deposited TaN biaxial stress and post-processing HZO biaxial stress for both Bottom (orange) and Top (blue) Varied sample series. 139

Figure 6.5. t + o *d*-spacing (filled in points, left axis) and normalized t/o intensity (open points, right axis) dependence on ψ angle and associated linear fit (red lines) used to calculate the post-processing HZO biaxial stress states for the (a) 6.7, (b) 7.7, (c) 8.3, (d) 9.4, and (e) 10.1 mTorr background pressure sputtering conditions in the Top Varied sample series. The utilized background pressures during TaN sputtering and calculated post-processing HZO biaxial stress states are indicated in the lower left of each panel. 140

Figure 6.6. Nested hysteresis loop measurements made on the Top Varied sample series with TaN electrodes deposited with (a) 6.7, (b) 7.7, (c) 8.3, (d) 9.4, and (e) 10.1 mTorr background pressure sputtering conditions. The background pressures utilized for sputter deposition of the stress varied (top) TaN electrodes and resulting post-processing HZO biaxial stress states are indicated in the lower right of each panel. 141

Figure 6.7. Nested hysteresis measurements made on the Bottom Varied series with TaN electrodes deposited with (a) 6.7, (b) 7.7, (c) 8.3, (d) 9.4, and (e) 10.1 mTorr background pressure sputtering conditions. The background pressures utilized for sputter deposition of the stress varied (bottom) TaN electrodes and resulting post-processing HZO biaxial stress states are indicated in the lower right of each panel. 142

Figure 6.8. Change in P_r with (a) post-processing HZO biaxial stress and (b) as-deposited TaN electrode biaxial stress. 144

Figure 6.9. XPS spectra for the N 1*s*/Ta 4*p* (left) and Ta 4*f* regions (right) for the 6.7 mTorr background pressure TaN sputtering condition. The summed fit (blue line) is plotted over the raw data (grey points) with associated peaks and background plotted below, residuals from the fit plotted above each panel (red), and the background pressure utilized during sputtering and resulting as-deposited biaxial stress indicated above. 146

Figure 6.10. XPS spectra for the N 1*s*/ Ta 4*p* (left) and Ta 4*f* regions (right) for the (a) 7.7, (b) 8.3, (c) 9.4, and (d) 10.1 mTorr background pressure TaN sputtering conditions. The summed fits (blue lines) are plotted over the raw data (grey points) with associated peaks and backgrounds plotted below, residuals from the fits plotted above each panel (red), and the utilized background pressures and resulting as-deposited biaxial stresses indicated above each residuals plot. 147

Figure 6.11. XPS spectra for Ta 4*f* region measured on the 6.7 mTorr background pressure sputtering condition at angles of (a) 30°, (b) 40°, (c) 50°, (d) 60°, and (e) 70°. The summed fits (blue lines) are plotted over the raw data (grey points) with associated peaks and backgrounds plotted below and measurement angle indicated in the upper left. (f) Measured Ta_2O_5/TaN intensity ratio plotted against measurement angle (orange points) with associated optimized fit (blue line) with infinite intensity (*k*) and oxide thickness (*d*) fitting parameters indicated in the lower left of the panel. 148

Figure 6.12. (a) N:Ta ratio as a function of background pressure utilized during sputter deposition of the TaN electrodes and (b) HZO P_r dependence on TaN stoichiometry for both Bottom (orange) and Top (blue) Varied sample series. 149

Figure 6.13. GIXRD patterns measured on TaN electrode layers sputter deposited with various background pressure conditions, as indicated above each pattern, with indexing (grey, dotted lines) for observed peaks indicated across the top of the panel. 150

Figure 6.14. Leakage current density measurements for (a) Bottom and (b) Top Varied Sample series. The legend indicates N:Ta ratio of sputtering condition-varied TaN electrode layer. 152

Figure 6.15. (a) Leakage current density measured at +2.0 MV cm^{-1} (open points) and -2.0 MV cm^{-1} (closed points) and (b) relative t + o phase fractions for HZO films as a function of the nitrogen content of the TaN electrodes. Orange circles and blue square points represent films in the Bottom and Top Varied sample series, respectively. 153

Figure 7.1. Applied voltage profiles (red, left axis) and resulting current densities (black, right axis) measured across devices with (a) 100 µm and (b) 1000 µm diameters. 162

Figure 7.2. GIXRD pattern measured on the RuO_2/HZO/RuO_2 sample with indexing for each peak provided above the panel. A logarithmic intensity scale was used owing to the high intensity of the RuO_2 110 reflection. 163

Figure 7.3. Nested polarization hysteresis measurements made following (a) 0, (b) 50,000, and (c) 10,000,000 cycles. Current loop measurements made following (d) 0, (e) 50,000, (f) 10,000,000 cycles. 165

Figure 7.4. Coercive fields extracted from hysteresis measurements made at each cycling interval. 165

Figure 7.5. Switchable polarization quantified from PUND measurements as a function of the number of 50% duty cycle, 2.0 MV cm^{-1}, 10 kHz bipolar pulses. 166

Figure 7.6. (a) Relative permittivity (lines, left axis) and loss (open circles, right axis) measured versus applied DC field at intervals between 0 and 10^8 field cycles, with number of cycles indicated by the color bar above the panel. (b) Relative permittivity measured at + 2.5 MV cm^{-1} (closed circles) and - 2.5 MV cm^{-1} (open circles) at intervals between 0 and 10^8 bipolar waves. 168

Figure 7.7. (a) Relative permittivity (left axis) and loss tangent (right axis) as a function of AC oscillator level measured at various intervals of bipolar waves, as indicated by the color bar above the plot. (b) Reversible Rayleigh coefficient, $\varepsilon_{\mathrm{init}}$, (left axis, closed points) and irreversible Rayleigh coefficient, α', (right axis, open points) measured at various cycling intervals. 170

Figure 7.8. Pyroelectric current (light red, left axis) and temperature oscillation (light grey, right axis) and associated sinusoidal fits (dark red and black, respectively) measured on devices cycled with (a) 1, (b) 50,000, and (c) 10,000,000 bipolar pulses.. 171

Figure 7.9. Pyroelectric coefficients (closed circles, left axis) and switchable polarizations (open circles, right axis) measured on devices cycled with various intervals of bipolar pulses........... 172

Figure 7.10. (a) Raw detector frame and (b) unwarped diffraction pattern measured on a singly poled device. Note that the intensities of the orthorhombic/tetragonal and monoclinic HZO peaks are too low to be easily discerned in the area detector pattern. 174

Figure 7.11. Diffraction patterns integrated from area detector patterns collected via microfocus XRD on individual devices following various intervals of bipolar waves, as indicated by the color bar on the right. Peak indices are provided above the plot and identified above the panel. A logarithmic intensity scale was used to increase the visibility of HZO peaks........................... 174

Figure 7.12. (a) Leakage current profiles measured on devices cycled at various intervals, as indicated by the color bar at the top of the panel. (b) Leakage current densities at ± 2.5 MV cm^{-1} extracted from leakage current profiles as a function of the number of field cycles................. 176

Figure 8.1. Nested *P*(*E*) responses measured on pristine (a) With TE, (b) TE Etched, and (c) No TE devices and awoken (d) With TE, (e) TE Etched, and (f) No TE devices........................... 187

Figure 8.2. FORC measurements made on pristine (a) With-TE, (b) TE-Etched, and (c) No-TE samples and on awoken (a) With-TE, (b) TE-Etched, and (c) No-TE samples......................... 189

Figure 8.3. CV permittivity (left axis, lines) and loss tangent (right axis, open points) made on (a) pristine and (b) awoken With-TE (blue), TE-Etched (orange), and (c) No-TE (grey) films...... 190

Figure 8.4. GIXRD patterns measured on the No-TE (grey), TE-Etched (orange), and With-TE (blue) films. The fits for each observed (111) monoclinic (red dotted line), t + o (green dotted line) and (111) monoclinic (purple dotted line) peak and fit background (black line) are offset below

each corresponding pattern. The indexing for each observed peak is indicated by grey vertical dotted line and listed above the panel, and the calculated t + o fraction is indicted to the left of each corresponding pattern.. 192

Figure 8.5. GIXRD patterns measured on the TE-Etched (orange) and re-exposed (blue) films. The fits for each observed (111) monoclinic (red dotted line), t + o (green dotted line) and (111) monoclinic (purple dotted line) peak and fit background (black line) are offset below each corresponding pattern. The indexing for each observed peak is indicated by grey vertical dotted line and listed above the panel, and the calculated t + o phase fraction is indicted to the left of each corresponding pattern.. 194

Figure 8.6. GIXRD patterns measured on the With-TE (blue), Partial RIE (red), and Full RIE (purple) films. The fits for each observed (111) monoclinic (red dotted line), t + o (green dotted line) and (111) monoclinic (purple dotted line) peak and fit background (black line) are offset below each corresponding pattern. The indexing for each observed peak is indicated by grey vertical dotted line and listed above the panel, and the calculated t + o phase fraction is indicted to the left of each corresponding pattern.. 195

Figure 8.7. IV measurements made on (a) pristine and (b) awoken With-TE (blue), TE-Etched (orange) and No-TE (grey) devices. 197

Figure 8.8. TEM micrographs measured on the (a) With-TE and (b) No-TE films. The layer materials are indicated on the left of each micrograph, and the scale bars and scan directions are provided on the right. EDS compositions measured for the Hf (blue line), Zr (red line), O (grey line), Ta (green dotted line), and N (red dotted line) species across the (c) With-TE and (d) No-TE films. The regions averaged to calculate $Hf_xZr_yO_z$ compositions (Comp. Calc.) for both samples are indicated with solid red vertical lines. 199

Figure 8.9. Plan-view SEM micrographs taken on (a) TE-Etched and (b) No-TE films. The results of grain size measurement are listed in the upper left of each panel. 200

Figure 8.10. HTXRD patterns collected on (a) With-TE and (b) No-TE samples. Indexing for each of the observed peaks is indicated above the plots, and the colors corresponding to the normalized intensities are provided to the right.. 202

Figure 8.11. XRR patterns (blue lines) and associated fits (orange lines) corresponding to (a) an unannealed TaN/HZO sample, (b) the With-TE sample, and (c) the No-TE sample. The XRR-fit HZO density is indicated in each respective panel. 203

Figure 8.12. XRR patterns (blue lines) and associated fits (orange lines) corresponding to an (a) unannealed and (b) annealed 100 nm-thick TaN layer. The XRR fit density is indicated in each respective panel... 204

Figure 8.13. Change in t + o *d*-spacing (closed points, left axis) and t + o normalized area (open points, right axis) with ψ angle relative to film normal fit from area detector XRD patterns measured on (a) With-TE, (b) TE-Etched, and (c) No-TE films. The linear fits (red dotted lines) plotted through the *d*-spacing data were utilized to calculate the biaxial stress following processing. 206

Figure 8.14. Area detector XRD patterns measured on (a) With-TE, (b) TE-Etched, and (c) No-TE samples. Unwarped area detector patterns measured on (d) With-TE, (e) TE-Etched, and (f) No-TE samples. Indexing of MgO and HZO Debye-Scherrer rings utilized for pattern unwarping and $\sin^2(\psi)$ analysis, respectively, are indicated on panels (a) and (d).. 207

Figure 8.15. Offset height profiles measured on (a) With-TE, (b) TE-Etched, and (c) No-TE samples on the initial substrates and following each processing step. The process steps corresponding to each height profile are listed to the right of each panel. The fit radii of curvature and calculated biaxial stresses are listed on each associated profile. 209

Figure 8.16. Cumulative (closed points) and individual process (open points) biaxial stresses quantified via wafer flexure measurements made on (a) With-TE, (b) TE-Etched, and (c) No-TE samples. The grey dashed line indicates the 0 GPa stress level, whereas the red dashed lines and red arrows indicate the biaxial stresses resultant from annealing with the top electrode, etching of the top electrode following annealing, and annealing without the top electrode in (a), (b), and (c), respectively. 210

Figure 8.17. Change in t + o *d*-spacing (closed points, left axis) and t + o normalized area (open points, right axis) with ψ angle relative to film normal fit from area detector XRD patterns measured on (a) Partial-RIE and (b) Full-RIE films. The linear fits (red dotted lines) plotted through the *d*-spacing data were utilized to calculate the biaxial stress following processing... 213

Figure 8.18. Change in t + o *d*-spacing (closed points, left axis) and t + o normalized area (open points, right axis) with ψ angle relative to film normal fit from area detector XRD patterns measured on (a) Single-TE and (b) Double-TE samples. The linear fits (red dotted lines) plotted through the *d*-spacing data were utilized to calculate the biaxial stress following processing. GIXRD patterns measured on the Single-TE (dark blue) and Double-TE (light blue) films. The fits for each observed (111) monoclinic (red dotted line), t + o (green dotted line) and (111) monoclinic (purple dotted line) peak and fit background (black line) are offset below each corresponding pattern. The indexing for each observed peak is indicated by grey vertical dotted line and listed above the panel, and the calculated t + o fraction is indicted to the left of each corresponding pattern. 214

Figure 9.1. Hysteresis response measured on a TiN/HZO/TiN device that employed the Oxford Plasma Technologies HfO_2 and ZrO_2 recipes. 225

Figure 9.2. Hysteresis responses measured on TiN/HZO/TiN devices prepared with 20 (red), 40 (green), and 60 ms (blue) H_2O pulse lengths. The maximum measurement fields are identified in the legend. 226

Figure 9.3. Hysteresis responses measured on TiN/HZO/TiN films prepared with TiN electrodes sputter deposited with atmospheres that were 17 (red), 19 (green) and 23% (blue) N_2. 227

Figure 9.4. Hysteresis responses measured on pristine (red) devices and after 10,000 (green) and 100,000 (blue) square waves. Devices were prepared with HZO recipes that had precursor purge steps that were (a) 30 and (b) 90 seconds long. 228

Figure 9.5. Hysteresis responses measured on a TiN/HZO/TiN device in the pristine state (red) and after 10,000 (green), and 100,000 (blue) square wave cycles. The HZO recipe utilized ozone as the oxidant. 229

Figure 9.6. Hysteresis responses measured on (a) TiN/HZO/TaN and (b) TaN/HZO/TaN devices in the pristine state (red), and after 10,000 (green) and 100,000 (blue) square wave cycles...... 230

Figure 9.7. Hysteresis responses measured in the pristine state (a) and after 10,000 (b) and 100,000 (c) square wave cycles on TaN/HZO/TaN devices processed with TaN with (a) 0, (b) 10, and (c) 20% N_2 in the sputtering atmosphere........ 231

Figure 9.8. Change in t + o *d*-spacing (closed points, left axis) and t + o normalized area (open points, right axis) with ψ angle relative to film normal fit from area detector XRD patterns measured at detector distances of (a) 0.069, (b) 0.070, and (c) 0.071 m. The linear fits (red dotted lines) plotted through the *d*-spacing data were utilized to calculate the biaxial stress following processing. 232

Figure 9.9. Change in t + o *d*-spacing (closed points, left axis) and t + o normalized area (open points, right axis) with ψ angle relative to film normal fit from area detector XRD patterns measured at locations near the (a) sample edge and about the (b) sample center. The linear fits (red dotted lines) plotted through the *d*-spacing data were utilized to calculate the biaxial stress following processing. 233

Figure 9.10. Change in t + o *d*-spacing (closed points, left axis) and t + o normalized area (open points, right axis) with ψ angle relative to film normal fit from area detector XRD patterns measured with φ rotational angle set at (a) 0°, (b) 30°, and (c) 90°. The linear fits (red dotted lines) plotted through the *d*-spacing data were utilized to calculate the biaxial stress following processing. 234

Chapter 1: Conventional Perovskite Ferroelectrics and Their Polarization and Field Cycling Properties

1.1 Introduction

Within this dissertation, an emergent system of silicon-compatible, scalable ferroelectric materials will be discussed. As such, this chapter provides information on what constitutes a ferroelectric material, how they are characterized, the mechanisms through which ferroelectric materials switch their polarization orientation, how they fatigue with progressive switching, and their major applications. The effects of incorporation of different electrode materials on these field cycling properties are discussed, followed by the hurdles preventing their widespread and commercial integration directly into silicon-based CMOS device platforms and technology.

1.2 Conventional Ferroelectric Materials, Applications, and Concepts

Ferroelectrics are a class of materials demonstrating a spontaneous crystallographic dipole that is reorientable through the application of an electric field, as diagramed in Figure 1.1. Such a property necessitates non-centrosymmetricity, a spontaneous polar axis, and the ability of the crystal to sustain an electric field strong enough to reorient said spontaneous polar axis without suffering dielectric breakdown. Ferroelectric materials are also necessarily pyroelectric because the magnitude of the spontaneous polarization can be altered with the addition or removal of thermal energy due to lattice expansion and contraction. Given that the crystallographic dipole can retain its orientation in the absence of applied electric fields or stresses, ferroelectric materials are ideal for applications in non-volatile computer memory, including ferroelectric random-access memory (FeRAM)[4] and ferroelectric tunnel junctions (FTJs).[5] As such, these materials are commonly characterized by their observable polarization at zero applied electric field, termed 'remanent polarization' (P_r). This value represents the electric dipole moment per unit volume, can be read as the aggregate of the accumulated surface polarization of all of the crystallographic dipoles within the material, and is useful in distinguishing between the 'up' and 'down' polarized states. The difference between these two states, the switchable polarization (P_{sw}), is a key element

of memory functionality. Moreover, the coupling between macroscopic polarization and mechanical strain[6,7] make ferroelectric materials ideal for applications in microelectromechanical systems (MEMS)[8,9] and radio frequency filters.[10] In tandem, recent progress in the integration of transistor and ferroelectric technologies has led to the realization of prototype low-power negative differential capacitance field effect transistors (NC-FETs).[11] Accordingly, conventional perovskite ferroelectric materials, including $Pb(Zr,Ti)O_3$ (PZT) and $BaTiO_3$ (BTO), have witnessed substantial development over the past 7 decades for many different device applications.[10,12,13]

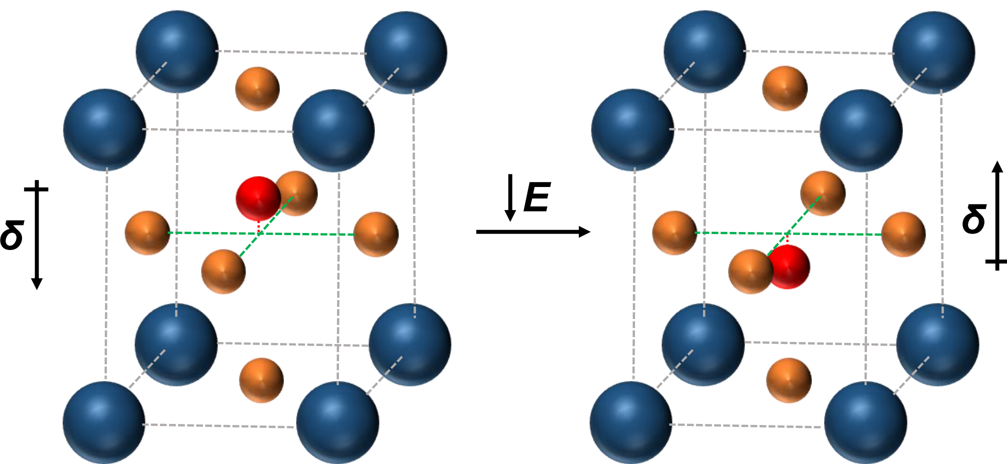

Figure 1.1. Diagram of conventional perovskite oxide ferroelectric switching. The orange spheres represent the oxygen atoms, whereas the red and blue spheres represent different cation species. The dipole orientation is indicated adjacent to each structure, and the orientation of the cation about the oxygen tetrahedra is indicated by green and red.

Real films and crystals of PZT and BTO contain separate regions with the same polarization orientation, referred to as ferroelectric domains.[14,15] Domains of different orientations form as a consequence of the competing electrostatic and mechanical energies of the system. Where it may be mechanically energetically favorable to have a uniform, uninterrupted polarization orientation, such a condition would be electrostatically unfavorable owing to the high energy required to maintain the surface polarization. Thus, domains of opposite polarization form to reduce the electrostatic energy of the system, at the expense of costing mechanical and surface energy to form a domain wall.[16,17] Domain walls, an example of which is diagramed in Figure

1.2(a), separate neighboring domains, which constitute crystallographic twins. Ferroelectric switching is driven by the nucleation and movement of domain walls, which propagate through the material to expand and contract domains in response to the applied electric field.[18]

Measurement of macroscopic polarization within a ferroelectric material is necessarily an examination of the relative populations of differently oriented domains. For example, if the polarization of a ferroelectric is examined immediately following cooling of the material from above its Curie Point (the temperature at which the spontaneous polarization is reduced to zero due to a change in symmetry), then nearly equal populations of 'up' and 'down' oriented domains will be observed (assuming no effects from external fields from processing or neighboring layers), as depicted in Figure 1.2(b). In this state, the material is said to be 'unpoled' and displays a macroscopic polarization of zero in spite of the presence of microscopic but 'canceling' spontaneous polarizations.[19] With the application of an electric field, the relative populations of domains will shift in response through the movement of domain walls, resulting in a 'poled' ferroelectric, as diagramed in Figure 1.2(c). It should be noted that this poling process is typically performed at elevated temperature in conventional perovskite ferroelectrics. If an electric field counter to the direction of the poling is applied, then the relative domain populations will switch to align with the new field accordingly.[20]

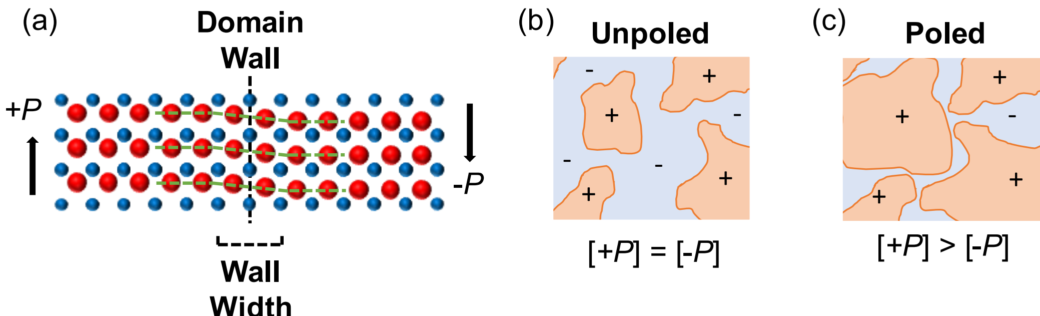

Figure 1.2. (a) Diagram of domains and domain wall in a generic ferroelectric material. The location of the domain wall, wall width, and polarization directions are indicated in black, whereas the shift of polarization orientation is indicated with a green dotted line. Plan view diagram of (b) unpoled and (c) poled ferroelectric surface. Positively and negatively oriented regions are indicated in orange and blue, respectively.

In PZT and BTO perovskite ferroelectrics, it has been shown that ferroelectric switching occurs via the nucleation of oppositely oriented domains at the electrode interfaces.[21] The nucleation sites are provided by defects, which locally create nanodomains that prevent a completely homogenous orientation from being attained, as diagrammed in Figure 1.3(a-c).[22] Nucleation of oppositely orientated domains with application of an opposite electric field at these nanodomain sites provides a practical explanation for the occurrence of switching, given that such an event would intrinsically require 10^3 kT (Boltzmann constant multiplied by temperature in K) of energy input.[23] These defects provide local biases that prevent the nanodomains from switching, allowing them to continually provide nucleation sites for oppositely oriented domains to grow.[21]

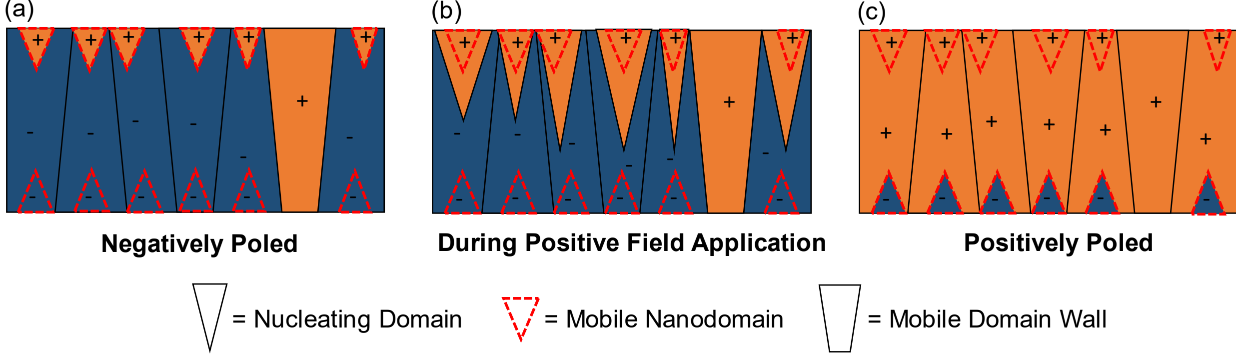

Figure 1.3. Diagrams of (a) negatively poled domain structure, (b) domain structure switching during the application of a positive field, and (c) positively poled domain structure. The locations of the nucleation sites at the interfaces are indicated with red dotted lines, and the regions comprising the positively and negatively oriented domains are indicated by orange and blue, respectively.

A conventional method by which the ferroelectric switching process is examined is the hysteresis (polarization-electric field, $P(E)$) loop. A $P(E)$ loop probes the macroscopic polarization response of a material with the application of a bipolar triangular wave, as diagramed in Figure 1.4(a). From the polarization response to the electric field stimulus, diagramed in Figure 1.4(b), information including a bulk coercive field (E_c) for the material and a switchable polarization magnitude can be directly quantified while the relative permittivity (ε_r) can be estimated. The coercive field (E_c), defined as the electric field magnitude at which ferroelectric switching occurs, is a material property[24] that can be affected by microstructural features,[25,26] mechanical stress,[27] and the presence of domain-pinning point defects.[28] It should be noted, as well, that displacement-electric field loops ($D(E)$) are often reported synonymously as $P(E)$ responses, which more correctly identifies that the polarization characterized in a hysteresis measurement contains contributions from both ferroelectric polarization and dielectric displacement, as described by Equation 1.1:[29]

$$D(E) = \varepsilon_r \varepsilon_0 E + P(E) \qquad 1.1$$

Where $D(E)$ is the dielectric displacement, ε_0 is the vacuum permittivity constant, E is the electric field, and $P(E)$ is the ferroelectric polarization. If a field is applied that does not exceed the coercive field, then complete ferroelectric switching will not occur. In addition, leakage current contributions to the polarization response can be identified by examining the polarization behavior in the vicinity of the electric field at which polarization saturation occurs, as shown in Figure 1.4(c).

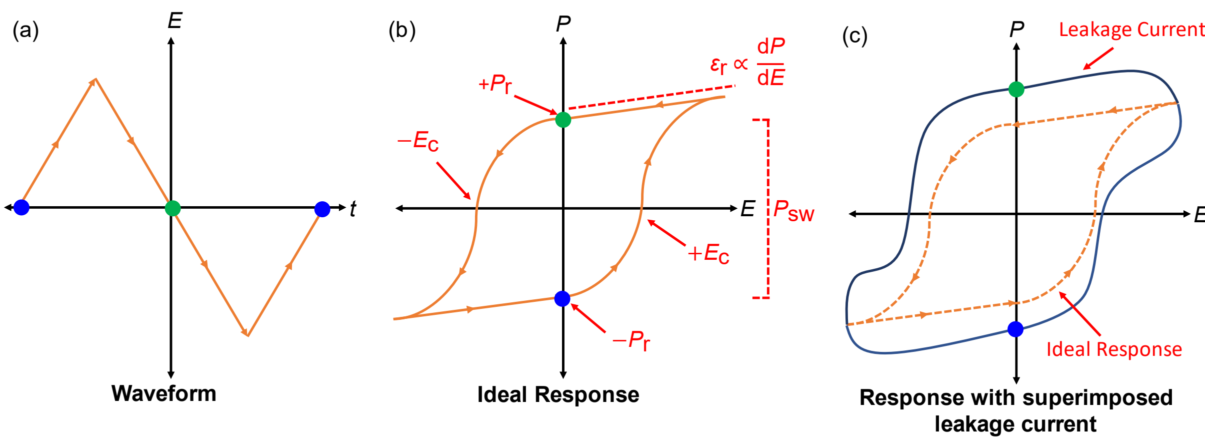

Figure 1.4. (a) Electric field pulse shape and polarization response associated with an (b) ideal ferroelectric hysteresis loop and (c) a hysteresis loop with substantial leakage current contributions. Blue and green dots represent the beginning/end and middle of a typical measurement, respectively. Relevant characteristics which can be easily extracted from a hysteresis loop, including P_r, E_c, P_{sw}, and ε_r estimate, are indicated in red on diagram (b). In diagram (c), the blue line represents the total $P(E)$ response, including the film polarization and leakage current contribution.

Polarization saturation occurs when the domain structure is completely switched, resulting in a linear polarization response as the electric field increases further. Leakage current superimposes curvature in hysteresis responses at saturation fields resulting in the appearance of larger polarizations, and has been known to result in misidentification of ferroelectric materials.[30] External contributions to the polarization response such as leakage current can make direct assessment of the switchable polarization difficult in highly cycled or damaged ferroelectric

films.[31] Thus, the Positive-Up, Negative-Down (PUND) pulsed polarization measurement is frequently employed as a more direct assessment of remanent polarizations.[32,33] The PUND pulse shape examines the polarization of the ferroelectric with minimal contributions from leakage current by pre-switching the device ahead of polarization measurement, as diagramed in Figure 1.5(a). Through subtraction of the non-switching related polarization ($P_{r^{\wedge}}$) from the total polarization (P_{r*}) at zero applied field, P_r and P_{sw} quantities can be calculated, as detailed in Figure 1.5(b). Accordingly, PUND measurements are frequently utilized to examine the variations in macroscopic polarization behavior driven by changes in relative domain abundance, wall mobility, and domain density that occur with electric field cycling.

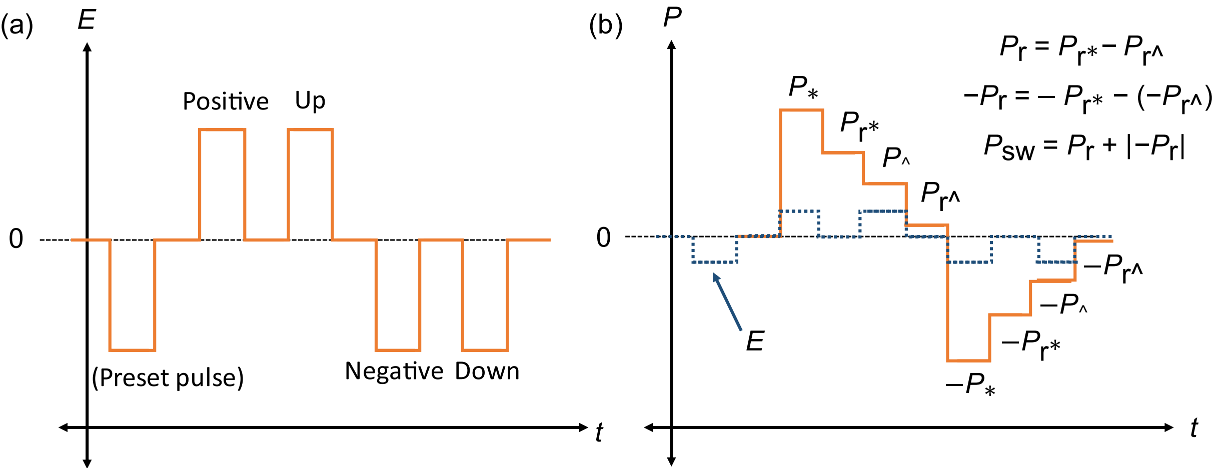

Figure 1.5. (a) Pulse train utilized for PUND measurement. (b) Polarizations associated with each phase of measurement (orange solid line) with the corresponding electric field pulses (blue dotted line). Positive and negative maximum with switching contribution (P_*), remanent with switching contribution (P_{r*}), maximum without switching contribution ($P_{\wedge}$) and remanent without switching contribution ($P_{r^{\wedge}}$) polarizations are indicated along with mathematical relationships between these quantities and the reported P_r and P_{sw} magnitudes (upper right).

1.3 Field Cycling Behavior of Conventional Perovskite Ferroelectrics

Examination of the field cycling behavior of ferroelectric-based devices is necessary for their ultimate integration into device structures, as this provides information on how the material can be expected to change with use and age. The field cycling process consists of application of cyclic electric fields across the ferroelectric to simulate the environment that a real device would operate within. Utilizing *P*(*E*) and PUND measurements, reductions in polarization magnitudes of perovskite ferroelectrics with field cycling have been widely observed, as diagrammed in Figure 1.6(a).[21,34–36] This occurrence is referred to as polarization fatigue, and has been shown to be driven by two main mechanisms; bulk domain wall pinning and nanodomain nucleation inhibition.[21] Both of these scenarios involve a restriction in the movement domain walls by external charge carrying defects, which accumulate at the interfaces, domain walls, and grain boundaries during cycling.[35,37,38] In the bulk domain wall pinning scenario, bound charges that accumulate at domain boundaries electrostatically couple with mobile carriers to locally satisfy electroneutrality.[21] This electrostatic couple produces an energetic landscape, which is unfavorable to the motion of the domain wall.[39,40] With field cycling, charge injection from neighboring electrode layers occurs and the concentration of charged defects increases, resulting in increased coupling between domain walls and mobile carriers, ultimately reducing the switchable polarization.[41] This process is diagrammed in Figure 1.6(b). Separately, polarization fatigue has also been attributed to the inhibition of domain nucleation at nanodomain sites.[42] Owing to the accumulation of defects and injected charge at the interfaces,[35,38] propagation of oppositely oriented domains from these nanodomain sites is reduced. Thus, a reduction in the switchable polarization occurs, as diagrammed in Figure 1.6(c).

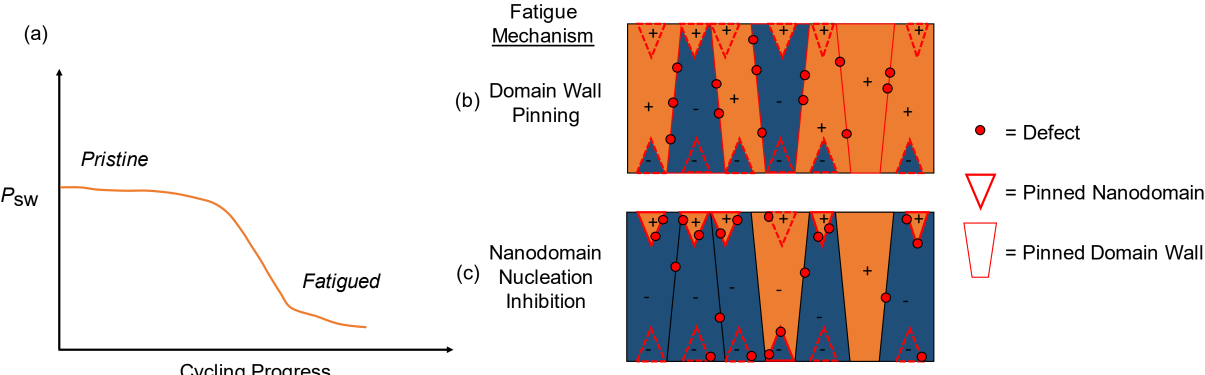

Figure 1.6. (a) Decrease in switchable polarization with field cycling due to fatigue. Domain structure experiencing (b) bulk domain wall pinning and (c) nanodomain nucleation inhibition following field cycling. Defect positions are indicated with red circles, whereas pinned nanodomains and domains are shown as solid red lines.

The polarization fatigue behavior with field cycling of perovskite ferroelectrics has been demonstrated to strongly depend on the utilized electrode material. A number of studies have reported polarization fatigue with cycling of PZT and BTO-based MIM devices with metallic platinum or palladium electrodes.[35,36,42,43] Conversely, when RuO_2 or IrO_2 materials were utilized for at least one of the electrodes, the polarization was not observed to substantially change with field cycling.[36,43] The lack of substantial polarization fatigue when conductive oxides were employed instead of metallic materials is evidence that the oxide electrodes yield different charge injection and mass transfer behaviors than their metallic counterparts with field cycling.

The mechanism by which polarization fatigue is mitigated through utilization of oxide electrode materials has been revealed to be a combination of two processes. It has been shown that the field cycling-driven transfer of oxygen and oxygen vacancies between the electrode and ferroelectric layers is facilitated by neighboring oxide electrodes.[35] This transfer prevents the accumulation of these defects at interfaces, which reduces the amount of domain pinning due to field cycling.[36] Separately, the localized doping of domain walls from electrode layers has been shown to yield charge relaxation, which reduces the coupling between them and mobile carriers.[21,44] It is not explicitly known whether oxygen vacancy transfer or localized interface doping is the main contributor to polarization fatigue reduction and it is also unknown whether

nanodomain nucleation inhibition or bulk domain wall pinning more dominantly drive polarization fatigue. Regardless, development of a functional device that can be extensively field cycled requires engineering of polarization fatigue behavior, which has been shown to proceed via nanodomain or domain pinning due to defect accumulation at domain boundaries, which are mitigated through utilization of oxide electrodes.

1.4 Common Applications of Conventional Perovskite Ferroelectric Materials

With development of perovskite ferroelectric materials that are nearly fatigue-free with field cycling, a number of important applications have emerged, which harness their large piezoelectric coefficients (d_{33}). The piezoelectric coefficient quantifies a material's coupling between electric field and strain.[29] Larger values are indicative of a more pronounced strain effect due to an applied electric field (or *vice versa*) and are useful in acoustic applications, energy harvesting devices, and MEMS. Ferroelectric materials possess large piezoelectric coefficients (d_{33} = 50 – 100 pm V^{-1} for PZT[45,46]) owing to their extrinsic domain wall contributions[47] while also providing the opportunity to vary this value through application of an electric field.[45] For these reasons, ferroelectric materials are commonly implemented in microcantilevers, actuators, and stress sensors.[10]

Another common commercial application for perovskite ferroelectric materials, specifically doped BTO, is in multilayer ceramic capacitors (MLCCs).[48] These devices harness the large relative permittivities of BTO[49] in tandem with planar, layered device designs, which maximize available volumetric capacitance to separate and filter large AC-DC voltages.[17] Further research has endeavored to change the Curie temperatures of these materials, through inclusion of dopants and substituents (such as Zr and Sr),[50] to vary the operating temperature of the yielded MLCC.

Beyond devices which employ the large, variable piezoelectric coefficients and capacitances demonstrated by perovskite ferroelectrics, a number of structures harness their pyroelectric properties to convert between thermal and electrical energy.[51] These devices are capable of generating current or voltage in response to temperature oscillations, which can be stored as energy[51] or read as a thermal signal.[52] Such applications rely on large pyroelectric

coefficients, which quantify the coupling between thermal energy and current or voltage production. PZT, commonly employed in pyroelectric devices and sensors, boasts a large pyroelectric coefficients in excess of ~200 $\mu C\ m^{-2}K^{-1}$.[52,53] Other ferroelectric materials, which may demonstrate smaller pyroelectric coefficients, have also witnessed development in these applications owing to competitive figures of merit that have permittivity, thermal conductivity, and loss tangent contributions. Moreover, chemical compatibility with materials present in the final device is also a consideration in selecting a pyroelectric material.[51,53]

An additional commercialized application of these materials is Ferroelectric Random-Access Memory (FERAM), which is already commonly sold by companies including Fujitsu and Texas Instruments. These structures incorporate thin ferroelectric layers with transistors (one capacitor, one transistor, 1C1T), commonly $Sr_{0.8}Bi_{2.2}Ta_2O_9$ or PZT,[54,55] to hold a binary memory state.[4] This memory state can be read and rewritten and is non-volatile, meaning that it does not require energy input to keep. Additional memory structures, including ferroelectric tunnel junctions (FTJs),[5,56,57] which harness the effect of the switchable surface polarization on the band structure to alter tunneling characteristics between the 'up' and 'down' states, have been reported as viable memory units. In both of these device structures, large, scalable, switchable polarizations facilitate the ease with which the up and down states can be delineated.

1.5 Factors Preventing Direct Integration of Perovskite Ferroelectrics into Silicon CMOS Technology

While nearly fatigue-free ferroelectric materials can be developed for capacitive, sensor, energy harvesting, and memory applications, a number of scaling and compatibility issues prevent their widespread direct implementation into silicon-based CMOS technology. Scalability presents an issue for conventional oxide ferroelectrics due to the commonly observed decrease in switchable polarization with film thickness, driven by a corresponding decrease domain wall mobility.[49,58] Domain walls can vary in width depending on the ferroelectric material, processing history, and domain orientations, but tend to be several unit cells wide.[59–61] In addition, domain wall propagation through the ferroelectric is sensitive to the presence of line[62] or point defects,[63] grain boundaries,[64] polarizations from neighboring materials,[65–67] and mechanical clamping from adjacent layers.[68] Given that the interfacial regions between the ferroelectric and neighboring

layers contain larger quantities of mechanical strain and higher concentrations of point and line defects, these locations typically demonstrate reduced domain wall mobility and lower spontaneous polarizations.[69] In tandem, the influence of depolarization fields from incomplete electrode charge screening increases as interface separation decreases.[58] Hence, conventional polycrystalline thin film perovskite ferroelectrics suffer scaling effects, including diminished polarizations and piezoresponses when film thicknesses below ~100 nm are utilized.[49,58,70–72] Such a size limit for the switchability of a conventional perovskite ferroelectric means that ferroelectric device structures utilizing these materials lag behind the scaling of Moore's Law-abiding CMOS transistor devices.[73,74]

Aside from a lack of scalability, compatibility issues between PbO_x, BaO_x, and Si/SiO_x have also prevented on-chip development of common perovskite ferroelectric-based device structures. Formation of and reactions with these deleterious oxides during processing have been shown to be thermodynamically favorable,[75] preventing utilization of PZT and BTO materials in direct contact with silicon. Thus, between a lack of scalability and material incompatibility, devices utilizing conventional ferroelectric materials are unable to realize full implementation in contemporary Si-based CMOS transistor technology.

1.6 Summary

In summary, some useful properties of perovskite oxide ferroelectric materials have been described. It has been shown that ferroelectric switching occurs due to propagation of domain walls in response to applied electric fields. The macroscopic domain switching and polarization properties of ferroelectric materials can be measured and analyzed using $P(E)$ and PUND measurements. These measurements commonly observe decreases in switchable polarization with field cycling when metallic materials are implemented as electrodes. This polarization fatigue has been shown to occur due to accumulations of defects at ferroelectric domain boundaries and nanodomain nucleation sites, which reduces the ability for domains of opposite orientation to grow. These field cycling behaviors have been revealed to be strongly dependent on the selection of electrode material. For example, when conductive oxide materials are employed, instead of metallic electrodes, the polarizations of PZT and BTO ferroelectrics are not measured to fatigue with field cycling. This difference in behavior has been attributed to mass transfer of oxygen

vacancies between the ferroelectric and oxide electrode layers and local interfacial doping, which both reduce the amount of domain wall pinning during field cycling. While nearly fatigue-free ferroelectric materials are ideal for applications in piezoelectrics, energy harvesting, and memory, their implementation directly into silicon-based CMOS device platforms is hindered by a lack of scalability and silicon compatibility.

Chapter 2: Factors Affecting the Ferroelectric and Field Cycling Properties of Hafnium Oxide-Based Thin Films

2.1 Introduction

While ferroelectric materials can be implemented in memory, nonlinear optics, and transistor applications, conventional perovskite lead zirconate titanate and barium titanate materials are not silicon compatible and cannot scale competitively with contemporary complementary metal-oxide-semiconductor CMOS technology. Hafnium oxide-based ferroelectrics have emerged as materials that are silicon compatible and scalable, making them ideal for implementation in these applications. Current research endeavors to understand the roles that film chemistry, stress, and processing play in the stabilization of the non-equilibrium ferroelectric orthorhombic phase. Within this chapter, a review of the current understanding of the mechanisms and factors that govern the ferroelectricity and field cycling properties of HfO_2-based thin films is provided. Electrode materials, in particular, are identified as a means to tailor these behaviors for implementation in the next generation of silicon-based CMOS technology.

2.2 Ferroelectric Hafnium Oxide

In 2007, amorphous HfO_2, commonly grown via atomic layer deposition (ALD), was introduced as a gate dielectric to replace SiO_2 in Si-based transistors.[76] HfO_2 is silicon compatible[77] and has a dielectric constant ideal for equivalent oxide thickness scaling in its amorphous state, while maintaining low electron tunneling and leakage currents.[78] Thus, when this binary oxide was reported to demonstrate ferroelectricity when doped with SiO_2 in thin films in 2011,[1] a wide range of on-chip non-volatile memory,[79,80] integrated infrared sensor,[81] and nonlinear optics[82] applications became feasible.

Crystalline HfO_2 is stable in a $P2_1/c$ monoclinic phase at room temperature and pressure. This monoclinic phase, shown in Figure 2.1(a), demonstrates a relative permittivity of 15-20[83,84] and a unit cell volume of 35.1 Å^3.[85–87] At high temperatures or pressures or in small crystallite sizes, HfO_2 is stable in a $P4_2/nmc$ tetragonal phase.[88] This tetragonal phase, shown in Figure 2.1(b), demonstrates a dielectric constant of 35-70,[84,89] and maintains a unit cell volume of 33.8 Å^3.[87] This

phase is a field-induced ferroelectric, meaning that it is centrosymmetric at equilibrium, which can be broken through application of an applied electric field,[90,91] resulting in a polarization response that is similar in appearance to an antiferroelectric.[1] Henceforth, the polarization response of this phase will be referred to antiferroelectric-like. The stable ferroelectric response in HfO_2-based thin films is attributed to a metastable $Pca2_1$ orthorhombic phase, which is modeled to have lattice parameters of a = 5.06, b = 5.09, and c = 5.27 Å and a unit cell volume of 33.9 $Å^3$.[87,92,93] This orthorhombic phase, shown in Figure 2.1(c), is calculated to have a theoretical spontaneous polarization of 50 μC cm^{-2} along its short b-axis,[87,94] which results in a maximum polarization of ~25 μC cm^{-2} in a randomly oriented polycrystalline film.[90] This remanent polarization is achieved via the of oxygen atoms bonded within the orthorhombic unit cell about the short axis.[94,95] Such a feature distinguishes ferroelectric HfO_2 from ferroelectric perovskites such as BTO, which switch polarization states primarily through the reorientation of positive ions about their respective long axes. By comparison, the orthorhombic phase in HfO_2 has a unit cell volume that is 1.1 $Å^3$ smaller than the room-temperature monoclinic phase and 0.1 $Å^3$ larger than the high-temperature tetragonal phase.[87] In tandem, the orthorhombic phase has been calculated to have a lower surface energy than the monoclinic and tetragonal phases at room temperature.[96]

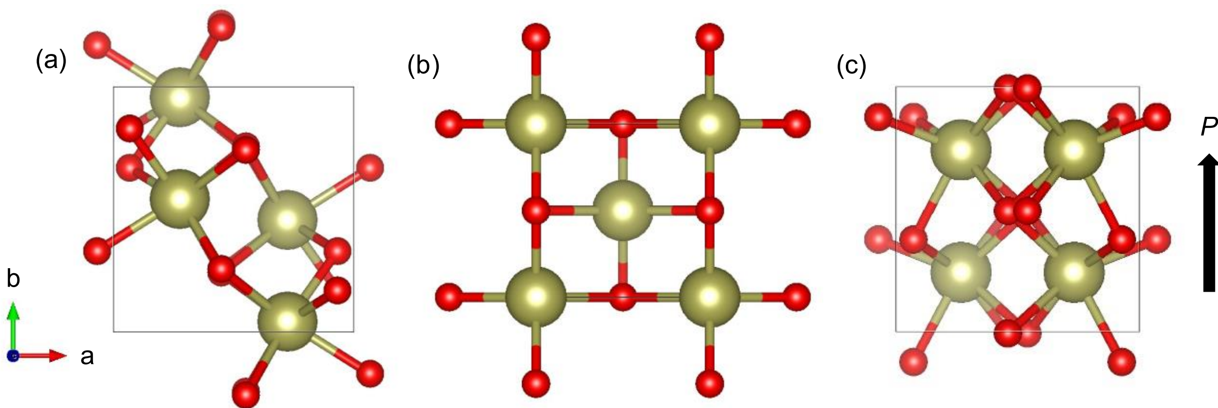

Figure 2.1. Crystal structures of (a) $P2_1/c$ monoclinic, (b) $P4_2nmc$ tetragonal, and (c) ferroelectric $Pca2_1$ orthorhombic phases of hafnium oxide. The arrow denotes the spontaneous polarization direction of the orthorhombic phase.

The ferroelectric orthorhombic phase does not appear on equilibrium phase diagrams of HfO_2 and is energetically metastable compared to the monoclinic and tetragonal phases.[88,93] Its stability relative to these two equilibrium phases has been theoretically calculated to be strongly related to the aforementioned surface energy effect,[96–98] which phenomenologically explains why ferroelectricity is generally observed in HfO_2-based films that are less than only 30 nm-thick.[98–100] Utilization of sub-30 nm film thicknesses truncates grain sizes, thus harnessing this surface energy effect to enhance the stability of the orthorhombic phase.[98,101]

While the explicit reasons for the enhanced scalability of HfO_2-based ferroelectrics compared to conventional PZT and BTO are still under investigation, recent modeling work has shown the domain walls in orthorhombic HfO_2 can theoretically be a single unit cell wide.[102] In tandem, stable polarization responses are widely observed in ferroelectric HfO_2-based films that are less than 10 nm-thick,[98,100,103,104] and have even been characterized in a film with a thickness of 1 nm.[105] Thus, HfO_2-based ferroelectrics demonstrate scalability that is superior to conventional ferroelectrics for transistor[106,107] and memory[108,109] applications while also maintaining silicon compatibility.[77]

2.3 Stabilization of the Ferroelectric Orthorhombic Phase in HfO_2-Based Thin Films

While silicon compatibility and ferroelectric scalability make HfO_2-based thin films advantageous for the next generation of on-chip transistor and memory devices, prepared films often contain substantial contents of the monoclinic and tetragonal phases[100,110] due to the aforementioned metastability of the orthorhombic phase. Accordingly, external effects such as the oxygen content within prepared films,[110,111] inclusion of dopants,[112–114] and imparting of biaxial stress[115,116] have been investigated as means to stabilize orthorhombic phase relative to the monoclinic and tetragonal phases in HfO_2 thin films.

Oxygen and oxygen vacancy content have been theoretically calculated[117] and experimentally shown[110,111] to be an important factor in the stabilization of the orthorhombic phase in undoped HfO_2-based thin films. As a result, deposition processes that aim to reduce the amount of oxygen within the HfO_2 layer, thus increasing the concentration of oxygen vacancies, have been developed. Such process modifications have included modulation of the oxidative ozone or water

pulses during atomic layer deposition (ALD)[111,118,119] and reducing the amount of oxygen in the processing atmosphere during sputtering.[110,120] These alterations modify the energy landscape to destabilize the monoclinic phase and increase orthorhombic phase contents and film polarizations at the expense of increasing the leakage current produced by the films,[111,118] which is facilitated by point defects.[121,122]

Separate from oxygen content engineering, incorporation of numerous dopant species, including Si,[1,91] Gd,[117,123] La,[124,125] Y,[126,127] Al,[128,129] and Zr,[3,130] among others,[94,112,113] have been investigated as avenues to prepare films with larger contents of the orthorhombic phase without directly increasing film leakage current densities. Mechanistically, dopant-driven ferroelectric phase stabilization has been attributed to a size mismatch between the dopant and hafnium ions.[125,131,132] This ionic size mismatch has been calculated to mechanically expand or contract the lattice, which destabilizes the equilibrium monoclinic phase.[113,124,125] In general, dopants with larger ionic sizes appear to facilitate larger remanent polarizations,[125,132] and dopant concentrations at which maximum remanent polarizations are achieved tend to be between 1 – 5%,[132] except for La[124] and Zr,[3] which boast larger dopant concentration windows within which the orthorhombic phase is stabilized.

Dopants including Y,[133] La,[124] and Zr[104] have been shown to stabilize the ferroelectric orthorhombic phase in film thicknesses larger than in pure HfO_2. In tandem, doped films have been broadly shown to demonstrate enhanced remanent polarizations compared to pure HfO_2. While remanent polarizations of 10 - 12 μC cm^{-2} have been reported for pure polycrystalline HfO_2 with engineered oxygen contents,[110,111] polarizations of 25,[124] 17,[123] 15,[128] 15,[134] 24,[126] and 18[3] μC cm^{-2} have been measured on La, Gd, Al, Si, Y, and Zr-doped films, respectively. These increases are mostly due to enhanced orthorhombic phase purity; however, it should also be noted that lattice expansion plays a role in the theoretical polarization of the unit cell, and effects of crystallographic texture facilitate larger measured values.[125] More recent investigations have noted the possibility of enhancing polarizations further through the utilization of more than one dopant[135,136] and simultaneously engineering the oxygen content of the film while adding doping species.[137]

Another advantage that has been widely observed when adding dopants to stabilize the ferroelectric phase in HfO_2 is a reduction in thermal budget. In pure HfO_2, thermal processing generally occurs at temperatures between 650 – 1000 °C.[100,110,111] Anneals at these temperatures

typically occur in an inert atmosphere and only for 20 – 30 seconds in order to yield the nanocrystalline grain sizes necessary for orthorhombic phase stabilization.[138] These elevated temperatures, however, are incompatible with back-end-of-the-line (BEOL) processing, in which lower temperatures are desirable to minimize diffusion of implanted species to maintain device feature definition.[139] Alternatively, doping of HfO_2 with Al, Gd, or Sr has been observed to reduce the necessary annealing temperatures for orthorhombic phase stabilization to ~500 °C.[140] Further, incorporation of dopants such as Y[126] and Zr[3,141–143] has been observed to reduce the crystallization temperature of the orthorhombic phase down to ~380 °C in polycrystalline films, with room-temperature growth demonstrated for 7% Y-doped HfO_2.[144] Thus, doping of HfO_2 has been widely shown to reduce the thermal budgets of these materials to more BEOL-compatible temperatures while still promoting the stabilization of the orthorhombic phase.

ZrO_2 has emerged as a promising alloying oxide for ferroelectric HfO_2 ($Hf_{1-x}Zr_xO_2$, HZO) owing to an advantageous compositionally-based polarization behavior control in addition to the aforementioned enhanced orthorhombic phase stabilization and superior low thermal budget.[3] Similar to HfO_2, bulk ZrO_2 is stable in a monoclinic phase at room temperature and pressure[85,145,146] and a tetragonal phase at high temperatures and in small crystallite sizes.[147] The high-temperature tetragonal phase, once again similar to HfO_2, demonstrates an antiferroelectric-like polarization response to applied electric fields.[3] This phase has been shown to crystallize in thin films at ~300 °C,[142] which likely contributes to the lower thermal budget of HZO alloys. In between the linear dielectric response of monoclinic HfO_2 and antiferroelectric-like response of tetragonal ZrO_2, alloyed compositions demonstrate mixed ferroelectric and antiferroelectric responses,[3] as diagramed in Figure 2.2, within a compositional window that is larger than the 1 – 5% observed for other dopant species.[112] The $Hf_{0.5}Zr_{0.5}O_2$ film composition, specifically, has been widely evaluated as an alloy demonstrating polarization responses and orthorhombic phase contents[2] superior to pure HfO_2[1] while maintaining equivalent silicon compatibility[42] and similarly harnessing mature deposition techniques already employed in CMOS fabrication technology.[77,148] Owing to these advantages, the HZO alloys have witnessed wide investigation of their polarization,[3] thermal budget,[142] nonlinear optics,[82] and pyroelectric properties,[149] among others.

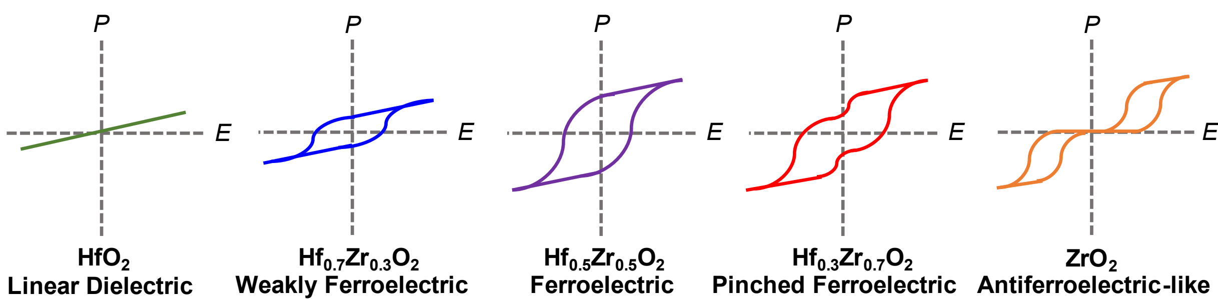

Figure 2.2. Diagrams of $P(E)$ responses for HZO thin films with compositions varying between pure HfO_2 and pure ZrO_2. Approximate film compositions and qualitative descriptions of responses are shown below each diagram.

Separate from oxygen content engineering and doping of HfO_2 to stabilize the orthorhombic phase, the presence of biaxial stress has been widely observed to affect the polarization properties. Computational works have reported that compressive hydrostatic and biaxial stresses can lower the free energies of the orthorhombic phase compared to the equilibrium monoclinic phase.[87,150] This stabilization is attributed to constraint of the aforementioned volume expansion during phase transformation between the tetragonal and monoclinic phases.[87] Conversely, experimental works have widely observed strong tensile stresses accompanying large polarizations in fully processed HfO_2-based ferroelectrics between binary nitride electrodes.[115,116,125,151,152] This correlation has been attributed to the short *b*-axis polarization in the orthorhombic structure, which results in increasing alignment between the domain structure and the film normal with increasing tensile biaxial stress.[153] The larger concentration of domains with polar vectors pointing toward the film surface results in larger measured polarization values. In tandem, larger tensile biaxial stresses have also been experimentally correlated with smaller monoclinic phase compositions using XRD,[115] in contrast to behavior predicted by calculations.[87,150] Regardless, combined with thickness scaling and incorporation of oxygen vacancies and dopants, application of biaxial stress provides another processing dimension within which the ferroelectric properties of HfO_2-based thin films can be investigated, as summarized in Figure 2.3.

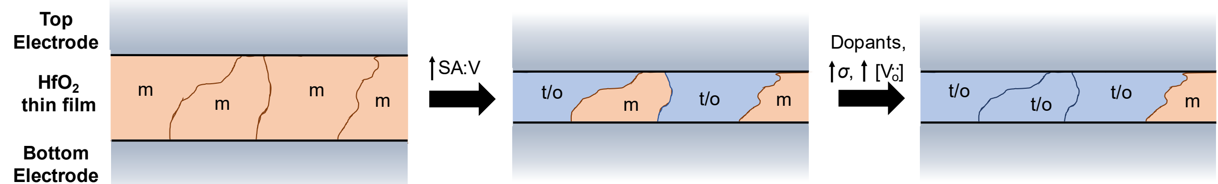

Figure 2.3. Diagram of orthorhombic phase stabilization model showing effects of increasing grain surface area to volume ratio (SA:V) through decreasing film thickness and subsequent polarization enhancement with the addition of dopants, application of biaxial stress, and incorporation of oxygen vacancies.

2.4 Overview of Electrode Interactions with HZO and HfO_2-based Thin Films

Owing to the strong dependencies of orthorhombic phase contents and film polarization responses on film chemistry and stress, the selection of electrode materials, which neighbor the HfO_2-based layer, has also been observed as a key contributor to the ferroelectric properties. Investigations of HfO_2-based ferroelectrics most commonly incorporate binary nitride electrodes, including TiN[1,154] and TaN,[117,149] into metal-insulator-metal (MIM) structures. These materials have been revealed to chemically interact with the neighboring HfO_2-based layer via the formation of oxide and oxynitride reaction interlayers during thermal processing, which have been widely observed via X-ray photoelectron spectroscopy (XPS) and Transmission Electron Microscopy (TEM), as diagramed in Figure 2.4.[155–157] Formation of these interlayers removes oxygen from the HfO_2-based film, referred to as oxygen scavenging,[117,156] which drives increased oxygen vacancy concentrations. Aside from oxygen content effects, the presence of interfacial oxide and oxynitride layers has been shown to shift the coercive fields of pristine HfO_2-based ferroelectrics owing to the presence of internal biases imposed by the asymmetric interfaces.[158] Further, effects of electrode stoichiometry[159] and nitride reactivity[117] have both been noted as contributors to HfO_2-based thin film oxygen content, providing a path for electrode chemistry engineering to affect the ferroelectric properties of the device.

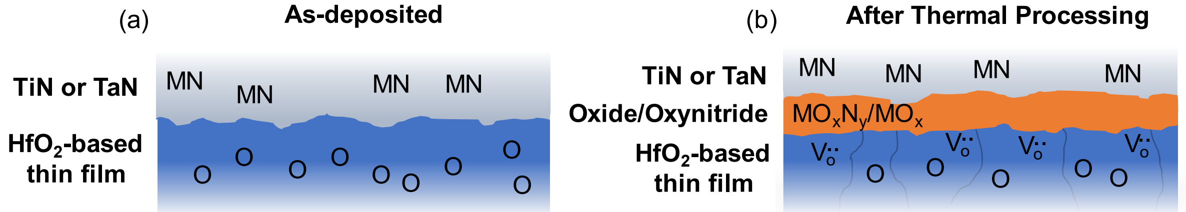

Figure 2.4. Diagram of the interface between a HfO_2-based thin film (blue), TiN or TaN top electrode (gray) and oxide/oxynitride (orange) in the (a) as-deposited and (b) following processing states. The locations of oxygen (O), oxygen vacancies ($V_o^{\cdot\cdot}$), and metal-nitride (MN) species as well as oxide/oxynitride layers (MO_xN_y/MO_x) are indicated.

Irrespective of the chemical interactions and interfacial layer formation between neighboring binary nitrides and HfO_2-based thin films, electrode stress engineering has also been reported as a potential avenue for ferroelectric property optimization.[115,116,151] Through the utilization of different substrate materials, which altered the biaxial stress state of HZO films following thermal processing through different coefficient of thermal expansion (CTE) mismatches, tensile biaxial stresses were shown to result in larger polarization responses and films with more compressive biaxial stress were revealed to have larger monoclinic phase contents.[115,116] Separately, through varying the thickness of TiN top electrodes, which resulted in different HZO biaxial stress states following processing, tensile biaxial stresses were once again shown to enhance polarization magnitudes.[151] These investigations, which isolated away chemical interactions as experimental variables, illustrate the degree to which neighboring layers can influence the stress state and polarization response of the HfO_2-based films. Thus, both chemical and stress interactions between electrode layers and HfO_2-based films present means to control their ferroelectric properties.

To date, oxide electrodes including RuO_2 and IrO_2 have also been investigated in HfO_2-based ferroelectrics. Examinations of the effects of the processing atmosphere on IrO_2/HZO/IrO_2 devices has revealed P_r magnitudes between $5 - 20\ \mu C\ cm^{-2}$,[160,161] whereas an investigation of RuO_2/HZO/RuO_2 devices revealed a P_r magnitude of $10\ \mu C\ cm^{-2}$.[162] These polarizations are competitive with more commonly investigated devices with binary nitride electrodes; however,

the effects of processing with the oxide electrode on interlayer formation and film oxygen content have yet to be fully explored.

Beyond binary nitrides and oxides, the effects of the utilization of metallic materials as electrode layers on the properties of HfO_2-based ferroelectrics have also been investigated. Examinations of symmetric platinum,[163–166] platinum/palladium, palladium/nickel, platinum/nickel,[167] and tungsten[168,169] have revealed strong pristine hysteresis responses and orthorhombic phase contents in various HfO_2-based thin films deposited via chemical solution deposition (CSD) and ALD. To date, the effects of the presence of interfacial oxide layers and the occurrence of oxygen scavenging have been less investigated in MIM structures with metallic electrodes. However, the lack of variable stoichiometry in an elemental electrode material presents a potential repeatability advantage over binary nitride and conductive oxide materials, given the aforementioned chemical interactions on the ferroelectric properties.

Aside from affecting the oxygen content and stress state of the neighboring HfO_2-based ferroelectric layer, the presence of the top electrode during thermal processing has been credited with the stabilization of the orthorhombic phase and increased polarization, termed the 'clamping effect.' Within the first report of ferroelectricity in SiO_2-doped HfO_2,[1] diffraction patterns revealed larger orthorhombic phase contents only in devices that were thermally processed following top metallization. Subsequent reports[100,170] also observed this effect while examining films processed with and without top electrode layers, crediting the orthorhombic phase stabilization and increase in polarization to the presence of biaxial stress imparted through the inclusion of this layer during annealing. However, while biaxial stress is frequently cited as the driving force for the clamping effect, the aforementioned chemical interactions between electrodes and HfO_2-based layers could also be playing a role in the orthorhombic phase stabilization.

2.5 Field Cycling Properties of HZO and HfO_2-Based Thin Films

Beyond affecting the pristine phase compositions and polarizations of HfO_2-based thin films, the selection of electrode material has also been shown to strongly influence the field cycling behavior of these ferroelectrics. Through electric field cycling, the polarization magnitudes of HfO_2-based ferroelectrics are observed to increase and decrease, during processes termed wake-

up and fatigue,[171] respectively, as diagramed in Figure 2.5. These processes are predominantly driven by the redistribution and generation of charged oxygen vacancies, which move in response to the switching electric field applied during cycling.[164,172,173] Polarization wake-up, commonly observed during initial field cycling of ferroelectric HfO_2-based thin films,[174] has been shown to be driven by a combination of phase transformations from the tetragonal to the orthorhombic phase,[154] domain depinning processes,[171,175] ferroelastic domain switching,[176] and interlayer breakdown.[177] Phase transformations and domain depinning have been observed to occur during initial field cycling owing to the accumulation of oxygen vacancies at the electrode interfaces during processing.[155] As field cycling begins, these accumulated vacancies redistribute toward the bulk of the film,[134] which simultaneously stabilizes the metastable ferroelectric orthorhombic phase from the structurally-similar tetragonal phase[117] and de-pins domains, allowing them to contribute to the switchable polarization.[171,178] These processes result in increasing polarization as field cycling initially progresses owing to the additional orthorhombic phase stabilized and enhanced homogeneity of domain switchability.

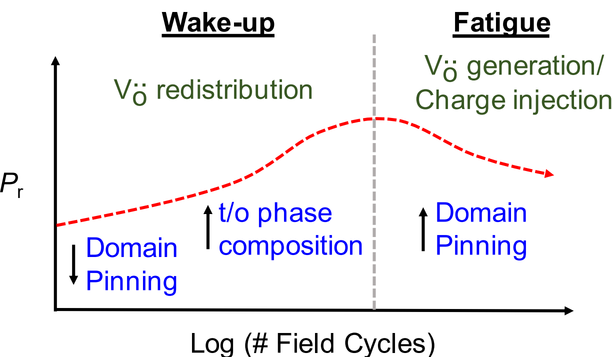

Figure 2.5. Diagram of typical field cycling behavior of a HfO_2-based ferroelectric. The oxygen vacancy behaviors are indicated in green, the resulting effects on the film properties are indicated in blue, the film polarization and separation between the wake-up and fatigue regimes are shown as red and gray dotted lines, respectively, and the qualitative regime descriptions are indicated in their respective regions.

Polarization wake-up processes are strongly dependent on the magnitude and frequency of the electric field utilized during cycling.[158,178–180] When lower electric field magnitudes (<2.0 MV cm^{-1}) are utilized for cycling, less dramatic changes in polarization are typically observed, whereas utilization of larger field cycling magnitudes (>2.0 MV cm^{-1}) yields more substantial increases in polarization.[135,178] Separately, higher frequencies have been observed to cause less substantial polarization increases,[180] which is likely due to some combination of time-constant limited capacitor loading and inhomogeneous defect migration. While most investigations employ bipolar square waves (100% duty cycle) for field cycling experiments,[122,135,158,179] experimental details are often underreported,[178] and such procedures may not accurately simulate the cycling profile that would be utilized for a real world device.

Following the increase in polarization magnitude during wake-up, field cycling investigations of HfO_2-based thin films have widely observed polarization fatigue, as diagrammed in Figure 2.5.[117,172,181] It has been found that this decrease in polarization magnitude is driven by the generation of oxygen vacancies, which serve as pinning sites for domains and prevent them from contributing to the switchable polarization.[171,173] These newly-generated defects are conductive and lead to increases in leakage current with extended field cycling.[122] With excessive oxygen vacancy generation and accumulation, conductive paths can form through the thickness of the film, causing dielectric breakdown and device failure.[165] It should be noted as well that charge injection from electrode layers during field cycling, observed to cause domain pinning and polarization fatigue in conventional perovskite ferroelectric materials,[21,182] has also been noted as a potential contributor to polarization fatigue observed in HfO_2-based systems.[127]

The number of cycles at which wake-up, fatigue, and breakdown occur, as well as the magnitude of the wake-up and fatigue processes, are strongly influenced by the selection of electrode material. For example, investigations that incorporate binary nitride electrode layers into HfO_2-based ferroelectric MIM structures typically report initial polarization wake-up with field cycling, followed by fatigue.[117,172,181] Direct comparisons between TaN and TiN have revealed that TaN electrodes generally result in larger wake-up magnitudes and no fatigue, whereas TiN electrodes yield devices that both wake-up and fatigue and can withstand more electric field cycles before breaking down.[117] Similar to binary nitrides, incorporation of symmetric RuO_2 and IrO_2 electrode layers, which have been shown to mitigate polarization fatigue in conventional

perovskite ferroelectrics,[35,36,183] has been shown to yield HfO_2 devices that both wake-up and fatigue with field cycling.[160–162] Conversely, utilization of metallic electrode materials such as Pt, Ti/Pd, Ti/Au, and W have widely been observed to yield MIM devices that do not wake-up, and instead immediately fatigue with initial field cycling,[129,167] similar to what has been experimentally shown for oxide perovskite ferroelectrics.[35,42]

The field cycling response dependence on electrode material is indicative of the role that the electrode layers play in electric field-driven mass transfer in HfO_2-based thin films. Within HfO_2-based ferroelectric systems, the function of oxygen vacancies is two-fold, causing both the stabilization of additional orthorhombic phase and domain pinning. Thus, it is likely that the utilization of oxide electrodes or electrodes that form stable oxide or oxynitride interlayers in contact with HfO_2-based thin films, aids in the stable transfer of oxygen vacancies out of the ferroelectric layer during field cycling, as diagramed in Figure 2.6. To date, however, such behaviors can only be inferred based upon the field cycling responses[117,167] and theoretical comparisons[184] reported for oxide and nitride electrodes compared to metallic materials in HfO_2-based ferroelectric thin films.

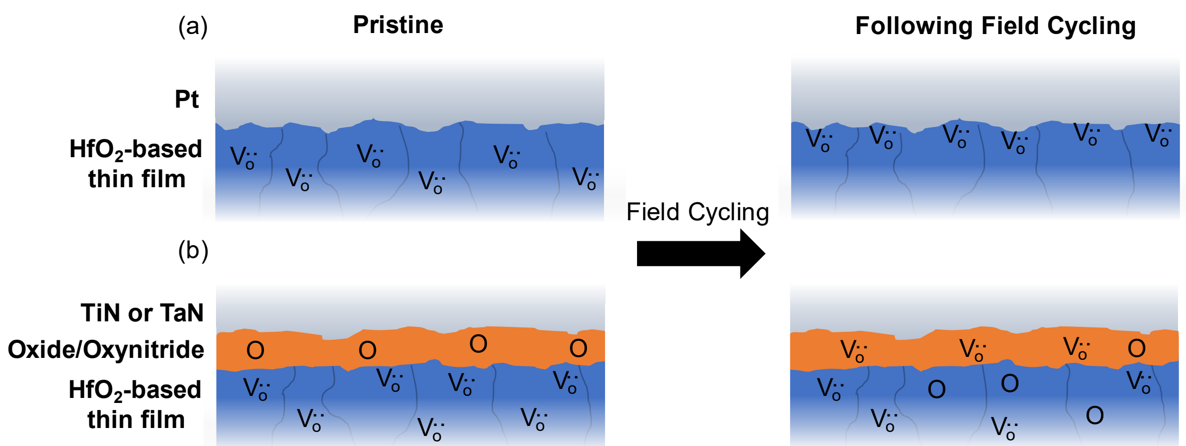

Figure 2.6. Diagram comparing oxygen vacancy behavior before (Pristine) and following field cycling of HfO_2-based ferroelectric thin films processed with (a) Pt and (b) binary nitride electrodes. The layers are indicated on the left, and the general positions of the oxygen atoms (O) and oxygen vacancies ($V_O^{\cdot\cdot}$) are identified.

Given that the metastable ferroelectric orthorhombic phase has both stress and oxygen content contributions to its stabilization in the silicon compatible, scalable, low-thermal budget HZO system, electrode layers, which have been shown to strongly interact with HZO ferroelectrics and influence their phase composition, polarization, and field cycling characteristics, present vehicles to understand the interplay between these characteristics. Further, given these dependencies, electrodes and their processing can be utilized to tailor the ferroelectric properties of HZO thin films, allowing for direct implementation into on-chip applications in contemporary CMOS technology.

2.6 Summary

Within this chapter, emergent HfO_2-based ferroelectric systems have been discussed. Owing to their scalability and silicon compatibility, these materials are ideal candidates for implementation in on-chip, silicon-based CMOS memory, sensor, and transistor technology. The ferroelectric properties in these systems are attributed to a metastable orthorhombic phase which can be stabilized through the utilization of thin film thicknesses to harness its favorable surface energy, incorporation of oxygen vacancies and dopants to destabilize the equilibrium monoclinic phase, and application of biaxial stress to yield films with ideally oriented domain structure. These stabilization factors have opened a wide materials processing space for optimization of the polarization properties and phase constitutions of HfO_2-based thin films. In particular, HZO has been identified as an alloy system that boasts linear dielectric, ferroelectric, and antiferroelectric-like polarization responses depending on film composition, making it a leading candidate for device implementation. Among the avenues for structure and property optimization of HZO ferroelectrics, selection and process development of electrode materials have been identified as means to tailor the phase assemblage, polarization, and field cycling behavior of these materials.

Chapter 3: Development of Deposition Processes and Characterization Techniques for Investigations of Ferroelectric Hafnium Zirconium Oxide

3.1 Introduction

Given the aforementioned interdependencies of stress, chemistry, and interlayer formation on the ferroelectric properties of HZO, effort has been undertaken to design a repeatable, robust process to produce HZO-based MIM devices at the University of Virginia that could be utilized as a vehicle to examine electrode effects on ferroelectric performance. In parallel, characterization and analysis techniques capable of quantifying film biaxial stress and pyroelectric coefficient have been built and adapted at the University of Virginia to enable investigation of properties of films that are predominantly in a metastable crystalline phase and <25 nm-thick. Within this chapter, the development of the electrode sputtering, ALD of HZO, thermal processing, and etching procedures are discussed, followed by the yielded device characteristics and descriptions of the measurement techniques utilized to investigate film properties.

3.2 Development of ALD, Sputtering, Annealing, and Etching Processes for HZO Devices

MIM devices are commonly utilized to examine the polarization, permittivity, and field cycling properties of HfO_2-based thin films.[1,154,172] These structures consist of a bottom electrode material deposited on a substrate, the ferroelectric layer, and a top electrode material. Through utilization of different electrode materials,[117] asymmetric electrodes,[167] or different electrode deposition conditions,[159] this device allows for examinations of processing variations on the polarization properties of the ferroelectric layer. As discussed in Chapter 2, binary nitride electrode materials are most commonly incorporated into HZO-based MIM devices owing to their important stress[87,115,151] and chemical interactions[155,156] with the HZO layer, which stabilize the orthorhombic phase. While TiN is the most common binary nitride employed as an electrode in HfO_2-based thin films,[1,3,154] a number of investigations have also examined TaN,[82,149,185] which has been found to yield larger orthorhombic phase contents and polarization magnitudes at the expense of reduced numbers of cycles-to-breakdown.[117]

For MIM devices prepared at the University of Virginia for the investigations detailed in this dissertation, 100 nm-thick TaN layers were utilized as the conductive bottom electrode material. These planar electrodes were deposited via a DC sputtering process in a lab-constructed system, which demonstrated a base pressure of 7×10^{-7} Torr. For this room-temperature deposition process, the substrate rotation was kept at 15 rpm, the 99.5% pure, sintered 2" TaN (Kurt J. Lesker) target was kept at an incident angle of 45° and a distance of 8 cm, and the target power density was fixed at 3.31 W cm^{-2}, provided via an Advanced Energy MDX 1.5K DC power supply through a Meivac 2.0" MAK sputter gun. Deposition occurred under an argon pressure of 5 mTorr, which was produced with a flow of 20 sccm provided by an Alicat Scientific mass flow controller (MFC) that was further regulated using an Meivac Vari-Q Throttle Valve automated with an MKS 600 Series Pressure Controller.

Polycrystalline TaN films from this process were observed to deposit in a cubic $Fm\bar{3}m$ phase at room temperature, assessed using grazing incidence X-ray diffraction (GIXRD) patterns collected on blanket films using a Rigaku Smartlab diffractometer (Cu Kα, $\lambda = 1.5406$ Å) with an ω incident angle fixed at 0.7°, as shown in Figure 3.1(a). Area detector XRD measurements of devices with TaN electrodes, discussed and shown in Chapter 5, also reveal a preferential (111) out-of-plane texture from this process. X-Ray Reflectivity (XRR) measurement and fitting, shown in Figure 3.1(b) indicate a yielded film density of 12.93 ± 0.01 g cm^{-3}, lower than the theoretical density of 14.3 g cm^{-3}, and a growth rate of 0.13 nm s^{-1} for these deposition conditions. Moreover, film roughnesses of 1.2 and 1.8 nm (RMS) were fit for films which were grown to thicknesses of 20 and 100 nm, respectively, using this process. Further, the TaN produced by this process demonstrated a sheet resistance of 85.8 μΩ sq^{-1} for a resistivity of 8.58×10^{-4} μΩ cm^{-1}, measured using a Keithley 2612A System Source Meter and a four-point probe procedure. XPS measurements and analysis (detailed Further in Chapter 6), revealed a N:Ta stoichiometric ratio of 0.93 ± 0.08:1 in TaN films produced by this process, with the spectra and fit used for this calculation provided in Figure 3.1(c). This process was also noted to yield films with a dense columnar grain structure using Dark Field Scanning Transmission Electron Microscope (STEM) micrographs (detailed further in Chapter 8), shown in Figure 3.1(d).

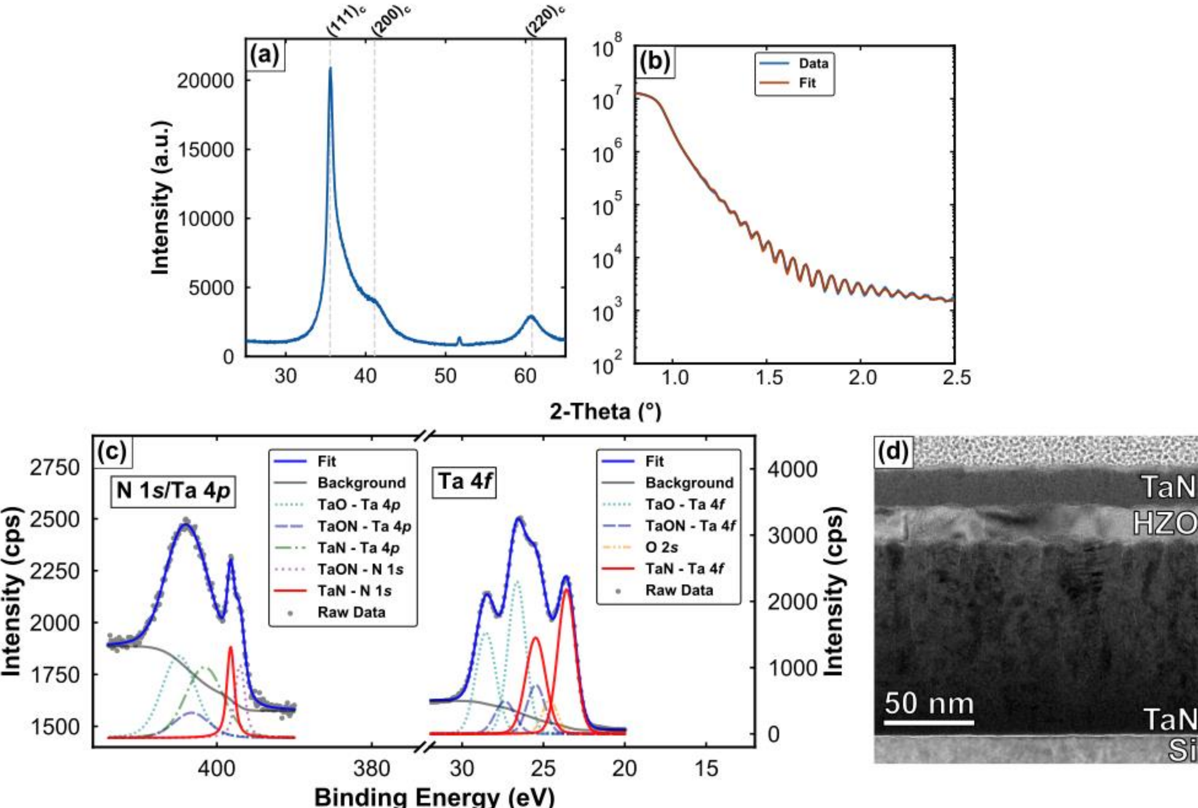

Figure 3.1. (a) GIXRD pattern measured on a 100 nm-thick as-deposited TaN film on a silicon substrate with associated (b) XRR pattern (blue) and fit (orange). (c) XPS spectra measured in the N 1*s* and Ta 4*f* regions with associated fits. (d) Dark Field STEM micrograph measured on thermally processed TaN/HZO/TaN film stack.

Separate from electrode material DC sputter deposition procedures, an ALD process capable of producing ferroelectric HZO was also developed. ALD is a deposition technique commonly utilized to deposit oxides, nitrides, and metallic inorganic species.[186–188] ALD processing relies on the sequential exposure of a substrate to a reactant, in the form of an organometallic precursor, followed by a purge step and then exposure with a second reactant, either an oxidant or second organometallic molecule, and subsequent purge, as diagramed in Figure 3.2:

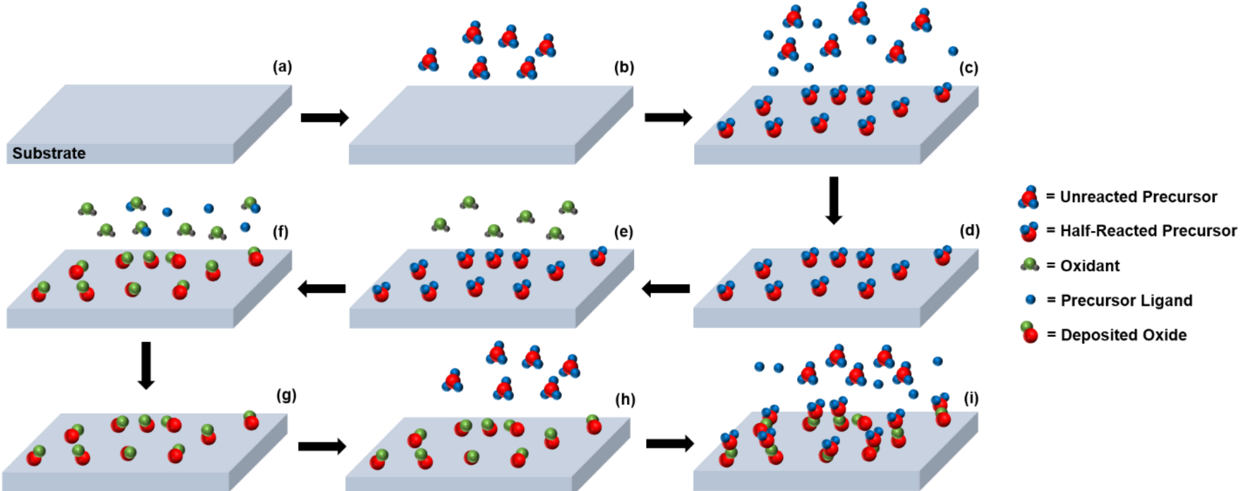

Figure 3.2. Diagram of typical ALD process in which the (a) bare substrate is (b) exposed to precursor molecules, which (c) half-react with the substrate and remain on the surface. The precursor gas is then (d) purged from the atmosphere and (e) replaced with an oxidant (or second precursor species). This oxidant (f) fully reacts with the half-reacted precursor to form the near-monolayer of deposited species, followed by another (g) purge step, after which the substrate is then (h) re-exposed to precursor molecules which (i) half-react with this new layer.

Precursors generally consist of the inorganic atomic species bonded with organic ligands, referred to as a metalorganic. Upon exposure of the precursor compound to the substrate, the inorganic atom bonds with the inorganically terminated substrate surface (or deposited oxide), ideally forming a near-monolayer of half-reacted precursor with organic ligands presenting sterically away from the substrate. Exposure of this ligand-terminated surface to an additional reactant or oxidant results in the replacement of the remaining organic ligands with the new reactant species and thus reactivation of the surface to subsequent cycles. Common oxidants for the second reaction step include H_2O, ozone, and N_2 or O_2 plasmas, and growth tends to take place in the mTorr-Torr pressure regimes. Given that the surface reactions at each step are sequential and self-terminating at ALD temperatures, they proceed via near-monolayer growth.[186] Owing to this, ALD films tend to be highly smooth and conformal,[188] in contrast to other chemical vapor deposition (CVD)-based techniques, which grow via a surface-catalyzed gas phase reaction.[186,187,189]

ALD is one of the most common deposition techniques for preparation of HfO_2-based ferroelectric thin films[1,3] due to the ease of thickness control, through variation in the number of cycles, producing amorphous HfO_2 and ZrO_2 films at common growth temperatures (< 330 °C).[82] In tandem, ALD HfO_2 and ZrO_2 processes have already been implemented in semiconductor fabrication foundries[76,190] owing to their utility as high-κ dielectric layers.[78] Accordingly, research has been undertaken to optimize ALD parameters and characteristics such as the selection of precursor species,[191] growth temperature,[104] precursor purge time,[98] oxidant species,[192] and oxidant exposure duration[111] for superior film quality and ferroelectric performance in yielded films.

ALD-growths of ferroelectric HZO films typically utilize $Hf(NEtMe)_4$ (TEMA-Hf) or $Hf(NMe_2)_4$ (TDMA-Hf) and $Zr(NEtMe)_4$ (TEMA-Zr) or $Zr(NMe_2)_4$ (TDMA-Zr) as HfO_2 and ZrO_2 precursors, respectively, as detailed in Table 3.1.[2,3,130,149,193] However, a number of other inorganic compounds have been evaluated and utilized for these processes.[191] Precursor selection constitutes a balance between stable growth temperature, in which the precursor is reactive with the substrate surface but unlikely to prematurely break down, and minimization of residual chemical defects from the attaching species.[194] Most investigations control film composition through alteration of the ratio of HfO_2:ZrO_2 ALD cycles within a super cycle (s. cyc.),[3,195] which has been shown to result in chemically homogeneous films following thermal processing.[82] Further, mixing of precursors in-*situ* has also been investigated.[196]

Table 3.1. Common HfO_2 and ZrO_2 precursors utilized for atomic layer deposition.

Depositing Species	IUPAC Name	Chemical Formula	Abbreviation	Structure
Hf	Tetrakis(ethylmethylamido) hafnium(IV)	$[(CH_3)(C_2H_5)N]_4Hf$	TEMA-Hf*	
Hf	Tetrakis(dimethylamido) hafnium(IV)	$[(CH_3)_2N]_4Hf$	TDMA-Hf†	
Hf	Hafnium(IV)chloride	$HfCl_4$	$HfCl_4$	
Zr	Tetrakis(ethylmethylamido) zirconium(IV)	$[(CH_3)(C_2H_5)N]_4Zr$	TEMA-Zr*	
Zr	Tetrakis(dimethylamido) zirconium(IV)	$[(CH_3)_2N]_4Zr$	TDMA-Zr†	
Zr	Zirconium(IV)chloride	$ZrCl_4$	$ZrCl_4$	

*Utilized for HZO ALD at the University of Virginia (Chapters 3, 5, 8)

†Utilized for HZO ALD at Sandia National Laboratories (Chapters 4, 6, 7)

Ideal growth temperatures for each species are precursor-dependent, however growths utilizing TDMA Hf/TEMA Hf and TDMA Zr/TEMA Zr precursors tend to occur between 150 and 300 °C.[149,197,198] This temperature window simultaneously yields a low contamination from carbon impurities leftover from precursor reactions[197] while also producing amorphous films.[142] A number of investigators[197,198] have examined the effects of different growth temperatures on the film characteristics and ferroelectric properties of the yielded HfO_2-based layer, reporting decreases in growth-per-cycle and increases in film density as the deposition temperature was increased. Moreover, one of these studies reported that reduced carbon concentration within fully processed films, due to the utilization of higher deposition temperatures, correlated with larger orthorhombic phase compositions in the yielded HZO devices.[197]

Oxidants for ALD HZO depositions are most commonly H_2O,[98,149] oxygen plasma (plasma-enhanced ALD, PEALD),[199] or ozone.[111] Experimental variation in water pulse time,[118] ozone flow time,[111,119,137] or degree of plasma exposure[200] during deposition has revealed that such parameters affect the oxygen content within the yielded films, and thus their resulting phase compositions and polarization properties. Reports to date that have compared the ferroelectric performance of films prepared using H_2O and O_2 plasma oxidants report a reduced thermal budget when plasma was utilized[192] as well as higher P_r magnitudes.[201] Moreover, utilization of additional plasma treatments during ALD has been shown to enhance the cycles-to-breakdown of prepared devices,[200] further identifying oxygen plasma as an advantageous oxidation route compared to ozone and H_2O-based thermal processes.

For the HZO deposited at the University of Virginia for the investigations detailed in this dissertation, depositions were conducted using TEMA-Hf and TEMA-Zr as HfO_2 and ZrO_2 precursors, respectively, within an Oxford FlexAL II ALD system. This system is equipped to utilize water vapor, ozone, and oxygen/nitrogen plasmas as oxidative species, and maintains a base pressure of 2×10^{-6} Torr. Owing to low vapor pressures, TEMA-Hf and TEMA-Zr precursors were kept at temperatures of 70 °C and 85 °C, respectively, and during their respective 1.0 and 1.5 second exposure steps, 250 and 350 sccm argon carrier/bubbler gas flows were employed. During depositions, the substrate table temperature was kept at a constant 260 °C, which has been identified as a temperature at which the utilized precursors readily react with substrates without leaving behind adverse carbon impurities.[197] For oxidation, an oxygen plasma was produced using an oxygen pressure of 15 mTorr and 250 and 300 W of power, respectively, for HfO_2 and ZrO_2 cycles. Throughout the non-precursor reaction steps the chamber was kept under a 15 mTorr argon pressure, whereas during precursor exposure and purge steps, the argon pressure was raised to 80 mTorr. Precursor purge length, identified as a critical variable to produce HZO films with high orthorhombic phase contents using TEMA-Hf and TEMA-Zr precursors,[98] was kept at 90 seconds for both species. Utilizing these processing conditions yielded growth rates of 0.11 and 0.13 nm cycle^{-1} for HfO_2 and ZrO_2, respectively, with thickness uniformities of both processes determined to be ± 1% across a 100 mm-diameter wafer using ellipsometry.

HZO film thicknesses were controlled through variation in the number of cycles. For alloyed films, 10 cycle s. cyc. were utilized in which the ratio of HfO_2:ZrO_2 cycles was varied to

control film composition. Due to the higher growth rate for ZrO_2, alloyed films tended to be more ZrO_2-rich than indicated solely by the utilized s. cyc. ratio. Further, XRR analyses of amorphous 20 nm-thick, 6:4 HfO_2:ZrO_2 films on silicon revealed a roughness of 0.8 nm RMS.

Following ALD HZO deposition, planar TaN top electrodes were deposited using a process identical to that utilized for the bottom electrode. Completed TaN/HZO/TaN stacks were then thermally processed within an Allwin21 AccuThermo 610 Rapid Thermal Processor (RTP) under a nitrogen atmosphere at atmospheric pressure. Given the wealth of experimental investigations examining the effects of thermal processing conditions on the stabilization of the orthorhombic phase in HZO thin films,[98,138,202] an annealing duration of 30 seconds was selected and ramp and cooling rates of 50 and ~2 °C s^{-1} (on average) were utilized, respectively. For 20 nm-thick HZO films, a processing temperature of 600 °C was found to yield a large orthorhombic phase composition, whereas for 10 nm-thick films, a processing temperature of 700 °C was required.[104]

After thermal processing, circular palladium contacts with diameters between 100 and 500 μm were sputter deposited on the surfaces of the TaN/HZO/TaN film stacks through a shadow mask. The conditions for the palladium deposition process were identical to the TaN process, however instead from a palladium target (99.9% pure, 2” diameter, Kurt J. Lesker). These palladium contacts were subsequently utilized to define device areas by acting as hard masks during RCA Standard Clean 1 (SC-1) etch removal of the TaN top electrode layer. The SC-1 etch procedure, commonly utilized for MIM film stacks with binary nitride electrodes and metal contacts,[110] was found to be selective against removal of HZO and palladium. For this procedure, NH_4OH (30% in H_2O), H_2O_2 (30% in H_2O), and H_2O were combined, without mixing, in a 1:1:5 volumetric ratio and heated to 58 °C using a hot plate, measured with a thermometer, as shown in Figure 3.3. For a typical etch a 300 mL beaker was employed to hold 56 mL of etchant, and the hot plate was set to 130 °C to achieve the desired temperature. The 40 mL of H_2O was added to the beaker first followed by the thermometer, which was suspended ~1.5 mm from the bottom of the beaker near the center with the bulb fully submerged. Once the water temperature reached 50 °C, 8 mL of the H_2O_2 solution was added, followed directly by 8 mL of NH_3OH solution. Samples were then immediately submerged in the solution with the etch side facing up, and separated such that there was no surface overlap. The temperature was monitored continuously to ensure a constant temperature of 58 °C (following the initial decrease when the etchants were

added) throughout the procedure. The etch rate was found to be approximately 2 nm min^{-1} for TaN films using this procedure, and 45 minutes of exposure was allotted for 20 nm-thick TaN top electrodes to ensure their complete removal.

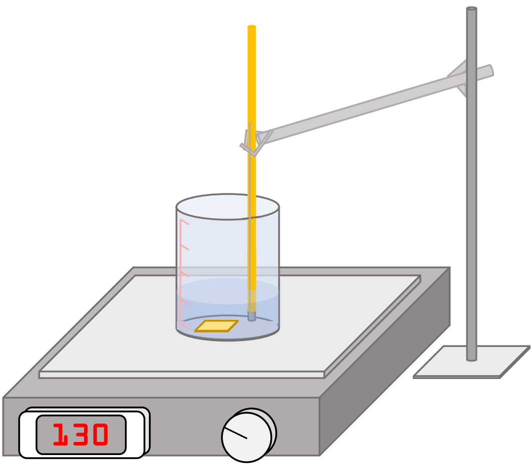

Figure 3.3. Diagram of setup utilized to remove TaN layers with SC-1 etch procedures.

For the standardized Si/SiO_2(native)/TaN/HZO/TaN/Pd devices, diagramed in Figure 3.4, thicknesses of 100 and 20 nm were selected for the top and bottom electrode layers, respectively. 100 nm was chosen for the bottom electrode such that the bottom electrode and HZO layers could be easily distinguished during XRR analysis, whereas 20 nm top electrodes were utilized given the slow removal rate of TaN using the SC-1 etch. Palladium contacts were deposited to a thickness of 50 nm to negate any nonuniformity effects related to shadow mask utilization. Further detail about the development of the HZO MIM process is available in the Appendix of this dissertation.

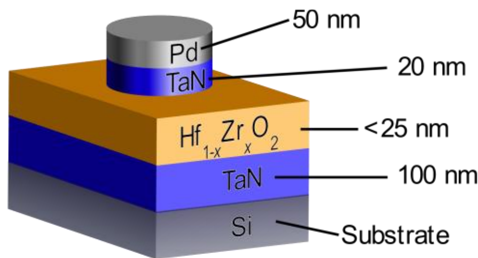

Figure 3.4. The standard MIM device used for investigations utilizing films prepared at the University of Virginia. The layer species are indicated on their respective locations, and the layer thicknesses are indicated on the right.

Through control of both composition and thickness, films with compositions spanning from pure HfO_2 to pure ZrO_2 could be processed to produce devices demonstrating all three monoclinic, orthorhombic, or tetragonal phases, as assessed by GIXRD patterns, plotted in Figure 3.5, collected using a Rigaku Smartlab diffractometer (Cu Kα, λ = 1.5406 Å) with *ω* incident angle fixed at 0.7°. Utilizing XPS measurements of fully processed devices, s. cyc. ratios of 8:2, 6:4, and 3:7 HfO_2:ZrO_2 were determined to result in compositions of $Hf_{0.69}Zr_{0.31}O_2$, $Hf_{0.54}Zr_{0.46}O_2$, and $Hf_{0.21}Zr_{0.79}O_2$, respectively. The growth rate per 10 cycle s. cyc. was also revealed to fall between 1.21 and 1.29 nm cycle^{-1}, depending on the cycle ratio.

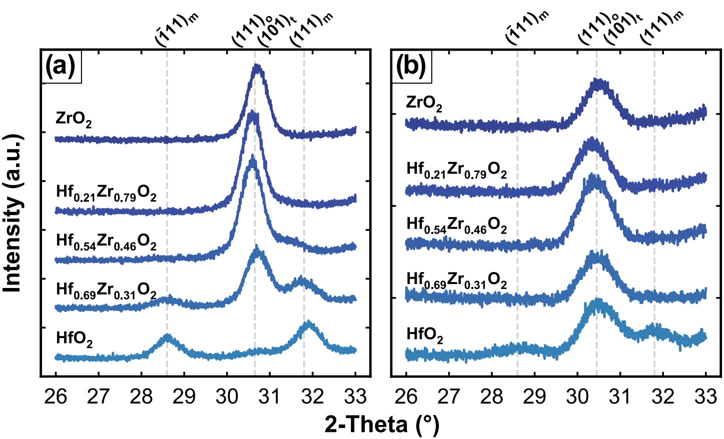

Figure 3.5. GIXRD patterns measured on (a) 20 and (b) 10 nm-thick HZO films with compositions ranging from pure HfO_2 (bottom) to pure ZrO_2 (top). The compositions of the films are indicated to the left of each respective pattern, and indexing for each of the observed reflections are indicated above each panel by grey dotted lines.

For the 20 nm-thick films, shown in Figure 3.5(a), pure HfO_2 crystallized in a pure monoclinic phase, as evidenced by the two monoclinic reflections present at 28.6 and 31.8°. Alloyed films demonstrated a reflection at 30.6°. This peak is frequently indexed as both the (111) orthorhombic and (101) tetragonal reflections (t + o), or some combination thereof, owing to similar *d*-spacings of the two phases. As film compositions approached pure ZrO_2, the intensities of the monoclinic peaks decreased and the intensity of the superimposed t + o peak increased. The pattern measured on the 20 nm-thick pure ZrO_2 film demonstrated only a single peak, which was indexed to the tetragonal phase. For the 10 nm-thick films, shown in Figure 3.5(b), the same trends in phase and composition were observed, however the pure HfO_2 film demonstrated peaks consistent with some mixture of all three monoclinic, orthorhombic, and tetragonal phases. With the addition of 31% ZrO_2, the intensities of the monoclinic peaks were observed to completely diminish, and patterns measured on all subsequent compositions revealed only a single peak consistent with the superimposed t + o reflection.

Given the difficulty in unambiguously separating the phases present in HZO devices utilizing only diffraction patterns, $P(E)$ and PUND responses were measured on each of the 20 and 10 nm-thick films, using a Radiant Technologies Precision LC II Precision Materials Analyzer, to

further analyze phases present and investigate polarization behavior. $P(E)$ measurements were completed out to 2.5 MV cm^{-1} (HfO_2, $Hf_{0.69}Zr_{0.31}O_2$, $Hf_{0.54}Zr_{0.46}O_2$, $Hf_{0.21}Zr_{0.79}O_2$) or 3.0 MV cm^{-1} (ZrO_2) with a period of 1 ms, whereas PUND measurements were completed with a pulse amplitude of 2.5 MV cm^{-1}, a pulse width of 1 ms, and a pulse delay of 100 ms. $P(E)$ responses measured on the 20 nm-thick films, shown in Figure 3.6(a-e), revealed linear dielectric behavior for pure HfO_2 before and following cycling with 10^4, 1 kHz, 2.0 MV cm^{-1} square waves. As the concentration of ZrO_2 was increased, the pristine and field cycled polarization responses became more ferroelectric, with a maximum remanent polarization observed for the $Hf_{0.54}Zr_{0.46}O_2$ composition. With further increases in ZrO_2 content, the pristine polarization response became more pinched, antiferroelectric-like, ultimately arriving at a pure antiferroelectric-like response when a tetragonal pure ZrO_2 film was measured. Utilization of 10 nm-thicknesses, plotted in Figure 3.6(f-j), once again yielded trends similar to those observed when 20 nm film thicknesses were utilized, however with the HfO_2-rich compositions producing responses that were more ferroelectric. For example, the 10 nm-thick pure HfO_2 film was measured to have a clear ferroelectric response following field cycling, in contrast to its 20 nm-thick equivalent, which only showed linear dielectric behavior. Once again, the largest polarization responses before and after field cycling were observed for the $Hf_{0.54}Zr_{0.46}O_2$ in this thickness series, and the responses became more antiferroelectric-like as the film compositions approached pure ZrO_2.

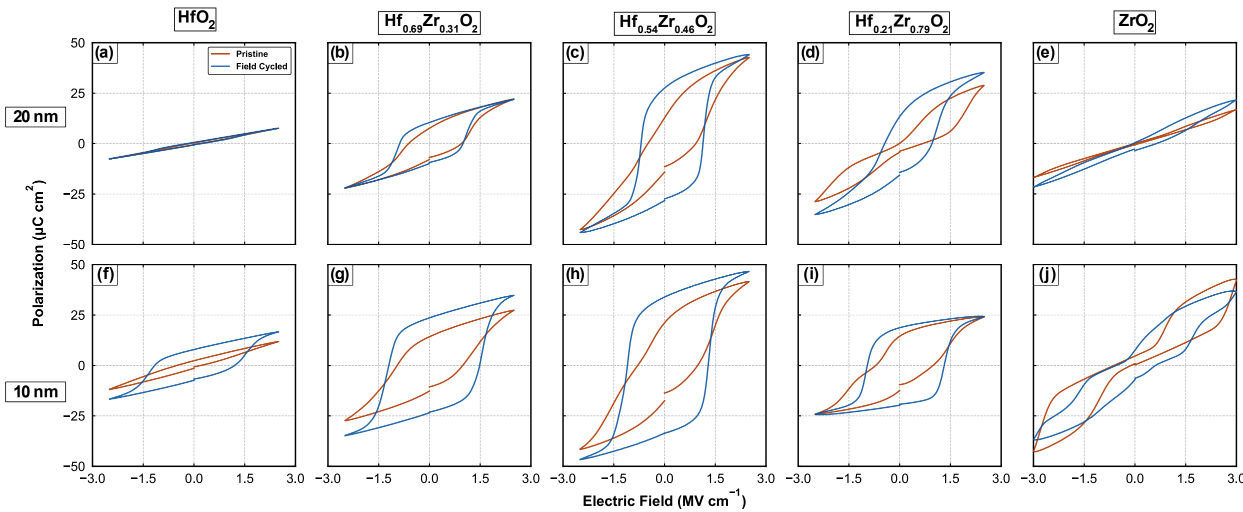

Figure 3.6. $P(E)$ responses measured before (orange) and after (blue) field cycling on (a-e) 20 and (f-j) 10 nm-thick HZO films with compositions spanning from pure HfO_2 to pure ZrO_2, as indicated above.

PUND measurements conducted before and after field cycling, shown in Figure 3.7, allowed for quantification of the remanent polarizations present in each of the films as a function of their composition and thickness. For measurements made on the 20 nm-thick films, shown in Figure 3.7(a), the end-member HfO_2 and ZrO_2 films demonstrated no remanent polarizations before or after field cycling, whereas remanent polarizations, which increased with field cycling, were measured on the alloyed films, with the highest magnitude measured on the $Hf_{0.54}Zr_{0.46}O_2$ composition. Once again, measurements of the 10 nm-thick films, shown in Figure 3.7(b), similarly revealed strong remanent polarizations in the alloyed films, which increased with field cycling, with the $Hf_{0.54}Zr_{0.46}O_2$ film demonstrating the highest magnitude. While PUND measurements of the 10 nm-thick pure ZrO_2 film yielded no remanent polarization before or after field cycling, the pure HfO_2 film demonstrated a pristine P_r, which increased following cycling.

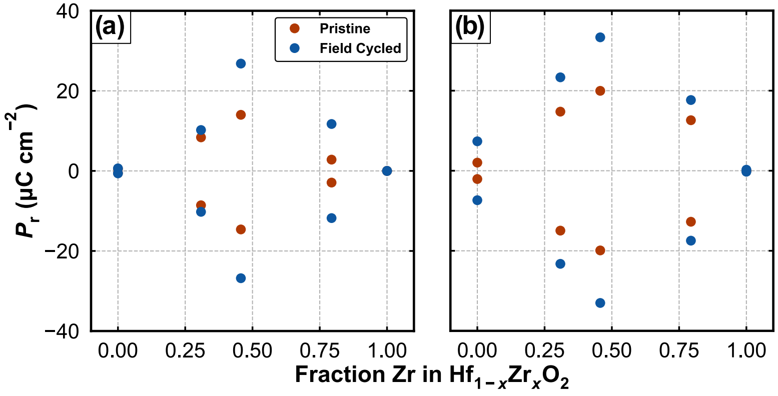

Figure 3.7. Remanent polarization magnitudes extracted from PUND measurements made on (a) 20 and (b) 10 nm-thick HZO films before (orange) and after (blue) field cycling as a function of composition.

For a further understanding of the changes in phase and switching behavior that accompany variation in HZO composition and thickness with the MIM devices, capacitance-voltage (CV) measurements were carried out between ± 2.5 MV cm^{-1} on each HZO MIM device, as plotted in Figure 3.8, using a Keysight E4980A LCR meter with AC oscillator of 50 mV and a frequency of 10 kHz. The CV responses measured on the 20 nm-thick films, shown in Figure 3.8(a-e), show trends expected based upon the $P(E)$ responses and diffraction measurements. The relative permittivity values increase from 22 to 50 as the films vary from pure monoclinic phase HfO_2 to pure tetragonal phase ZrO_2, which is consistent with modeling and experimental work examining the permittivity behavior of this system.[3,154] The switching peaks observed in the profiles measured on the $Hf_{0.69}Zr_{0.31}O_2$ and $Hf_{0.54}Zr_{0.46}O_2$ films coincide with the coercive fields observed in the films' corresponding $P(E)$ measurements. In tandem, the profile measured on the $Hf_{0.21}Zr_{0.79}O_2$ film demonstrates multiple switching peaks consistent with the multiple coercive fields observed in its corresponding pristine antiferroelectric-like $P(E)$ response. For the responses measured on the 10 nm films, plotted in Figure 3.8(f-j), all relative permittivity magnitudes were found to be larger, in general, than for the responses measured on the 20 nm series. This is indicative of larger orthorhombic and tetragonal phase contents, which is supported by $P(E)$ and diffraction behavior. Once again, switching peaks in CV profiles measured on the 10 nm-thick samples also occur at fields consistent with the coercive fields observed in the films' respective $P(E)$ responses.

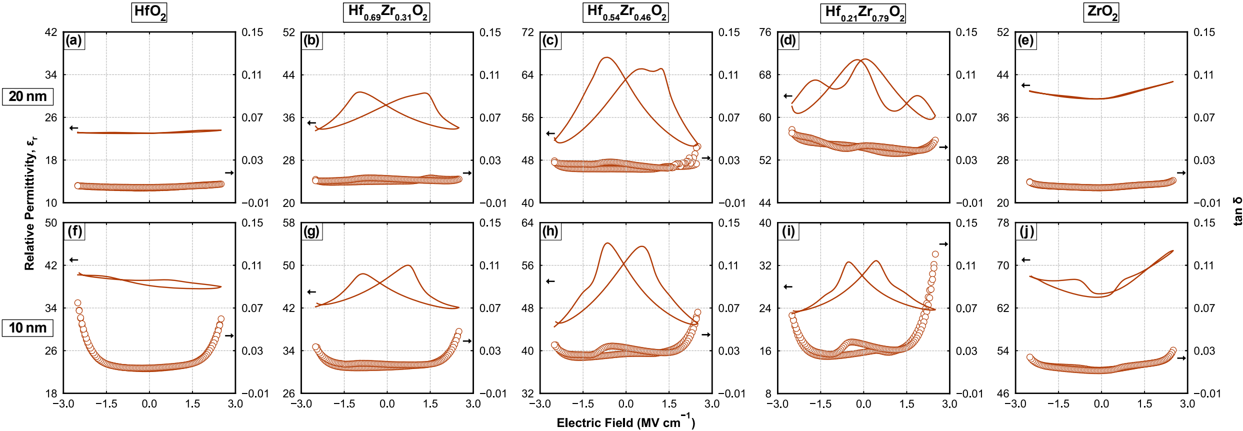

Figure 3.8. CV profiles (orange line, left axis) and associated loss tangents (open points, right axis) measured on (a-e) 20 and (f-j) 10 nm-thick HZO films with varying composition, as indicated above the plots.

The electrical and structural measurements of the TaN/HZO/TaN MIM devices yielded by the detailed process above show that the devices crystallize in the expected phases, demonstrate the expected polarization responses, and show expected permittivity behavior given previous reports on the HZO system.[3,149] By varying the electrode characteristics, materials, and deposition conditions, this MIM device provides a vehicle through which the effects of the electrode layers on the polarization properties of ferroelectric HZO can be investigated.

3.3 Quantifying Biaxial Stress in HZO Devices

In conventional oxide ferroelectrics, effects of biaxial stress on the domain structure displayed by the material have been widely observed through electrical, mechanical, and structural measurements made while intentionally loading,[203] and made on films processed using different substrate or template materials.[204,205] Such experiments have identified that, either through altering crystallographic texture or domain orientation, biaxial stresses can ultimately affect the polarization responses,[203] dielectric properties,[204] and Curie temperatures[206] of ferroelectric films. In sol-gel deposited PZT specifically, imparting of compressive biaxial stress directly on films

resulted in larger measured polarizations, owing to the long polar axis in this material,[203,204] which directly showcases the utility in examining film biaxial stress as an avenue for property optimization.

As discussed in Chapter 2, the role of biaxial stress on the properties of HfO_2-based and HZO thin films is more complicated than in other conventional oxide ferroelectrics. Where effects of tensile biaxial stress directly on the domain structure and polarization responses have been observed to be similar to other conventional materials,[115,116,151] the stabilization of the orthorhombic phase due, in-part, to the presence of biaxial stress[87,150] also may play a role in these effects. Thus, development of characterization techniques, which allow for precise quantification of stress magnitudes in HZO thin films is necessary to rigorously examine these effects on their ferroelectric properties.

As crystallographic strain is necessarily a deviation in equilibrium atomic spacing related to the application of an external stress, diffraction measurements have been widely harnessed to assess and quantify these effects through $\sin^2(\psi)$ analysis.[207–210] These analyses rely on examining the changes that occur in *d*-spacing (ε_ψ) relative to the angle between the diffracting crystallographic planes and film normal (ψ). By making the assumption of a uniform biaxial stress and an isotropic solid, the stress tensor takes the form of Equation 3.1:[209]

$$\sigma_{ij} = \begin{bmatrix} \sigma_{||} & 0 & 0 \\ 0 & \sigma_{||} & 0 \\ 0 & 0 & 0 \end{bmatrix} \tag{3.1}$$

Where $\sigma_{||}$ is the biaxial stress magnitude. In this case, the normal component of the tensor, σ_{33}, is 0 because the film cannot support a normal stress. With the above simplification, a generalized form of Hooke's law, and a matrix transformation between the laboratory and sample frames, the strain and out of plane angle can be related using Equation 3.2:[209]

$$\varepsilon_{\psi} = \frac{1+v}{E}\sigma_{\|} \sin^2 \psi - \frac{2v}{E}\sigma_{\|} \qquad 3.2$$

Where the strain as a function of ψ angle can be taken as Equation 3.3:

$$\varepsilon_{\psi} = \frac{d_{\psi}-d_0}{d_0} \qquad 3.3$$

In these expressions, ε_{ψ} is the crystallographic strain as a function of out of plane angle ψ, v is Poisson's ratio, E is Young's Modulus, and d_0 is the strain-free d-spacing. While an experimental, strain-free d-spacing may be readily available for a well-known powder standard, knowledge of this quantity for orthorhombic HfO_2 to date has entailed DFT calculations[93,211] and experimental STEM measurements of heavily strained Gd-doped thin films.[92] Given that an experimental value for orthorhombic HZO would be different due to the inclusion of ZrO_2, and that modeled values may not represent a realistic experimental strain-free d-spacing, utilization of these numbers could potentially reduce measurement accuracy. Instead of these values, with the continued assumptions of a uniform biaxial stress state and isotropic solid, a strain-free d-spacing can be estimated to occur at an angle, ψ*, at which Equation 3.4 is fulfilled:[209,210]

$$\sin(\psi^*) = \sqrt{\frac{2v}{1+v}} \qquad 3.4$$

Thus, a strain-free d-spacing and biaxial stress magnitude can both be calculated for a film with the singular assumptions of a uniform biaxial stress state and an isotropic solid. It should be noted that positive slopes in d-spacing vs. $\sin^2(\psi)$ are indicative of tensile biaxial stress, whereas negative slopes in this relationship are indicative of compressive biaxial stress. Utilizing this technique, large tensile biaxial stresses (2 – 3 GPa) have been widely observed in HfO_2-based

films with binary nitride electrodes.[124,125,152] However, these reports have only estimated these values using the strong positive slopes of the linear fits of *d*-spacing versus $\sin^2(\psi)$, and employed calculated values for Poisson's ratio and Young's Modulus to provide lower and upper bounds for stress magnitudes.

Utilization of this technique to directly examine the magnitudes of biaxial stress states present within ferroelectric HZO thin films is made difficult by two factors; the films are necessarily less than 25 nm-thick and the *d*-spacings of the orthorhombic and tetragonal phases are similar enough to be undifferentiable in diffraction patterns collected on thin polycrystalline films. Owing to the small interacting sample volumes, GIXRD geometries are frequently employed when collecting diffraction patterns on these materials in order to maximize the beam footprint on the sample surface.[3,110,149] Such a geometry is not ideal for collecting patterns with χ angles far from ~0° using laboratory instruments. Further, as discussed in section 3.2, the (111) orthorhombic and (101) tetragonal planes, both producing the most intense reflections in their respective structure factors, are frequently indexed as some combination of the two phases owing to similar *d*-spacings.[3,142] Ultimately, these two considerations make unambiguous assessment of the biaxial stresses within a mixed-phase HZO thin film experimentally difficult, precipitating the need to further adapt the $\sin^2(\psi)$ technique for this material system.

To maximize the amount of diffracted intensity produced by HZO films examined using the $\sin^2(\psi)$ technique at the University of Virginia, Bruker D8 Venture and APEXII Duo diffractometers equipped with Photon III and APEXII detectors, respectively, were employed to collect area detector diffraction patterns, as diagrammed in Figure 3.9. These diffractometers both harness Incoatec IµS Cu Kα microfocus radiation sources, which utilize focused electron beams between their tungsten filaments and copper anodes to produce photon fluxes superior to traditional X-ray tubes in conventional laboratory-based powder diffraction instruments. In tandem, utilization of area detectors allows for collecting of diffracted intensity at wide γ angles (± 45°) with single frame captures, in contrast to point or line detectors, which require tilting of the sample or optics and multiple measurements for similar information. It should be noted as well that ω incident angles of 15 - 20° were required based upon goniometer geometry in these measurements.

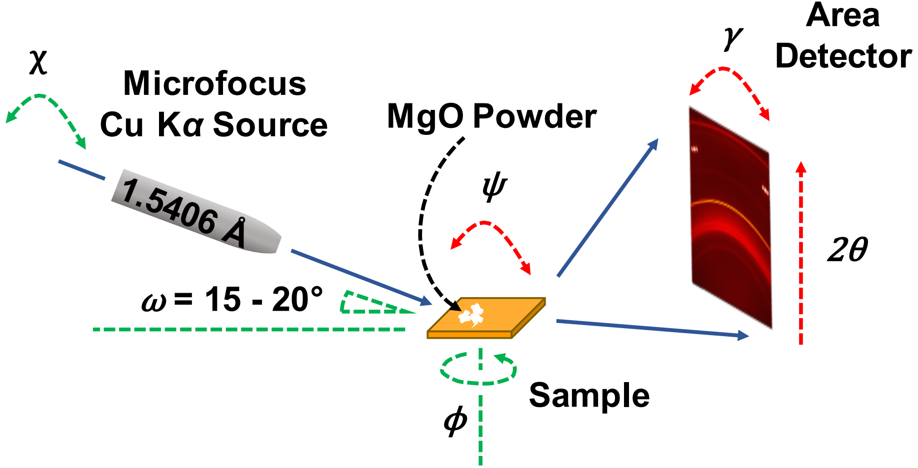

Figure 3.9. Area detector X-ray diffraction measurement setup utilized to collect patterns for $\sin^2(\psi)$ analyses. The programmable sample orientations, including incident angle (ω), sample tilt (χ), and sample rotation (ϕ), are indicated with green dotted lines and arrows, whereas the measurement frame angles, including angle from film normal (ψ), angle from detector normal (γ), and diffraction angle (θ) are indicated with red dotted arrows. The location of the MgO powder standard is indicated with a black dotted arrow, whereas the X-ray path is indicated with blue arrows.

Given that quantitative knowledge of a number of spatial relationships, including sample height, detector angles and distance, and radiation incident angle, is required for analysis of area detector patterns collected with both of these diffraction systems, a strain-free MgO powder was adhered to the film surfaces with vacuum grease to allow for sample displacement, detector, and sample alignment during post processing. This powder is utilized initially in the measurement procedure as an optical focus for the instrument camera, to provide the initial sample displacement. This standard has known *d*-spacings, none of which produce diffracted intensity in the same angular regions as the high intensity orthorhombic, tetragonal, and monoclinic reflections in HZO (26 – 33° in 2θ). This powder was employed, in conjunction with pyFAI azmithual integration software,[212] to align and unwarp area detector patterns following their measurement, as shown in Figure 3.10(a-b). During this unwarping process, γ angles (angle relative to film normal in the detector frame) are also converted to ψ angles (angle relative to film normal in the film frame), which is necessary given that the area detector measures a flat section in diffraction space.[213] This

flat detection scheme is different than conventional diffraction geometries, in which distance between the sample and the detector is assumed to be fixed regardless of detector angle. The unwarping process converts the Debye-Scherrer diffraction rings to diffraction lines, where their vertical position is their ψ angle relative to film normal and their horizontal position is diffraction angle, 2θ. While the diffraction lines from the MgO strain-free standard are essentially completely straight and vertical following this process, variations in the angular position of HZO peaks with ψ angle occur due to crystallographic strain.

Following unwarping and conversion between γ and ψ, intensity line profiles were extracted at individual ψ angles, an example of which is shown in Figure 3.10(c). Pearson VII peak shapes were then fit to these individual line profiles (essentially θ-2θ diffraction patterns measured at an angle ψ) using LIPRAS fitting software[214] to extract the *d*-spacings of the (111) orthorhombic/(101) tetragonal planes. The deviations from the equilibrium *d*-spacing as ψ angle changed were then fit using Equations 3.2-3.4 to quantify the amount of biaxial stress present within the film, as shown in Figure 3.10(d).

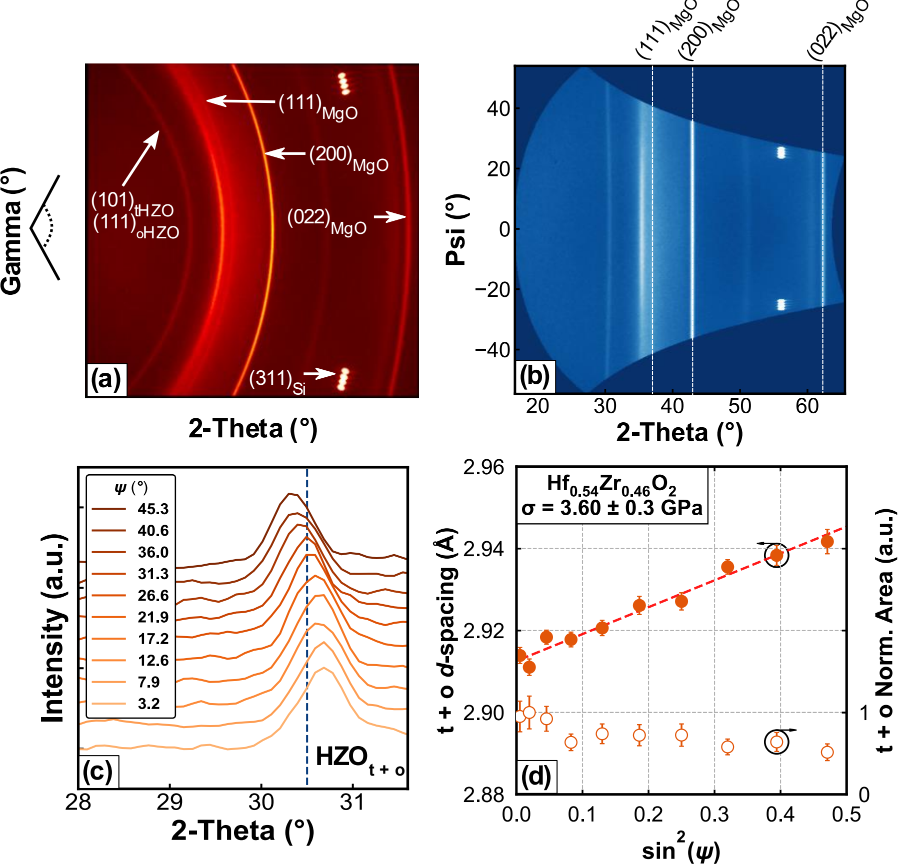

Figure 3.10. (a) Area detector diffraction pattern measured on a processed TaN/20 nm HZO/TaN film stack with indexing for HZO, silicon, and MgO reflections indicated with white arrows. (b) Unwarped area detector diffraction pattern with MgO diffraction lines indicated by white dotted lines and above panel. (c) Line scans extracted at various ψ angles, as indicated by the legend, with indexing for the HZO t + o reflection indicated with a blue dotted line. (d) Change in d-spacing (filled circles, left axis) and normalized t + o peak area (open circles, right axis) with ψ angle, along with linear fit of d-spacing data (red dotted line), calculated film biaxial stress (upper left), and XPS-measured film composition (upper left).

Through analysis of measured area detector patterns and TEM micrographs of fully processed TaN/HZO/TaN film stacks, the validity of the required assumptions of a uniform biaxial stress state and an isotropic solid can be assessed. To begin, the change in d-spacing with ψ angle, plotted in Figure 3.10(d), is strongly linear, which is evidence that there are not strong biaxial shear stresses present in the film.[125] In tandem, measurements at various ϕ angles did not yield strongly

different biaxial stress values, as detailed in the appendix. Both of these observations validate the utilization of Equation 3.1 to derive Equation 3.2.[125] Further, the integrated intensities of t + o diffraction peaks with ψ angle, also plotted in Figure 3.10(d), remain essentially constant, and examination of the HZO microstructure, shown in Figure 3.1(d), reveals no strongly preferred grain orientation. With these two factors combined, it is evident that the films do not have strong crystallographic texture and the assumption of an isotropic solid is validated.[125]

With the assumptions of a uniform biaxial stress and isotropic solid validated, utilization of area detector diffraction-based $\sin^2(\psi)$ analyses offer the ability to unambiguously and accurately quantify the amount of biaxial stress present within < 25 nm-thick ferroelectric HZO thin films following their processing. A further discussion of the repeatability of this measurement technique and the propagation of fitting errors, associated peak positions, and linear *d*-spacing fits can be found in the Appendix.

Aside from examinations of diffraction-based crystallographic strain analyses, wafer flexure measurements also provide a means to examine deposition and processing stresses in thin films.[215–217] Such measurement rely on assumptions of a uniform biaxial stress state and an isotropic solid, similar to diffraction-based measurements, with the added assumption of a uniform film thickness, which is substantially smaller than the thickness of the substrate.[216,218] For these analyses, 250 μm-thick, 50 mm-diameter silicon substrates were utilized, and roughness values for HZO films, extracted from fitting of XRR patterns measured on processed TaN (100 nm)/HZO (20 nm) film stacks, were found to be 0.9 nm RMS. Thus, these assumptions are validated through utilization of sufficiently smooth, uniform, and thin HZO films. Harnessing these assumptions, the curvature of a substrate material is related to the stress present from a thin deposited or processed film on its surface according to the Stoney Equation (Equation 3.5):[219]

$$\kappa = \frac{6\sigma_{||} h_f (1-\nu_s)}{E_s h_s} \qquad 3.5$$

Where κ is the curvature (in m), h_f is the thickness of the film (in m), ν_s is Poisson's ratio for the substrate, E_s is Young's Modulus for the substrate (in Pa), and h_s is the thickness of the

substrate (in m). This expression can be further adapted for deposition or processing stress by examining the radius of curvature before and after individual steps using Equation 3.6:[218]

$$\sigma_{\parallel} = \frac{E_s h_s^2}{6(1-\nu_s)h_f}\left(\frac{1}{R_F} - \frac{1}{R_0}\right) \tag{3.6}$$

Where R_F and R_0 are the radii of curvature (κ^{-1}, in m^{-1}) after and before the processing step, respectively.

Using Equation 3.6, it is possible to quantify the amount of stress incurred within a substrate with the completion of a deposition or processing step with only the experimental measurement of the substrate height profiles before and after said step, knowledge of mechanical properties of the substrate, and knowledge of the film thicknesses. In developing wafer flexure-based procedures for stress quantification at the University of Virginia, utilization of a Bruker DektaxXT stylus profilometer was found to offer the combination of sufficient height resolution, translational capability, and measurement speed to adequately characterize 50 mm-diameter circular wafers, as diagramed in Figure 3.11(a). Within this procedure, profiles were compared along both perpendicular diameters to ensure a truly biaxial stress state. While the curvature of the substrate theoretically varies similarly at all length scales, a measurement of the entire wafer diameter was found to reduce effects from localized curvature variations and film imperfections. Measured profiles were then fit with 2nd degree (2d) polynomials, as shown in Figure 3.11(b), to extract their radii of curvature.

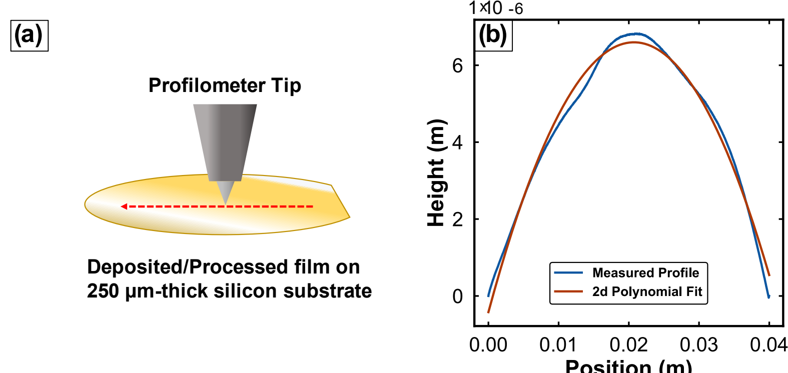

Figure 3.11. (a) Diagram of stylus profilometer measurement with substrate and profilometer tip labeled and scan profile direction indicated with a red dotted arrow. (b) Example height profile (blue) and associated 2d polynomial fit (orange) measured following HZO deposition on a TaN bottom electrode on a silicon substrate.

With a polynomial fit of the height profile, the radius of curvature of the wafer can be calculated using Equation 3.7:

$$R_{\mathrm{F},0} = \frac{\left[1+y'(x)_{\mathrm{F},0}^{2}\right]^{\frac{3}{2}}}{\left|y''(x)_{\mathrm{F},0}\right|} \tag{3.7}$$

Where $R_{\mathrm{F},0}$ is the radius of curvature (in m^{-1}) after (F) and before (0) the processing step, and $y'(x)_{\mathrm{F},0}$ and $y''(x)_{\mathrm{F},0}$ are the first and second derivatives of the 2d polynomial fit to the measured height profiles, respectively. It should be noted that the direction of curvature change is not captured by this calculation because the absolute value of the derivatives is utilized in each occurrence in Equation 3.7. Because of this, direct comparison of the height profiles before and after each step is required to confirm the sign of the biaxial stress change. Measurements of this variety have already been utilized to qualitatively examine the stresses present within processed HfO_2-based thin films.[151] However, in this prior report, only the relative magnitudes of biaxial stresses were discussed for HZO films processed with TiN top electrodes of different thicknesses,

and specific values were not stated. While this technique is less common for strain analysis than previously mentioned $\sin^2(\psi)$ analyses in the HZO system, it is widely utilized in clean room facilities for process development owing to its ease of measurement and data interpretation.

In total, these two stress measurement and analysis techniques provide the capability to unambiguously identify and quantify the signs and magnitudes of biaxial stresses in < 25 nm-thick HZO films. Both of these techniques rely on assumptions of uniform biaxial stress states and isotropic solids, which are validated through examination of area detector diffraction patterns and micrographs captured on processed HZO films. It should be noted as well that diffraction-based measurements necessarily examine the stress of specific crystallized layers whereas flexure-based measurements probe the strain of all films, crystalline or amorphous, present on the substrate surface.

3.4 Pyroelectric Measurements of HZO

Aside from techniques assessing strain in HZO thin films, which allow for the investigation of its effects on the polarization properties, examination of film pyroelectric responses provide information on their ferroelectric domain structures. Ferroelectric materials are necessarily pyroelectric, meaning that oscillations in their temperature produce magnitude changes of their crystallographic dipoles due to lattice expansion and contraction. These crystallographic dipole magnitude changes manifest as current. The amount of current produced by a change in temperature, referred to as the pyroelectric coefficient, can be calculated as Equation 3.8:[220]

$$p = \frac{i_{\mathrm{I}}\sin(\theta)}{A\omega T_{\mathrm{I}}} \quad (3.8)$$

Where p is the pyroelectric coefficient (usually reported in μC m^{-2}K^{-1}), i_{I} is the amplitude of the experimentally measured pyroelectric current, θ is the difference in phase between the temperature and current oscillations, A is the planar area of the device, and ω and T_{I} are the angular frequency and amplitude of the temperature oscillations, respectively. Pyroelectric current is generated 90°

out-of-phase with temperature oscillations, meaning that the inclusion of the $\sin(\theta)$ term removes non-pyroelectrically generated contributions. While, in an ideal system, all generated current would be 90° out-of-phase with temperature oscillations, real materials have charged defects and real apparatuses have circuit elements, which may also produce current due to these changes.

Pyroelectric materials have found application in IR sensor devices, where thermal energy is detected and converted to current or voltage to produce an image or distinguish a warm signature.[52] They have also been investigated for waste heat harvesting, where they can passively generate current in contact with a component experiencing regular temperature oscillations.[53] Applications in active energy harvesting, in which the material is poled at lower temperature and discharged at higher temperature, taking advantage of the Olsen cycle, have also been examined.[51] While HfO_2-based ferroelectric materials offer the possibility for integration of these sensor and energy harvesting systems directly into silicon CMOS platforms, generation of pyroelectric current is separately a useful means to unambiguously identify the orthorhombic phase. Given that the centrosymmetric monoclinic and tetragonal phases are incapable of producing pyroelectric current, all generated currents can be ascribed to any orthorhombic phase present, which can aid in distinguishing it when diffraction and electrical measurements are insufficient.[149,185]

To characterize the pyroelectric coefficient of ferroelectric thin films, experimental measurements of generated currents and temperature oscillation profiles are necessary. A number of reports have made these measurements on ferroelectric silicon-doped HfO_2 thin films via thermally resolved electrical measurements[221] and current monitoring during kHz-frequency temperature oscillations.[222,223] While these studies report coefficients between -27 and -60 $\mu C\ m^{-2}K^{-1}$ for nearly phase-pure orthorhombic silicon-doped HfO_2,[222,223] they also suffer current contributions from the piezoelectric effect owing to their quick temperature loading,[224] and rely on specific knowledge of the thermal properties of the neighboring device materials.[223]

As an alternative, utilization of low frequency temperature oscillations with direct current measurements reduces extrinsically generated current contributions, and allows for more accurate quantification of pyroelectric coefficients.[224,225] These measurements are most readily completed using Sharp and Garn method,[226] which has been widely employed to investigate the pyroelectric properties of HfO_2-based thin films.[149,185,225,227,228] This method relies on an external heat source, typically a thermoelectric Peltier cooler, to oscillate device temperature while the generated current

is monitored by a low-noise ammeter, often an electrometer, as diagramed in Figure 3.12. The thermoelectric temperature oscillation amplitude and frequency can be controlled via the programming of drive waveforms from a waveform generator. This temperature is then read either directly off of the device or off of a neighboring substrate of equivalent thermal mass using a thermocouple.

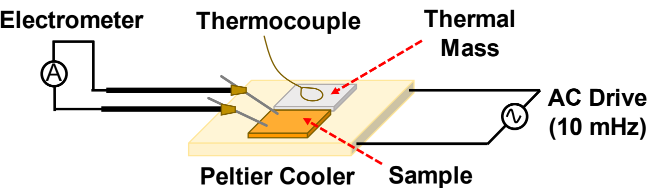

Figure 3.12. Diagram of pyroelectric measurement apparatus based on Sharp and Garn[226] method. Electrometer, thermocouple, Peltier cooler, sample, thermal mass, and AC drive components are indicated in black.

The resulting temperature and current profiles can be fit with sinusoidal waves to discern their phase differences. Then, using this phase difference, their identical angular frequencies and their respective amplitudes, pyroelectric coefficients can be calculated using Equation 3.8. Example temperature and current profiles, measured on a fully processed 20 nm-thick $Hf_{0.54}Zr_{0.46}O_2$ device before and after poling (prepared using the process detailed in this chapter), are shown in Figure 3.13. For these measurements, a temperature oscillation frequency of 10 mHz was produced using a Keysight 33500B Waveform Generator, where a waveform amplitude of 10 V peak-to-peak was found to produce a temperature amplitude of ± 2 °C on the surface of the utilized Peltier cooler (TE Technology model VT-127-1.0-1.3-71). The temperature of the Peltier cooler was monitored using an Type E Surface Thermocouple (Omega Engineering SA1XL-E-SRTC), whereas generated currents were read using a Keithley 6514 Electrometer. Before poling, temperature oscillations produce a weak current response, as plotted in Figure 3.13(a). In this state, the film was calculated to have a pyroelectric coefficient of -4 $\mu C\ m^{-2}K^{-1}$. This signal is generated by a domain structure that is only partially poled (likely by some aspect of device processing), and so produces competing currents in opposite directions. Following poling, the domain structure is

effectively fully aligned, and so produces a strong current response, as plotted in Figure 3.13(b). Once poled, the film demonstrated a pyroelectric coefficient of -28 μC $m^{-2}K^{-1}$. This value is consistent with other reported low frequency temperature oscillation measurements of 20 nm-thick $Hf_{0.5}Zr_{0.5}O_2$ films.[149,185,228]

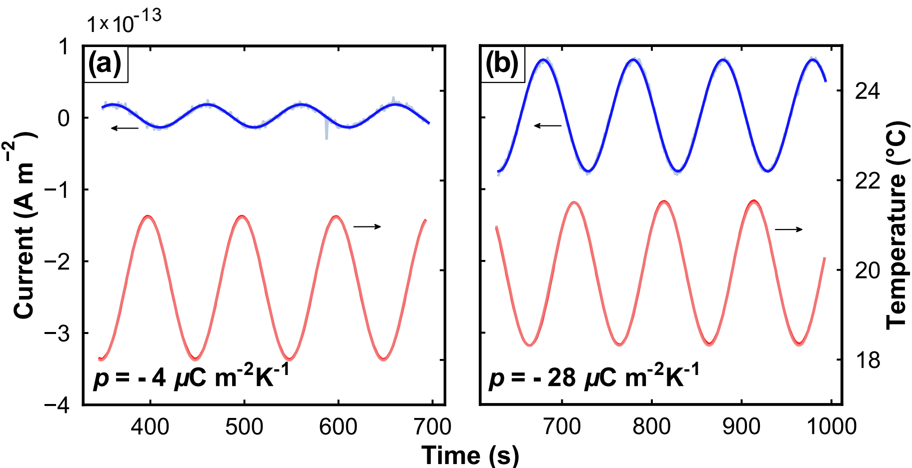

Figure 3.13. Sinusoidal temperature oscillation (red line, right axis) and resulting pyroelectric current (blue line, left axis) generated by a TaN/20 nm HZO/TaN device (a) before and (b) after poling with a single $P(E)$ measurement. The pyroelectric coefficients, calculated using the temperature and current profiles, are indicated in the lower left of each respective plot.

It should be noted that pyroelectric coefficients measured on HZO and other HfO_2-based ferroelectric thin films are more modest than those reported for more commonly utilized ferroelectric perovskites. Where the maximum pyroelectric coefficients reported for HZO, silicon-doped HfO_2, and lanthanum-doped HfO_2 are -55,[185,228] -72[223] and -80[225] μC $m^{-2}K^{-1}$, respectively, values in excess of -200 μC $m^{-2}K^{-1}$ are regularly reported for PZT and BTO.[51] While this ultimately translates to less efficient conversion between heat and current than their conventional perovskite counterparts, many figures of merit take into account relative permittivity factors which favor HfO_2, and the silicon compatibility and scalability of HfO_2-based ferroelectrics give them access to scaled, on-chip applications which are not possible with lead and barium containing materials. Regardless, characterization of pyroelectric currents produced by HZO and HfO_2-based ferroelectrics provides a means to unambiguously identify the orthorhombic phase.

3.5 Summary

Within this chapter, detail is provided on the processing and characterization methods developed to complete the bulk of the research further discussed in this dissertation. The sputtering and atomic layer deposition, etching, and thermal processing procedures, synthesized and improved upon from details reported by other groups, are described. The electrical properties of the yielded HZO devices are shown to be equivalent to those reported by other groups in literature, confirming that these devices can be harnessed for further experimentation on electrode effects on their polarization properties. Further, methods for area-detector diffraction and wafer flexure-based quantification and analysis of biaxial stresses are described. It is determined that the required assumptions of uniform biaxial stress states and isotropic solids are valid in the TaN/HZO/TaN devices through analysis of area detector diffraction patterns and TEM micrographs of fully processed HZO layers. Finally, a detailed description and review of the procedures utilized to reliably quantify the pyroelectric coefficient in HfO_2-based ferroelectric thin films is provided. It is also noted that characterization of pyroelectric coefficients provides a means to unambiguously identify the orthorhombic phase, which can be difficult in < 25 nm-thick, mixed phase HZO films.

Chapter 4: Phase-Transformation-Driven Wake-Up and Fatigue in Ferroelectric Hafnium Zirconium Oxide Films

The contents of this chapter are published in *ACS Applied Materials and Interfaces* (**12**, 126577-26585, 2020, DOI: https://dx.doi.org/10.1021/acsami.0c03570) with the following as authors:

Shelby S. Fields,[1] Sean W. Smith,[2] Philip J. Ryan,[3] Samantha T. Jaszewski,[1] Ian A. Brummel,[1] Alejandro Salanova,[1] Giovanni Esteves,[2] Steve L. Wolfley,[2] Michael D. Henry,[2] Paul S. Davids,[2] and Jon F. Ihlefeld.[1,4]

[1]Department of Materials Science and Engineering, University of Virginia, Charlottesville VA, 22904, USA

[2]Sandia National Laboratories, Albuquerque NM, 87123, USA

[3]Advanced Photon Source, Argonne National Laboratory, Lemont IL, 60439, USA

[4]Charles L. Brown Department of Electrical and Computer Engineering, University of Virginia, Charlottesville VA, 22904, USA

The body of text of this chapter has been adapted to include the supplemental information and figures, where appropriate.

4.1 Motivation

This chapter provides a survey of the field cycling behavior of ferroelectric HZO thin films with different electrode materials. While the ALD conditions for the HZO are nominally identical, the field cycling and polarization properties of the resulting MIM devices, prepared at Sandia National Laboratories, are different owing to the utilization of symmetric TaN, W, or Pt layers as electrodes. These differences are explored through synchrotron microdiffraction measurements of pre-cycled discreet devices. This first investigation provides the context through which additional electrode effects are explored, revealing that polarization fatigue and wake-up with initial field cycling can be observed in the same HZO with different electrode materials.

4.2 Abstract

Ferroelectric hafnium zirconium oxide holds great promise for a broad spectrum of CMOS compatible and scaled microelectronic applications, including memory, low voltage transistors, and infrared sensors, among others. An outstanding challenge hindering implementation of this material is polarization instability during field cycling. In this study, the nanoscale phenomena contributing to both polarization fatigue and wake-up are reported. Using synchrotron X-ray diffraction, the conversion of non-polar tetragonal and polar orthorhombic phases to a non-polar monoclinic phase while field cycling devices comprising noble metal contacts is observed. This phase transformation accompanies a diminishing ferroelectric remanent polarization and provides device-scale crystallographic evidence of phase transformation leading to ferroelectric fatigue in these structures. A reduction in the full width at half maximum of the superimposed tetragonal (101) and orthorhombic (111) diffraction reflections is observed to accompany wake-up in structures comprising tantalum nitride and tungsten electrodes. Combined with polarization and relative permittivity measurements, the observed peak narrowing and a shift in position to lower angles is attributed, in part, to a phase transformation from the non-polar tetragonal to the polar orthorhombic phase during wake-up. These results provide insight into the role of electrodes on the performance of hafnium oxide-based ferroelectrics, mechanisms driving wake-up and fatigue, and demonstrate a non-destructive means to characterize the phase changes accompanying polarization instabilities.

4.3 Introduction

HfO_2-based thin films have witnessed substantial investigation as CMOS compatible ferroelectrics following the first report of polarization hysteresis in 2011.[1] For device applications for which size scaling is required, such as ferroelectric random access memory (FE-RAM),[2,229] negative differential capacitance field-effect transistors (NC-FETs),[230] and ferroelectric tunnel junctions (FTJs),[231,232] HfO_2-based films are promising. This is owed to two major factors. First, ferroelectricity in polycrystalline HfO_2-based films has been demonstrated at thickness scales (1 – 5 nm)[185,233,234] at which conventional ferroelectrics, such as $Pb(Zr,Ti)O_3$ and $BaTiO_3$, exhibit significant scaling effects.[58] Second, large scale deposition tools and processes have already been

developed for incorporation of HfO_2 thin films as high-κ dielectric layers in current CMOS processes, making integration of the ferroelectric phase into contemporary semiconductor technology attractive.

HfO_2 is at equilibrium in a centrosymmetric monoclinic phase (space group $P2_1/c$) under atmospheric temperature and pressure. At elevated temperatures, other polymorphs, including tetragonal ($P4_2nmc$) and cubic ($Fm\bar{3}m$), are known to exist in the bulk. The ferroelectric response has been attributed to a metastable, non-centrosymmetric orthorhombic phase ($Pca2_1$) that does not appear on phase diagrams. Its existence has been associated with a combination of factors, including a low surface energy that increases its stability for small crystal sizes,[90] presence of tensile biaxial stress,[115] large electric fields,[87] and oxygen vacancies. In particular, oxygen vacancies appear to be strongly correlated with the phase assemblage in HfO_2-based films, stabilizing the tetragonal, orthorhombic, and monoclinic phases at high, intermediate, and low concentrations, respectively.[117]

Two standing challenges toward implementation of ferroelectric HfO_2-based materials into the next generation of CMOS platforms are the inability to prepare phase-pure films consisting solely of the ferroelectric orthorhombic phase and the variation of polarization with field cycling. The polarization variation with field cycling behavior can be categorized as follows: wake-up, where the remanent polarization (P_r) has been observed to increase upon exposure of the capacitor structure to DC or AC electric fields, and fatigue, where P_r decreases with field cycling, often culminating in dielectric breakdown. For wake-up, the increase in polarization with field cycling has been attributed to four mechanisms: phase transformation, where the non-ferroelectric tetragonal and monoclinic phases convert to the orthorhombic ferroelectric phase, possibly via oxygen vacancy redistribution,[164] domain depinning, whereby charged oxygen vacancies are redistributed away from pinning positions near domain nuclei,[179] ferroelastic domain switching where the polar axis, which is initially aligned in the plane of the film, switches to be out of plane,[176] and breakdown of an interfacial linear dielectric layer, which contributed to large depolarization fields in the as-prepared state.[177] Evidence of phase transformation occurring during wake-up has previously been observed via scanning transmission electron microscopy (STEM) through comparison between the phase assemblage in capacitor structures with differing numbers of field cycles.[154,171] It was observed that capacitors, before field cycling, had microstructures comprising a tetragonal phase at the electrode/dielectric interfaces with orthorhombic and

monoclinic phases in the bulk of the dielectric. After wake-up field cycling, the capacitors contained less of the tetragonal and monoclinic phases and increased fractions of the orthorhombic phase. While these observations were extremely localized, owing to the limited volume that can be investigated by STEM techniques, global electrical property measurements by many different research groups also support a phase transformation-related mechanism. For example, studies have revealed decreases in overall relative permittivity (ε_r),[154,158,235] decreased differences between saturation and remanent polarization values,[130] and changes in impedance response,[154] all of which support some degree of phase transformation. Domain depinning mechanisms, evidenced by decreasing pinching of polarization hysteresis loops upon field cycling due to reduced back-switching from inhomogeneous distributions of charged defects, are supported by a range of global electrical[181,235] and local electromechanical measurements.[175,236] Synchrotron X-ray diffraction and STEM measurements on an epitaxial film revealed ferroelastic domain switching as being a contributor to wake-up during the initial application of an electric field.[176] Depolarization fields associated with non-ferroelectric and non-conducting interfacial layers have also recently been applied to explain the pinching of polarization hysteresis response. A breakdown of this interfacial layer with field cycling and a concomitant decrease in depolarization fields may lead to increased polarization response.[177]

While both phase transformations and domain-related affects appear to contribute to wake-up, results to date point toward fatigue being driven primarily by increased domain pinning. Prior STEM studies have revealed nearly identical orthorhombic phase content in both fatigued and woken-up devices,[154] which supports domain pinning being a dominant factor in polarization reduction. However, it should be emphasized that STEM studies inherently measure only isolated regions and are subject to grain overlap and crystal orientation challenges in obtaining artifact-free images. Device-scale electrical measurements support domain pinning resulting from the presence of charged defects, such as oxygen vacancies, that trap charges injected at the electrode/dielectric interfaces. In addition, the fatigue process may also be accelerated by the generation of new oxygen vacancies, which can lead to further domain pinning.[171,172]

As wake-up and fatigue appear to be related to the presence of oxygen non-stoichiometry, differing trends of polarization response with field cycling depending on the electrode material may be expected. Prior work investigating the role of ion transport between electrode layers and conventional $Pb(Zr,Ti)O_3$ and $BaTiO_3$ ferroelectrics, in which oxygen vacancies also play an

important role in polarization response,[39] demonstrated differing fatigue properties depending on the chosen electrode material. For example, it was shown that oxide electrodes that allow for oxygen transport across the electrode/ferroelectric interface yield improved fatigue performance.[237–239] Platinum electrodes devices, however, were observed to fatigue and this has been attributed to an interfacial oxygen vacancy buildup.[38,237,239] Experimental work on electrode effects in HfO_2 have revealed a few trends: 1) Metal nitride electrodes, such as TiN or TaN, which are reactive in contact with the oxide dielectrics,[155] yield modest oxygen vacancy concentrations within HfO_2-based films. Such electrode materials are most commonly utilized for ferroelectric HfO_2 studies and devices constructed with these electrodes generally exhibit increases in P_r when cycled at fields of ~2.0 MV cm^{-1};[117,149,158] 2) Oxide electrodes, which may allow transport of oxygen across the electrode/dielectric interface, but have not been significantly studied, result in fatigue directly from the as-prepared (pristine) state, demonstrating immediate and substantial reductions in P_r with cycling at 2.0 MV cm^{-1};[240] 3) Devices with oxygen blocking contacts, such as platinum, have been shown to exhibit moderate wake-up or direct fatigue, depending on the magnitude and frequency of the applied wake-up field. To date, studies utilizing symmetric platinum electrodes have demonstrated wake-up only when cycling at large fields (*e.g.*, 3.2 – 4.0 MV cm^{-1}),[163,164] while lower fields of 2 MV cm^{-1} have been observed to cause fatigue immediately upon field cycling of devices with palladium electrodes.[167] Studies with non-noble elemental contacts, such as nickel or tungsten, for which oxygen vacancy contributions are less well studied, also exhibit fatigue under cycling fields of 2 MV cm^{-1}.[129,167] While these prior data suggest trends exist for the impact of field magnitude on wake-up versus fatigue response, the origin of the field dependence on these effects is not yet fully understood. Regardless, it is evident that electrode chemistry impacts HfO_2-based ferroelectric performance.

While global electrical property measurements and localized STEM observations support the occurrence of phase transformations during wake-up, to date there exists a lack of equivalent device-scale structural evidence in structures with unperturbed electrical and mechanical boundary conditions (*i.e.,* capacitor structures not subject to sectioning into a TEM foil, which may alter the stress state and electron bombardment during imaging, potentially impacting oxygen stoichiometry[241]). Prior efforts to study phase assemblage in functioning capacitors in differing states of wake-up and fatigue have included lab-scale and synchrotron X-ray diffraction,[117] but these results have been inconclusive regarding the degree of structural change due to field cycling.

In this study, synchrotron X-ray diffraction was utilized to examine the phases present in 20 nm thick ferroelectric hafnium zirconium oxide (HZO) capacitor structures, with a nominal composition of $Hf_{0.58}Zr_{0.42}O_2$. Tantalum nitride, tungsten, and platinum electrodes, which are anticipated to present different HZO wake-up/fatigue responses, were incorporated into symmetric metal-insulator-metal (MIM) capacitor devices. Individual devices of each capacitor structure were subjected to electric field cycling at 2 MV cm^{-1} and 1 kHz with square wave profiles. The total number of cycles ranged from 0 (pristine) to 5×10^4. Following cycling, the individual devices were structurally investigated with synchrotron X-ray diffraction and electrically characterized. The results provide insights into the phase transformation mechanisms resulting in wake-up and fatigue behavior on the device scale.

4.4 Experimental Procedures

MIM device structures were fabricated utilizing the three different electrode materials and a nominal HZO composition of $Hf_{0.58}Zr_{0.42}O_2$ at Sandia National Laboratories. 100 nm thick bottom electrodes of each metal were deposited onto 100 mm diameter silicon substrates using pulsed DC (30 kHz / 4μs reverse time) sputtering in a Denton Discovery 550 system with an argon background pressure. For the tungsten electrode sample, a chemical mechanical polishing (CMP) process followed deposition to reduce film surface roughness. Following bottom electrode deposition/preparation, 20 nm-thick $Hf_{0.58}Zr_{0.42}O_2$ films were deposited via thermal atomic layer deposition using H_2O as the oxidant on each substrate at a temperature of 150 °C within an Ultratech Savannah flow-through style reactor using the same precursors and conditions as reported previously.[149] Following HZO deposition, continuous 20 nm thick top electrode layers were deposited onto the respective TaN and tungsten electrode samples. The platinum electrode sample received 100 nm thick 1 x 1 mm platinum contact pads patterned through a shadow mask. All samples were annealed at 600 °C for 30 seconds in N_2 within a Surface Science Integration Solaris 150 rapid thermal annealer. After, 100 nm thick circular platinum contacts of diameters varying from 288 – 90 μm were prepared via lithography, sputtering, and liftoff onto the tungsten and TaN samples and isolated MIM structures were subsequently defined by reactive ion etching through the top electrode layers using the platinum contacts as a hard mask.

Following device preparation, intrinsic relative permittivity,[242] polarization-field, positive up, negative down polarization switching, and capacitance-voltage measurements were performed on devices in their pristine state. For the TaN and tungsten samples, $P(E)$ responses were measured with a period of 1 ms, with maximum fields progressing from 1 MV cm^{-1} to 2.5 MV cm^{-1}. For the platinum sample, owing to the large electrode area, a hysteresis period of 100 ms was required. For PUND measurements, a 1000 ms delay and 1 ms pulse width were utilized with applied fields spanning 1 MV cm^{-1} and 2.5 MV cm^{-1} to measure remanent polarization (P_r) values. The intrinsic relative permittivities (*i.e*. the permittivity of the lattice, devoid of extrinsic domain wall and phase boundary motion contributions) were extracted from a Rayleigh formalism[242] as the low AC-field intercept of the permittivity dependence on oscillator level at 10 kHz, measured between 5 and 180 mV (RMS), while permittivities at 2.5 MV cm^{-1} were extracted from 10 kHz capacitance-voltage measurements with a 50 mV oscillator. $P(E)$ and PUND measurements were performed utilizing a Radiant Precision Multiferroic II Tester and dielectric measurements utilizing a Keysight E4980A LCR Meter. Following initial characterization, individual devices were cycled ahead of structural characterization. Separate contacts on each of the samples were subject to square waves at 1 kHz and 2.0 MV cm^{-1} for 1×10^3, 5×10^3, 2×10^4, and 5×10^4 cycles, or until dielectric breakdown occurred. Following cycling, electrical measurements, as described above, were carried out on each contact.

Synchrotron X-ray diffraction measurements were performed at the 6-ID-B beamline at the Advanced Photon Source at Argonne National Laboratory. An X-ray wavelength of 1.3776 Å and a 100k Platus area detector were utilized to collect diffracted intensity between 24° - 29° in 2θ. The beam energy was held at 8.9 keV to avoid possible fluorescence related emission. The samples were oriented 13.5° toward the incident beam from normal. Incident slits were adjusted such that the X-ray beam formed a 200 µm x 200 µm footprint on the TaN and tungsten electrodes, and a 700 µm x 700 µm footprint on the platinum electrodes. Diffraction patterns on each pre-cycled pad were collected with a step size of 0.025° and an integration time of 10 seconds/step. LIPRAS[214] fitting software and Pearson VII peak shapes were utilized to perform all diffraction pattern fits. The backgrounds of TaN and platinum diffraction patterns were fit utilizing 3rd-degree polynomials, while for tungsten a linear fit was utilized.

4.5 Results and Discussion

Figure 4.1 shows the polarization response, remanent polarization, and intrinsic relative permittivity of the pristine devices. Devices with tungsten electrodes possessed the largest P_r of 12.0 ± 0.2 μC cm^{-2}, followed by those with platinum (9.8 ± 0.6 μC cm^{-2}) and TaN (8.6 ± 0.2 μC cm^{-2}) electrodes. Polarization-field ($P(E)$) responses of the pristine devices revealed saturated hysteresis behavior, indicative of low electrical leakage in each case. The intrinsic relative permittivities of each sample, extracted from Rayleigh measurements, shown in Figure 4.2, were 30.7, 28.4, and 23.0 for tungsten, platinum, and TaN, respectively.

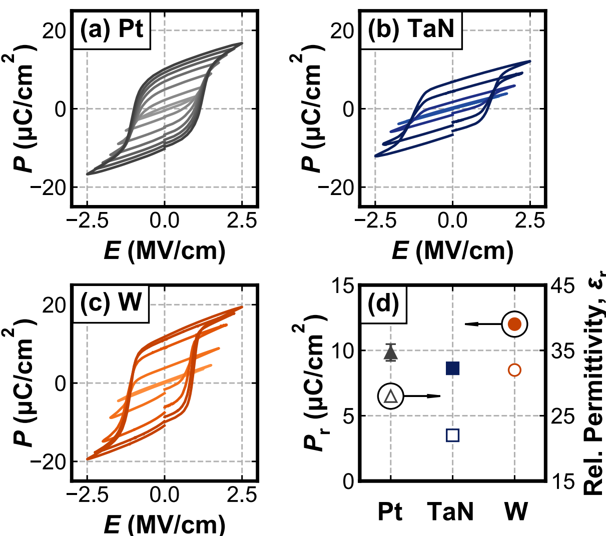

Figure 4.1. $P(E)$ response measured on symmetric MIM devices with (a) platinum (Pt), (b) TaN, and (c) tungsten (W) electrodes. (d) shows measured P_r and intrinsic ε_r for each structure in the pristine condition.

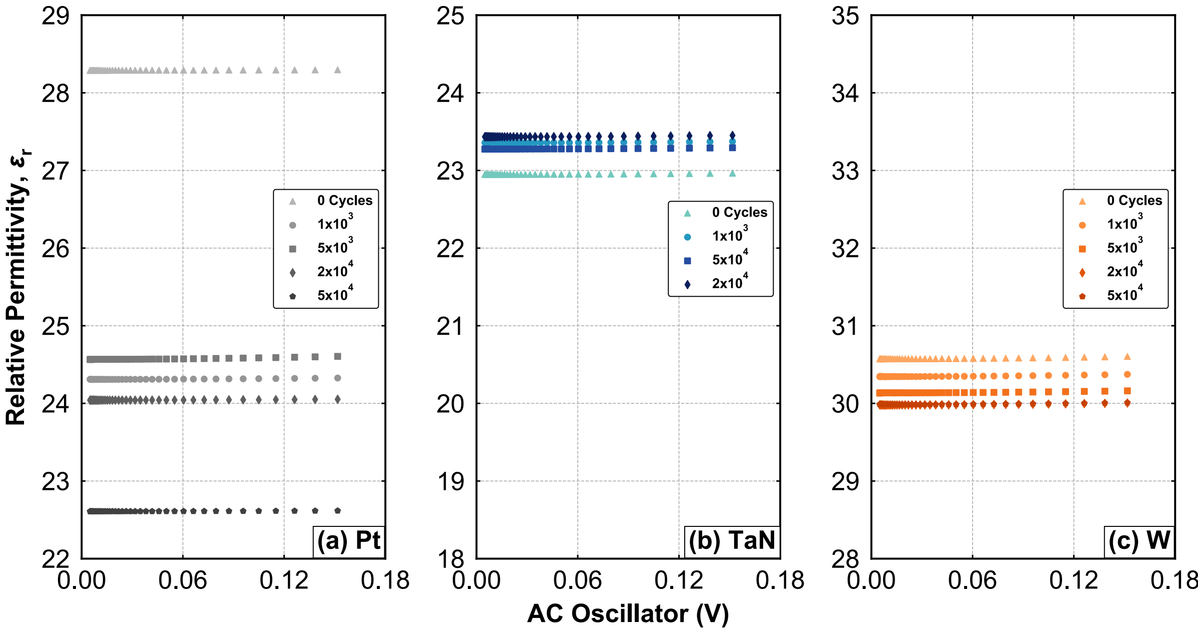

Figure 4.2. Rayleigh measurements at 10 kHz on symmetric MIM devices with (a) Pt, (b) TaN, and (c) W electrodes as a function of oscillator voltage.

Representative synchrotron X-ray diffraction patterns for the three capacitors in the pristine condition are shown in Figure 4.3 along with fits used to calculate relative volume fractions of each phase. Background shape differences are due to reflections of the different electrode materials. For all diffraction measurements performed, peaks at 25.3° and 28.1° in 2θ were indexed as the ($\bar{1}$11) and (111) monoclinic reflections, respectively, and the peak at 27° as the superimposed (101) tetragonal and (111) orthorhombic reflections. The observed diffraction angles are lower than those generally reported for these reflections in HfO_2 due to the utilization of an X-ray wavelength of 1.3776 Å, which is shorter than the Cu Kα wavelength (1.5406 Å) typically employed in lab-based diffractometers. It should be noted that it is historically difficult to separate the tetragonal and orthorhombic phases via diffraction methods owing to the similar *d*-spacings of the phases and peak broadening associated with small crystallite sizes. For the remainder of this study, these reflections will be referred to as the tetragonal + orthorhombic (t + o) peak. As is evident from this diffraction data, all films comprise mixed phases with the capacitors prepared with TaN electrodes qualitatively having the most intense t + o peak relative to the monoclinic (m) peaks. It was also observed that the measured *d*-spacing of the t + o peak from the device with platinum electrodes was slightly larger than that of TaN and tungsten devices: 2.9558 ± 0.00041 Å,

compared to 2.9453 ± 0.0004 Å and 2.9427 ± 0.0004 Å, respectively, and that the monoclinic phase *d*-spacings were nearly identical for all samples. The origin of the *d*-spacing differences is unknown at this time, but may be due to differing t + o phase fractions or differing strain states.

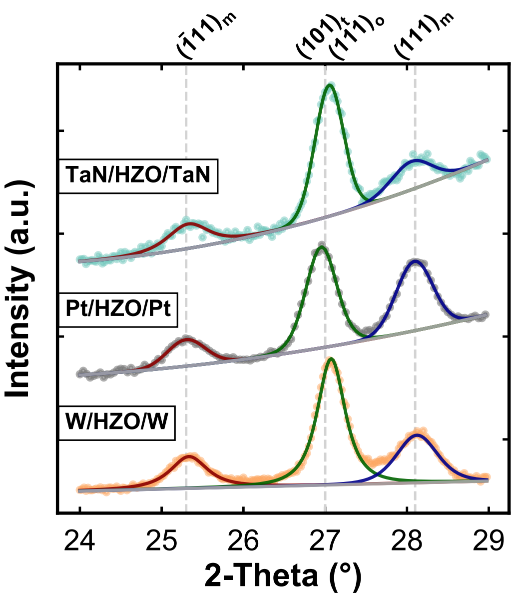

Figure 4.3. X-ray diffraction patterns measured on each MIM device structure, TaN (top), Pt (middle), and W (bottom) with fits (solid lines) to each of the peaks shown. An X-ray wavelength of 1.3776 Å was utilized for diffraction measurements.

Figure 4.4 shows the changes in the P_r of devices of each electrode stack over the course of field cycling, as calculated from positive up, negative down (PUND) measurements. The field cycling behaviors were observed to depend strongly on electrode material. For the platinum devices, P_r was observed to decrease by 27% through 5×10^4 cycles, while the P_r values of the TaN and tungsten devices increased. Focusing first on the platinum devices, diffraction patterns and fits for each cycling interval are shown in Figure 4.5(a) along with their respective $P(E)$ responses. Qualitatively, the t + o peak decreases in intensity and the monoclinic peaks increase as the hysteresis response shows increasing evidence of leakage currents. The quantified peak intensities are shown in Figure 4.4(b) as the ratio of the integrated peak intensity of the t + o peak to the integrated intensity sum of all three peaks, which provides a relative t + o intensity ratio and will be denoted as the relative t + o phase fraction throughout this study. Normalized intensity changes

of each peak after the cycling intervals are shown in Figure 4.6. The value of the intensity ratio decreased with field cycling from 0.48 ± 0.03 in the uncycled electrode to 0.32 ± 0.07 for the electrode exposed to 5×10^4 cycles – a relative change of 33%. This device-scale diffraction data indicates that the tetragonal/orthorhombic phases have converted to the monoclinic phase. While the diffraction data is a clear indication that the P_r reduction is related to a phase transformation, additional evidence of this mechanism is provided in the evolution of the relative permittivity shown in Figure 4.4(c). The relative permittivity of the platinum electrode devices was observed to decrease from 28.4 to 22.6 from the pristine condition to 5×10^4 cycles. Considering that the orthorhombic and tetragonal phases are reported to have ε_r values between 27 and 70 and the monoclinic phase between 16 and 20,[154] this decrease in permittivity further supports the transformation in phase observed in diffraction measurements. Combined, evaluation of the peak intensities of the t + o and monoclinic phases and the relative permittivity of the platinum electrode devices suggests that phase transformation from tetragonal/orthorhombic to monoclinic is the primary factor leading to polarization fatigue in symmetric platinum MIM devices cycled at 2.0 MV cm^{-1} and 1 kHz.

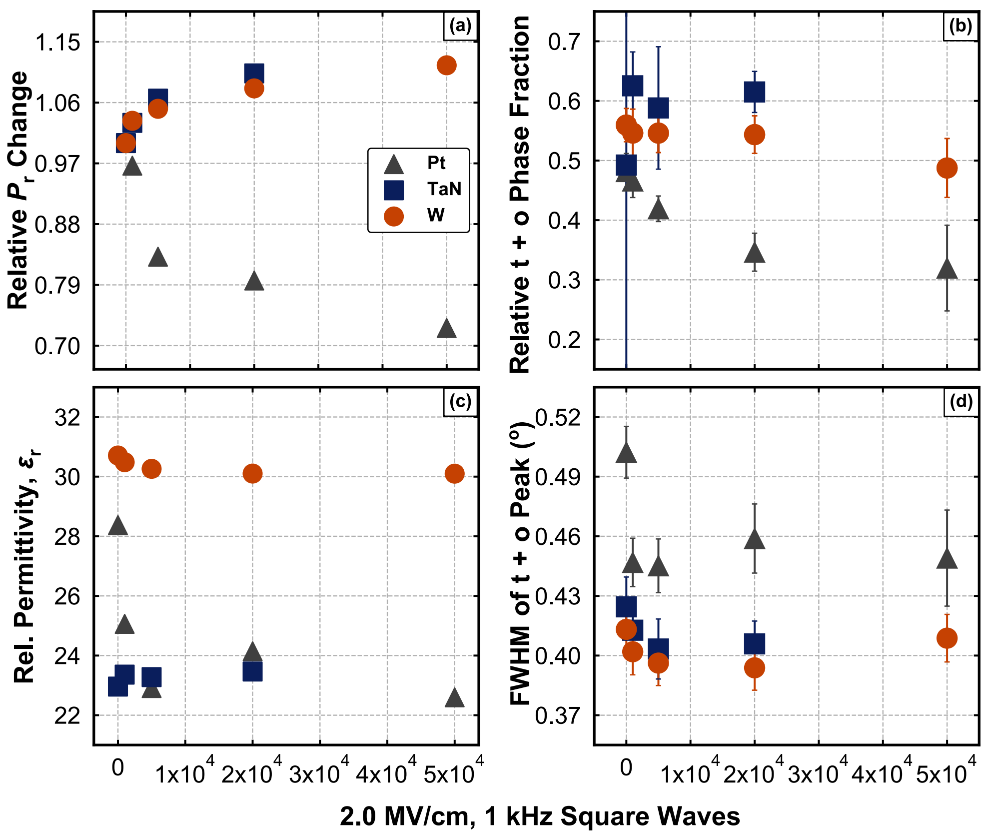

Figure 4.4. (a) Relative P_r, (b) relative t + o phase fraction, (c) relative permittivity, and (d) FWHM of the tetragonal/orthorhombic peak as a function of the number of 2.0 MV cm^{-1}, 1 kHz square wave cycles for symmetric MIM structures with Pt (grey triangles), TaN (blue squares), and W (orange circles) electrodes.

Field cycling of the TaN and tungsten samples with 2×10^4 and 5×10^4 cycles revealed increases in relative P_r of 10.3% and 11.5%, respectively, as shown in Figure 4.4(a). The TaN sample was limited to 2×10^4 cycles due to the onset of dielectric breakdown, while the tungsten (and platinum) samples broke down following 5×10^4 square waves, which prevented further analysis. The diffraction patterns and corresponding $P(E)$ responses associated with the TaN and tungsten devices are shown in Figure 4.5(b) and (c), respectively. No clear correlation between P_r and relative t + o phase fraction exists for either device, as shown in Figure 4.4(a) and (b), respectively. For these devices, the relative t + o phase fraction values remained constant, within error. Considering the clear evidence for a phase transformation leading to P_r reduction in the platinum devices, this lack of substantial correlation suggests that the wake-up process for the TaN

and tungsten electrode devices is not strongly driven by a phase transformation between the monoclinic and tetragonal/orthorhombic phases.

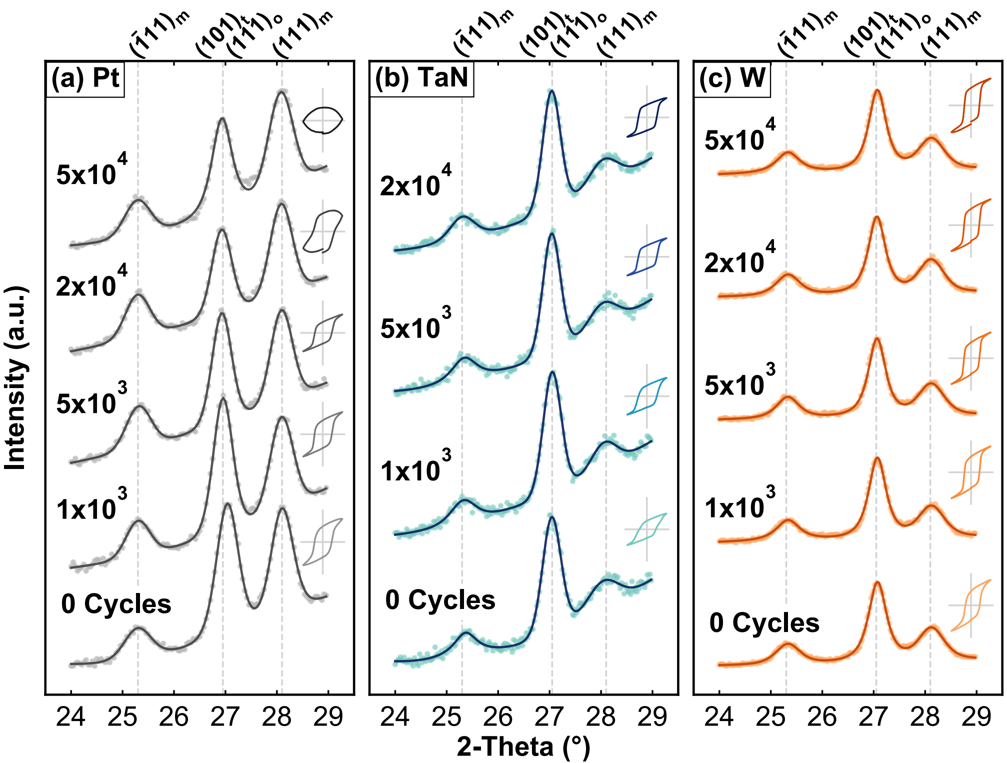

Figure 4.5. Diffraction patterns measured on each cycling interval pad for symmetric MIM devices with (a) Pt, (b) TaN, and (c) W electrodes. The number of 2.0 MV cm^{-1}, 1 kHz square wave cycles is indicated to the left of each pattern. The corresponding 2.5 MV cm^{-1}, 100 ms (Pt) or 1 ms (TaN, W) $P(E)$ response is plotted to the right of each pattern. An X-ray wavelength of 1.3776 Å was utilized for diffraction measurements. The magnitudes for the inset polarization and electric field axes are ± 25 μC cm^{-2} and ± 3.0 MV cm^{-1}, respectively.

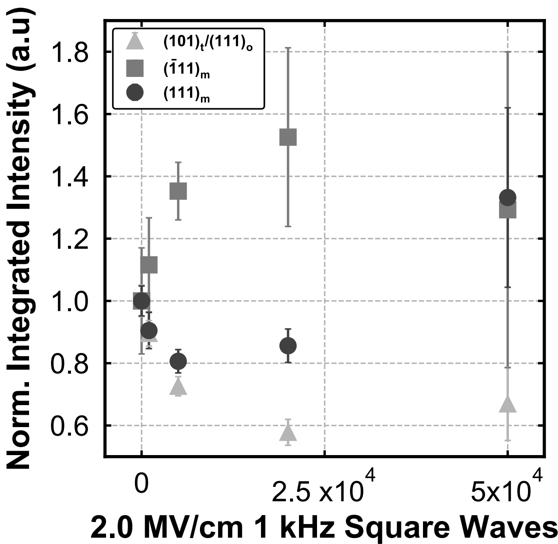

Figure 4.6. Normalized integrated intensities for the ($\bar{1}$11) monoclinic, (111) monoclinic, and (101) tetragonal/(111) orthorhombic diffraction peaks measured on devices with platinum electrodes cycled at various intervals of 2.0 MV cm^{-1}, 1 kHz square waves.

The most significant diffraction-related change observed during the field cycling for both the TaN and tungsten samples was a decrease in the full-width at half maximum (FWHM) of the t + o superimposed peak, which is shown in Figure 4.4(d). In both device stacks, the relative P_r increased through field cycling while the FWHM of the t + o superimposed peak was observed to decrease from 0.425 ± 0.015° to 0.406 ± 0.012° for TaN, and from 0.413 ± 0.010° to 0.408 ± 0.012° for tungsten. It is important to note that these changes are within error for both datasets. However, the identical FWHM decrease and relative P_r increase trends with field cycling for both samples are suggestive that a phase transformation has occurred between the tetragonal and orthorhombic phases. Importantly, as homogeneous strain has been observed in polycrystalline ferroelectric HfO_2-based films previously,[125] this FWHM reduction is likely not related to strain evolution due to ferroelastic switching.[176] Additionally, the FWHM of the t + o superimposed peak in the platinum electrode devices, which were not observed to wake up, also decreased from 0.502 ± 0.013° to 0.449 ± 0.024° with field cycling (Figure 4.4(d)). This suggests that a tetragonal to orthorhombic phase transformation is also occurring for the platinum electrode devices and is concomitant with the tetragonal/orthorhombic transformation to monoclinic phase in the fatigue process.

To better understand the origin of the t + o peak FWHM decrease upon field cycling for the TaN and tungsten electrode devices the change in ε_r (Figure 4.4(c)) was considered. Comparing the intrinsic relative permittivities through wake-up revealed a slight reduction for tungsten devices with values of 30.7 for pristine devices and 30.1 after 5×10^4 cycles (Figure 4.4(c)). This decrease may indicate some transformation of a high permittivity non-ferroelectric tetragonal phase to a lower permittivity ferroelectric orthorhombic phase has occurred. No significant changes were observed for the TaN devices and it should be noted that the ε_r values were substantially lower than those for tungsten devices despite having higher relative t + o phase fractions. It is known that reaction layers can form at metal nitride/hafnia interfaces[154,235] and it is hypothesized that such layers formed in this study and have contributed to reducing the overall device permittivity and measured polarization. The addition of interfacial capacitive layers in series with the HZO dielectric might also affect the observed coercive field, which is larger for TaN devices compared to tungsten devices (Figure 4.1(b) and (c)). These interlayers may also mask permittivity reductions that result due to phase transformations from the tetragonal to orthorhombic phase; however, they do not seem to affect the wake-up process as the relative increase in P_r is nearly the same for both tungsten and TaN devices.

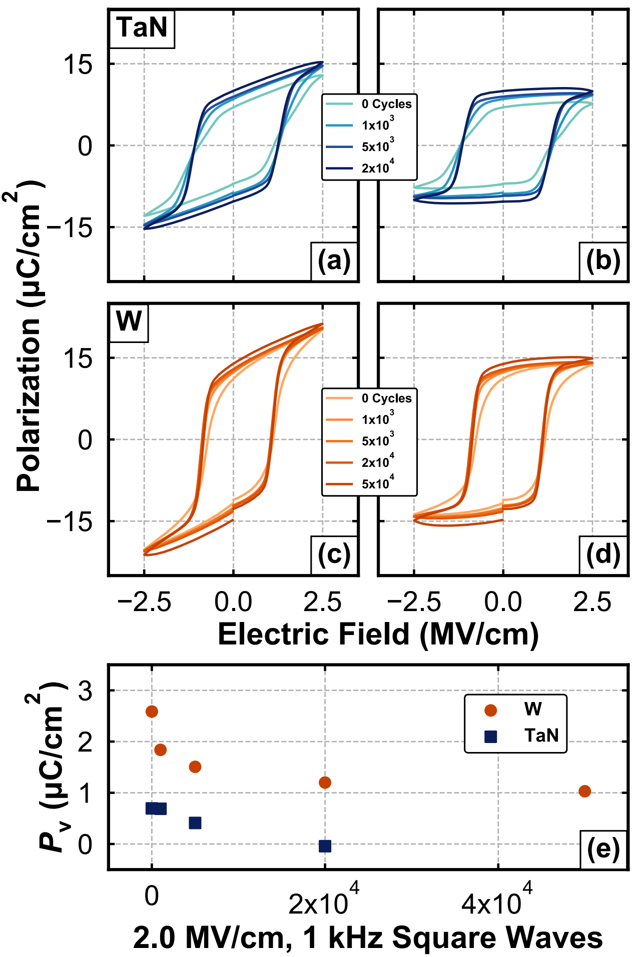

Figure 4.7. Dielectric displacement dependence measured at each square wave interval for MIM devices with TaN (blue) and W (orange) electrodes (a, c, respectively), and corresponding $P(E)$ response with linear dielectric displacement subtracted (b, d, respectively). (e) Corresponding variable polarizations (P_v) for each square wave interval for devices constructed with TaN (blue) and W (orange) electrodes.

As an alternative means of assessing possible tetragonal to orthorhombic phase transformation contributions to wake-up, the change in variable polarization response, P_v, with field cycling, was calculated following the approach of Park, *et al.*,[130] as shown in Figure 4.7(a-e). In this method, the linear dielectric contribution to polarization was separated from the total dielectric displacement to isolate the polarization contribution from ferroelectric dipoles. This was performed by subtracting $E\varepsilon_r\varepsilon_0$ from the measured total dielectric displacement response, where E

is the applied electric field, ε_r is the relative permittivity (measured at 2.5 MV cm^{-1}, Figure 4.8), and ε_0 is the permittivity of free space. P_v is equal to the difference between the isolated ferroelectric dipole polarization under an applied field of 2.5 MV cm^{-1} and P_r (*i.e.* the difference between the maximum and remanent polarization values after subtracting the linear dielectric contribution). The total dielectric displacement and isolated polarization responses are shown in Figure 4.7(a, c) and (b, d), respectively, for the TaN and tungsten electrode devices. The P_v value as a function of wake-up cycling is shown in Figure 4.7(e). This value was found to decrease during field cycling of the device with tungsten electrodes from 2.58 to 1.02 μC cm^{-2} through 5×10^4 cycles, and from 0.69 to 0 μC cm^{-2} for the device with TaN electrodes through 2×10^4 cycles. A positive P_v value has been attributed to the presence of field-induced ferroelectric contributions to the maximum observed polarization, and its decrease with an irreversible phase transformation between the ferroelectric orthorhombic and antiferroelectric tetragonal phases.[130] To examine potential changes in switching behavior due to cycling, switching current measurements, provided in Figure 4.9(a) and (b) for TaN and tungsten electrode devices, respectively, were derived from corresponding polarization responses shown in Figure 4.7(a) and (c). For the TaN sample, two switching current peaks were observed to merge between the pristine and 1000 cycle state, which could be an indication of charged defect de-trapping and subsequent domain de-pinning affecting the switching behavior,[174,236] a thin dielectric interface layer leading to strong depolarization fields that degrades with field cycling,[177] or that the devices have different relative contents of field-induced ferroelectric tetragonal and ferroelectric orthorhombic phases.[117] Following this initial merge, a single peak is observed to sharpen with continuing field cycling, similar to behavior observed in the tungsten devices in which a single switching current peak was observed throughout the wake-up process. Examining the increasing maximum polarizations (Figure 4.7(a) and (c)) and the slope of the $P(E)$ response at the coercive field (Figure 4.9(c) and (d)) for both TaN and tungsten devices, the change in $P(E)$ response is consistent with the reduction in thickness of a non-ferroelectric interlayer with field cycling, as described by Tagantsev *et al.*[243] Thus, the decrease in P_v and change in $P(E)$ characteristics, specifically the increase in remanent and maximum polarizations and slope of the polarization response with field at the coercive field with cycling in both devices, supports that a tetragonal to orthorhombic phase transformation has occurred. Domain depinning is almost certainly occurring and contributing, in-part, to the wake-up process, particularly for the TaN devices. Degradation of an insulating TaO_xN_y layer may also

be occurring, as has been suggested to occur for linear dielectric interfacial layers.[177] These effects could be present for the wake-up in the first 1000 cycles, but the data provided here suggests that the phase transformation from non-ferroelectric tetragonal to ferroelectric orthorhombic is also a major contributor, especially since the wake-up behavior of the tungsten and TaN devices are so similar after the first 1000 cycles and the tungsten electrodes are not anticipated to form an insulating interfacial reaction layer as discussed later.

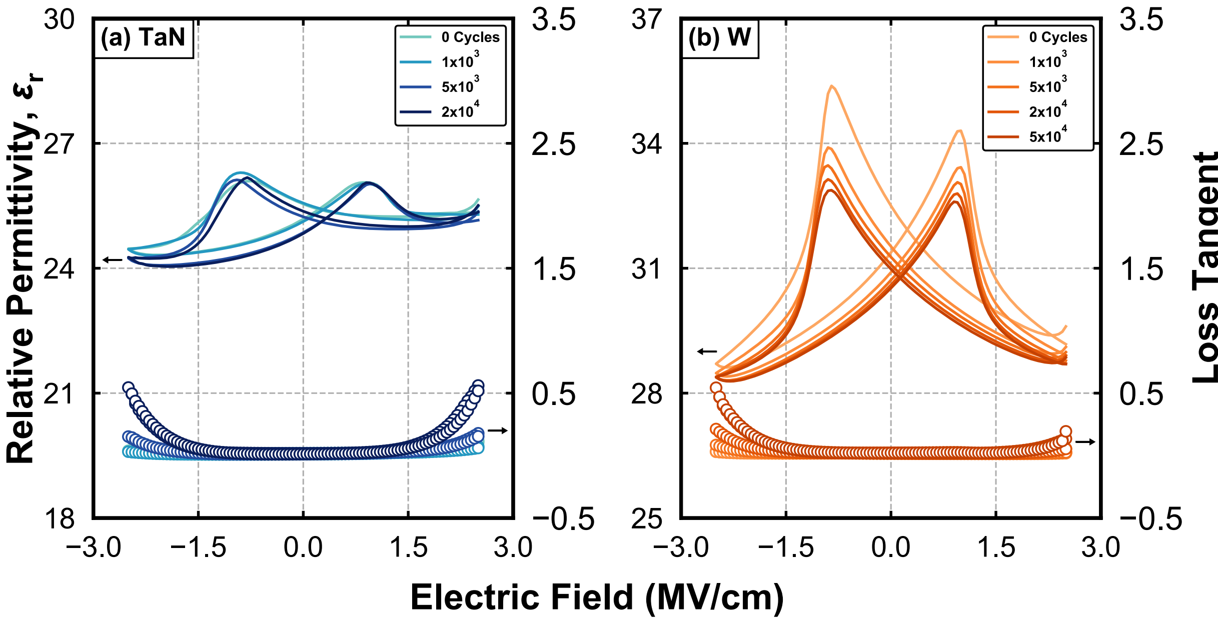

Figure 4.8. Relative permittivity versus electric field measurements on symmetric MIM devices with (a) TaN and (b) W electrodes cycled with 2.0 MV/cm, 1 kHz square waves at various intervals.

Such a phase transformation may be anticipated to result in changes in X-ray scattering peaks as well. Since the *d*-spacings of the (101) tetragonal and (111) orthorhombic phases are similar, but not identical, the transformation of one phase to another will affect the intensity of the portion of the composite reflection attributed to that phase. Due to the ferroelectric character of the polarization-electric field response, as shown in Figure 4.7(a-d), the orthorhombic phase is expected to dominate the initial peak width. Therefore, if the tetragonal phase is converting to the orthorhombic phase, the peak will narrow as a greater portion of the diffracting volume is of the *d*-spacing of the orthorhombic phase and the relative thickness of the orthorhombic phase increases

as the thickness of the tetragonal phase at the electrode interfaces decreases. Further, one may expect the center of the peak, and thus extracted *d*-spacings, to shift if phase transformation has occurred. Figure 4.10 details the changes in interplanar spacing of the t + o reflection resultant from cycling for all three device stacks. For the tungsten device, 5×10^4 electrical cycles resulted in a t + o *d*-spacing increase from 2.9426 ± 0.0003 Å to 2.9433 ± 0.0004 Å, while for the TaN device, an increase from 2.9461 ± 0.0005 Å to 2.9464 ± 0.0005 Å through 2×10^4 electrical cycles was observed. The magnitudes of these *d*-spacing shifts are smaller than those observed for the platinum device, which increased from 2.9464 ± 0.0004 Å to 2.9588 ± 0.0007 Å over the course of 5×10^4 cycles. While the magnitudes of the peak shifts are small, the increase in *d*-spacing is consistent with a transformation from the tetragonal to the orthorhombic phases, as previously observed in high temperature diffraction experiments.[140] It should be noted, however, that changes in strain state due to ferroelastic domain switching cannot be completely discounted to affect peak position, but are unlikely to affect peak width because of degeneracy of the orthorhombic (111) reflection, an expected homogeneous strain condition,[125] and diffracting volume conservation. Thus, the electrical data, which supports a transformation from the tetragonal to the orthorhombic phases in both tungsten and TaN electrode devices suggests that the t + o peak FWHM narrowing and the shift to lower angles is diffraction-based evidence of phase transformation occurring concurrent with wake-up of ferroelectric hafnium oxide films.

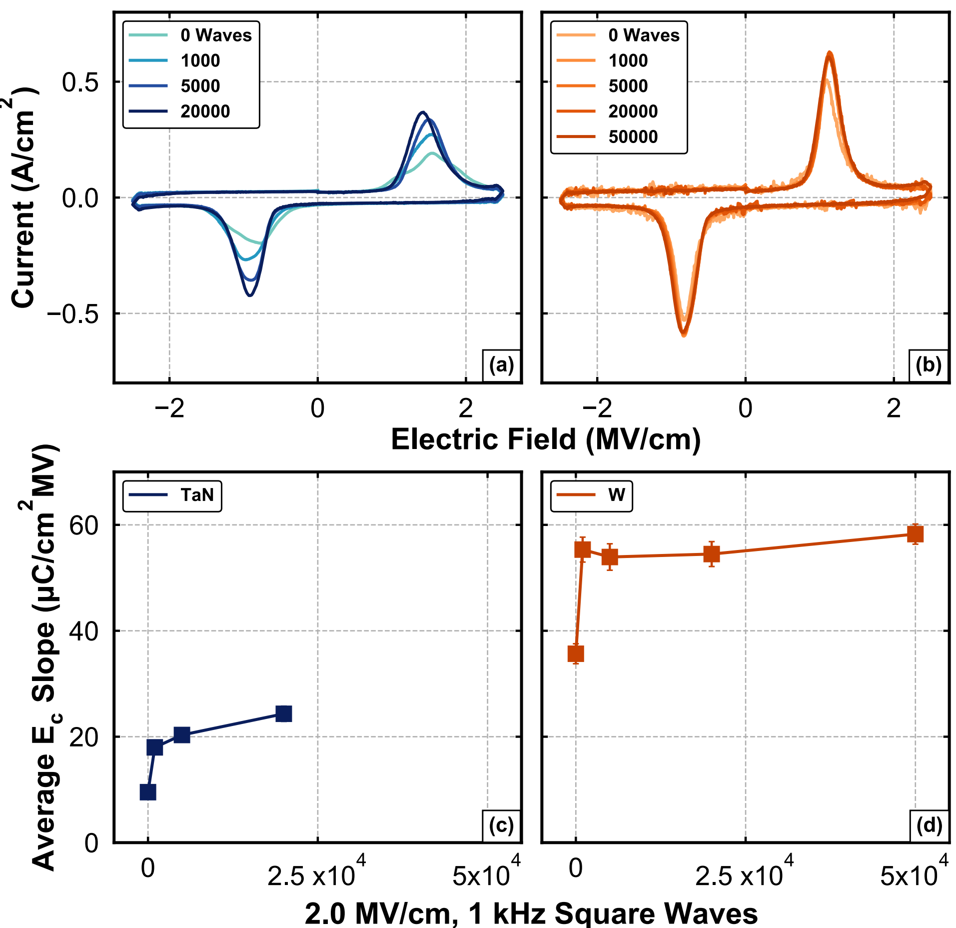

Figure 4.9. Switching current responses (a, b) derived from *P*(*E*) response shown in Figure 4.7(a, c). Associated average *P*(*E*) slope at the coercive field (c, d) measured on devices with TaN (blue) and W (orange) electrodes for P_v analysis in Figure 4.7(a-e).

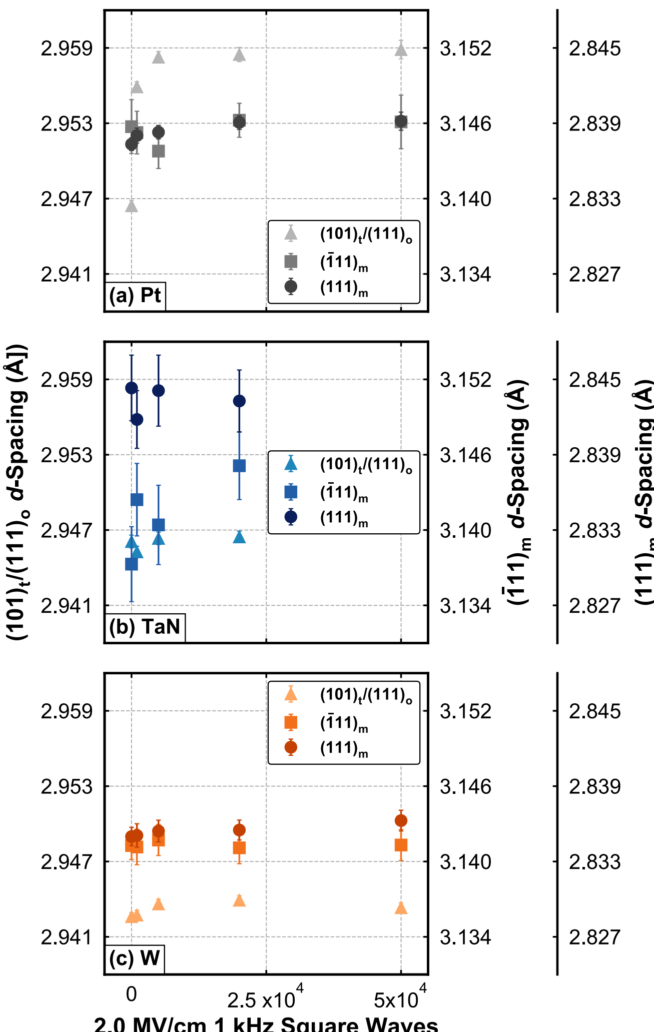

Figure 4.10. Interplanar spacings of the (101) tetragonal/(111) orthorhombic, ($\bar{1}11$) monoclinic, and (111) monoclinic planes from symmetric MIM devices with (a) Pt, (b) TaN, and (c) W electrodes cycled at various intervals with 2.0 MV/cm, 1 kHz square waves.

It is evident from the results of this study that the electrode material chemistry impacts the propensity for the HZO film to wake-up or fatigue. Use of noble metal contacts, which are anticipated to be blocking to oxygen ions[239] led to direct fatigue and phase transformation of ferroelectric orthorhombic phases to non-ferroelectric monoclinic. Nitride electrodes, however, are susceptible to oxygen incorporation and may act as a sink for both oxygen and oxygen vacancies.[184] As such, a difference in wake-up versus fatigue behavior between these different

electrode classes may be expected. Furthermore, while the chemistry of the interfaces of tungsten electrodes and the dielectric is unknown, it may be anticipated that oxidation of the tungsten in the immediate vicinity of the interface is possible, given the relatively low free energy of tungsten oxide, particularly compared to platinum. As many tungsten oxide phases and sub-stoichiometric tungsten oxides may be expected to be semiconducting or conducting,[244] its presence may not lead to an obvious electrical signature. It could however, serve as a sink or source for oxygen vacancies similar to the TaN electrodes, which would explain why its wake-up behavior was more similar to TaN devices than platinum devices. While we are unable to assess the exact reason why devices with platinum electrodes fatigued via a phase conversion to the monoclinic phase and the TaN and tungsten devices displayed primarily tetragonal to orthorhombic phase conversion, the different electrode materials and their interfacial electrode chemistries are likely dominant factors. For example, for the platinum electrode devices it may be anticipated that vacancies already present in the HZO film primarily redistribute within the HZO layer with field cycling while those present in the TaN and tungsten electrode devices may redistribute and exchange with the interfacial phases changing their total concentration, as previously suggested by Starschich, *et al.*[165] Given that oxygen vacancy concentration is linked to phase stability in the HfO_2 system, it is not surprising that these different electrode chemistries impact phase evolution with field cycling. Regardless of the exact mechanisms, the data presented in the present work provides evidence that for the same electric field cycling conditions, phase transformation mechanisms lead to either fatigue or wake-up behavior and the electrode used dictates the response. Given that prior research has observed wake-up behavior with platinum electrodes while using larger electric fields than those used in this study,[165] additional research will be needed to understand the impact of electric field magnitudes and electrode chemistry on the phase transformations driving wake-up and fatigue.

4.6 Conclusions

The field cycling behavior of MIM capacitor devices comprising 20 nm thick ferroelectric $Hf_{0.58}Zr_{0.42}O_2$ films between symmetric TaN, tungsten, and platinum electrode layers has been evaluated electrically and structurally. The following observations were made: 1) For the platinum devices, which exhibited ferroelectric fatigue, a decrease in the relative t + o phase fraction was correlated with a decrease in both P_r and ε_r during electric field cycling, indicating that the physical

mechanism responsible for the polarization fatigue is a phase transformation from the tetragonal/orthorhombic to the monoclinic phases. 2) Diffraction measurements of the TaN and tungsten devices, which both demonstrated increasing P_r with field cycling, did not exhibit a strongly correlated change in the relative t + o phase fraction. This lack of change indicates that phase transformation from the monoclinic to the tetragonal/orthorhombic phases is not the physical mechanism responsible for the observed polarization wake-up in these structures. The FWHM of the tetragonal/orthorhombic superimposed diffraction peak, however, was observed to decrease for both samples. A decrease in the variable polarization response and change in $P(E)$ characteristics with wake-up, coupled with the FWHM reduction and shift of the peak to larger *d*-spacings suggests that a phase transformation from the tetragonal to the orthorhombic phases is occurring during wake-up, as has been observed through STEM measurement of HfO_2 ferroelectrics.[154] 3) Non-destructive synchrotron X-ray diffraction measurements, concurrent with electrical characterization, have sufficient sensitivity to study the phase transformation mechanisms impacting performance of ferroelectric hafnium oxide films at the device scale. This new insight is vital for identifying and enabling solutions to polarization instabilities in ferroelectric hafnium oxide films.

4.7 Acknowledgement

This work was supported, in part, by the Laboratory Directed Research and Development program at Sandia National Laboratories. Sandia National Laboratories is a multimission laboratory managed and operated by National Technology and Engineering Solutions of Sandia, LLC, a wholly owned subsidiary of Honeywell International, Inc., for the U.S. Department of Energy's National Nuclear Security Administration under contract DE-NA0003525. This work is supported, in part, by the Semiconductor Research Corporation (SRC). This research used resources of the Advanced Photon Source, a U.S. Department of Energy (DOE) Office of Science User Facility operated for the DOE Office of Science by Argonne National Laboratory under the contract DE-AC02-06CH11357. This paper describes objective technical results and analysis. Any subjective views or opinions that might be expressed in the paper do not necessarily represent the views of the U.S. Department of Energy or the United States Government. The authors wish to

acknowledge the staff of Radiant Technologies for their technical support and technical discussions with Jacob L. Jones.

Chapter 5: Compositional and Phase Dependence of Elastic Modulus of Crystalline and Amorphous $Hf_{1-x}Zr_xO_2$ Thin Films

The contents of this chapter are published in *Applied Physics Letters* (**118**, 102901, 2021, DOI: https://doi.org/10.1063/5.0044702) as an *Editor's Pick* with the following as authors:

Shelby S. Fields,[1] David H. Olson,[2] Samantha T. Jaszewski,[1] Chris M. Fancher,[3] Sean W. Smith,[4] Diane A. Dickie,[1,5] Giovanni Esteves,[4] Michael D. Henry,[4] Paul S. Davids,[4] Patrick E. Hopkins,[1,2,6] and Jon F. Ihlefeld.[1,7]

[1]Department of Materials Science and Engineering, University of Virginia, Charlottesville VA, 22904, USA

[2]Department of Mechanical and Aerospace Engineering, University of Virginia, Charlottesville VA, 22904, USA

[3]Materials Science and Technology Division, Oak Ridge National Laboratory, Oak Ridge TN, 37831, USA

[4]Sandia National Laboratories, Albuquerque NM, 87123, USA

[5]Department of Chemistry, University of Virginia, Charlottesville VA, 22904

[6]Department of Physics, University of Virginia, Charlottesville VA, 22904

[7]Charles L. Brown Department of Electrical and Computer Engineering, University of Virginia, Charlottesville VA, 22904, USA

The body of text of this chapter has been adapted to include the supplemental information and figures, where appropriate.

5.1 Motivation

As subsequent investigations seek to examine the effects of stress on the ferroelectric properties of HZO MIM devices, it is necessary to first experimentally quantify the elastic modulus of HZO. In this chapter, HZO devices with compositions between pure HfO_2 and ZrO_2 are characterized using an optical picosecond acoustic technique, which is employed to quantify the speed of sound through the films. Using this data, the elastic moduli are calculated, which are then employed to quantify the amount of biaxial stress present in the films. These elastic moduli values are further harnessed in subsequent investigations throughout this dissertation.

5.2 Abstract

The elastic moduli of amorphous and crystalline atomic layer-deposited $Hf_{1-x}Zr_xO_2$ (HZO, $x = 0$, 0.31, 0.46, 0.79, 1) films prepared with TaN electrodes on silicon substrates were investigated using picosecond acoustic measurements. The moduli of the amorphous films were observed to increase between 161 ± 4 GPa for pure HfO_2 and 231 ± 7 GPa for pure ZrO_2. In the crystalline films it was found that the moduli increased with increasing zirconium composition from 190 ± 5 GPa for monoclinic HfO_2, to 204 ± 7 GPa for tetragonal ZrO_2. Positive deviations from this increase were observed for the $Hf_{0.69}Zr_{0.31}O_2$ and $Hf_{0.54}Zr_{0.46}O_2$ compositions, which were measured to have moduli of 202 ± 6 GPa and 209 ± 6 GPa, respectively. These two compositions contained the largest fractions of the ferroelectric orthorhombic phase, as assessed from polarization and diffraction data. The biaxial stress states of the crystalline films were characterized through $\sin^2(\psi)$ X-ray diffraction analysis. The in-plane stresses were all found to be tensile and observed to increase with increasing zirconium composition, between 1.94 ± 0.5 GPa for pure HfO_2 and 3.98 ± 0.4 GPa for pure ZrO_2. The stresses are consistent with large thermal expansion mismatches between the HZO films and silicon substrates. These results demonstrate a device-scale means to quantify biaxial stress for investigations on its effect on the ferroelectric properties of hafnia-based materials.

5.3 Introduction

Since the first reporting of ferroelectric responses nearly a decade ago,[1] HfO_2-based thin films have witnessed research and development for applications including ferroelectric random access memory,[2,229,232,245] energy harvesting,[221,246] and negative differential capacitance field effect transistors.[230,247] The ferroelectric response has been attributed to a non-centrosymmetric orthorhombic phase (space group $Pca2_1$), which is energetically metastable between the room-temperature, linear dielectric monoclinic ($P2_1/c$) and high-temperature field-induced-ferroelectric tetragonal ($P4_2nmc$) phases.[87,114] The stability of this orthorhombic phase has been attributed to small crystallite sizes,[90] inclusion of specific dopants,[113,248] and the presence of biaxial stress,[115,151] among others. HfO_2-based ferroelectrics are typically grown to thicknesses of 5 – 20 nm, which limits the grain size via thickness truncation, and doped to enhance orthorhombic phase stability.

ZrO_2 alloying has been observed to stabilize the orthorhombic phase through a broad composition window ($x \approx 0.1 - 0.8$)[3,130] and result in a reduced thermal budget compared to many other ferroelectric HfO_2 compositions.[142,249] In spite of the many mechanisms to increase orthorhombic phase stability, $Hf_{1-x}Zr_xO_2$ (HZO) thin films often exhibit mixtures of the orthorhombic, tetragonal, and monoclinic phases, with Hf-rich and Zr-rich compositions resulting in monoclinic-rich and tetragonal-rich phase constitutions, respectively.[3,130,149,195]

Biaxial stress impacts both the phase stability and the domain structure. Computational works have suggested that compressive biaxial stresses facilitate stabilization of the orthorhombic phase compared to the equilibrium monoclinic.[87] Experimental studies, alternatively, have observed enhanced polarization responses under conditions that yield biaxial tensile stress,[115,116] or favorable texture,[125] both of which alter the domain structure to maximize the degree to which the short polar axis is oriented normal to the film surface. Such experimental works examining stress effects in HfO_2-based ferroelectrics rely on combinations of experimental and computationally predicted bulk elastic constants for the monoclinic, tetragonal, and orthorhombic phases for analysis. Measurement of these values in planar, mixed phase thin films is important because utilization of bulk, phase-pure elastic constants may discount effects of microstructural features such as the high density of grain boundaries and presence of interface segregated phases,[130,154] both of which may affect the elastic properties. Thus, the direct measurement of elastic constants in relevant phases and phase mixtures present in HZO thin films provides necessary information for investigations of stress effects on phase stabilization, domain structure, and ferroelectric performance. Additionally, knowledge of the elastic behavior of these ferroelectric materials is critical for emergent piezoMEMS applications, such as resonator device structures.[250,251]

In this study, the elastic moduli (E) of amorphous and crystalline 20 nm-thick $Hf_{1-x}Zr_xO_2$ ($0 \leq x \leq 1$) thin films prepared with TaN electrodes on silicon substrates are directly investigated using picosecond acoustic measurements. The crystallized films comprise pure monoclinic HfO_2, pure tetragonal ZrO_2, and phase mixtures in the alloy compositions, which include the ferroelectric orthorhombic phase. The experimental elastic moduli from these measurements are utilized to quantify the stress states of the crystalline 20 nm-thick HZO films through $\sin^2(\psi)$ X-ray diffraction analyses.

5.4 Experimental Procedures

Metal-Insulator-Metal (MIM) devices comprising $Hf_{1-x}Zr_xO_2$, with $x = 0$, 0.31, 0.46, 0.79, and 1, between TaN top and bottom electrodes were prepared. 100 nm-thick TaN bottom electrodes were deposited via DC sputtering from a TaN target onto (001)-oriented silicon substrates under an argon background pressure of 5 mTorr at a power density of 3.3 W cm^{-2} with a 45 degree off-axis geometry. 20 nm-thick $Hf_{1-x}Zr_xO_2$ films were deposited via plasma-enhanced atomic layer deposition (PEALD) at a substrate temperature of 260 °C using tetrakis(ethylmethylamido)hafnium (TEMA Hf) and tetrakis(ethylmethylamido)zirconium (TEMA Zr) as hafnium and zirconium precursors, respectively, and an oxygen plasma as the oxidant within an Oxford FlexAL II instrument. The ratio of Hf:Zr cycles within each 10-cycle super cycle was altered to control the film composition. The growth rates were determined to be 1.05 Å/cycle and 1.15 Å/cycle for HfO_2 and ZrO_2, respectively. Film compositions were determined via X-ray Photoelectron Spectroscopy measurements of fully processed devices. For these measurements, spectra were collected with a 200 µm diameter spot size using Al Kα radiation with an incidence angle of 45°, a 15 kV accelerating voltage, and an anode power of 50 W. Hf *4f* and Zr *3d* peak intensities were fit using KolXPD XPS analysis software. Following HZO deposition, films meant for crystallization received planar, sputtered 20 nm-thick TaN top electrodes and the samples were annealed at 600 °C for 30 seconds under N_2 at atmospheric pressure. Following annealing, samples on which electrical analyses were to be performed received 50 nm-thick circular Pd contacts through a shadow mask with diameters spanning 100 – 500 µm via DC sputtering utilizing the same conditions as for the electrodes. Samples were subsequently exposed to an SC-1 etch solution (5:1:1 H_2O:30% H_2O_2 in H_2O:30% NH_4OH in H_2O) at 60 °C for 25 minutes to remove the exposed TaN and define devices for electrical analyses using the Pd contacts as a hard mask. Polarization versus electric field hysteresis ($P(E)$, 10 ms test period), current-voltage, and positive up negative down (PUND, 1 ms pulse and 1000 ms delay) measurements were made between 1.0 – 2.5 MV cm^{-1} using a Radiant Technologies Precision LC II Tester. Capacitance-voltage (CV) measurements were made using a Keysight E4980A LCR meter at 10 kHz with a 50 mV oscillator amplitude. The phase constitution and thickness/density of each of the films were examined using grazing incidence X-ray diffraction (GIXRD) and X-ray reflectivity (XRR), respectively, on samples processed without Pd contacts using a Rigaku

SmartLab diffractometer with Cu Kα radiation in a parallel beam configuration. GIXRD was performed with ω fixed at 0.7° and XRR patterns were fit with GSAS-II software.[252] 80 nm of aluminum was e-beam evaporated onto each film, which had been measured with GIXRD and XRR to serve as a transducer for picosecond acoustic measurements. The resulting acoustic signatures were fit using LIPRAS line-profile analysis software.[214] 2D diffraction patterns were collected on crystallized samples using a Bruker APEXII Duo diffractometer equipped with an Incoatec IμS Cu Kα microfocus source and an APEXII CCD area detector with ω fixed at 18°. MgO powder was placed on film surfaces for use as a stress-free standard and for sample displacement alignment. Area detector patterns were unwarped using the pyFAI azmithual integration package.[212] $Sin^2(\psi)$ analyses were carried out on the crystallized films using intensity profiles extracted at ψ angles between 0° and 45° relative to the film surface normal to calculate the stress state of each film using the elastic moduli determined from picosecond acoustic measurements.

5.5 Results and Discussion

Figure 5.1(a) shows the $P(E)$ response measured on each HZO film. Responses were observed to be linear for HfO_2 and ZrO_2, hysteretic for $Hf_{0.69}Zr_{0.31}O_2$ and $Hf_{0.54}Zr_{0.46}O_2$, and pinched hysteretic for $Hf_{0.21}Zr_{0.79}O_2$. The largest polarization was observed for the $Hf_{0.54}Zr_{0.46}O_2$ film. The pure ZrO_2 film required electric fields in excess of 2.5 MV cm^{-1} to exhibit the typical field-induced ferroelectric response. The remanent polarizations (P_r, from PUND measurements at 2.5 MV cm^{-1}) for each composition within the series are shown in Figure 5.1(b) and confirm the composition dependence of polarization observed in the $P(E)$ data. These responses are consistent with prior reports on the compositional dependence of polarization response in HZO and suggest non-trivial orthorhombic phase fractions in the $Hf_{0.69}Zr_{0.31}O_2$ and $Hf_{0.54}Zr_{0.46}O_2$ films.[3,130,149] Switching current measurements corresponding to these devices are shown in the Figure 5.2.

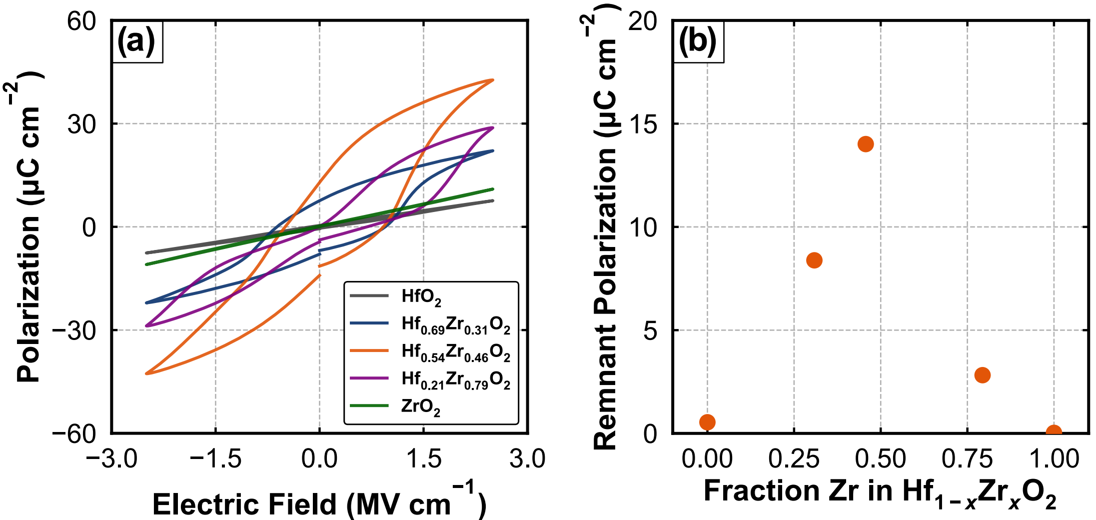

Figure 5.1. (a) $P(E)$ measurements of HfO_2 (grey), $Hf_{0.69}Zr_{0.31}O_2$ (blue), $Hf_{0.54}Zr_{0.46}O_2$ (orange), $Hf_{0.21}Zr_{0.79}O_2$ (purple), and ZrO_2 (green) films. (b) P_r extracted from PUND measurements.

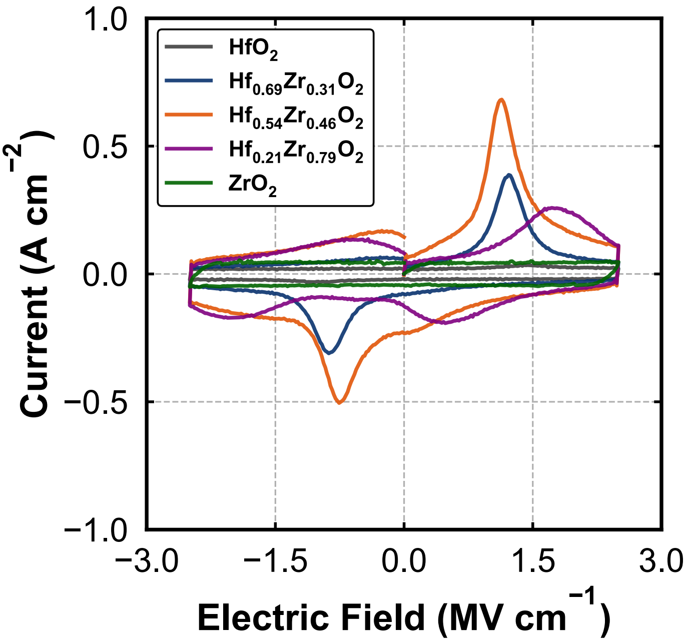

Figure 5.2. Current loops measured on HfO_2 (grey), $Hf_{0.69}Zr_{0.31}O_2$ (blue), $Hf_{0.54}Zr_{0.46}O_2$ (orange), $Hf_{0.21}Zr_{0.79}O_2$ (purple), and ZrO_2 (green) films.

Figure 5.3 shows GIXRD patterns corresponding to each crystallized film, indicating the phases present at each composition. The diffraction pattern measured on the pure HfO_2 film contained two peaks at 28.6° and 31.9° in 2θ, which were indexed as the $(\bar{1}11)$ and (111) monoclinic (m) reflections, respectively. Diffraction patterns measured on the $Hf_{0.69}Zr_{0.31}O_2$ and $Hf_{0.54}Zr_{0.46}O_2$ films contained an additional peak at 30.7° in 2θ, which was indexed as the superimposed (101) tetragonal/(111) orthorhombic (t + o) reflections, and observed to increase in intensity with increasing ZrO_2 concentration. The diffraction patterns measured on the $Hf_{0.21}Zr_{0.79}O_2$ and pure ZrO_2 films contained only t + o peaks. The t + o peak position increased in diffraction angle in the ZrO_2 pattern, which is consistent with previous observations of the diffraction behavior in composition-varied HZO thin films and has been attributed to the tetragonal phase.[142] GIXRD patterns for the un-annealed films lacked distinct Bragg reflections and are shown in Figure 5.4. Combined, the GIXRD patterns and electrical measurements suggest that the $Hf_{0.54}Zr_{0.46}O_2$ film contained the largest orthorhombic phase content: it exhibited the highest measured P_r and an intense, low angle t + o diffraction peak. The $Hf_{0.69}Zr_{0.31}O_2$ film, which had the second highest P_r and diffraction peaks corresponding to all three phases, likely had the second largest orthorhombic phase content. The $Hf_{0.21}Zr_{0.79}O_2$ film had a higher content of the tetragonal phase, as evidenced by the pinched hysteresis response, low P_r, and single t + o diffraction peak. The pure HfO_2 and ZrO_2 films had diffraction patterns and electrical responses consistent with pure monoclinic and tetragonal phases, respectively. The high field permittivities (2.5 MV cm^{-1}), extracted from CV measurements, shown in Figure 5.5, further support a transition from a low permittivity monoclinic phase to higher permittivity orthorhombic and tetragonal phases as the film composition is varied from pure HfO_2 to pure ZrO_2.

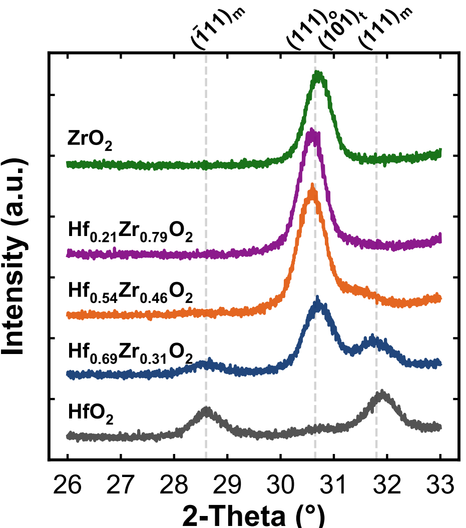

Figure 5.3. GIXRD patterns measured on HfO_2 (grey), $Hf_{0.69}Zr_{0.31}O_2$ (blue), $Hf_{0.54}Zr_{0.46}O_2$ (orange), $Hf_{0.21}Zr_{0.79}O_2$ (purple), and ZrO_2 (green) films.

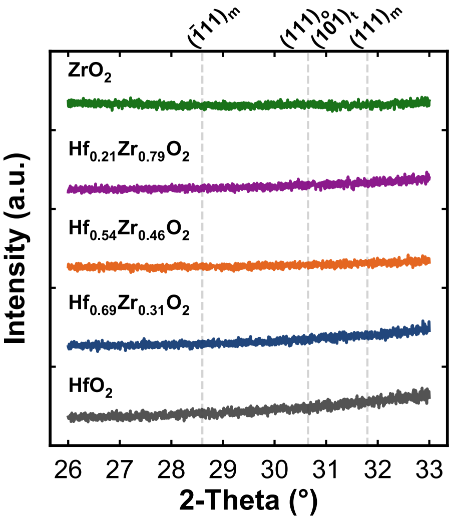

Figure 5.4. GIXRD patterns measured on amorphous HfO_2 (grey), $Hf_{0.69}Zr_{0.31}O_2$ (blue), $Hf_{0.54}Zr_{0.46}O_2$ (orange), $Hf_{0.21}Zr_{0.79}O_2$ (purple), and ZrO_2 (green) films.

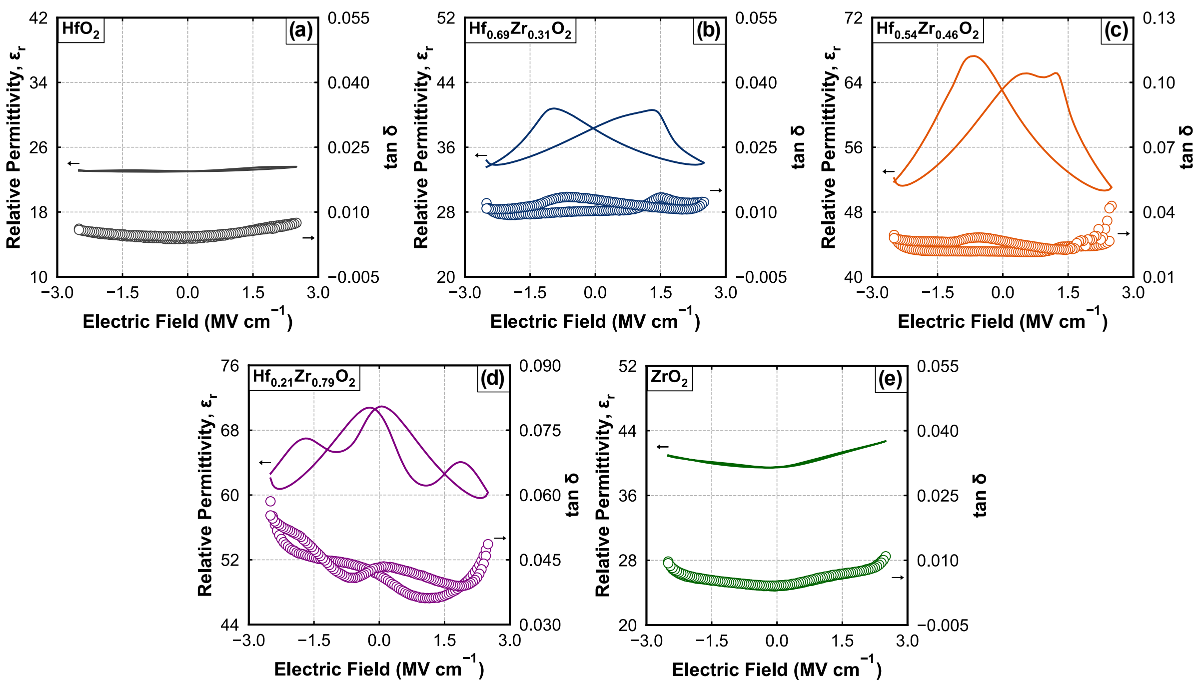

Figure 5.5. Relative permittivity (lines, left axis) and loss tangent (open points, right axis) measured on (a) HfO_2, (b) $Hf_{0.69}Zr_{0.31}O_2$, (c) $Hf_{0.54}Zr_{0.46}O_2$, (d) $Hf_{0.21}Zr_{0.79}O_2$, and (e) ZrO_2 films.

XRR measurements of each sample were used to quantify film densities and obtain thickness values. The measurements and associated fits can be found in Figure 5.6 and Figure 5.7 for the crystallized and amorphous sample series, respectively. The densities of the crystallized and amorphous films were observed to decrease approximately linearly as the composition changed from pure HfO_2 to pure ZrO_2, as provided in Table 5.1 and shown in Figure 5.8 along with the film thicknesses.

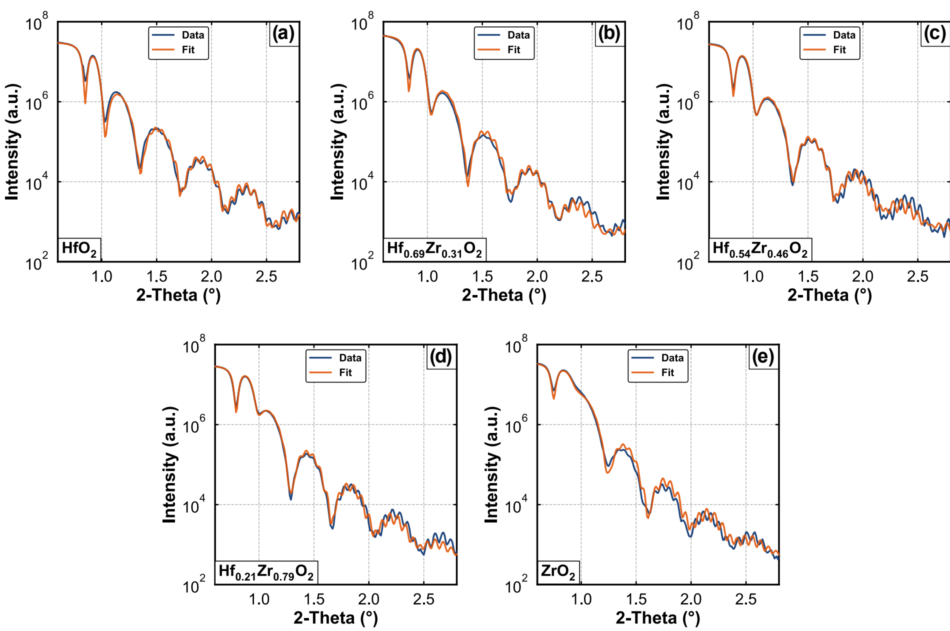

Figure 5.6. XRR patterns (blue line) and associated fits (orange line) corresponding to crystalline (a) HfO_2, (b) $Hf_{0.69}Zr_{0.31}O_2$, (c) $Hf_{0.54}Zr_{0.46}O_2$, (d) $Hf_{0.21}Zr_{0.79}O_2$, and (e) ZrO_2 samples.

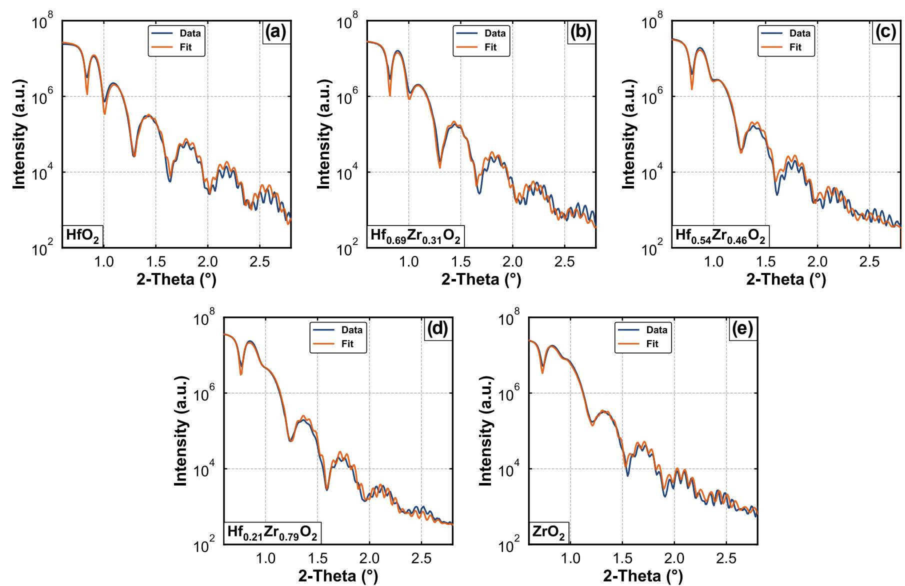

Figure 5.7. XRR patterns (blue line) and associated fits (orange line) corresponding to amorphous (a) HfO_2, (b) $Hf_{0.69}Zr_{0.31}O_2$, (c) $Hf_{0.54}Zr_{0.46}O_2$, (d) $Hf_{0.21}Zr_{0.79}O_2$, and (e) ZrO_2 samples.

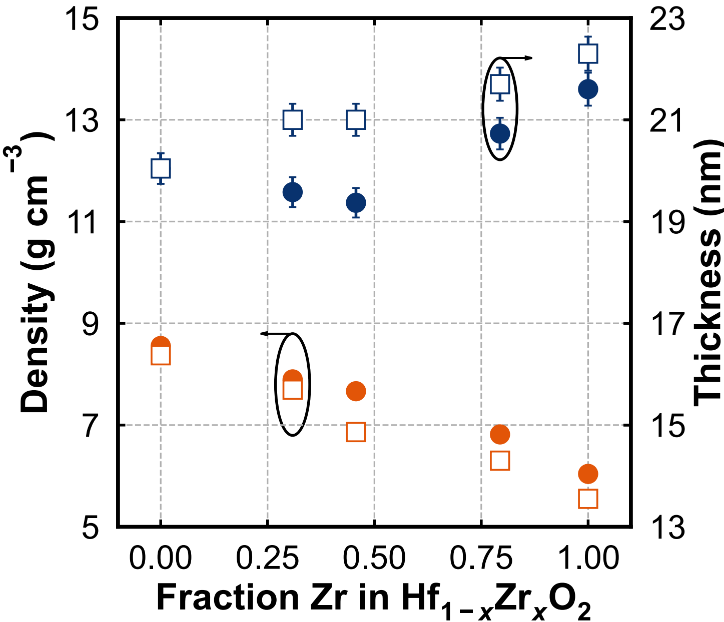

Figure 5.8. Film density (orange, left axis) and thickness (blue, right axis) extracted from XRR patterns for crystallized (filled in circles) and amorphous (open squares) films with each composition.

The longitudinal speed of sound was extracted from optical pump-probe picosecond acoustic measurements[253–255] using a two-tint time-domain thermoreflectance system, which is described elsewhere.[256,257] Briefly, the output of a Ti:Sapphire oscillator (100 fs pulses, 80 MHz) is energetically separated into high-energy pump and low-energy probe paths. The pump is electro-optically modulated at 8.4 MHz, and creates a periodic heating event at the surface of the samples coated with aluminum. This heating event also generates a strain pulse that propagates through the film stack, partially transmitting/reflecting at the interfaces between the layers. The reflectivity of the aluminum transducer is interrogated using the probe, which is mechanically delayed ~100 ps following the incident pump pulse. Because the reflectivity of the aluminum is proportional to both temperature and strain, signatures at short pump/probe delay times are indicative of the acoustic propagation times within each layer. Acoustic responses for the 20 nm-thick crystallized HZO films are shown in Figure 5.9(a), where signatures from the Al/HZO and HZO/TaN interfaces are identified, with equivalent data for the amorphous films provided in Figure 5.10. The delay time between these two signatures, τ, represents the round-trip propagation time of the strain wave within the film, as diagrammed in Figure 5.11. Gaussian peaks were fit to both acoustic signatures to determine this delay, as shown for the $Hf_{0.54}Zr_{0.46}O_2$ film in Figure 5.12.

Utilizing the measured film thicknesses, d, and the round-trip propagation times, the longitudinal speed of sound in each film was calculated via $v_L = 2d/\tau$. Elastic moduli were then calculated from the longitudinal wave velocities and the density measurements using Equations 5.1 and 5.2 with the assumptions of a linear elastic isotropic randomly oriented, polycrystalline solid or isotropic amorphous layer:[258–260]

$$C_{11} = \rho v_L^2 \tag{5.1}$$

$$E = \frac{C_{11}\,(1+\nu)\,(1-2\nu)}{(1-\nu)} \tag{5.2}$$

Where C_{11} is an axial normal component of the strain tensor, ρ is the film density, v_L is the longitudinal speed of sound, E is the elastic modulus of the film, and ν is Poisson's ratio for HZO, assumed to be 0.29[261–263] for this analysis. A description of error propagation using these equations is available in the appendix. The elastic moduli, provided in Table 5.1 and shown in Figure 5.9(b), were observed to increase with increasing ZrO_2 composition, between 190 ± 5 GPa for the pure monoclinic HfO_2 film and 204 ± 7 GPa for the pure tetragonal ZrO_2 film, with positive deviations from this trend observed for the $Hf_{0.69}Zr_{0.31}O_2$ (202 ± 6 GPa) and $Hf_{0.54}Zr_{0.46}O_2$ (209 ± 6 GPa) compositions. The elastic moduli of the amorphous films were observed to increase with increasing ZrO_2 composition, from 161 ± 4 GPa to 231 ± 7 GPa between pure HfO_2 and pure ZrO_2. Additional thickness, density, and sound velocity data for the amorphous films are provided in Table 5.2.

Table 5.1. Calculated elastic moduli and biaxial stress magnitudes along with parameters used for calculations, remanent polarizations, and relative permittivities for each HZO composition. *HfO_2 area detector data indicated preferred orientation. †Value represents the average of calculations from both ($\bar{1}11$) and (111) monoclinic peaks.

	HfO_2	$Hf_{0.69}Zr_{0.31}O_2$	$Hf_{0.54}Zr_{0.46}O_2$	$Hf_{0.21}Zr_{0.79}O_2$	ZrO_2
Thickness (nm)	20.04 ± 0.30	19.58 ± 0.29	19.37 ± 0.29	20.73 ± 0.31	21.60 ± 0.32
v_L (m s^{-1})	5392 ± 96	5788 ± 115	5984 ± 114	6164 ± 110	6656 ± 151
τ (ps)	7.43 ± 0.07	6.76 ± 0.09	6.47 ± 0.08	6.72 ± 0.07	6.37 ± 0.11
ρ (g cm^{-3})	8.55 ± 0.03	7.90 ± 0.04	7.67 ± 0.04	6.82 ± 0.06	6.04 ± 0.05
P_r (µC cm^{-2}, at 2.5 MV cm^{-1})	0.54	8.38	14.01	2.82	0.03
ε_r (at 2.5 MV cm^{-1}, 10 kHz)	23.6	34.1	51.1	60.3	42.7
C_{11} (GPa, crystallized)	*248 ± 6	264 ± 8	274 ± 8	259 ± 7	267 ± 9
E (GPa, Amorphous)	161 ± 4	173 ± 5	201 ± 8	202 ± 6	231 ± 7
E (GPa, Crystallized)	*190 ± 5	202 ± 6	209 ± 6	198 ± 5	204 ± 7
σ (GPa)	*,†1.94 ± 0.5	2.86 ± 0.2	3.60 ± 0.3	3.81 ± 0.2	3.98 ± 0.4

Given that the $Hf_{0.69}Zr_{0.31}O_2$ and $Hf_{0.54}Zr_{0.46}O_2$ films contained the second largest and largest contents of the orthorhombic phase, respectively, according to diffraction and electrical characterization, these positive deviations from the apparent increase indicate that the orthorhombic phase has an elastic modulus larger than the monoclinic and tetragonal phases. These values are in agreement with DFT predictions,[96,97] and experimental trends between the bulk modulus of the monoclinic and non-ferroelectric orthorhombic phases of HfO_2.[264] The elastic moduli measured for the $Hf_{0.54}Zr_{0.46}O_2$ film (209 ± 6 GPa), which possessed the largest content of the orthorhombic phase, is lower than the reported 340 GPa value extracted from fitting of acoustic vibrational responses of 10 nm-thick HZO nano-membrane resonators,[251] and is larger than the reported ~170 GPa value measured on 10-100 nm-thick $Hf_{0.55}Zr_{0.45}O_2$ films by atomic force microscopy.[265] These differences may be related to varying phase purities, mechanical boundary conditions, and/or the indirect nature of moduli calculation from these other techniques.

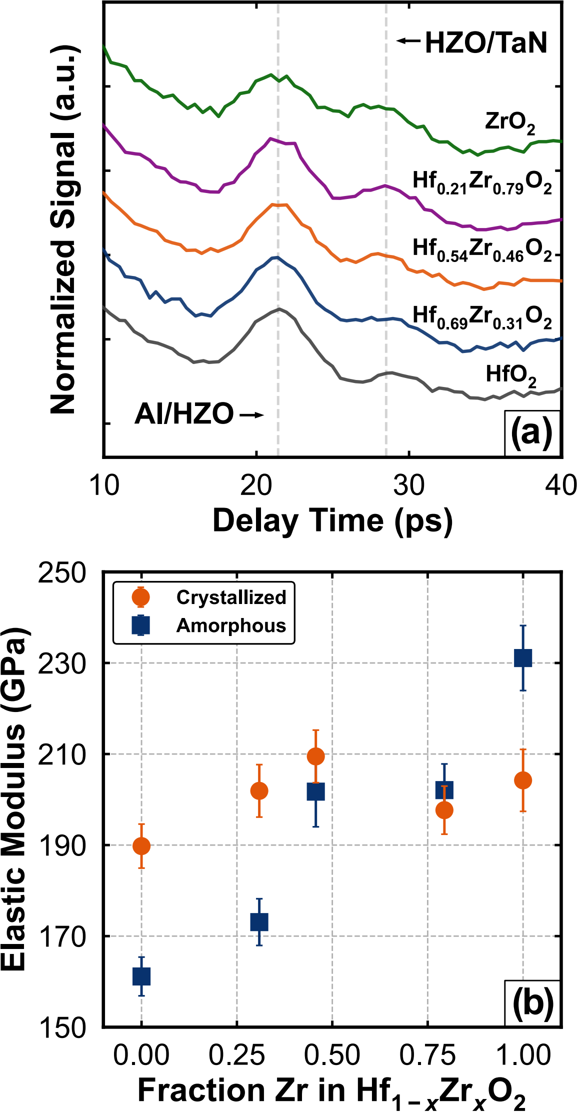

Figure 5.9. (a) Acoustic responses measured on crystallized HfO_2 (grey), $Hf_{0.69}Zr_{0.31}O_2$ (blue), $Hf_{0.54}Zr_{0.46}O_2$ (orange), $Hf_{0.21}Zr_{0.79}O_2$ (purple), and ZrO_2 (green) films, with signatures corresponding to the Al/HZO and HZO/TaN interfaces indicated. (b) Elastic moduli calculated for crystallized (orange circles) and amorphous (blue squares) HZO films.

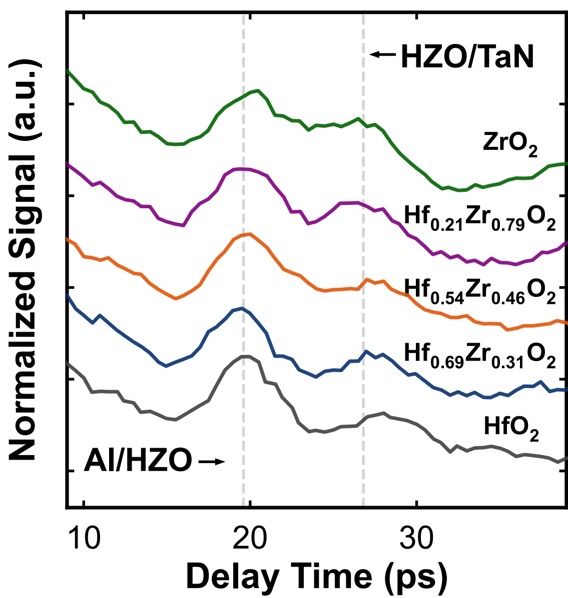

Figure 5.10. Acoustic responses measured on amorphous HfO_2 (grey), $Hf_{0.69}Zr_{0.31}O_2$ (blue), $Hf_{0.54}Zr_{0.46}O_2$ (orange), $Hf_{0.21}Zr_{0.79}O_2$ (purple), and ZrO_2 (green) films, with signatures corresponding to the Al/HZO and HZO/TaN interfaces indicated.

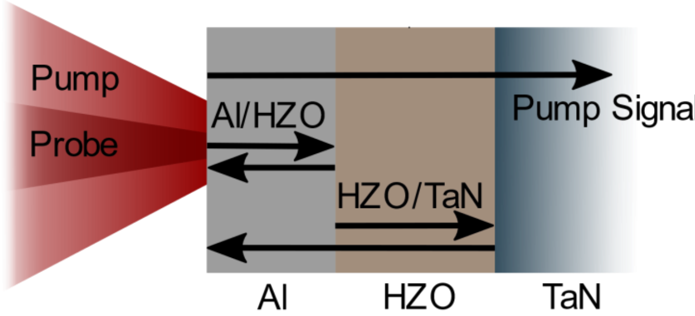

Figure 5.11. Schematic of picosecond acoustic wave propagation through sample.

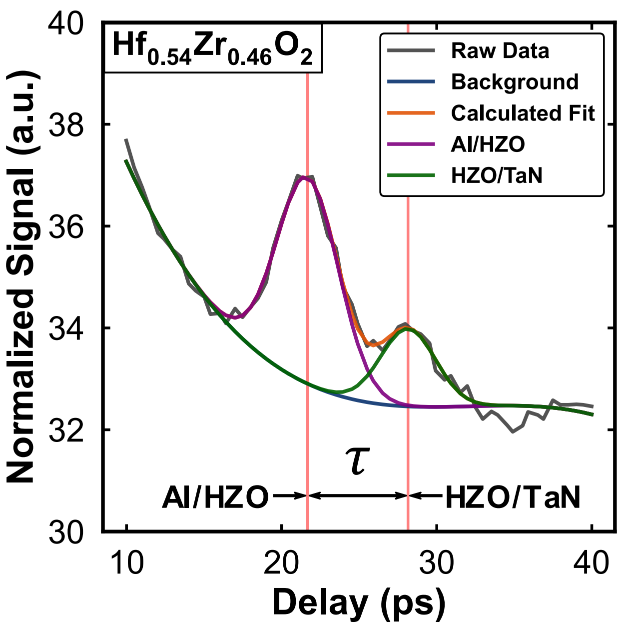

Figure 5.12. Picosecond acoustic data (grey) and associated fitted background (blue), summed calculated fit (orange), Al/HZO signature gaussian fit (purple), and HZO/TaN signature gaussian fit (green) for the crystallized $Hf_{0.54}Zr_{0.46}O_2$ film. The positions of the acoustic signatures of the two interfaces (red lines) separated by a delay time, τ are indicated below. The composition of the film is indicated in the upper left of the panel.

Table 5.2. Thickness, acoustic delay (τ), sound velocity (v_L), density (ρ), and axial normal elastic stiffness tensor component (C_{11}) for each amorphous HZO film. †Value represents the average of calculations from both ($\bar{1}11$) and (111) monoclinic peaks.

	HfO_2	$Hf_{0.69}Zr_{0.31}O_2$	$Hf_{0.54}Zr_{0.46}O_2$	$Hf_{0.21}Zr_{0.79}O_2$	ZrO_2
Thickness (nm)	20.04 ± 0.30	19.58 ± 0.29	19.37 ± 0.29	20.73 ± 0.31	21.60 ± 0.32
τ (ps)	7.43 ± 0.07	6.76 ± 0.09	6.47 ± 0.08	6.72 ± 0.07	6.37 ± 0.11
v_L (m s^{-1})	5392 ± 96	5788 ± 115	5984 ± 114	6164 ± 110	6656 ± 151
ρ (g cm^{-3})	8.37 ± 0.01	7.70 ± 0.01	6.90 ± 0.01	6.30 ± 0.01	5.55 ± 0.01
C_{11} (GPa)	†211 ± 6	226 ± 7	267 ± 10	264 ± 8	302 ± 9

Utilizing measured elastic moduli, $\sin^2(\psi)$ analyses were performed to assess the biaxial stress present in each of the crystalline films following processing. 2D diffraction patterns were collected using an area detector, with an example shown in Figure 5.13(a) for the $Hf_{0.54}Zr_{0.46}O_2$ sample. Area detector data were unwarped using the MgO diffraction peaks, with an example shown in Figure 5.14. The $(\bar{1}11)$ and (111) m (in the case of the HfO_2 film) and (101)/(111) t + o reflections (in the case of the other films) were fit to quantify changes in *d*-spacing with ψ angle relative to film normal, as shown in Figure 5.13(b) for the $Hf_{0.54}Zr_{0.46}O_2$ sample. The normalized intensities of the superimposed t + o diffraction peaks, also shown in Figure 5.13(b) for the $Hf_{0.54}Zr_{0.46}O_2$ film, were observed to be effectively constant throughout the Debye ring, validating the assumption of a randomly oriented polycrystalline material. A similar lack of texture was observed in all other samples, except pure HfO_2, with the 2D patterns shown in Figure 5.15. These observed changes in *d*-spacing with ψ angle were fit using Equations 3.2 and 3.3, with the assumption of a randomly oriented, polycrystalline solid with isotropic elastic behavior.[209] Note that this calculation accounts for the biaxial modulus in an equi-biaxially stressed thin film.

$$\varepsilon_\psi = \frac{1+v}{E}\sigma_{||}\sin^2(\psi) - \frac{2v}{E}\sigma_{||} \quad 3.2$$

$$\varepsilon_\psi = \frac{d_\psi - d_0}{d_0} \quad 3.3$$

Where d_ψ is the *d*-spacing at each ψ angle, v is Poisson's ratio (assumed to be 0.29[261–263]), E is the measured elastic modulus for each composition, and $\sigma_{||}$ is the biaxial stress state. The strain-free *d*-spacings (d_0) of the HZO films were calculated to occur at ψ angles (ψ^*) at which Equation 3.4 was fulfilled:[209]

$$\sin(\psi^*) = \sqrt{\frac{2v}{1+v}} \quad (3.4)$$

The *d*-spacings of the MgO powder resting on the film surface, shown in Figure 5.14 and Figure 5.16, were not observed to vary with ψ angle, indicating that the observed m/t/o *d*-spacing slopes are not measurement artifacts.

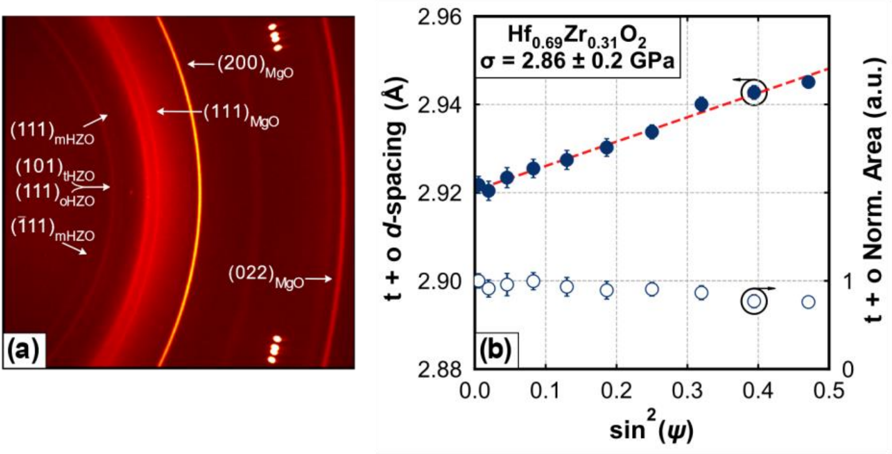

Figure 5.13. (a) 2D XRD pattern measured on the $Hf_{0.69}Zr_{0.31}O_2$ sample with indexed m, t + o and MgO Debye rings indicated. (b) Change in t + o *d*-spacing with ψ angle relative to film normal (filled blue circles, left axis) with associated linear fit (red dotted line) used to calculate biaxial stress magnitude and normalized peak intensities (open blue circles, right axis) for the $Hf_{0.69}Zr_{0.31}O_2$ film.

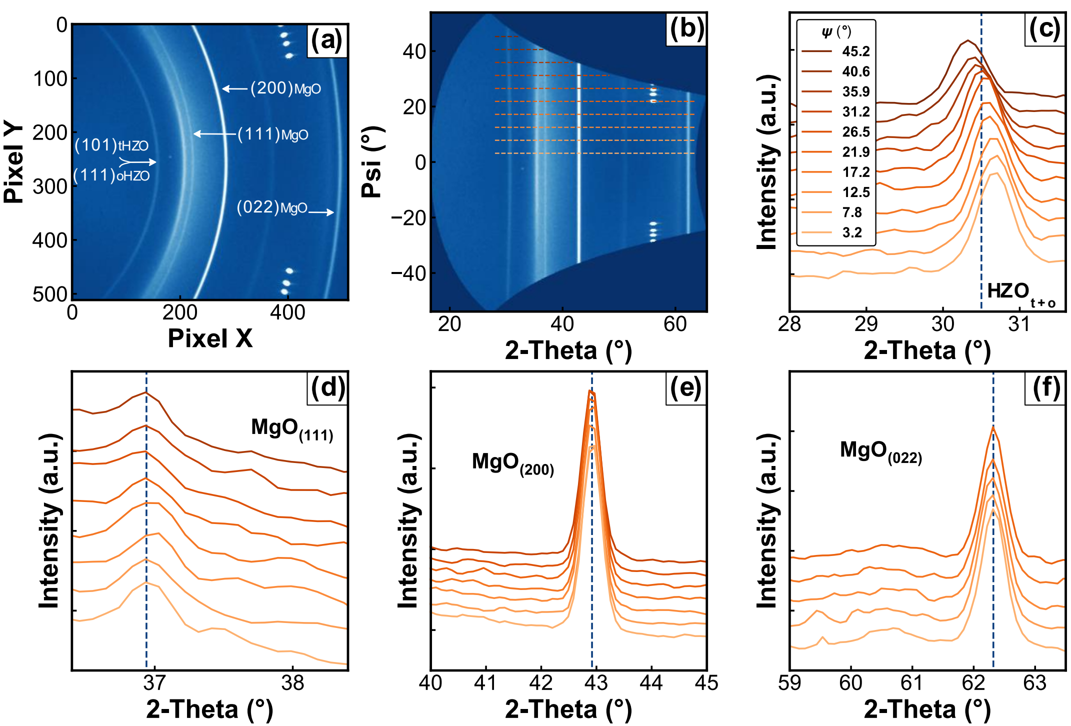

Figure 5.14. (a) 2D XRD pattern measured on the $Hf_{0.21}Zr_{0.79}O_2$ sample with indexed HZO and MgO Debye rings indicated along (b) the associated unwarped pattern with intensity line scan profiles indicated as dotted lines. Intensity line scans are shown for the (c) HZO t/o diffraction peak used for $\sin^2(\psi)$ analysis and (d) (111), (e) (200), and (f) (022) MgO diffraction peaks used for pattern unwarping, with the associated ψ angle colorations identified in the legend in panel (c). Dashed lines represent the indexing for each diffraction peak.

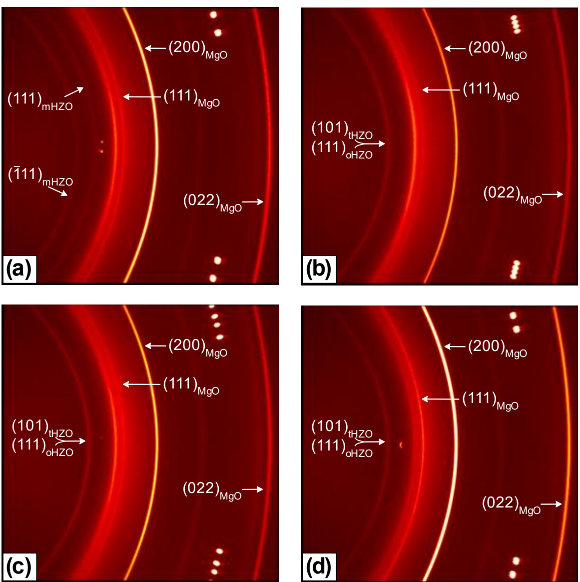

Figure 5.15. 2D XRD patterns measured on (a) HfO_2, (b) $Hf_{0.54}Zr_{0.46}O_2$, (c) $Hf_{0.21}Zr_{0.79}O_2$, and (d) ZrO_2 samples with indexed monoclinic, tetragonal, and orthorhombic Debye rings indicated. The Debye rings from the stress-free MgO powder standard are also indicated.

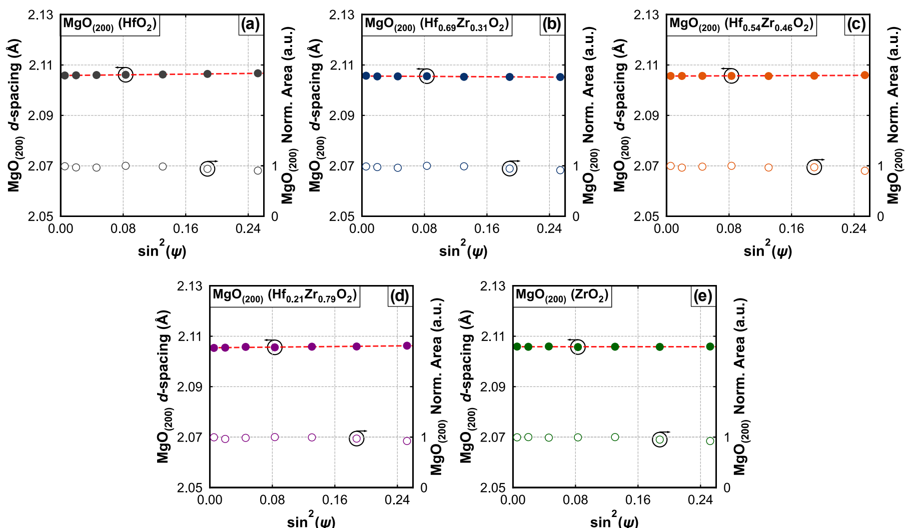

Figure 5.16. Change in d-spacing with ψ angle relative to film normal (filled circles, left axis) with associated linear fit (red dotted line) and normalized peak intensities (open circles, right axis) for the (200) diffraction peak of the MgO stress-free standard adhered to the (a) HfO_2, (b) $Hf_{0.69}Zr_{0.31}O_2$, (c) $Hf_{0.54}Zr_{0.46}O_2$, (d) $Hf_{0.21}Zr_{0.79}O_2$, and (e) ZrO_2 samples.

The biaxial stress states of the crystalline films were found to be 1.94 ± 0.5 GPa for the pure HfO_2 film (averaged between the $(\bar{1}11)$ and (111) monoclinic peaks), 2.86 ± 0.2 GPa, 3.60 ± 0.3 GPa, and 3.81 ± 0.2 GPa, for the $Hf_{0.69}Zr_{0.31}O_2$, $Hf_{0.54}Zr_{0.46}O_2$, and $Hf_{0.21}Zr_{0.79}O_2$ compositions, respectively, and 3.98 ± 0.4 GPa for the ZrO_2 film, as shown in Figure 5.13 and Figure 5.17. Values utilized for stress quantification can be found in Table 5.1. The large tensile biaxial stresses present following processing are consistent with other studies examining stress states of HfO_2-based ferroelectrics grown on binary nitride electrodes and suggest significant stress resulting from thermal expansion mismatch with the silicon substrates.[125] Given that monoclinic HfO_2 possesses a smaller coefficient of thermal expansion than tetragonal ZrO_2,[266] and that clear evidence of monoclinic ferroelastic twin texturing was observed in the 2D diffraction patterns,[267] it is anticipated that the monoclinic HfO_2 and mixed phase $Hf_{0.69}Zr_{0.31}O_2$ films could better accommodate thermal strains compared to the other compositions, and thus maintain lower biaxial stress following processing. The texture of the $(\bar{1}11)$ and (111) reflections in the pure HfO_2 film does mean that the assumption of a randomly oriented, isotropic crystalline solid used throughout the stress calculations is less valid for this film than for the other compositions. Furthermore, it should be emphasized that all of the crystal structures present in this study are elastically anisotropic. An implicit assumption of the $\sin^2(\psi)$ technique used is that the elastic properties of the planes considered do not significantly differ. The complete elastic compliance tensor for each phase and composition would be necessary to account for any differences and, to date, this information is not available. Regardless, the random orientation of most compositions, linearity of d-spacing versus $\sin^2(\psi)$, and use of the same atomic plane in each phase suggests that these results are reliable.

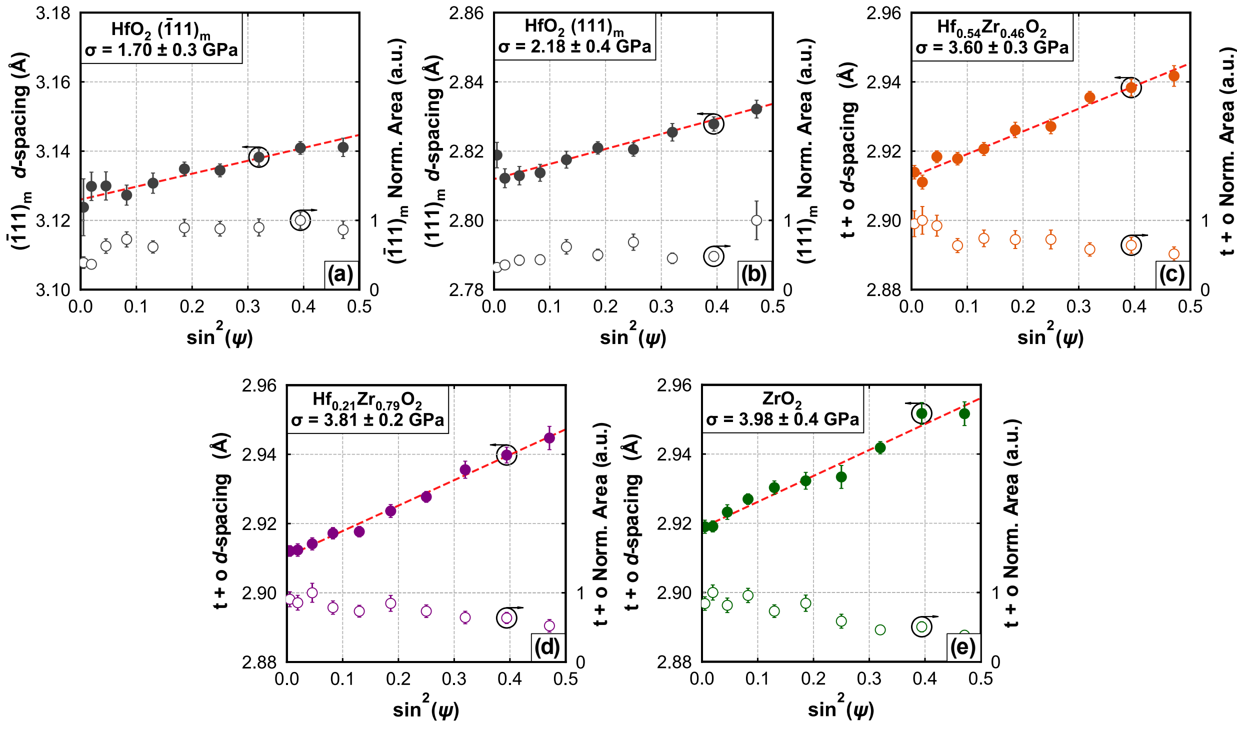

Figure 5.17. Change in t + o *d*-spacings with ψ angle relative to film surface normal (filled circles, left axis) with associated linear fits (red dotted line) used to calculate biaxial stress magnitudes and normalized peak intensities (open circles, right axis) for the (a-b) HfO_2 (($\bar{1}11$) and (111) reflections, respectively), (c) $Hf_{0.54}Zr_{0.46}O_2$, (d) $Hf_{0.21}Zr_{0.79}O_2$, and (e) ZrO_2 films. The calculated biaxial stress magnitudes are tabulated in the upper left of each panel along with the HZO composition.

5.6 Conclusions

In summary, the elastic moduli of amorphous and crystalline 20 nm-thick $Hf_{1-x}Zr_xO_2$ films have been directly quantified using picosecond acoustic measurements. For the crystallized films, the elastic moduli were found to increase from 248 ± 6 GPa to 267 ± 9 GPa between the monoclinic HfO_2 and tetragonal ZrO_2 films, respectively. The $Hf_{0.69}Zr_{0.31}O_2$ and $Hf_{0.54}Zr_{0.46}O_2$ films, which were determined to have the largest content of orthorhombic phase, exhibited larger elastic moduli of 202 ± 6 GPa and 209 ± 6 GPa, respectively. The larger elastic moduli of films containing the

orthorhombic phase is consistent with computational predictions. The moduli of the amorphous films were observed to linearly increase between 161 ± 4 GPa and 231 ± 7 GPa as the composition was varied from pure HfO_2 to pure ZrO_2. The biaxial stresses of the crystalline films, quantified using their measured elastic moduli values through $\sin^2(\psi)$ analysis, were found to increase from 1.94 ± 0.5 GPa, for pure HfO_2, to 3.98 ± 0.4 GPa, for pure ZrO_2. Direct investigation of these elastic properties, through utilization of picosecond acoustic measurements, allows for enhanced analysis of stress effects on phase stability, domain structure, and polarization properties in HfO_2-based ferroelectric thin films.

5.7 Acknowledgement

This work was supported, in part, by the Laboratory Directed Research and Development program at Sandia National Laboratories. Sandia National Laboratories is a multimission laboratory managed and operated by National Technology and Engineering Solutions of Sandia, LLC, a wholly owned subsidiary of Honeywell International, Inc., for the U.S. Department of Energy's National Nuclear Security Administration under contract DE-NA0003525. This paper describes objective technical results and analysis. Any subjective views or opinions that might be expressed in the paper do not necessarily represent the views of the U.S. Department of Energy or the United States Government. This work is also supported, in part, by the Semiconductor Research Corporation's (SRC) Global Research Collaboration Program. This research utilized a PHI VersaProbe III XPS system, which was supported by National Science Foundation Award # 162601. STJ acknowledges support from the National Science Foundation Graduate Research Fellowship Program under award DGE-1842490. DHO is grateful for funding from the National Defense Science and Engineering Graduate (NDSEG) Fellowship. DHO and PEH appreciate funding from the National Science Foundation, Grant Number DMR EPM 2006231. This manuscript has been coauthored by UT-Battelle, LLC, under Contract No. DE-AC05-00OR22725 with the U.S. Department of Energy. The United States Government retains and the publisher, by accepting the article for publication, acknowledges that the United States Government retains a non-exclusive, paid-up, irrevocable, world-wide license to publish or reproduce the published form of this manuscript, or allow others to do so, for United States Government purposes.

Chapter 6: Metal Nitride Electrode Stress and Chemistry Effects on Phase and Polarization Response in Ferroelectric $Hf_{0.5}Zr_{0.5}O_2$ Thin Films

The contents of this chapter are published in *Advanced Materials Interfaces* (**8**, 2100018, 2021, DOI: https://doi.org/10.1002/admi.202100018) with the following as authors:

Shelby S. Fields,[1] Sean W. Smith,[2] Chris M. Fancher,[3] Michael D. Henry,[2] Steve L. Wolfley,[2] Maria G. Sales,[1] Samantha T. Jaszewski,[1] Mark A. Rodriguez,[2] Giovanni Esteves,[2] Paul S. Davids,[2] Stephen J. McDonnell,[1] and Jon F. Ihlefeld.[1,4]

[1]Department of Materials Science and Engineering, University of Virginia, Charlottesville VA, 22904, USA

[2]Sandia National Laboratories, Albuquerque NM, 87123, USA

[3]Materials Science and Technology Division, Oak Ridge National Laboratory, Oak Ridge TN, 37831, USA

[4]Charles L. Brown Department of Electrical and Computer Engineering, University of Virginia, Charlottesville VA, 22904, USA

The body of text of this chapter has been adapted to include the supplemental information and figures, where appropriate.

6.1 Motivation

With differences in field cycling properties showing an electrode dependence in Chapter 4, and the elastic moduli of the system experimentally measured in Chapter 5, this investigation focused on effects of electrode stress and chemistry on the polarization properties of HZO. All of the devices measured in this work utilized ALD-grown HZO prepared with identical conditions. All of these devices also utilized sputtered TaN electrodes, although with different background pressure conditions to produce different as-deposited stress states. It is shown that the stress state of the HZO following processing is not strongly dependent on the as-deposited stress state of the TaN electrodes, and that electrode chemistry, instead, more strongly governs the polarization properties of the yielded devices. Within this work, the development of a process to determine the stoichiometry of binary nitride electrodes using Angle-Resolved XPS (ARXPS) is described.

6.2 Abstract

Ferroelectric phase stability in hafnium oxide has been reported to be influenced by factors that include composition, biaxial stress, crystallite size, and oxygen vacancies. In the present work, the ferroelectric performance of atomic layer deposited $Hf_{0.5}Zr_{0.5}O_2$ (HZO) prepared between TaN electrodes that were processed under conditions to induce variable biaxial stresses is evaluated. The post-processing stress states of the HZO films reveal no dependence on the as-deposited stress of the adjacent TaN electrodes. All HZO films maintain tensile biaxial stress following processing, the magnitude of which is not observed to strongly influence the polarization response. Subsequent composition measurements of stress-varied TaN electrodes reveal changes in stoichiometry related to the different preparation conditions. HZO films in contact with Ta-rich TaN electrodes exhibit higher remanent polarizations and increased ferroelectric phase fractions compared to those in contact with N-rich TaN electrodes. HZO films in contact with Ta-rich TaN electrodes also have higher oxygen vacancy concentrations, indicating that a chemical interaction between the TaN and HZO layers ultimately impacts the ferroelectric orthorhombic phase stability and polarization performance. The results of this work demonstrate a necessity to carefully consider the role of electrode processing and chemistry on performance of ferroelectric hafnia films.

6.3 Introduction

HfO_2-based thin films have experienced significant research and development following observation of their ferroelectric properties in 2011,[1] which have been attributed to a metastable, non-centrosymmetric $Pca2_1$ orthorhombic phase. HfO_2 exists at equilibrium in a monoclinic $P2_1/c$ phase at standard temperature and pressure. However, owing to a surface energy effect, a metastable tetragonal $P4_2/nmc$ phase, that is normally stable only at high temperatures, persists in small crystallite sizes.[87] The ferroelectric orthorhombic phase, which exhibits a theoretical spontaneous polarization (P_s) of 50 μC cm^{-2} along its short *c*-axis, has been shown to be stabilized with respect to the tetragonal phase through the application of biaxial mechanical stress,[115,116,151] inclusion of dopants[1,3,123,126,128,132] or alloying with other fluorite-structured oxides,[268] or incorporation of point defects.[103,110] These ferroelectric properties and their development have opened up a wide array of applications in non-volatile memory,[2,232,245] energy harvesting,[221,246]

negative differential capacitance field-effect transistors,[230,247] infrared sensing,[149] and nonlinear optics.[82,269] Incorporation of this material into next-generation device structures is attractive because it demonstrates inherent silicon/CMOS process compatibility,[77] is manufacturable using mature atomic layer deposition (ALD) processes, and maintains stable ferroelectricity at thickness scales (1 – 30 nm)[102,233,234] at which conventional ferroelectrics typically exhibit diminished polarization response.[58] Hafnium zirconium oxide ($Hf_{1-x}Zr_xO_2$, HZO) alloys, in particular, have generated wide interest due to the observation of robust hysteresis behavior with a lower thermal budget compared to most other HfO_2-based ferroelectrics.[142,249] Zirconium oxide also demonstrates the largest dopant concentration window in which ferroelectric polarization response is observed (c.a. 10 – 80 at. %).[3] For other dopants, a ferroelectric response is generally observed for concentrations between 1 – 10 at. %, excluding lanthanum,[124] which has been shown to stabilize orthorhombic HfO_2 with doping concentrations up to 20 at. %.

Irrespective of the presence of dopants, oxygen vacancy concentration and distribution have been determined to play a key role in ferroelectric phase stabilization. First principles calculations have shown enhanced stabilization of the low surface energy tetragonal and orthorhombic phases over the monoclinic phase by ~5 - 10 meV $f.u.^{-1}$ and ~4 meV $f.u.^{-1}$, respectively, at an oxygen vacancy concentration of 2 at. % in HfO_2.[117,270] Similar observations of larger remanent polarizations in films containing greater quantities of oxygen vacancies have been made experimentally,[103,110,111] leading to further development of HfO_2 deposition processes designed to enhance the concentrations of these defects. Such process modifications have included alteration of the oxygen content in the process gas during sputtering[103,110] or duration of the ozone dose during ALD.[111] Aside from HfO_2 processing conditions, studies have observed varied ferroelectric performance dependent upon the selected electrode material. Comparisons between common binary nitride electrode materials have noted enhanced polarization in HfO_2 films when utilizing TaN electrodes compared to TiN, which has been attributed to increased reactivity between the ferroelectric and neighboring TaN electrode.[117]

Using angle-resolved X-ray photoelectron spectroscopy (XPS), experimental works have directly observed large oxygen vacancy concentrations at HZO/TiN interfaces related to an oxygen scavenging phenomenon, driven by the formation of a TiO_xN_y reaction layer.[155] Reaction layers have also been observed at HfO_2/TaN interfaces,[158] affecting the symmetry of ferroelectric

switching of the capacitors in the as-prepared state. The oxidation behavior of binary nitride electrodes depends on their stoichiometry,[271,272] which is a function of their deposition conditions.[273,274] As oxygen transport in binary nitride electrodes is facilitated by nitrogen vacancies,[184] differences in oxygen vacancy contents in hafnia films prepared on nitrogen-deficient electrodes may be expected. Typical anneals for HZO and other HfO_2-based ferroelectrics have been carried out between 500 – 900 °C for 20 – 60 seconds, with films typically grown between 5 – 20 nm. Owing to large oxygen diffusivities, the diffusion length for an oxygen vacancy in both HfO_2[275] and ZrO_2[276] under these conditions is greater than the thickness of typically grown ferroelectric HZO films (including those grown for this study). Diffusion of oxygen vacancies related to a reaction with binary nitride electrodes could, therefore, affect the entire volume of the HZO film. Recent experimental work has subsequently explored the impact of the binary nitride electrode/ferroelectric interface[277] and nitrogen content in the nitride electrode[159] on HfO_2-based ferroelectric polarization performance. In the former, it was shown that oxygen content prior to deposition of the ferroelectric layer played a role in the interface chemistry and performance. In the latter, more stable field cycling performance was observed for devices with TiN electrodes prepared with nitrogen enriched conditions, which presumably resulted in fewer oxygen vacancies in the HZO films. Mass transport between the ferroelectric and neighboring electrode layers, affected by electrode deposition conditions, can, therefore, impact the oxygen vacancy concentration within the ferroelectric film, and thus affect polarization performance.

Deposition conditions are well known to affect the mechanical stress of physical vapor deposited films.[278,279] It is therefore important to understand how the deposition-related stress of neighboring layers affects the stabilization of the orthorhombic phase in HZO thin films. Stress-induced orthorhombic phase stabilization has been attributed to constraint of a volume expansion during the phase transformation from tetragonal (high temperature, small crystallite size) to monoclinic (room temperature, bulk) of +7.3 $Å^3$.[96] When constrained, the orthorhombic phase, which falls energetically between the tetragonal and monoclinic phases, forms as a metastable intermediate. Owing partly to this volume constriction, computational studies have predicted an increase in orthorhombic phase stabilization with hydrostatic and epitaxial compressive stresses,[96,104,280] although such behaviors have not been experimentally observed. Volume constriction-related phase stabilization aside, stress can also affect ferroelectric domain structure and polarization magnitude. Previous experiments[115,116,151] have revealed increases in remanent

polarization with increasing tensile biaxial stress and decreases with compressive biaxial stress, contrary to what is observed for conventional perovskite ferroelectrics, such as $Pb(Zr,Ti)O_3$[204] and $BaTiO_3$.[206] These ferroelectrics display larger polarization magnitudes under biaxial compressive stress due to their polarization axis orienting perpendicular to the biaxial stress plane. Under biaxial tensile stress the effect is opposite and domain orientation with the long, polar axis parallel to the biaxial stress plane is facilitated. Conversely, owing to the short *b*-axis[87] polarization vector, orthorhombic HfO_2 polarization responses are observed to increase with biaxial tensile stress and decrease with biaxial compressive stress.[115,151] As both orthorhombic phase stabilization and ferroelectric domain structure have demonstrated stress state dependencies, the development of processes that optimize ferroelectric performance of HfO_2-based thin films will necessarily involve an understanding of deposition-related stress effects.

Repeatable and reliable polarization response must be demonstrated for ferroelectric HfO_2-based thin films to witness full adoption into the next generations of microelectronics. Repeatability presents a challenge for these ferroelectric films because the orthorhombic phase is sensitive to stress and point defect concentration, both of which may be affected by interactions with adjacent layers and can cause additional challenges if implemented in CMOS fabrication. Understanding the interplay of deposition conditions on orthorhombic phase stabilization is, therefore, a critical step toward the implementation of this material into future computing technologies.

6.4 Experimental Procedures

To examine electrode chemistry and stress effects on the stabilization of the orthorhombic phase in HZO thin films, devices were prepared between TaN electrodes deposited under conditions that resulted in varying as-deposited biaxial stress states. The samples in this study were prepared at Sandia National Laboratories. 20 nm-thick films of nominal composition $Hf_{0.5}Zr_{0.5}O_2$ were deposited between 100 nm-thick (111)-oriented TaN top and bottom electrodes on (001)-oriented *n*-type silicon substrates using thermal ALD with a flow-through style reactor (Ultratech Savannah) with a substrate temperature of 150 °C. Tetrakis(dimethylamino)hafnium (TDMA Hf, at 75 °C) and tetrakis(dimethylamino)zirconium (TDMA Zr, at 75 °C) precursors were utilized in a 5:5 super cycle ratio to control film composition, both utilizing nitrogen as a carrier gas and

water as an oxidant. Due to a difference in the growth per cycle between the two precursors, the films were hafnium-rich with a composition of $Hf_{0.58}Zr_{0.42}O_2$.[149] The TaN top and bottom electrodes were deposited from a sintered TaN target using pulsed DC (30 kHz, 4 μs reverse time) magnetron sputtering in a Denton Discovery 550 system under variable argon background pressure to control the as-deposited biaxial stress states of the films. Background pressure was varied by controlling argon gas flow rates under a constant dynamic pumping condition. The as-deposited biaxial stress states of the TaN electrodes were quantified via witness wafer curvature measurements using a Toho FLX-2320-S Thin Film Stress Measurement System and the Stoney equation. A schematic of the final device structure is shown in Figure 6.1(a).

Two series of samples were prepared. One series had the bottom electrode deposited in a near-neutral stress state (-43 MPa) and the top electrode stress varied; this series is denoted as the *Top Varied* series throughout this chapter. The second series had the bottom electrode stress varied while the top electrode was deposited in a near-neutral stress state; this series is denoted as the *Bottom Varied* series. The completed TaN/HZO/TaN stacks were annealed at 600 °C for 30 seconds in a nitrogen atmosphere in a rapid thermal annealer (Surface Science Integration Solaris 150). Lithographically defined 50 nm-thick platinum contacts of various diameters (288 – 90 μm) were isolated by reactive ion etching through the top TaN electrode layer to form discrete Pt/TaN/HZO/TaN/Si capacitor structures. Following processing, 2D XRD patterns were collected on each HZO film with a Rigaku Oxford Diffraction system equipped with a Rigaku Dectris Eiger R 4M detector using Cu Kα radiation for $\sin^2(\psi)$ biaxial stress analyses. Area detector data unwarping was completed using the pyFAI python data analysis package.[212] GIXRD patterns were also collected between 26° and 33° in 2θ on each sample using a Rigaku SmartLab diffractometer in a parallel beam geometry utilizing Cu Kα radiation with ω fixed at 0.7° in 2θ.

All samples were characterized with polarization-electric field ($P(E)$) and Positive Up, Negative Down (PUND) measurements between 1 and 2.5 MV cm^{-1}, which were performed using a Radiant Technologies Precision LC II Ferroelectric Tester. $P(E)$ measurements had a period of 1 ms and PUND measurements had pulse widths of 10 ms with pulse delays of 100 ms. Remanent polarization values were extracted from the PUND measurement, which probes switchable polarization and is less influenced by leakage current contributions to polarization than conventional polarization-field measurements. On each sample, five devices were characterized to

establish confidence intervals. Leakage current was measured for each sample between -2.5 and 2.5 MV cm^{-1} using a Keysight B2901A Precision Source/Measure Unit.

N:Ta ratios for witness blanket TaN electrode layers were determined using a PHI Versaprobe X-Ray Photoelectron Spectroscopy III instrument utilizing monochromated Al Kα radiation with an incidence angle of 45°, a pass energy of 26 eV, an anode bias of 15 kV, and an anode power of 50 W. Angle-resolved XPS measurements were made using a Scientia Omicron system equipped with Al Kα radiation and a R3000 Analyzer described elsewhere.[281] XPS spectra were fit using KolXPD spectral fitting software. Shirley backgrounds were fit for each spectrum, and Voigt peaks were fit to each known feature to assess and compare amplitudes. GIXRD patterns were also collected on witness blanket TaN electrode layers, using a Rigaku SmartLab Diffractometer with conditions identical to those used for GIXRD measurements of the HZO film.

6.5 Results and Discussion

To evaluate the effects of different electrode stress conditions on the polarization properties of HZO, two series of samples, diagramed in Figure 6.1(a), were prepared in which either the top (referred to as the *Top Varied* series) or bottom (referred to as the *Bottom Varied* series) TaN electrodes were processed to impose different quantities of biaxial stress. During sputter deposition of the stress-varied TaN electrodes from a pure TaN target in the Bottom Varied sample series, variation in argon background pressure within the sputter chamber between 6.7 and 10.1 mTorr resulted in as-deposited biaxial stresses between -1455 and 234 MPa, respectively, as shown in Figure 6.1(b). As the background pressure was increased, the resultant biaxial stress was observed to become more tensile, consistent with previous observations of sputter deposition processing of metal nitride films.[282] Identical variable background pressure conditions were utilized during deposition of the top electrode in the Top Varied series to establish a stressed top electrode. In both series, the non-stress-varied electrode was deposited with the 8.3 mTorr background pressure condition which produced -43 MPa of biaxial stress in the Bottom Varied series. It should be noted that an unavoidable processing difference between the Top and Bottom Varied sample series exists where the bottom TaN layer was prepared on native SiO_2, heated to 150 °C in vacuum for HZO synthesis, and subject to ALD processes of the 20 nm HZO layer. The top TaN layer was grown

on the 20 nm thick HZO layer and was not exposed to the HZO deposition process. Both TaN layers, however, were subject to the 600 °C rapid thermal anneal to crystallize the HZO film.

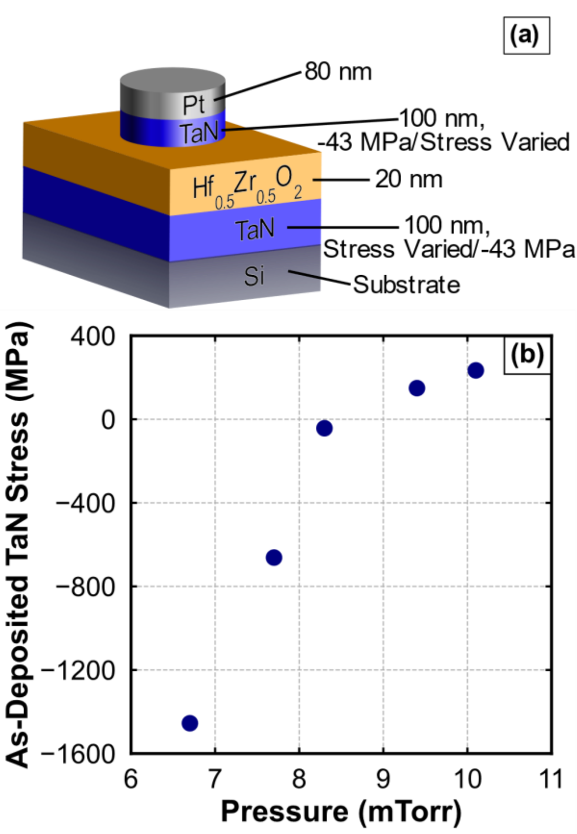

Figure 6.1. (a) Diagram of device structure with layer materials, thicknesses, and as-deposited biaxial stress states indicated (where applicable). (b) Variation in as-deposited biaxial stress of the TaN electrodes with argon background pressure utilized during sputter deposition.

Following processing, the biaxial stress state in the HZO layer in each sample was quantified through $\sin^2(\psi)$ analysis of area detector X-ray diffraction (XRD) data. An example of an unwarped 2D diffraction pattern is shown in Figure 6.2(a) for the Bottom Varied sample with the 6.7 mTorr background pressure TaN sputtering condition. Line segments at ψ angles between ± 65° were extracted from the intensity maps, with each segment comprising 2θ data with the diffraction vector oriented away from the film normal at an angle ψ. In all diffraction segments, peaks were observed at 28.4°, 30.4°, and 31.6° in 2θ, which were indexed as the $(\bar{1}11)$ monoclinic

(m), superimposed (101)/(111) tetragonal/orthorhombic (t + o), and (111) monoclinic reflections, respectively. Representative intensity versus scattering angle data, extracted from the area detector diffraction pattern from the Bottom Varied sample with the 6.7 mTorr background pressure TaN electrode sputtering condition, are shown in Figure 6.2(b). Additional indexed Grazing Incidence XRD (GIXRD) patterns measured on each sample are shown in Figure 6.3.

The changes in *d*-spacing of the t + o diffraction peak as a function of ψ angle were used to quantify the HZO stress states through fitting to Equations 3.2 and 3.3:[209]

$$\varepsilon_{\psi} = \frac{1+v}{E}\sigma_{||}\sin^2(\psi) - \frac{2v}{E}\sigma_{||} \quad 3.2$$

$$\varepsilon_{\psi} = \frac{d_{\psi} - d_0}{d_0} \quad 3.3$$

Where d_{ψ} is the *d*-spacing at each ψ angle, v is Poisson's ratio, E is the elastic modulus, and $\sigma_{||}$ is the biaxial stress. Through an assumption of a randomly oriented polycrystalline film, the strain-free *d*-spacing (d_0) was calculated at a ψ angle (ψ^*) at which Equation 3.4 was fulfilled:[209]

$$\sin(\psi^*) = \sqrt{\frac{2v}{1+v}} \quad 3.4$$

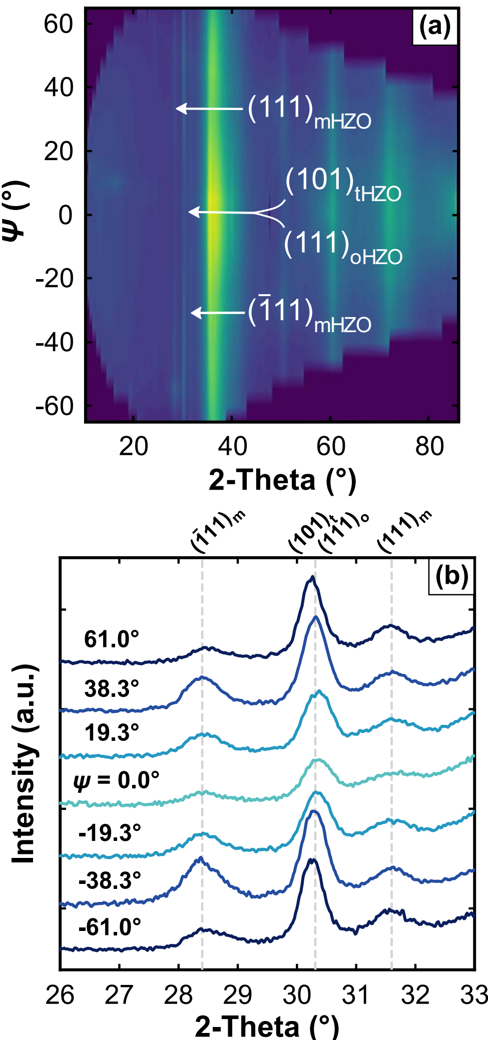

Figure 6.2. (a) Unwarped XRD area detector data from the Bottom Varied sample with the 6.7 mTorr background pressure TaN sputtering condition following processing with indexed Debye rings indicated. (b) Diffraction line scans extracted from the area detector data at specific ψ angles (indicated to the left of corresponding patterns) with indexing (grey dashed lines) indicated across the top of the panel.

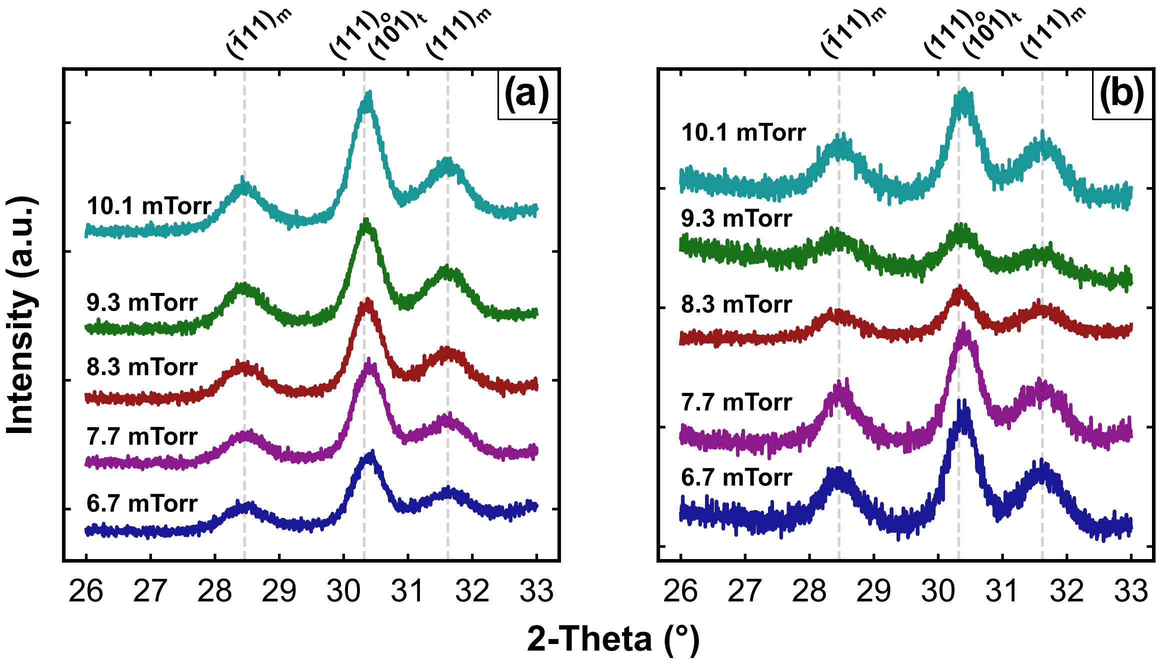

Figure 6.3. Grazing Incidence XRD patterns measured on (a) Top Varied and (b) Bottom Varied Sample series. Indexing for each of the observed peaks is indicated above the panels and the sputtering background pressure of the condition-varied TaN electrode is indicated to the left of each pattern.

A value of 0.29[261–263] was assumed for v and a modulus value of 265 ± 8 GPa[283] was used. Shown in Figure 6.4(a-e) are the changes in d-spacings and normalized integrated areas of the t + o diffraction peaks as a function of ψ angle for the Bottom Varied sample series. Equivalent data for the Top Varied sample series are shown in Figure 6.5. The positive linear slope present in data from each sample is an indication that the HZO films are all under tensile biaxial stress following processing, which is consistent with similar analyses of La-doped HfO_2 ferroelectric thin films prepared on silicon substrates with TiN electrodes,[125] as well as analyses discussed in Chapter 5 of samples prepared at the University of Virginia. In tandem, the lack of substantial change in normalized t + o integrated area with out-of-plane angle indicates that the HZO did not possess any strong crystallographic texture, validating the assumption of a randomly oriented polycrystalline film used for the biaxial stress calculations. Based upon the fit slopes and intercepts, HZO biaxial stress values were determined to fall between 1282 ± 85 MPa and 626 ±

59 MPa for the Bottom Varied series and 918 ± 45 MPa and 489 ± 40 MPa for the Top Varied series. The post-processing HZO stress state was not observed to correlate with the as-deposited stress state of the TaN electrode layers, as shown in Figure 6.4(f).

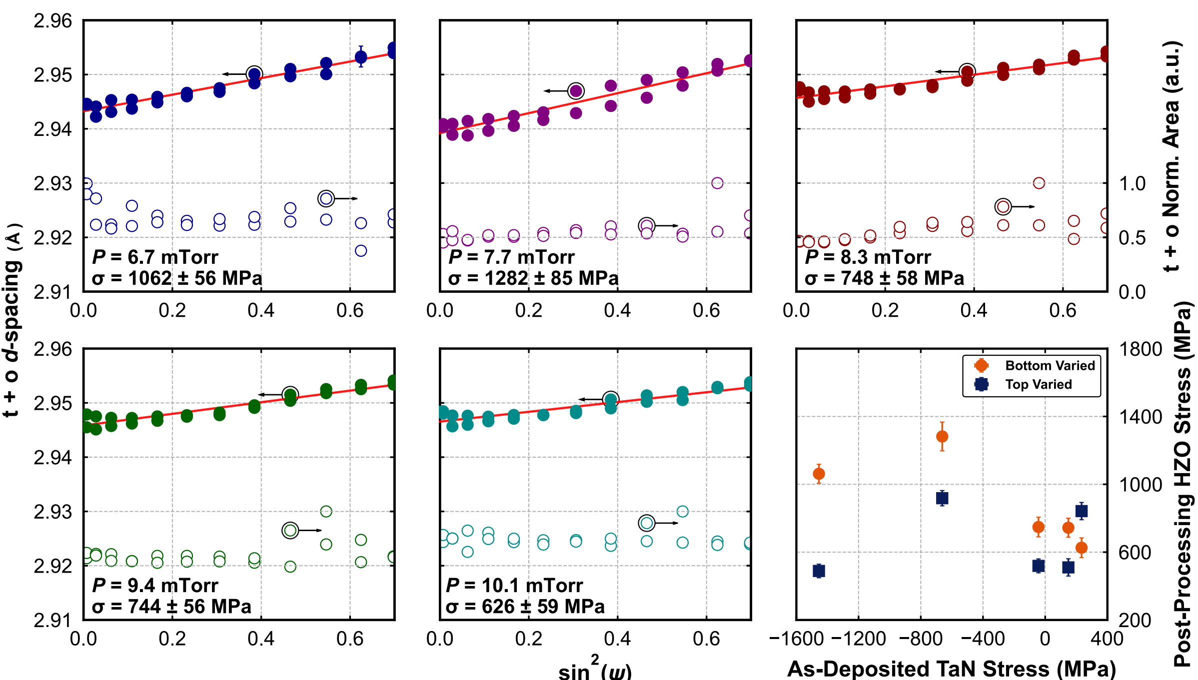

Figure 6.4. t + o *d*-spacing (filled in points, left axis) and normalized t/o intensity (open points, right axis) dependence on ψ angle and associated linear fit (red lines) used to calculate the post-processing biaxial stress states for the (a) 6.7, (b) 7.7, (c) 8.3, (d) 9.4, and (e) 10.1 mTorr background pressure TaN sputtering conditions in the Bottom Varied sample series. The utilized background pressures during stress-varied electrode sputtering and calculated post processing HZO biaxial stress states are indicated in the lower left of each panel. (f) Comparison between as-deposited TaN biaxial stress and post-processing HZO biaxial stress for both Bottom (orange) and Top (blue) Varied sample series.

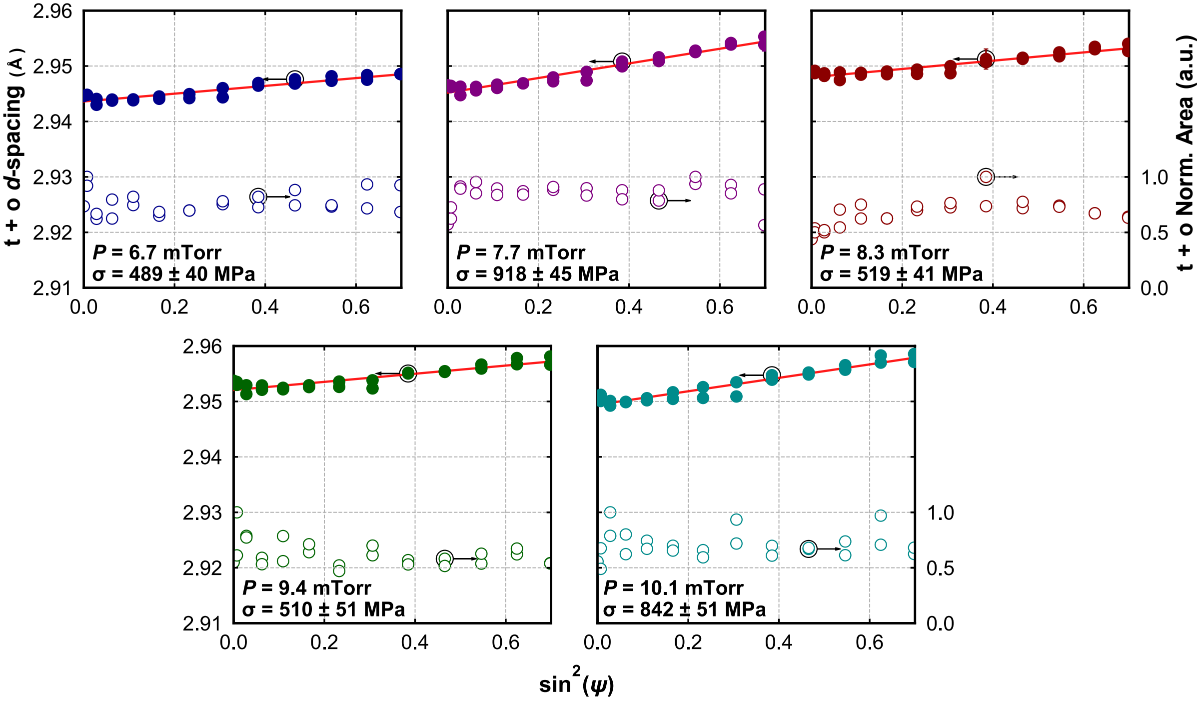

Figure 6.5. t + o *d*-spacing (filled in points, left axis) and normalized t/o intensity (open points, right axis) dependence on ψ angle and associated linear fit (red lines) used to calculate the post-processing HZO biaxial stress states for the (a) 6.7, (b) 7.7, (c) 8.3, (d) 9.4, and (e) 10.1 mTorr background pressure sputtering conditions in the Top Varied sample series. The utilized background pressures during TaN sputtering and calculated post-processing HZO biaxial stress states are indicated in the lower left of each panel.

Polarization versus electric field ($P(E)$) hysteresis responses, measured between 1.0 and 2.5 MV cm^{-1} with a frequency of 1 kHz on the Top Varied sample series, are shown in Figure 6.6(a-e) corresponding to each TaN sputter background pressure condition. The equivalent measurements for the Bottom Varied series are shown in Figure 6.7. Regardless of the background pressure utilized during electrode deposition, all samples maintained average coercive fields between 1.1 and 1.3 MV cm^{-1} and exhibited saturated hysteresis behavior consistent with low leakage current contributions to polarization responses. Additional data, including remanent polarization, saturation polarization, and coercive field from $P(E)$ measurements is provided in Table 6.1. Remanent polarization values, recorded from positive-up negative-down analysis after a pulse amplitude of 2.5 MV cm^{-1}, are shown in Figure 6.8(a) for both the Top and Bottom Varied

sample series. While the largest remanent polarization values were observed for the HZO films with the largest magnitudes of tensile stress, consistent with previous studies on stress effects in HfO_2-based ferroelectrics,[115,151] no clear P_r dependence on HZO stress state could be discerned, which suggests that additional factors impacted the polarization magnitude.

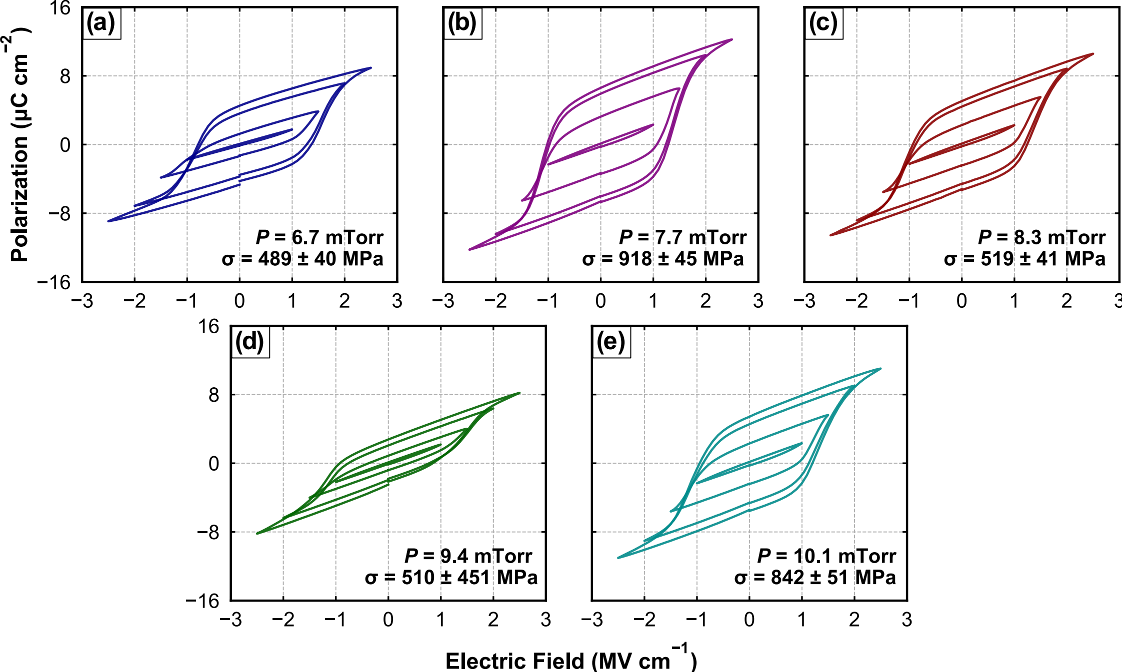

Figure 6.6. Nested hysteresis loop measurements made on the Top Varied sample series with TaN electrodes deposited with (a) 6.7, (b) 7.7, (c) 8.3, (d) 9.4, and (e) 10.1 mTorr background pressure sputtering conditions. The background pressures utilized for sputter deposition of the stress varied (top) TaN electrodes and resulting post-processing HZO biaxial stress states are indicated in the lower right of each panel.

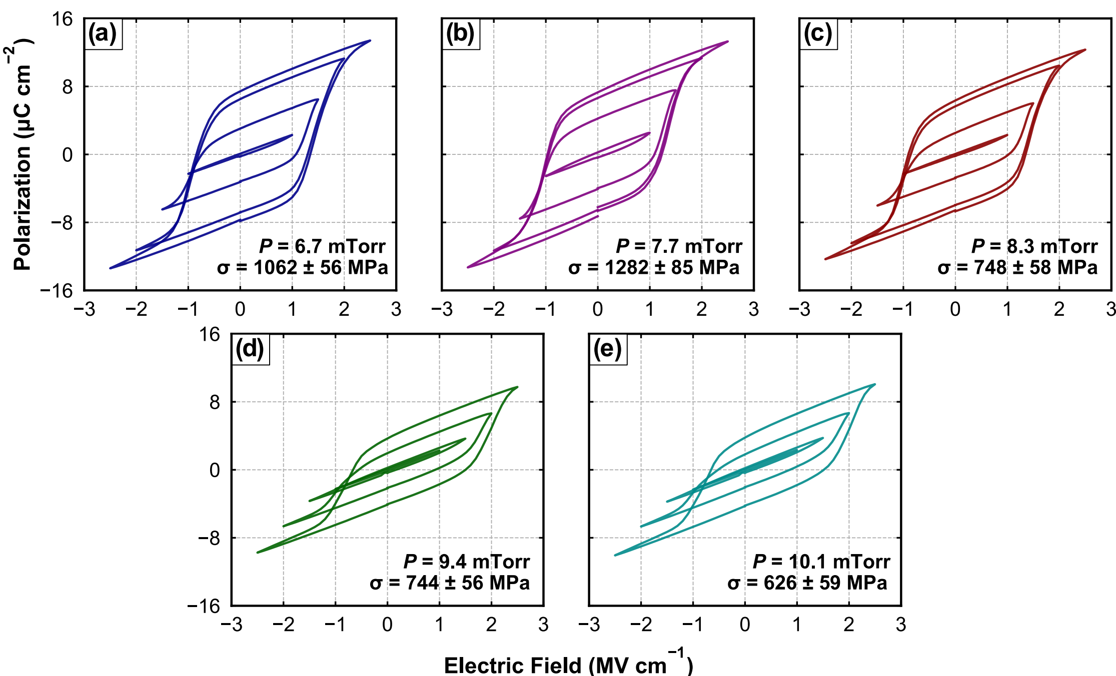

Figure 6.7. Nested hysteresis measurements made on the Bottom Varied series with TaN electrodes deposited with (a) 6.7, (b) 7.7, (c) 8.3, (d) 9.4, and (e) 10.1 mTorr background pressure sputtering conditions. The background pressures utilized for sputter deposition of the stress varied (bottom) TaN electrodes and resulting post-processing HZO biaxial stress states are indicated in the lower right of each panel.

Table 6.1. Coercive field (E_C), hysteresis saturization polarization (P_S) and remanent polarization (P_r), and PUND P_r measured on both Top and Bottom Varied sample series. The column heads identify the background sputtering condition utilized for the stress-varied electrode. $P(E)$ measurements were made with a 1 ms period (1 kHz) and PUND measurements were made with 10 ms voltage pulses.

Sputtering Condition (mTorr)	6.7	7.7	8.3	9.4	10.1
E_C (+/-, Top Varied, MV cm^{-1})	1.5/-0.82	1.42/-1.14	1.44/-1.07	1.49/-1.29	1.40/-1.15
E_C (+/-, Bottom Varied, MV cm^{-1})	1.48/-0.92	1.35/-1.07	1.46/-1.02	1.91/-0.87	1.99/-0.83
Hysteresis P_s (+/-, Top Varied, μC cm^{-2})	9.03/-8.82	12.25/-12.04	10.68/-10.38	8.19/-8.00	11.12/-10.93
Hysteresis P_s (+/-, Bottom Varied, μC cm^{-2})	13.32/-13.30	13.32/-13.30	12.44/-12.14	9.75/-9.56	10.14/-10.05
Hysteresis P_r (+/-, Top Varied, μC cm^{-2})	4.54/-4.33	6.88/-6.67	5.22/-5.21	2.82/-2.34	5.40/-5.46
Hysteresis P_r (+/-, Bottom Varied, μC cm^{-2})	7.47/-7.75	7.47/-6.96	6.29/-6.47	3.70/-4.00	3.89/-4.00
PUND P_r (Top Varied, μC cm^{-2})	7.15 ± 076	7.05 ± 0.24	6.62 ± 0.40	3.30 ± 0.97	6.61 ± 0.23
PUND P_r (Bottom Varied, μC cm^{-2})	8.50 ± 0.21	8.22 ± 0.16	7.70 ± 0.01	5.65 ± 0.17	6.27 ± 0.11

While there was no clear dependence of remanent polarization on magnitude of post-processing biaxial tensile stress in the HZO films, a correlation between remanent polarization and TaN sputtering condition was observed, as shown in Figure 6.8(b). Samples prepared with TaN electrodes with the largest quantities of as-deposited compressive biaxial stress (-1455 MPa) demonstrated the largest measured remanent polarizations of both the Top and Bottom Varied sample series, 7.15 ± 0.8 and 8.50 ± 0.2 μC cm^{-2}, respectively. Oppositely, samples deposited with TaN electrodes with 149 MPa of as-deposited tensile biaxial stress were measured to have the smallest remanent polarizations in both the Top and Bottom Varied sample series of 3.29 ± 1.0 and 5.66 ± 0.2 μC cm^{-2}, respectively. Given that the background pressure utilized during TaN electrode deposition was altered in order to induce the different biaxial stress states, it was suggestive that chemical variation in the TaN electrodes may be responsible for the polarization variation.

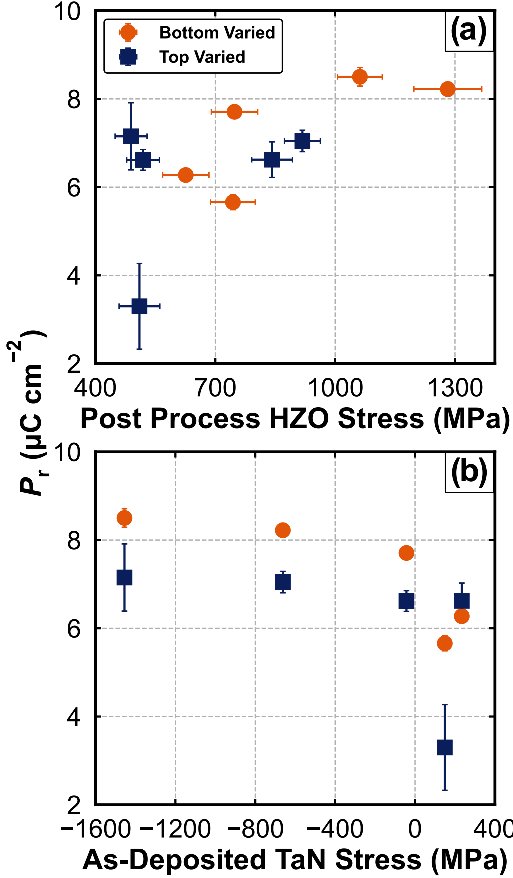

Figure 6.8. Change in P_r with (a) post-processing HZO biaxial stress and (b) as-deposited TaN electrode biaxial stress.

As it is known that processing conditions can impact the stoichiometry of nitride electrodes, the composition of the TaN electrodes was assessed through XPS measurements of witness TaN films. Oxide overlayer attenuation corrections on direct surface measurements were utilized for this analysis instead of sputter depth profiling through oxide overlayers to avoid effects from differential sputter yields of tantalum and nitrogen species that could result in artifacts in the measurements. Example spectra from the N 1*s*/Ta 4*p* and Ta 4*f* regions measured on the TaN film deposited with the 6.7 mTorr background pressure condition are shown in Figure 6.9. The corresponding residuals from the fits to the raw data are indicated above the XPS spectra. Equivalent measurements for the TaN films prepared with the other sputtering conditions are shown in Figure 6.10. Peaks corresponding to Ta_xO_y, TaO_xN_y, and TaN_x were observed in each

region, indicating the presence of a native oxide and interfacial layer on top of a TaN film.[284] An angle-resolved XPS (ARXPS) measurement of a TaN film with Ta_xO_y overlayer was made in order to evaluate the infinite intensity ratio (k) between Ta_xO_y/TaN_x, and ultimately determine oxide overlayer thicknesses for attenuation corrections using Equations 6.1 and 6.2:[285]

$$d = EAL_{\mathrm{Ta4}f(\mathrm{Ta_2O_5})} \cos\theta \ln\left(1 + k\left(\frac{I_{\mathrm{Ta4}f(\mathrm{Ta_2O_5})}}{I_{\mathrm{Ta4}f(\mathrm{TaN})}}\right)\right) \quad 6.1$$

$$I^{\infty}_{\mathrm{N1}s,\mathrm{Ta4}f(\mathrm{TaN})} = I_{\mathrm{N1}s,\mathrm{Ta4}f(\mathrm{TaN})} \exp\left(\frac{d}{\mathrm{EAL}_{\mathrm{N1}s,\mathrm{Ta4}f(\mathrm{Ta_2O_5})} \cos\theta}\right) \quad 6.2$$

Where d is the oxide overlayer thickness, $EAL_{\mathrm{Ta4}f(\mathrm{Ta_2O_5})}$ and $\mathrm{EAL}_{\mathrm{N1}s,\mathrm{Ta4}f(\mathrm{Ta_2O_5})}$ are the effective attenuation lengths for Ta 4f and N 1s electrons in Ta_2O_5,[286] respectively, θ is the take-off angle for photoelectrons, k is the infinite intensity ratio between Ta_xO_y/TaN_x from ARXPS measurements, $I_{\mathrm{Ta4}f(\mathrm{Ta_2O_5})}$ and $I_{\mathrm{N1}s,\mathrm{Ta4}f(\mathrm{TaN})}$ correspond to the measured intensities of the Ta 4f peaks from Ta_xO_y and Ta 4f and N 1s peaks from TaN_x, respectively, and $I^{\infty}_{\mathrm{N1}s,\mathrm{Ta4}f(\mathrm{TaN})}$ is the calculated intensity of N 1s and Ta 4f peaks from an infinitely thick TaN_x film. Spectra and fits for the infinite intensity ratio determination using ARXPS are shown in Figure 6.11. The infinite intensity ratio between Ta_2O_5 and TaN (k) was calculated through fitting of experimental intensity ratios measured at different angles on a TaN film (6.7 mTorr background pressure condition)[285] and least squares minimizing the of infinite intensity ratio and oxide thickness fitting parameters using Equation 6.3 with the assumption that the kinetic energy difference between TaN and Ta_2O_5 Ta 4f photoelectrons is negligible:

$$d = EAL_{\mathrm{Ta_2O_5}} \cos\theta \ln\left(1 + k\frac{I_{\mathrm{Ta_2O_5}}}{I_{\mathrm{TaN}}}\right) \quad 6.3$$

Following attenuation correction, the intensities of the N 1*s* and Ta 4*f* peaks corresponding to each species in TaN (peak fits shown in red in Figure 6.9) were compared using the relative sensitivity factor (RSF) method.[287,288] The same fit methodology was applied to each TaN deposition condition, allowing for direct comparisons between stoichiometries resulting from each process.

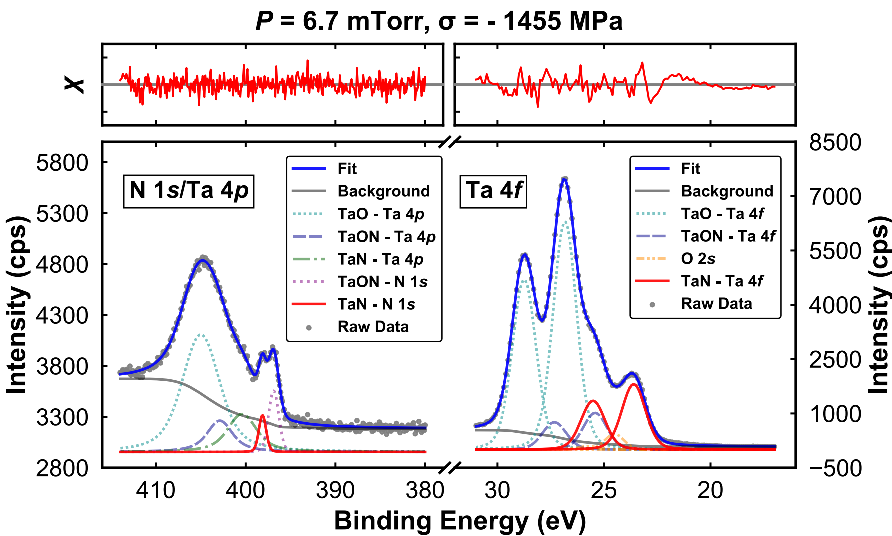

Figure 6.9. XPS spectra for the N 1*s*/Ta 4*p* (left) and Ta 4*f* regions (right) for the 6.7 mTorr background pressure TaN sputtering condition. The summed fit (blue line) is plotted over the raw data (grey points) with associated peaks and background plotted below, residuals from the fit plotted above each panel (red), and the background pressure utilized during sputtering and resulting as-deposited biaxial stress indicated above.

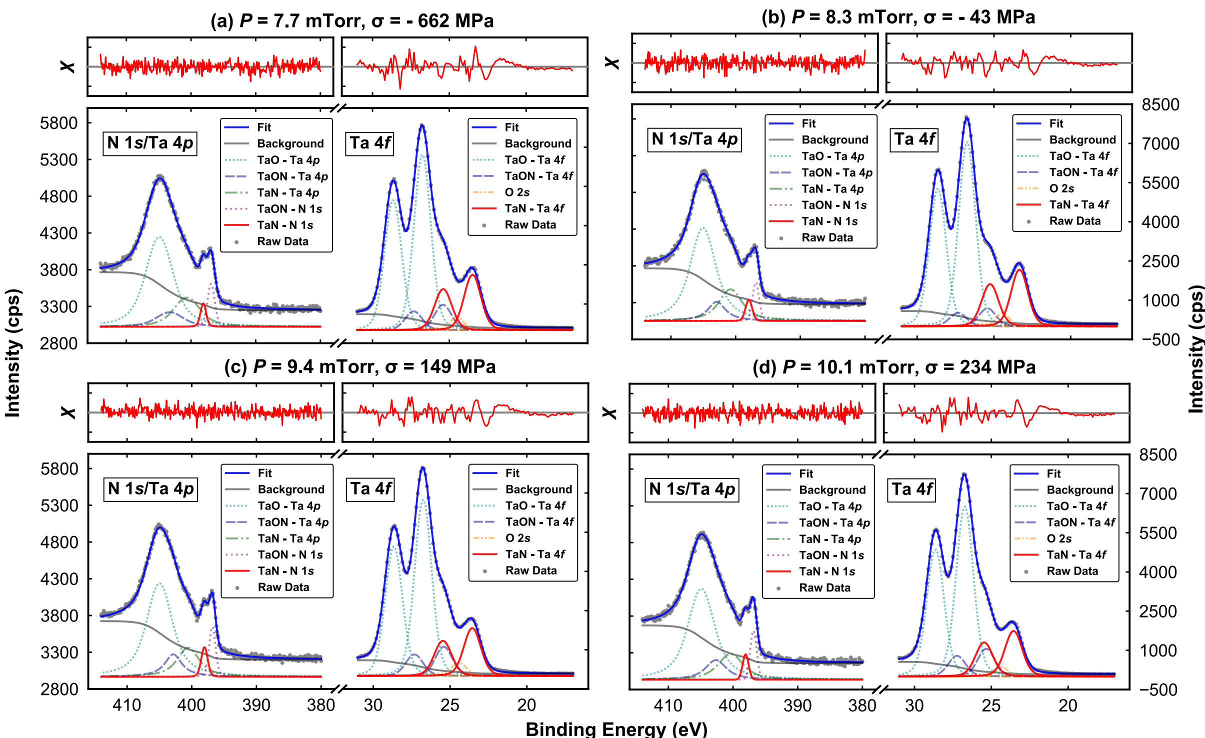

Figure 6.10. XPS spectra for the N 1*s*/ Ta 4*p* (left) and Ta 4*f* regions (right) for the (a) 7.7, (b) 8.3, (c) 9.4, and (d) 10.1 mTorr background pressure TaN sputtering conditions. The summed fits (blue lines) are plotted over the raw data (grey points) with associated peaks and backgrounds plotted below, residuals from the fits plotted above each panel (red), and the utilized background pressures and resulting as-deposited biaxial stresses indicated above each residuals plot.

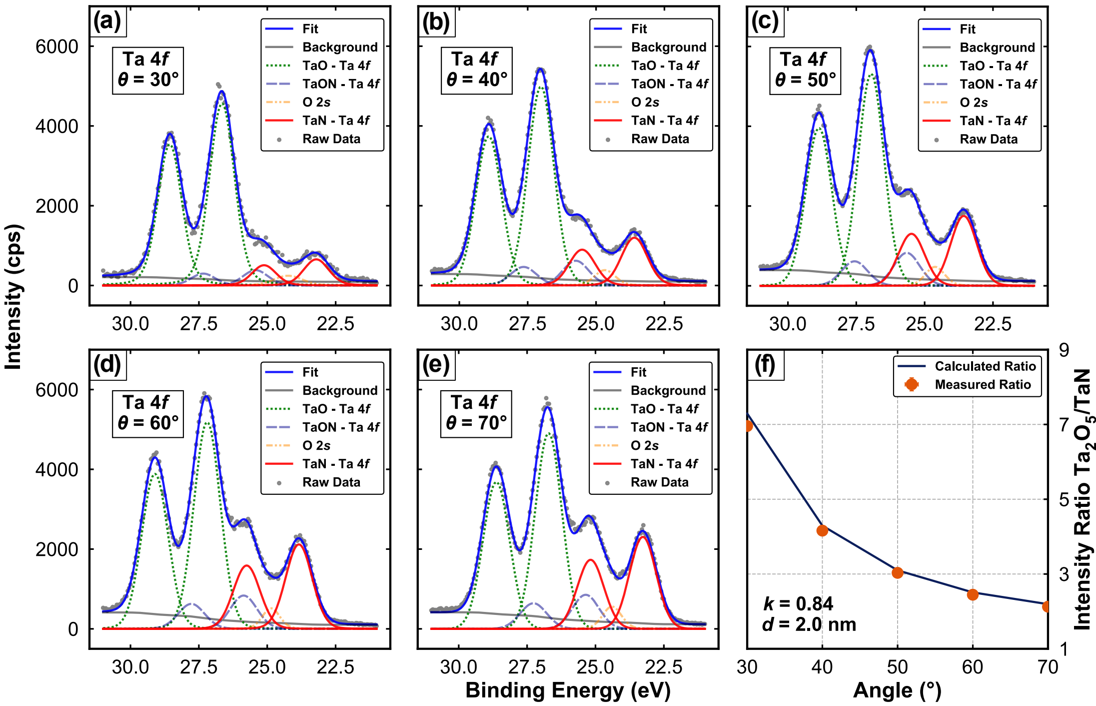

Figure 6.11. XPS spectra for Ta 4*f* region measured on the 6.7 mTorr background pressure sputtering condition at angles of (a) 30°, (b) 40°, (c) 50°, (d) 60°, and (e) 70°. The summed fits (blue lines) are plotted over the raw data (grey points) with associated peaks and backgrounds plotted below and measurement angle indicated in the upper left. (f) Measured Ta_2O_5/TaN intensity ratio plotted against measurement angle (orange points) with associated optimized fit (blue line) with infinite intensity (*k*) and oxide thickness (*d*) fitting parameters indicated in the lower left of the panel.

The N:Ta ratios of the deposited TaN electrode layers are compared in Figure 6.12(a) with the background pressure utilized during sputtering. In general, lower background pressures resulted in higher tantalum contents, while higher background pressures resulted in higher nitrogen contents. As the background pressure during sputtering was varied between 6.7 and 10.1 mTorr, the resulting TaN electrode nitrogen content was observed to vary between 0.66 ± 0.04:1 and 1.12 ± 0.08:1. It is important to note that while the range of these raw values is large and greater than may be expected for a line compound such as TaN, the relative compositions calculated using the RSF method have historically been observed to be precise but lack in accuracy.[288] Further, the room temperature deposition of a refractory compound, such as TaN, may result in phase stability

for compositions that are far from equilibrium.[271] Regardless, analysis of grazing incidence XRD (GIXRD) patterns measured on each TaN electrode sputtering condition, shown in Figure 6.13, indicated that all films were cubic $Fm\bar{3}m$ in phase, while significant compositional variations resulted from the changing deposition background pressure.

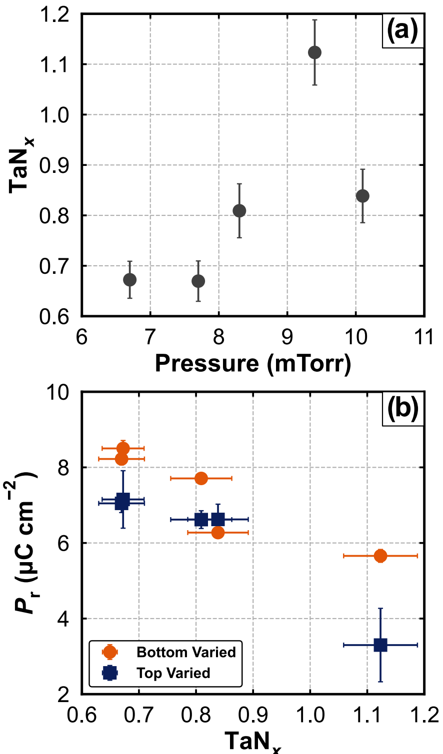

Figure 6.12. (a) N:Ta ratio as a function of background pressure utilized during sputter deposition of the TaN electrodes and (b) HZO P_r dependence on TaN stoichiometry for both Bottom (orange) and Top (blue) Varied sample series.

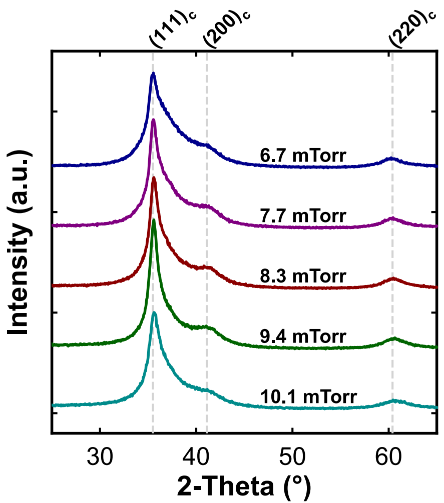

Figure 6.13. GIXRD patterns measured on TaN electrode layers sputter deposited with various background pressure conditions, as indicated above each pattern, with indexing (grey, dotted lines) for observed peaks indicated across the top of the panel.

The impact of the electrode stoichiometry on remanent polarization was assessed and is shown in Figure 6.12(b); a clear correlation of polarization and TaN composition was revealed. The largest remanent polarizations were observed for the samples for which the stress-varied electrode possessed the lowest N:Ta ratio. In tandem, the smallest remanent polarizations were measured for the samples with the most nitrogen-rich TaN electrodes. These trends held between both the top and bottom varied TaN stress series. In general, the Bottom Varied series exhibited larger remanent polarizations than the Top Varied series. This difference could be related to an adventitious oxide interlayer separating the HZO and the stress varied TaN electrode in the Bottom Varied series, owing to the aforementioned processing difference between the two sample sets.

It is apparent that electrode stoichiometry affects the polarization of the HZO films and that the effect is stronger than that from the tensile biaxial stress state. It has been established that oxygen point defect concentration is a contributor to ferroelectric phase stability and therefore it is likely that the non-stoichiometry of the TaN electrodes leads to differing oxygen vacancy contents in the HZO layers via an oxygen scavenging mechanism.[156,289] While direct examination of defect concentrations in HZO thin films has proven experimentally difficult, leakage current measurements have been utilized to estimate these quantities.[111,121,122] Larger leakage currents

have been attributed to higher oxygen point defect concentrations that enable current to flow via compensating electrons and trap-assisted tunneling where the oxygen vacancies serve as traps. Leakage current measurements were thus made on each of the films in both series and are shown in Figure 6.14. While asymmetry in the leakage current profiles prevented quantitative trap-assisted tunneling fitting of leakage current density data, an observable correlation was noted between electrode nitrogen content and measured leakage current at ± 2.0 MV cm^{-1}, as shown in Figure 6.15(a). As the electrode N:Ta ratio increased from 0.66 ± 0.04:1 to 1.12 ± 0.08:1, the measured leakage currents at -2.0 MV cm^{-1} decreased by over an order of magnitude, from 2.3×10^{-4} to 2.2×10^{-5} A cm^{-2} and from 7.3×10^{-4} to 3.8×10^{-5} A cm^{-2} for the Top and Bottom Varied sample series, respectively. A similar trend was observed for leakage currents at +2.0 MV cm^{-1}. These trends suggest that the HZO films prepared with TaN electrodes containing smaller N:Ta ratios (i.e. those that are deficient in nitrogen with respect to a 1:1 N:Ta ratio) contain higher levels of oxygen vacancies. This data supports the notion that TaN electrodes that are nitrogen-deficient are more reactive to the HZO films. Further, this leakage current trend reflects the trend of decreasing polarization with increasing electrode N:Ta ratio.

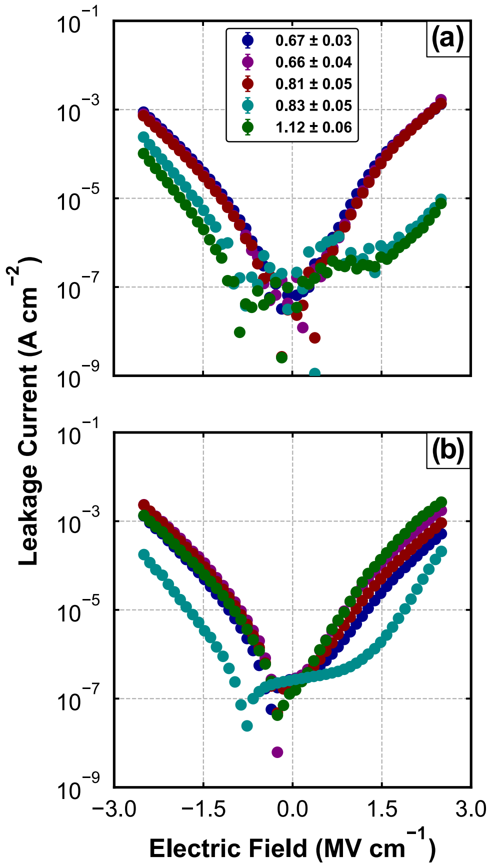

Figure 6.14. Leakage current density measurements for (a) Bottom and (b) Top Varied Sample series. The legend indicates N:Ta ratio of sputtering condition-varied TaN electrode layer.

Given the trends between electrode nitrogen content and leakage current and polarization, it follows that the films deposited with nitrogen-deficient electrodes have a larger content of the ferroelectric orthorhombic phase. To confirm this trend in phase constitution, the integrated intensities of the t + o diffraction peaks in all area detector linescan patterns corresponding to each film were compared with the integrated intensity sum of all three HZO peaks, thus providing a relative t + o intensity ratio, denoted as the relative t + o phase fraction in Figure 6.15(b). Similar to the trends observed in polarization and leakage current density, the relative t + o phase fractions were observed to decrease from 0.52 ± 0.01 to 0.44 ± 0.01 and 0.58 ± 0.01 to 0.51 ± 0.01 for the Top and Bottom Varied sample series, respectively, as the electrode N:Ta ratio increased from 0.66 ± 0.04:1 to 1.12 ± 0.08:1. Combined, these data indicate that it is the increasing oxygen

vacancy content in the HZO films, driven by electrode non-stoichiometry, that ultimately impacts the ferroelectric phase content and polarization response. This suggests that the electrode stoichiometry played a larger role in the polarization response than the post-processing HZO tensile biaxial stress and that the resulting oxygen vacancy content is a critical factor in the stability of the orthorhombic phase and polarization performance of these ferroelectrics.

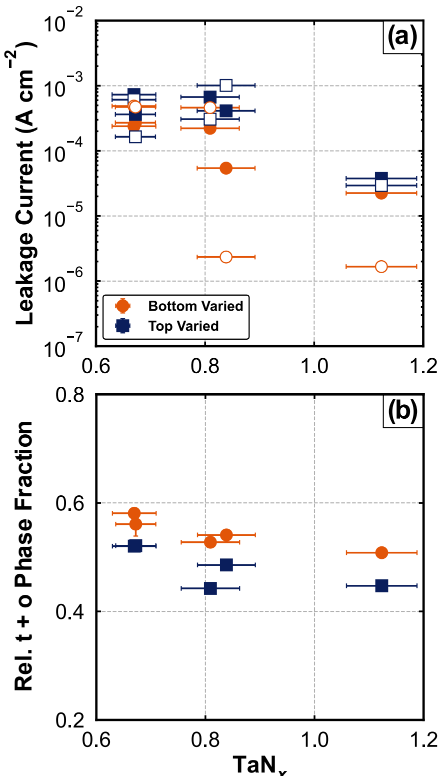

Figure 6.15. (a) Leakage current density measured at +2.0 MV cm^{-1} (open points) and -2.0 MV cm^{-1} (closed points) and (b) relative t + o phase fractions for HZO films as a function of the nitrogen content of the TaN electrodes. Orange circles and blue square points represent films in the Bottom and Top Varied sample series, respectively.

6.6 Conclusions

The post-processing biaxial stress states of ferroelectric HZO films, deposited between top and bottom TaN electrodes of varied as-deposited stress states, were quantified and compared to

polarization performance. A weak correlation between the magnitude of the tensile biaxial stress and measured remanent polarization was observed. Subsequent XPS analysis of TaN stoichiometry revealed differences in N:Ta ratios within the stress modulated electrode layers. These stoichiometry differences were observed to correlate with ferroelectric performance, as HZO devices with electrodes with lower N:Ta ratios exhibited higher measured remanent polarizations. Subsequent leakage current measurements were consistent with oxygen point defect concentrations within the HZO films being dependent upon the TaN stoichiometry. HZO films prepared between electrodes with lower N:Ta ratios had higher leakage currents. These data indicate that electrodes with lower N:Ta ratios yielded larger oxygen vacancy concentrations in the HZO films, which resulted in greater stability of the ferroelectric phase and increased polarization response. This enhanced orthorhombic phase stabilization, related to electrode chemistry, was also observed in analysis of relative phase fractions in each film through fitting of area detector XRD patterns. It was revealed that the relative content of the t + o phase was larger in samples deposited with nitrogen-deficient TaN layers. The electrode stoichiometry effect, and concomitant HZO oxygen vacancy dependence, presented a stronger influence on the polarization performance of the HZO than the tensile biaxial stress effect. These results suggest that nitride electrode stoichiometry is a critical factor that must be controlled for HZO ferroelectric devices.

6.7 Acknowledgement

This work was supported, in-part, by the Laboratory Directed Research and Development program at Sandia National Laboratories. Sandia is a multimission laboratory managed and operated by National Technology & Engineering Solutions of Sandia, LLC, a wholly-owned subsidiary of Honeywell International, Inc., for the U.S. DOE's National Nuclear Security Administration under contract DE-NA-0003525. The views expressed in the article do not necessarily represent the views of the U.S. DOE or the United States Government. This work was also supported, in part, by the Semiconductor Research Corporation's (SRC) Global Research Collaboration in the NanoMaterials and Processing program. This research was supported, in part, by the National Science Foundation through a major instrumentation grant (DMR-1626201). STJ acknowledges support from the National Science Foundation Graduate Research Fellowship Program under award DGE-1842490. A portion of this research used resources at the Spallation

Neutron Source, a DOE Office of Science User Facility operated by the Oak Ridge National Laboratory. This manuscript has been coauthored by UT-Battelle, LLC, under Contract No. DE-AC05-00OR22725 with the U.S. Department of Energy. The United States Government retains and the publisher, by accepting the article for publication, acknowledges that the United States Government retains a non-exclusive, paid-up, irrevocable, world-wide license to publish or reproduce the published form of this manuscript, or allow others to do so, for United States Government purposes.

Chapter 7: Wake-up and Fatigue Mechanisms in Ferroelectric $Hf_{0.5}Zr_{0.5}O_2$ Films with Symmetric RuO_2 Electrodes

The contents of this chapter are published in *Journal of Applied Physics* (**130**, 134101, 2021, DOI: https://doi.org/10.1063/5.0064145) as a *Featured Article* with the following as authors:

Shelby S. Fields,[1] Sean W. Smith,[2] Samantha T. Jaszewski,[1] Takanori Mimura,[1] Diane A. Dickie,[1,3] Giovanni Esteves,[2] Michael D. Henry,[2] Steve L. Wolfley,[2] Paul S. Davids,[2] and Jon F. Ihlefeld.[1,4]

[1]Department of Materials Science and Engineering, University of Virginia, Charlottesville VA, 22904, USA

[2]Sandia National Laboratories, Albuquerque NM, 87123, USA

[3]Department of Chemistry, University of Virginia, Charlottesville VA, 22904

[4]Charles L. Brown Department of Electrical and Computer Engineering, University of Virginia, Charlottesville VA, 22904, USA

The body of text of this chapter has been adapted to include the supplemental information and figures, where appropriate.

7.1 Motivation

The investigation described in Chapter 4 revealed that the field-cycling behavior of nominally identical HZO layers is different depending on whether TaN, W, or Pt electrodes are utilized. To date, oxide electrode materials, which have been observed to prevent field-cycling driven polarization fatigue in PZT and BTO ferroelectrics, have only recently begun to be examined for applications in HZO thin films. The polarization fatigue mitigation in PZT and BTO was been attributed to superior oxygen and defect transfer between the oxide electrode and ferroelectric layers during field-cycling compared with metallic equivalents. In HZO, the role of oxygen and oxygen vacancies in both orthorhombic phase stabilization and field-cycling behavior make comparisons directly with PZT and BTO difficult, precipitating the need to experimentally examine such electrode materials in this system. In this study, the field-cycling behavior of HZO with RuO_2 electrodes is investigated using polarization, pyroelectric, area detector microdiffraction, permittivity, and leakage current measurements.

7.2 Abstract

The mechanisms leading to wake-up and fatigue in ferroelectric hafnium zirconium oxide thin film devices with symmetric RuO_2 electrodes are investigated via polarization, relative permittivity, dielectric nonlinearity, pyroelectric coefficient, and microfocus X-ray diffraction (XRD) measurements. The devices are observed to wake-up for up to 10^3 bipolar pulsed field cycles, after which fatigue occurs with the polarization approaching zero following 10^8 cycles. Wake-up is accompanied by a decrease in both high-field permittivity and hysteresis loop pinching and an increase in pyroelectric coefficient, indicating that the wake-up process involves a combination of transformations from the tetragonal to the orthorhombic phase and domain depinning from defect redistribution. Fatigue is observed to coincide with an increase in irreversible domain wall motion and a decrease in pyroelectric coefficient. Finite pyroelectric coefficients are measured on fully fatigued devices, indicating that domain pinning is a strong contributor to fatigue and that fatigued devices contain domain structures that are unable to switch under the fields applied for measurement. Microfocus XRD patterns measured on each device reveal that the phase constitution is qualitatively unaffected by the field cycling and resultant polarization fatigue. This data indicates that the wake-up process has contributions from both phase transformations and domain depinning, whereas the fatigue process is driven primarily by domain pinning, and the near-zero measured switchable polarization is actually a poled device with immobile domains. These observations provide insight into the physical changes occurring during field cycling of HfO_2-based ferroelectrics while examining a possible oxide electrode material for silicon CMOS device implementation.

7.3 Introduction

The first report of ferroelectricity in HfO_2-based thin films in 2011[1] generated interest for implementation of this scalable[105,290] and silicon compatible[75,77] material for device applications, including ferroelectric random access memory,[2,229] energy harvesting,[291] non-linear optics,[82,269] infrared sensing,[149,222,223] and negative differential capacitance field effect transistors.[292,293] The ferroelectric properties of this system have been attributed to a metastable, space group $Pca2_1$ orthorhombic phase,[87,92] which is stabilized with respect to the room-temperature equilibrium,

linear dielectric $P2_1/c$ monoclinic and high-temperature, field-induced ferroelectric $P4_2/nmc$ tetragonal phases with doping,[3,124,126] reduced oxygen content,[110,111] presence of biaxial stress,[115,116] and utilization of sub-30 nm film thicknesses.[98,104] Of the many HfO_2-based ferroelectric dopants, zirconium oxide has been identified as an alloying material ($Hf_xZr_{1-x}O_2$, HZO) that stabilizes the orthorhombic phase through nearly the entire composition window[3,130] and reduces the thermal budget required for its formation compared to many other doped HfO_2 compositions,[142] and so has received significant attention.[3,105,130,249]

Investigations of the ferroelectric and field cycling properties of HfO_2-based thin films, including HZO, most commonly incorporate binary nitride electrode materials, including TiN[1,151,294] and TaN,[117] into metal-insulator-metal (MIM) device structures. These electrodes have been reported to induce tensile biaxial stress[124,125,283] within and scavenge oxygen from the adjacent HfO_2-based ferroelectric layer,[155,295] resulting in stabilization of the orthorhombic phase. With initial electric field cycling of these MIM devices above their coercive field, redistribution of oxygen vacancies within the ferroelectric layer has been reported to unpin ferroelectric domains[164,171,175,179] and drive a transformation from the tetragonal phase to the orthorhombic phase,[154,296] both of which result in an increased remanent polarization (P_r) and wake-up. With extended field cycling, domain pinning due to defect generation within the ferroelectric layer[171,172] and transformations from the tetragonal and orthorhombic phases to the monoclinic phase[296] cause a reduction in P_r and fatigue. Further field cycling often results in increasing defect concentration and the formation of conductive paths between the electrodes, causing dielectric breakdown.[165]

The field cycling behavior of ferroelectric hafnia has been observed to vary depending upon the utilized electrode material. A direct comparison between TiN and TaN electrodes, and various combinations thereof, observed that utilization of TaN electrodes yielded films that only woke up with field cycling and did not fatigue.[117] Devices with TaN electrodes also maintained higher P_r; however, they experienced a reduction in cycles-to-breakdown. The same study found that TiN electrodes, alternatively, increased the number of cycles-to-breakdown and yielded devices that both woke up and fatigued. These differences in field cycling behavior have been attributed to differences in oxygen vacancy concentration within the ferroelectric layers due to oxygen scavenging by the neighboring electrodes,[155,156] providing the potential for control of the wake-up, fatigue, and breakdown behavior via electrode engineering.

Beyond binary nitrides, conductive oxide electrodes, such as RuO_2[162,240,297] and IrO_2,[160,161] have been explored for ferroelectric HfO_2-based thin film applications. These and other conductive oxide electrode materials were experimentally shown to yield fatigue performance superior to noble metal electrodes in perovskite ferroelectrics, such as $Pb(Zr,Ti)O_3$, with the improvements attributed to a reduction of defect-driven domain pinning.[35,36,183,237,238] It was concluded that a large contributor to fatigue was an interfacial buildup of oxygen vacancies, which migrate to the ferroelectric/electrode interfaces during field cycling. Utilization of conductive oxide electrodes aided in mitigating this vacancy buildup by allowing oxygen vacancies to cross the ferroelectric/electrode interface, thus improving the fatigue performance.[21]

To date, investigations evaluating hafnia-based ferroelectrics with IrO_2 and RuO_2 electrodes have reported that the fatigue performance is not improved compared to more widely utilized TiN and TaN electrodes.[160,161,240,297] Reports of fatigue performance of HZO with symmetric IrO_2 electrodes observed 10^7 cycles to breakdown and fatigue onset after only 10^5 cycles, with low measured remanent polarizations (~5 μC cm^{-2}).[160,161] An investigation of asymmetric TiN/HZO/RuO_2 devices observed polarization fatigue following 10^5 cycles, low endurance (~10^7 cycles to breakdown), and low remanent polarizations (~5 μC cm^{-2}), all of which were attributed to a reduction of the RuO_2 top electrode to metallic ruthenium during processing due to the TiN bottom electrode.[240] A more recent work examining HZO with symmetric RuO_2 electrodes reported remanent polarizations of 15 μC cm^{-2} and with consistent wake-up during field cycling.[162] This work indicated that RuO_2 may be an advantageous oxide electrode for devices compared to IrO_2 owing to the larger reported P_r values and apparent lack of fatigue. This study did not report the utilized field cycling waveforms or procedure, but showed 10^8 cycles-to-breakdown. In contrast to these reports of devices with symmetric and asymmetric oxide electrodes, symmetric TiN electrode devices have been shown to yield HZO devices that demonstrate a higher cycles-to-breakdown of ~10^{10}, and maintain modest remanent polarizations of ~8-10 μC cm^{-2}.[135]

In this study, the mechanisms leading to fatigue in symmetric RuO_2/ HZO/RuO_2 devices cycled with 50% duty cycle, 10 kHz, 2.0 MV cm^{-1} bipolar pulses are investigated. Polarization, switching current, relative permittivity, dielectric nonlinearity, and leakage current measurements are used in conjunction with pyroelectric measurements and area detector X-ray diffraction (XRD)

analyses to elucidate how the phase constitution and domain dynamics evolve within the ferroelectric layer with field cycling and wake-up/fatigue. Understanding the mechanisms leading to the low remanent polarizations and cycles-to-breakdown reported for HZO between conductive oxide electrodes may facilitate the development of electrode materials that balance the requirements for ferroelectric layer oxygen content and oxygen vacancy driven degradation mitigation.

7.4 Experimental Procedures

RuO_2/HZO/RuO_2 devices were prepared with 20 nm-thick HZO films between symmetric 120 nm thick RuO_2 electrodes on silicon substrates at Sandia National Laboratories. The planar bottom RuO_2 electrode was deposited via pulsed DC reactive sputtering (30 kHz/4 μs reverse time) with a power density of 4.6 W cm^{-2} in a Denton Discovery 550 sputtering system. Following bottom electrode deposition, HZO with a targeted composition of $Hf_{0.5}Zr_{0.5}O_2$ was deposited via thermal atomic layer deposition at a temperature of 150 °C within an Ultratech Savannah instrument utilizing tetrakis(dimethylamino)hafnium (TDMA HF, at 75 °C) and tetrakis(dimethylamino)zirconium (TDMA Zr, at 75 °C) as hafnium and zirconium precursors, respectively, and H_2O as an oxidant. Due to per-cycle growth rate differences between HfO_2 and ZrO_2, the 5:5 super-cycle ratio resulted in a final film composition of $Hf_{0.58}Zr_{0.42}O_2$.[149] After HZO growth, planar RuO_2 electrodes were deposited to a thickness of 120 nm utilizing the same conditions as used for the bottom electrode. After top electrode deposition, samples were rapid thermal annealed in a Surface Science Integration Solaris 150 instrument at 600 °C for 30 seconds in a N_2 atmosphere. Following annealing, samples meant for pyroelectric current and XRD measurements received 1000 μm-diameter platinum contacts through a shadow mask, whereas samples meant for electrical characterization received 100 μm-diameter photolithographically defined platinum contacts. After contact deposition, the RuO_2 top electrodes were reactive ion etched to isolate discreet devices for characterization, utilizing the platinum contacts as a hard mask.

Electrical characterization, including polarization-electric field hysteresis loop ($P(E)$), switching current, and positive-up negative-down (PUND) pulsed polarization measurements, was carried out using a Radiant Technologies Precision LC II instrument. Nested $P(E)$

(1.0 – 2.5 MV cm^{-1} maximum fields) and switching current (2.5 MV cm^{-1} maximum field) measurements were performed with a period of 1 ms, whereas nested PUND (1.0 – 2.5 MV cm^{-1} maximum fields) measurements were performed with a pulse width of 1 ms and pulse delay of 100 ms. Dielectric nonlinearity (Rayleigh) and capacitance-voltage (CV) measurements were completed with a Keysight E4980A Precision LCR Meter. A 0.05 V, 10 kHz oscillator was utilized for CV measurements, while Rayleigh measurements were performed at 10 kHz with an oscillator amplitude ranging from 0.001 MV cm^{-1} to 0.09 MV cm^{-1}. CV measurements were conducted between ± 2.5 MV cm^{-1} with a step size of 0.05 MV cm^{-1}. Leakage currents were measured from -2.5 MV cm^{-1} to 2.5 MV cm^{-1} with a step size of 0.05 MV cm^{-1} using a Keysight B2901A Precision Source Measure Unit. Pyroelectric coefficients were measured using the technique described by Sharp and Garn[226] by measuring pyroelectric current with a Keithley 6514 Electrometer while oscillating the device temperature using a Peltier cooler (TE Technology model VT-127-1.0-1.3-71) connected to a Keysight 33500B Waveform Generator, similar to measurements described elsewhere.[149,185,226] For the temperature oscillation, a 10 V (peak-to-peak) sinusoidal 1 mHz waveform was applied to the Peltier cooler, resulting in temperature amplitudes of approximately 9 °C. Fatigue cycling was completed with an electric field of 2.0 MV cm^{-1} at a frequency of 10 kHz utilizing a 50% duty cycle waveform with a Keysight 33500B Waveform Generator. The fatigue pulses were meant to simulate application-relevant waveform shapes and had a rise and fall time of 2 μs and hold time of 300 ms.[33] A modified Sawyer-Tower circuit with the load capacitor replaced with a 50 Ohm resistor was used to analyze the switching behavior of the samples with both the small and large contact diameters to verify that full switching was occurring at the 10 kHz pulsing frequency. For this measurement, a Tektronix DPO7254 Oscilloscope, in series with a 50 Ω resistor, was utilized for signal processing while a Keysight 33500B Waveform Generator was used for pulse generation. The 10 kHz, 2.0 MV cm^{-1} 50% duty cycle square wave pulse shapes (rise and fall time of 1.5 μs) utilized for cycling are shown in Figure 7.1(a) and (b), along with the resulting current density across both contact sizes. It is evident, based on the voltage profiles reaching ± 4 V and the current densities returning to 0 A cm^{-2} after the field is removed in both measurements, that the ferroelectric devices are fully switching at 10 kHz regardless of contact size.

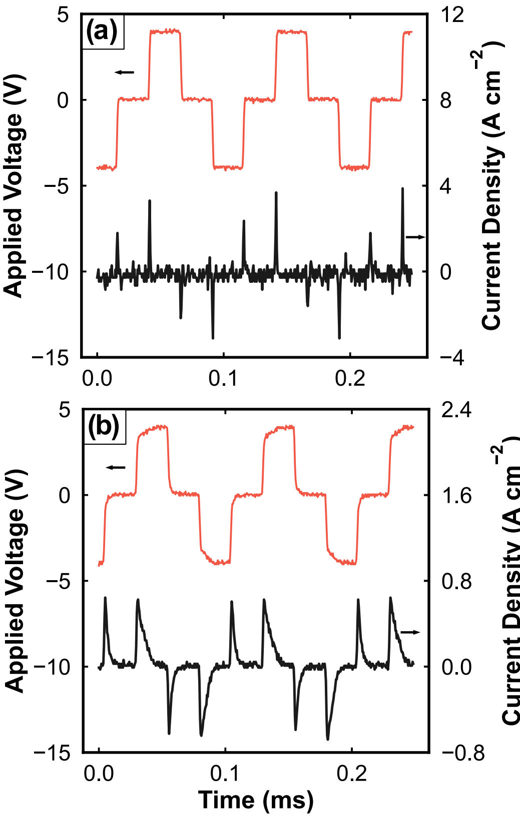

Figure 7.1. Applied voltage profiles (red, left axis) and resulting current densities (black, right axis) measured across devices with (a) 100 µm and (b) 1000 µm diameters.

Grazing incidence XRD (GIXRD) measurements were performed in a parallel beam geometry using a Rigaku Smartlab diffractometer utilizing Cu Kα radiation with ω incident angle fixed at 0.7°. Microfocused area detector XRD measurements were completed on individually field-cycled capacitors using a Bruker D8 Venture diffractometer equipped with an Incoatec IµS 3.0 Cu Kα radiation source and a Photon III detector with MgO powder adhered to device surfaces as a stress-free height alignment standard.[283] For these measurements, the ω angle was fixed at 20° and a 0.2 mm collimator was utilized to produce a beam footprint diameter of 600 µm on device surfaces.

7.5 Results and Discussion

Based upon the GIXRD pattern measured on the RuO_2/HZO/RuO_2 sample, shown in Figure 1, the processed devices contain predominantly monoclinic phase. The intensity of the superimposed (111)/(101) orthorhombic/tetragonal peak, present at 30.3° in 2θ, had a low intensity compared to the (111) monoclinic peak at 31.5°. The ($\bar{1}$11) monoclinic peak, typically indexed at 28.5°, was not observable due to the presence of an intense (110) RuO_2 reflection at 28.1° from the 120 nm-thick bottom electrode. Based upon this diffraction pattern, it is apparent that the samples contain comparatively more monoclinic phase than films with similar composition and processing but with TaN, tungsten, or platinum electrodes.[149] The higher amount of monoclinic phase for the samples in this study suggests that the HZO has a lower oxygen vacancy concentration,[110,111] which is likely related to processing with oxide electrodes.

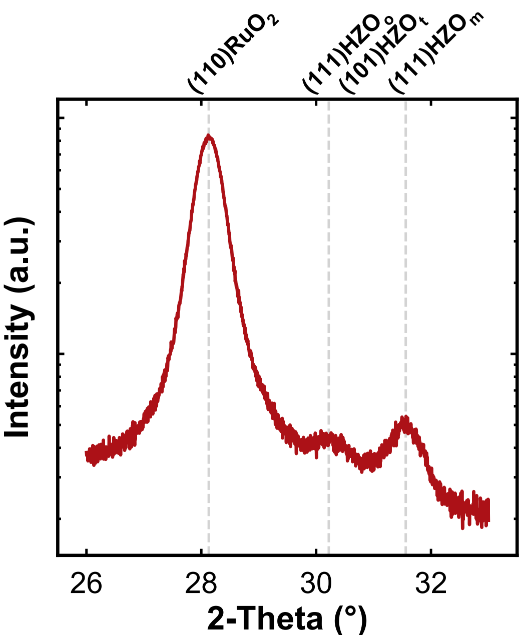

Figure 7.2. GIXRD pattern measured on the RuO_2/HZO/RuO_2 sample with indexing for each peak provided above the panel. A logarithmic intensity scale was used owing to the high intensity of the RuO_2 110 reflection.

Nested $P(E)$ measurements performed on the pristine device and after 5×10^4 field cycles, shown in Figure 7.3(a) and (b), respectively, revealed a decrease in loop pinching and increase in polarization response consistent with wake-up. All subsequent $P(E)$ measurements revealed decreasing polarizations and fatigue. As shown in Figure 7.3(c), the device response appeared as a linear dielectric following 10^7 bipolar pulses. The same trends are evident in the switching current. The switching current measured on the pristine device is plotted in Figure 7.3(d) and shows two distinct switching peaks that condense to a single peak in the measurement made following 5×10^4 cycles (Figure 7.3(e)). This merging of switching current peaks is consistent with wake-up.[117,161] After this initial wake-up, the switching current decreases with each additional field cycling interval until the response approaches that of a linear dielectric. The measurement made following 10^7 cycles, which lacks significant switching current peaks, is shown in Figure 7.3(f). The coercive fields (E_c) from hysteresis and switching current measurements are shown in Figure 7.4. The values were observed to increase from 0.65/-0.40 MV cm^{-1} to 1.12/-0.87 MV cm^{-1} following initial hysteresis de-pinching. The values then remained relatively constant until 10^5 cycles, at which point they decreased throughout the fatigue process to 0 MV cm^{-1}. The low polarizations and switching currents are consistent with the GIXRD phase analysis and indicate that the films contain substantial fractions of the non-ferroelectric monoclinic phase. Regardless, the electrical responses indicate that these devices wake-up with 10^4 bipolar pulses, fatigue with subsequent field cycling, and yield well-saturating polarization and switching current responses irrespective of field cycling progress.

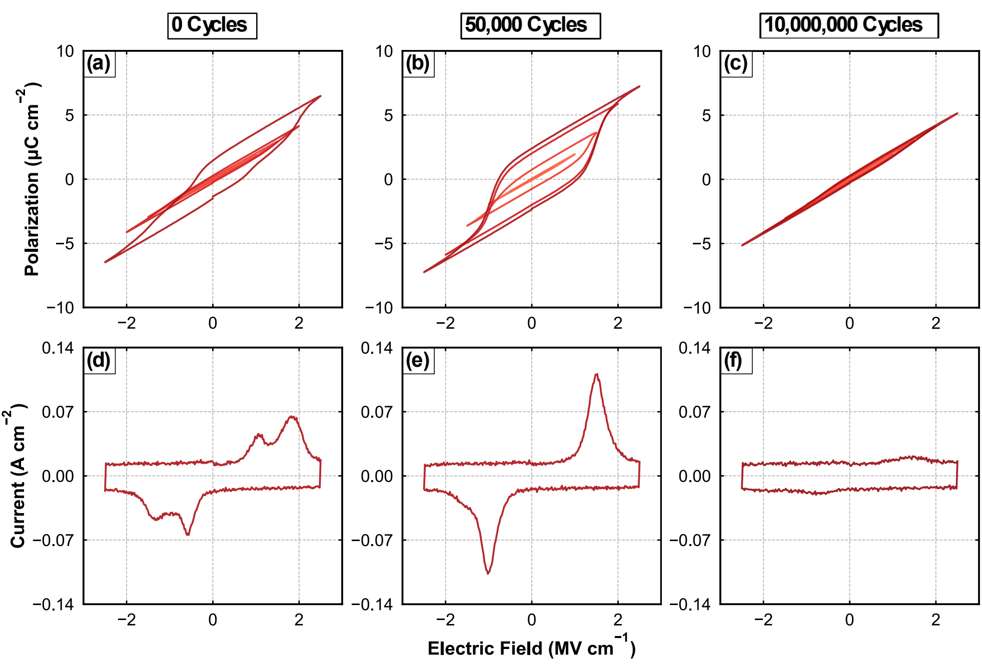

Figure 7.3. Nested polarization hysteresis measurements made following (a) 0, (b) 50,000, and (c) 10,000,000 cycles. Current loop measurements made following (d) 0, (e) 50,000, (f) 10,000,000 cycles.

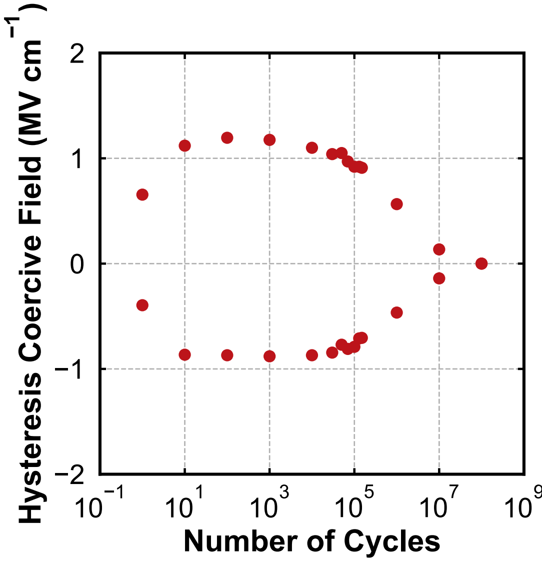

Figure 7.4. Coercive fields extracted from hysteresis measurements made at each cycling interval.

Wake-up and fatigue are also evident in the change in the switchable polarization (P_{sw}) with cycling, as assessed from PUND measurements and shown in Figure 7.5. The initial P_{sw} of 4.26 μC cm^{-2} increased to 6.38 μC cm^{-2} with wake-up through the first 10^3 cycles and then decreased to 0.14 μC cm^{-2} following 10^8 cycles during fatigue. The switchable polarization quantity characterizes the difference in polarization magnitude between the up-poled and down-poled states. Thus, while the switchable polarization decreases with field cycling, the PUND measurement does not necessarily indicate a lack of polar material, domain structure, or the orientation of any domain structure that is unable to switch under the fields applied for measurement. The magnitudes of these P_{sw} values are consistent with previous reports which examined HZO with symmetric IrO_2 electrodes,[160,161] and lower than investigations of HZO MIM devices with TiN and TaN electrodes. These values are also lower than values reported in the other recent study examining symmetric RuO_2 electrodes,[162] which may be related to the 20 nm HZO thickness utilized for this study, as thinner films typically contain more of the ferroelectric orthorhombic phase.[104] In contrast to the devices with IrO_2 electrodes that began to fatigue following 10^5 cycles, the fatigue in these RuO_2 devices began after 10^3 cycles, and they did not suffer dielectric breakdown after the switchable polarization became zero following 10^8 cycles.

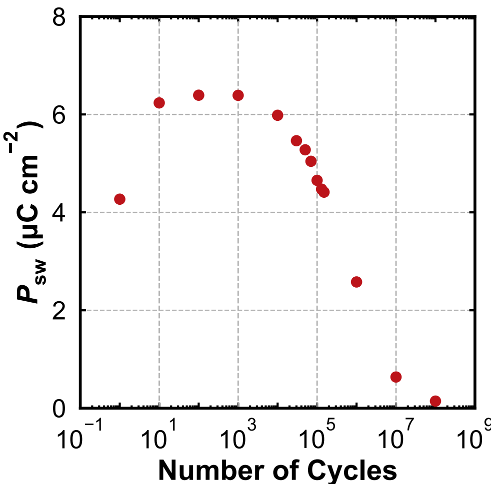

Figure 7.5. Switchable polarization quantified from PUND measurements as a function of the number of 50% duty cycle, 2.0 MV cm^{-1}, 10 kHz bipolar pulses.

While the decrease in P_{sw} reveals that the concentration of switchable domains decreases during fatigue, the mechanism by which this decrease is occurring is not evident based on field cycling-resolved $P(E)$, switching current, and PUND measurements. Analyses of CV and Rayleigh measurements provide insight into the mechanism. CV data is shown in Figure 7.6(a). Similar to the switchable polarizations, the relative permittivity maxima at the coercive fields also reveal a decrease in magnitude, and the behavior appears more consistent with a linear dielectric response following 10^8 cycles. The high-field permittivities extracted from the CV profiles are plotted in Figure 7.6(b) and reveal a decrease from 21.1 to 21.0 through 10^4 cycles during wake-up. The magnitude of these permittivities is lower than those reported in investigations utilizing TiN,[135] TaN,[283] and IrO_2[161] electrodes and is likely related to the high content of monoclinic phase in these samples. The decrease in high-field permittivity with wake-up is suggestive of a phase transformation from the tetragonal to the orthorhombic phase, as has been observed using synchrotron XRD measurements of W/HZO/W and TaN/HZO/TaN devices[296] and TEM analyses of field cycled Gd-doped HfO_2 with TiN electrodes,[154] respectively. However, this decrease is likely too small to completely account for the entire increase in P_{sw} of 153% with field cycling, indicating that domain depinning processes, widely observed during initial cycling of HfO_2-based ferroelectrics,[172,175] are also contributing to the observed wake-up. After decreasing during wake-up, the high-field relative permittivity is observed to increase during fatigue, from 21.0 to 21.1. By comparison, the same investigations, which examined field cycling of HZO (with Pt electrodes)[296] and Gd-doped HfO_2 (with TiN electrodes)[154] reported decreases in permittivity magnitude of approximately 3-5 throughout the fatigue process. In the case of the HZO with Pt electrodes, as discussed in Chapter 4, it was determined from combined microdiffraction and electrical analysis that a phase transformation from the orthorhombic and tetragonal phases to the monoclinic phase accompanied the polarization fatigue,[296] whereas in the Gd-doped HfO_2 investigation with TiN electrodes, it was concluded that an increase in oxygen vacancy concentration resulted in domain pinning.[154] While the polarization decreases similarly in the Pt/HZO/Pt, TiN/Gd-doped HfO_2/TiN, and RuO_2/HZO/RuO_2 devices during fatigue, the permittivity behavior is different. Polarization fatigue in devices with noble metal and binary nitride electrodes coincides with a decrease in permittivity, while the fatigue coincides with a permittivity increase in these devices with RuO_2 electrodes. This difference in permittivity behavior indicates that the fatigue mechanisms in devices with oxide electrodes may be different than in devices with binary nitride or noble metal

electrodes. The minimal permittivity change with fatigue, particularly in comparison to the Pt/HZO/Pt investigation, is also evidence that the phase constitution is not substantially changing with field cycling in these devices with RuO_2 electrodes.

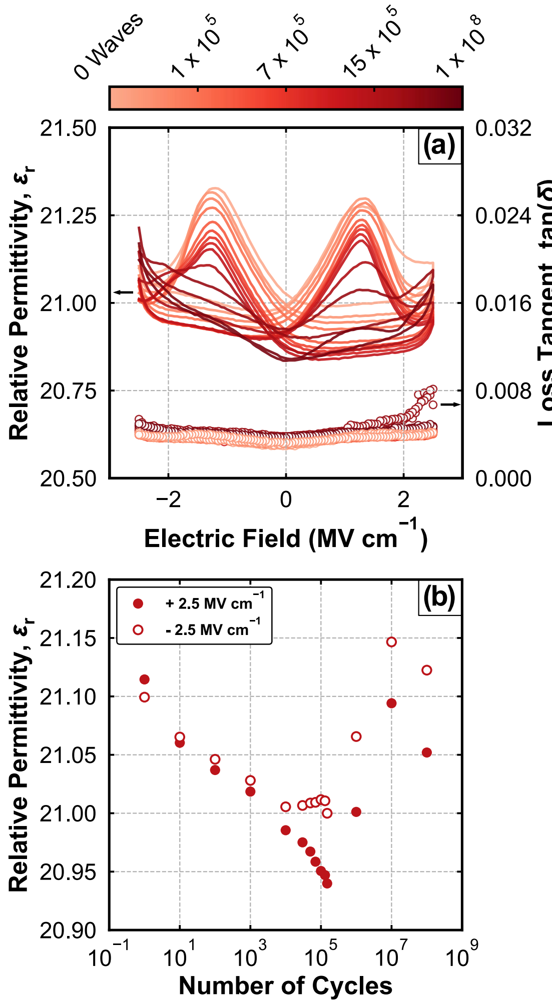

Figure 7.6. (a) Relative permittivity (lines, left axis) and loss (open circles, right axis) measured versus applied DC field at intervals between 0 and 10^8 field cycles, with number of cycles indicated by the color bar above the panel. (b) Relative permittivity measured at + 2.5 MV cm^{-1} (closed circles) and - 2.5 MV cm^{-1} (open circles) at intervals between 0 and 10^8 bipolar waves.

Figure 7.7(a) shows dielectric nonlinearity measurements that also reflect this decrease in permittivity magnitude and provide further insight into the mechanisms causing the polarization fatigue. The reversible Rayleigh coefficient values (ε_{init}), extracted at the threshold AC field (~0.02 MV cm^{-1}), are plotted in Figure 7.7(b). ε_{init} was observed to remain effectively constant at 20.95 through the first 10^4 bipolar pulses and then decrease, coinciding with the start of the polarization fatigue, to 20.75. Given that phase transformations were not obviously observed in the high DC field relative permittivities, the decrease in ε_{init} at the onset of fatigue is evidence that the domain boundaries move less freely as fatigue progresses. Figure 7.7(b) shows the irreversible Rayleigh coefficient (α') with field cycling. The irreversible Rayleigh coefficient can characterize the energetic barrier landscape encountered by domain boundaries as they traverse the ferroelectric film under an AC field below the coercive field.[242] Larger α' values are indicative of higher irreversible contributions to domain wall movement, which is consistent with increased domain wall pinning.[298] In these devices, α' was observed to increase from 0.40 to 0.70 cm MV^{-1} through field cycling; once again, a notable increase is observed at 10^4 cycles. Thus, the increase in α' coincides with the onset of fatigue observed in P_{sw}, $P(E)$, switching current, and high field permittivity measurements and is evidence that the energy landscape for domain wall motion is being altered at the same time that the switchable polarization decreases. Between 10^7 and 10^8 cycles, α' then decreased from 0.70 to 0.65 cm MV^{-1}, which may be related to increased energy barriers for domain movement as the final steps of fatigue are approached.

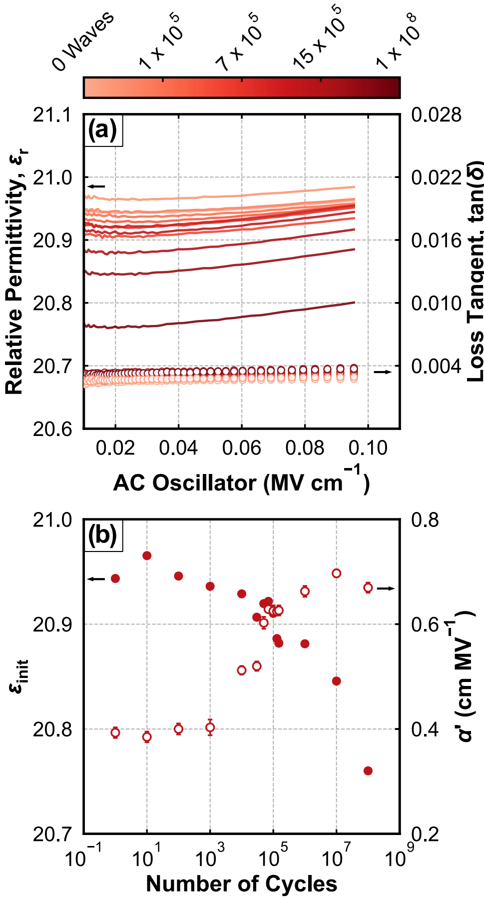

Figure 7.7. (a) Relative permittivity (left axis) and loss tangent (right axis) as a function of AC oscillator level measured at various intervals of bipolar waves, as indicated by the color bar above the plot. (b) Reversible Rayleigh coefficient, ε_{init}, (left axis, closed points) and irreversible Rayleigh coefficient, α', (right axis, open points) measured at various cycling intervals.

Despite the diminished switchable polarizations in the highly fatigued devices, the presence of a finite α' value is indicative that a domain structure remains within the ferroelectric layer. Given that PUND measurements can only evaluate the amount of switchable polarization, and do not indicate the degree to which or direction in which poled, but unswitchable domains exists in the film, pyroelectric coefficient measurements were made on devices cycled at each interval to further examine the evolution of polarization magnitude with field cycling. Pyroelectric measurements were made after initial poling/cycling and after 500 hours at rest to minimize possible contributions from electret effects.[185] The phase differences between the sinusoidal

current and temperature signals were fit to be -90 ± 3°, indicating that the current contributions were solely from crystallographic dipoles. The pyroelectric current generated by the initially poled device (i.e., after only a single PUND measurement and no fatigue cycling) is shown in Figure 7.8(a). A current density amplitude of 3.7 × 10^{-10} A cm^{-2} was measured while the temperature oscillated with an amplitude of 9 °C. With 10^4 cycles and wake-up, the current density amplitude remained approximately the same, as shown in Figure 7.8(b). Following 10^7 cycles and fatigue the current density amplitude decreased to 2.2 × 10^{-10} A cm^{-2}, as shown in Figure 7.8(c). Based on an analysis of the phase difference between the pyroelectric current and temperature, it was determined that the devices are poled in an up orientation during each measurement (i.e., the positive end of the dipole is oriented toward the top electrode), which is consistent with sequence and polarity of PUND pulses utilized to measure the devices prior to pyroelectric current measurement.

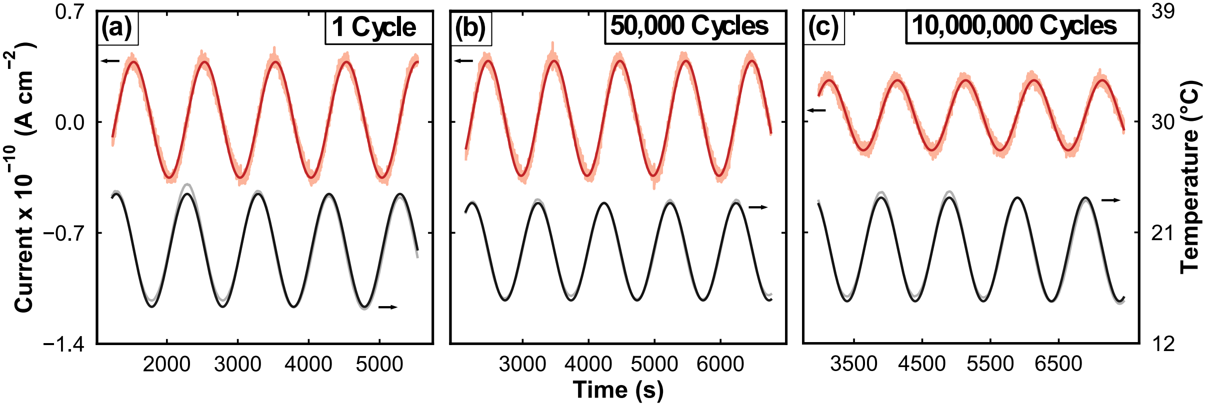

Figure 7.8. Pyroelectric current (light red, left axis) and temperature oscillation (light grey, right axis) and associated sinusoidal fits (dark red and black, respectively) measured on devices cycled with (a) 1, (b) 50,000, and (c) 10,000,000 bipolar pulses.

Given that the device that had been cycled with 10^7 waves was measured to have a significantly reduced P_{sw} of 0.62 μC cm^{-2}, the presence of a measurable pyroelectric current is evidence that a poled domain structure remains in the HZO layer in spite of the severe fatigue. It is hypothesized that the decrease in pyroelectric current with field cycling is due to the presence

of domains that are pinned in the poled-down direction and thus provide a current oscillation that partially cancels the response of the majority poled-up domains. Some decrease in the pyroelectric current could also be attributed to field-cycling related phase transformations from the orthorhombic to monoclinic phases, although this is not supported by the increasing high-field relative permittivity coinciding with fatigue. Thus, given that the pyroelectric current decreases with field cycling, but does not disappear completely, it is evident that domain pinning is a major contributor to the polarization decrease, and a domain structure persists in the device following complete fatigue. The derived pyroelectric coefficients are shown in Figure 7.9 along with the P_{sw} measured on each individual device. It is apparent that the 1000 μm-diameter devices on which pyroelectric measurements were performed have similar fatigue behavior to the 100 μm-diameter devices used for the previous electrical measurements. The pyroelectric coefficient was initially measured to be -11.5 μC $m^{-2}K^{-1}$. This value is consistent with previous measurements of the HZO system with sizable fractions of the monoclinic phase.[149] Upon wake-up the pyroelectric coefficient increased to -13.2 μC $m^{-2}K^{-1}$ and then decreased to -7.0 μC $m^{-2}K^{-1}$ through 10^8 cycles during fatigue. The fatigued pyroelectric coefficient represents a decrease of 39% from the initial value, while P_{sw} decreased by 95% for these devices.

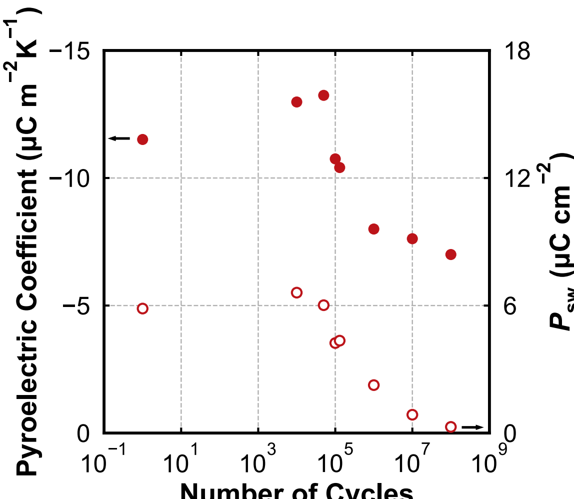

Figure 7.9. Pyroelectric coefficients (closed circles, left axis) and switchable polarizations (open circles, right axis) measured on devices cycled with various intervals of bipolar pulses.

To corroborate that the phases and phase fractions present within the RuO_2/HZO/RuO_2 structures remain essentially unchanged by fatigue, X-ray microdiffraction data were collected with an area detector on devices cycled with each interval of bipolar pulses. An example detector frame and unwarped 2D pattern are shown in Figure 7.10 for the singly poled device. Debye-Scherrer rings, which correspond to the RuO_2 electrodes, HZO layer, platinum contact, and MgO powder height alignment standard were present in each pattern. Each area detector pattern was integrated through all captured γ angles to produce 1D diffraction patterns[295] for devices pulsed at each cycling interval, as shown in Figure 7.11. Owing to the constrained beam footprint necessary to characterize the individual devices, the integrated counts for each pattern were too low to effectively fit and compare peak positions and intensities. Regardless, peaks corresponding to the superimposed (111) orthorhombic/(101) tetragonal and (111) monoclinic HZO reflections were indexed at 30.3° and 31.4°, respectively, while (110), (011), and (200) RuO_2 reflections were indexed at 28.1°, 35.2°, and 39.7°, respectively. A (111) MgO reflection, which was used for sample alignment, was indexed at 36.9°. All angles refer to the 2θ axis. Given the low integrated intensities and the presence of the intense (110) RuO_2 reflection overlapping the $(\bar{1}11)$ monoclinic HZO peak, quantitative phase fraction evaluations[295,296] were not possible. However, peaks consistent with all three HZO phases were observed regardless of the number of field cycles, and the relative intensity ratios of the (111) orthorhombic/(101) tetragonal to (111) monoclinic peaks appear to be qualitatively similar for each device. Thus, diffraction patterns indicate that the orthorhombic phase is likely present in the highly fatigued samples and its volume fraction is qualitatively consistent regardless of state of wake-up or fatigue. Further, the strong pyroelectric response in the fatigued devices is evidence that the orthorhombic phase remained present.

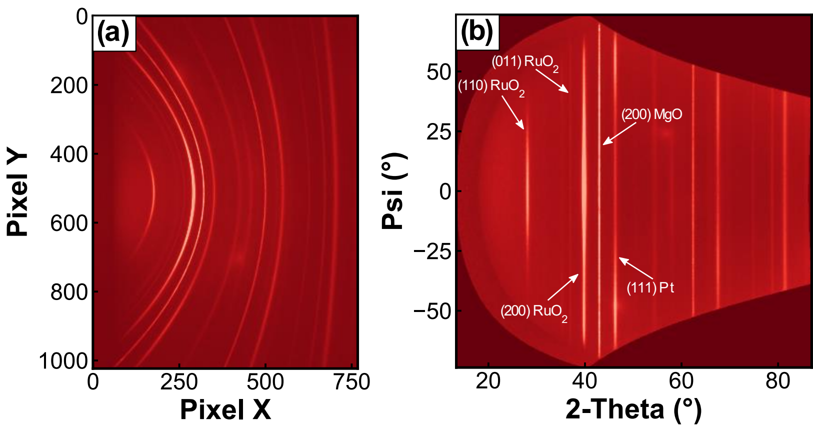

Figure 7.10. (a) Raw detector frame and (b) unwarped diffraction pattern measured on a singly poled device. Note that the intensities of the orthorhombic/tetragonal and monoclinic HZO peaks are too low to be easily discerned in the area detector pattern.

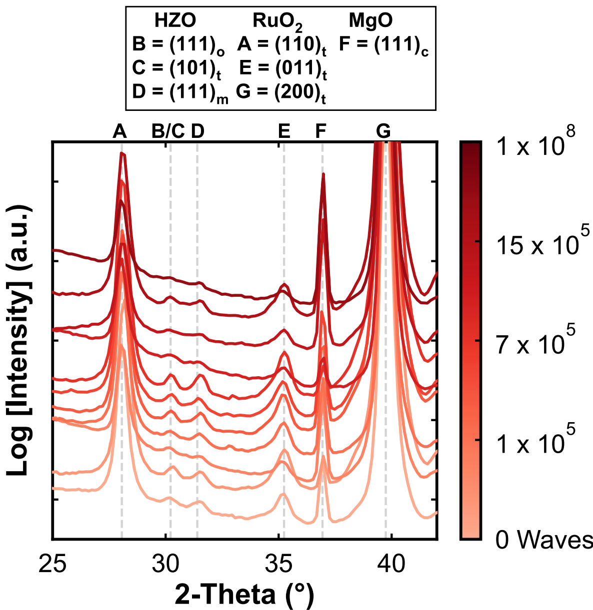

Figure 7.11. Diffraction patterns integrated from area detector patterns collected via microfocus XRD on individual devices following various intervals of bipolar waves, as indicated by the color bar on the right. Peak indices are provided above the plot and identified above the panel. A logarithmic intensity scale was used to increase the visibility of HZO peaks.

While domain pinning was found to be responsible for the observed polarization fatigue in these devices, the cause of the pinning was not revealed by polarization, relative permittivity, pyroelectric, or diffraction measurements. An increase in the number of point defects, which are known to be pinning centers for ferroelectric domains,[299] could be responsible for the observed increase in irreversible domain wall motion and polarization fatigue. Leakage current measurements have previously been utilized to estimate defect concentrations in other investigations[111,122] where the measured current is associated with trap-assisted tunneling occurring due to the presence of point defects. Larger leakage currents have been attributed to high defect concentrations.[173] Leakage current profiles measured following each field cycling interval on the HZO devices with RuO_2 electrodes are shown in Figure 7.12(a). Throughout the first 10^5 cycles, the leakage currents remain effectively at the noise level of the instrumentation, 10^{-7} A cm^{-2}. Following 10^5 cycles, however, the measured leakage currents increase, with a maximum measured at ~10^{-3} A cm^{-2} following 10^8 cycles and complete polarization fatigue. This trend is shown in Figure 7.12(b), in which the leakage current magnitudes at $\pm$ 2.5 MV cm^{-1} are plotted. The beginning of fatigue and the increase in irreversible domain wall motion coincide with an increase in leakage current, indicating that the increased energy barriers for domain motion may be caused by electrically active point defects. The specific chemistry of these point defects is not directly evident based upon the leakage current measurements. While the generation of oxygen vacancies is known to occur due to field cycling in HfO_2-based ferroelectrics,[171] the likelihood of these point defects remaining within the 20 nm-thick, fast-oxygen-ion conducting HZO layer[275] during field cycling is low given the conductive RuO_2 electrodes, which have been observed to mitigate interfacial oxygen vacancy buildup in other systems.[36] In tandem, the investigation of the fatigue behavior of HZO with an oxygen-blocking electrode, Pt, revealed that a phase transformation due to field cycling was causing the polarization decrease in the Pt/HZO/Pt devices.[296] Such a phase transformation was not observed in high-field relative permittivity or diffraction measurements in these devices. Furthermore, these devices were not observed to break down even after extensive cycling. These observations support the notion that oxygen vacancies, and their accumulation, may not be the point defects predominantly causing the polarization fatigue. Alternatively, electron accumulation at domain walls, known to both occur in and cause conduction in conventional perovskite oxide ferroelectrics,[300,301] may be responsible for the fatigue. Electron trapping at domain walls has been reported as a contributor to domain pinning

and fatigue in HfO_2-based ferroelectrics[127] via examination of activation energies for polarization regeneration, and is more likely to be causing the fatigue in these RuO_2/HZO/RuO_2 devices. While the exact nature of the accumulating defects can only be inferred based upon the electrode materials, a clear pyroelectric response was measured in devices that have near-zero switchable polarization. This data suggests that the devices maintain a spontaneous polarization, but that polarization cannot be switched due to domain pinning or domain seed nucleation inhibition.

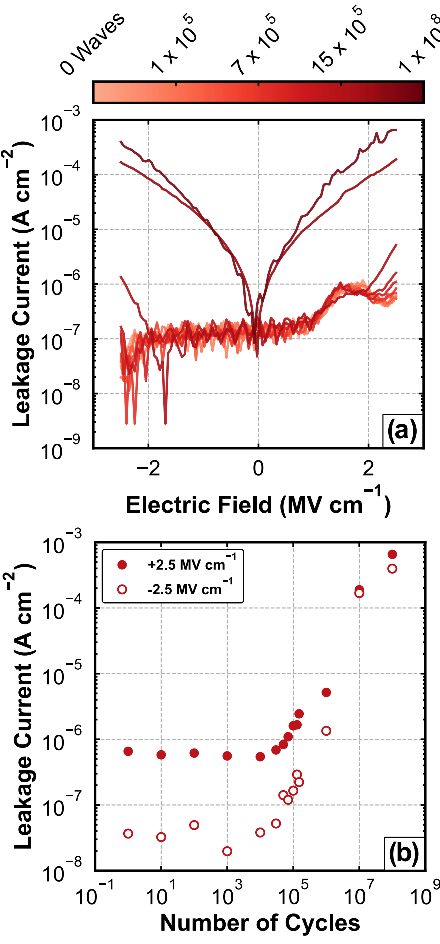

Figure 7.12. (a) Leakage current profiles measured on devices cycled at various intervals, as indicated by the color bar at the top of the panel. (b) Leakage current densities at ± 2.5 MV cm^{-1} extracted from leakage current profiles as a function of the number of field cycles.

7.6 Conclusions

In conclusion, the field cycling behavior and mechanisms leading to observed polarization wake-up and fatigue in RuO_2/HZO/RuO_2 ferroelectric devices have been investigated. Utilizing 50% duty cycle, 10 kHz, 2.0 MV cm^{-1} bipolar pulses, polarization wake-up, from P_{sw} = 4.26 μC cm^{-1} to 6.38 μC cm^{-1}, was observed through 10^3 cycles, followed by fatigue to ~0 μC cm^{-1} through 10^8 cycles. Pyroelectric coefficients increased from -11.5 $m^{-2}K^{-1}$ to -13.2 μC $m^{-2}K^{-1}$ during wake-up and then decreased to -7.0 μC $m^{-2}K^{-1}$ during fatigue through 10^8 cycles. The polarization wake-up, which coincided with a decrease in high field permittivity and increased pyroelectric coefficient, was determined to be related to a combination of domain depinning and transformations from the tetragonal to the orthorhombic phase, likely due to redistribution of point defects or transport of oxygen vacancies into the oxide electrodes. The polarization fatigue was shown to coincide with an increase in α', related to more irreversible domain wall movement. The pyroelectric coefficients were observed to decrease from -13.24 μC $m^{-2}K^{-1}$ to -7.0 μC $m^{-2}K^{-1}$, whereas the switchable polarization decreased to nearly zero. The finite pyroelectric coefficient indicates that fully fatigued devices contain an unswitchable domain structure and remained polar. The existence of the orthorhombic phase was qualitatively confirmed in devices cycled at each interval via microfocused XRD measurements, corroborating that the phase constitution necessary for pyroelectric response existed in the highly fatigued devices. Thus, domain pinning appears to be a significant factor in the fatigue of these RuO_2/HZO/RuO_2 devices. These observations reveal the origin of switchable polarization changes in HZO with RuO_2 electrodes due to field cycling while evaluating this electrode material for next-generation ferroelectric device implementation into silicon CMOS technology.

7.7 Acknowledgments

The authors wish to acknowledge Dr. Glen Fox for his guidance on application-relevant fatigue waveforms. This research is supported by the Laboratory Directed Research and Development program at Sandia National Laboratories (film growth and device preparation), the Semiconductor Research Corporation's (SRC) Nanomanufacturing Materials and Processes Program (material characterization, including X-ray diffraction and electrical measurements), the

U.S. National Science Foundation's Major Research Instrumentation program under grant CHE-2018870 (area detector X-ray diffractometer), and as part of the Center for 3D Ferroelectric Microelectronics (3DFeM), an Energy Frontier Research Center funded by the U.S. Department of Energy, Office of Science, Basic Energy Sciences under award number DE-SC0021118 (fatigue protocols and instrumentation). S.T.J. acknowledges support from the U.S. National Science Foundation's Graduate Research Fellowship Program under grant DGE-1842490. Sandia National Laboratories is a multimission laboratory managed and operated by National Technology and Engineering Solutions of Sandia, LLC, a wholly owned subsidiary of Honeywell International, Inc., for the U.S. Department of Energy's National Nuclear Security Administration under contract DE-NA0003525. This paper describes objective technical results and analysis. Any subjective views or opinions that might be expressed in the paper do not necessarily represent the views of the U.S. Department of Energy or the United States Government.

Chapter 8: Investigation of the Stresses Due to the Clamping Effect in Ferroelectric $Hf_{0.5}Zr_{0.5}O_2$ Thin Films with TaN Electrodes

The contents of this chapter currently being prepared for submission for publication with the following as authors:

Shelby S. Fields,[1] Samantha T. Jaszewski,[1] Truong Cai,[2] Alejandro Salanova,[1] Takanori Mimura,[1] Minseong Park,[3] Michael Cyberey,[3] Diane A. Dickie,[1,4] Helge H. Heinrich,[1] M. David Henry,[5] Kyusang Lee,[1,3] Patrick E. Hopkins,[1,6,7] Brian Sheldon,[2] and Jon F. Ihlefeld[1,3]

[1]Department of Materials Science and Engineering, University of Virginia, Charlottesville, Virginia, USA 22904

[2]Department of Engineering, Brown University, Providence, Rhode Island, USA 02912

[3]Charles L. Brown Department of Electrical and Computer Engineering, University of Virginia, Charlottesville, Virginia, USA 22904

[4]Department of Chemistry, University of Virginia, Charlottesville, Virginia, USA 22904

[5]Sandia National Laboratories, Albuquerque, New Mexico, USA 87185

[6]Department of Mechanical and Aerospace Engineering, University of Virginia, Charlottesville, Virginia, USA 22904

[7]Deparment of Physics, University of Virginia, Charlottesville, Virginia, USA 22904

The body of text of this chapter has been adapted to include the supplemental information and figures, where appropriate.

8.1 Motivation

Aside from affecting film oxygen content and field-cycling behavior, electrodes have also been reported to affect the stress state of processed HfO_2-based thin films and devices. Widely, the stress from mechanical confinement due to the top electrode is credited with enhanced stabilization of the orthorhombic phase during thermal processing, commonly referred to as the 'Clamping Effect.' Employing chemical, electrical, and structural analyses outlined in Chapters 4 – 7, the effects of the top electrode on the phases present following annealing of HfO_2-based films are investigated in this chapter. These techniques are employed to arrive at a mechanistic understanding of the clamping effect.

8.2 Abstract

The ‘Clamping Effect,’ frequently harnessed to enhance metastable ferroelectric orthorhombic phase fractions in HfO_2-based thin films, is typically ascribed to mechanical stress imparted on the film by annealing with a top electrode in place. However, a number of other important characteristics, including oxygen vacancy content and grain size, are electrode dependent and have also been shown to affect the phases present in the film following processing. In this work, the physical mechanisms driving the stabilization of the orthorhombic phase by the clamping effect in 20 nm-thick HZO films with TaN electrodes are investigated using chemical, structural, and stress measurements of samples processed with and without top electrodes, and which had the top electrode removed following processing. It is shown that the top electrode has a strong effect on the phases present and polarization responses of prepared films, but that these effects are not a result of differences in defect concentration, oxygen content, grain size, degree of densification, or crystallization temperature. Instead, the magnitudes biaxial stresses following processing are strongly different, as assessed using both $\sin^2(\psi)$ analyses and measurements of wafer flexure before and after processing. Using these stress measurement techniques in concert with top electrode removal experiments, it is shown that strains at the interface between the top electrode and ferroelectric layer can play a large role in the orthorhombic phase stabilization.

8.3 Introduction

HfO_2-based thin films have witnessed research and development for non-volatile memory,[2,232,245] negative differential capacitance field-effect transistor,[230,247] nonlinear optics,[82] and energy harvesting[149,185] applications following first reporting of their stable polarization hysteresis properties in thin films in 2011.[1] These properties have since been attributed to a metastable ferroelectric $Pca2_1$ orthorhombic phase,[1,87,92] which has been observed to have a coercive field of ~1.1 MV cm^{-1} [302] and calculated to have a theoretical spontaneous polarization of ~50 µC cm^{-2}.[87] This polar ferroelectric phase has been observed to be stabilized relative to the bulk, room temperature linear dielectric $P2_1/c$ monoclinic and high-temperature, field-induced ferroelectric $P4_2/nmc$ tetragonal phases through processing to produce small grain sizes,[90,99] inclusion of a variety of dopants,[1,3,124,303] imparting of biaxial stress,[115,116] and incorporation of

point defects.[111,117,122] Alloying with ZrO_2 ($Hf_{1-x}Zr_xO_2$, HZO), in particular, has been observed to yield a stable ferroelectric response through nearly the entire composition window ($0.0 < x < 0.8$).[3,149,195] The HZO material system is particularly attractive for device technologies owing to the scalability of the ferroelectric properties,[105,290] chemical compatibility of both HfO_2 and ZrO_2 with silicon,[75,77] and the presence of mature atomic layer deposition (ALD) processes in current fabrication facilities.

Since the first reports of ferroelectricity in HfO_2-based thin films, the presence of a capping layer, deposited on top of the dielectric before annealing, has been observed to enhance the resultant measured polarization response and orthorhombic phase fractions.[1,100] Early investigations of the top electrode-dependent polarization behavior suggested that the mechanical clamping from the top electrode, typically a metallic binary nitride such as TiN or TaN,[117] was absolutely necessary to stabilize the orthorhombic phase.[100,116,170] Subsequent investigations have since demonstrated stable ferroelectric polarization in thin films annealed without a capping top electrode.[138,303,304] Regardless, superior polarization performance and orthorhombic phase fractions are widely observed when HZO devices are processed with a top electrode in place,[151] with similar observations made for the Al and Y-doped HfO_2 thin film systems.[128,303] Such results associate the improved polarization response with the suppression of the transformation from the high temperature tetragonal phase to the room temperature monoclinic phase upon cooling from the crystallization temperature, yielding instead the orthorhombic phase due to mechanical confinement.[170]

The presence of the top electrode during annealing and resulting confinement may be anticipated to vary the stress state of the underlying dielectric layer.[305] Computational works have predicted enhanced orthorhombic phase stability due to biaxial and hydrostatic compressive stresses owing to a volumetric constriction during transformation from the high-temperature tetragonal to the room-temperature monoclinic phases.[87,96] Additionally, experimental works have demonstrated that biaxial tensile stresses yield domain structures which orient the short, polar *c*-axis perpendicular to the film surface, resulting in higher measured polarizations.[115,116,125] Thus, in HfO_2-based thin film systems, the ultimate effect of the imparted stress is a balance between the stabilization of the orthorhombic phase relative to the tetragonal and monoclinic phases and the orientation of the resulting domain structure.

While biaxial stresses imparted due to mechanical clamping are most commonly credited with impacting both the relative stability of the ferroelectric phase and the resulting domain structure within ferroelectric HZO thin films,[3,170] experimental works have also observed changes in grain size and microstructure associated with the presence of the top electrode.[306] Given that small grain sizes are widely observed to facilitate orthorhombic phase stabilization,[96] examination of composition and thickness-varied HZO devices have shown smaller grain sizes and higher polarizations in films thinner than 20 nm.[97] While, within this investigation, it was concluded that the presence of the top electrode did not influence the grain size of ~9.1 nm-thick HZO films, the effects of the top electrode presence during annealing on the grain size of the thicker films was not examined. In tandem, a separate study, which made atomic force microscopy (AFM) measurements of 4 nm-thick HfO_2 films, annealed with and without a TiN top electrode, reported that the presence of the top electrode resulted in smaller grain sizes and lower surface roughness. However, the annealing conditions selected in this referenced study, 400 °C in N_2 for 30 minutes, were widely different from the rapid thermal anneals typically utilized in processing of HfO_2-based ferroelectrics.[306] A more recent transmission electron backscatter diffraction (transmission-EBSD) investigation[101] of the phases present within a 10 nm-thick HZO film between TiN electrodes revealed large contents of the orthorhombic phase throughout the 10 - 50 nm equivalent diameter grain size distribution, with measurable quantities of the monoclinic phase present in grains with equivalent diameters in excess of 25 nm, confirming the influence of grain size on the phase constitution. Aside from effects of mechanical confinement-related stress and grain size distribution alteration due processing of the HZO with a top electrode, important chemical interactions between binary nitride electrodes and adjacent HZO layers[155,156,158,295] have also been identified which may affect the polarization response.

Oxygen vacancy content has been theoretically predicted[90] and experimentally demonstrated[110,111] to be an important factor in orthorhombic phase stabilization and resultant polarization response in HfO_2-based thin films. As such, deposition methods in which the ozone pulse length during ALD,[111,119] or oxygen flow during sputtering deposition,[103,110] have been optimized to yield large oxygen vacancy concentrations within the ferroelectric layers. Separate from ferroelectric layer deposition process optimization, interactions between these films and adjacent binary nitride electrodes have also been shown to affect the oxygen vacancy content and resultant polarization response.[295] Such electrode materials have been observed, using X-ray

photoelectron spectroscopy (XPS), to form oxynitride interlayers[119,155,295] at the electrode/dielectric interfaces due to scavenging of oxygen from the dielectric layer during processing.[156] This oxygen scavenging phenomenon has been shown to affect the defect content within the ferroelectric layer, and resulting phase constitution and polarization magnitude.[295] Thus, while the orthorhombic phase stabilization from the capping layer is typically attributed to imparted biaxial stress, chemical and microstructural interactions between the top electrode layer and the HfO_2-based ferroelectric may also contribute to this effect.

In this study, the chemical and physical interactions between the TaN top electrode and 20 nm-thick ferroelectric HZO are investigated electrically and structurally. The phases present within the HZO, and their post-processing biaxial stresses are characterized through area detector X-ray diffraction (XRD) measurements and $\sin^2(\psi)$ analyses. These biaxial stress values are compared with wafer flexure stress measurements, made after each processing step and during annealing, and high-temperature XRD measurements (HTXRD) to investigate how the biaxial stress evolves with processing of these HZO ferroelectrics. Separately, the effects of the top electrode on the resulting film densification, defect densities, and grain morphology within the processed devices are examined through XRR fitting, leakage current measurements, and analysis of scanning electron microscopy (SEM) micrographs. Through etching and stressing the top electrodes of fully processed devices, the important role of this layer in the stress state and phase within the HZO is revealed.

8.4 Experimental Procedures

Sample Preparation Procedures. TaN/HZO/TaN metal-ferroelectric-metal devices were prepared on 50.8 mm-diameter, 250 µm-thick, (001)-oriented silicon substrates. The 100 nm-thick planar TaN bottom electrodes were deposited via DC sputtering from a sintered TaN target with a power density of 3.3 W cm^{-2} under an argon background pressure of 5 mTorr in a 45° off-axis geometry. $Hf_{0.5}Zr_{0.5}O_2$ was next deposited using plasma-enhanced atomic layer deposition (PEALD) within an Oxford FlexAL II system at a temperature of 260 °C with tetrakis(ethylmethylamido)hafnium (TEMA Hf) and tetrakis(ethylmethylamido)zirconium (TEMA Zr) as HfO_2 and ZrO_2 precursors, respectively, and an oxygen plasma as the oxidant. Supercycles comprised of 5 cycles of HfO_2 and 5 cycles of ZrO_2 were utilized for deposition,

which yielded a film composition of $Hf_{0.37}Zr_{0.63}O_2$, measured via X-ray photoelectron spectroscopy (XPS) measurements made using a PHI Versaprobe III XPS system. Next, a planar 20 nm-thick TaN top electrode was deposited using the same conditions as the bottom electrode onto a subset of the HZO films. Samples prepared with and without a top electrode were then annealed at 600 °C within an Allwin21 AccuThermo 610 Rapid Thermal Processor for 30 seconds in a N_2 atmosphere. The temperature ramp and cooling rates were 50 and ~2 °C s^{-1} for this procedure, respectively. Following annealing, a subset of samples processed with the top electrode received 50 nm-thick palladium contacts, deposited via DC sputtering through a shadow mask. After, all samples with top electrodes were subjected to an SC-1 bath (5:1:1 H_2O:30% H_2O_2 in H_2O:30% NH_4OH in H_2O) for 45 minutes at 60 °C to remove the blanket top electrode layer. For the samples on which palladium was deposited, the contacts acted as a hard mask, yielding isolated TaN/HZO/TaN/Pd devices. On the samples that received only the blanket top electrode (which was etched following annealing) and samples that received no top electrode, 20 nm-thick TaN top electrodes and 50 nm-thick Pd contacts were deposited on to film surfaces through a shadow mask. Thus, in total, three sets of samples were prepared, a set that was processed without a top electrode (referred to as the 'No-TE' set for the remainder of the chapter), a set that was processed with a top electrode (referred to as the 'With-TE' set for the remainder of the chapter), and a set that was processed with a top electrode that was removed and replaced following annealing (referred to as the 'TE-Etched' set for the remainder of the chapter).

Electrical Characterization Procedures. Polarization-electric field ($P(E)$), positive up negative down (PUND), first order reversal curve (FORC), and switching current loop measurements were made using a Radiant Technologies Precision LC II Tester. Nested $P(E)$ measurements were made with maximum applied fields between 1.0 - 2.5 MV cm^{-1} with a period of 1 ms. Nested PUND measurements were made with maximum applied fields between 1.0 - 2.5 MV cm^{-1} with a pulse width 1 ms and a pulse delay of 1000 ms. FORC measurements were made between ± 2.5 MV cm^{-1} with a bias step size of 0.1 MV cm^{-1}, with the analysis completed using Matlab R2018a. Current loop measurements were made with a maximum applied field of 2.5 MV cm^{-1} with a 1 ms period. Capacitance-voltage (CV) measurements were carried out between ± 2.5 MV cm^{-1} with a 10 kHz, 50 mV AC oscillator using a Keysight E4980A LCR meter. Leakage currents were measured between ± 2.5 MV cm^{-1} using a Keysight B2901A

Precision Source Measure Unit. All measurements were completed before and after 5000 2.0 MV cm^{-1} square wave field cycles that were applied at a frequency of 1 kHz.

Structural Characterization Procedures. Grazing incidence X-ray diffraction (GIXRD) patterns were collected between 26 - 33° in 2θ using a Rigaku SmartLab diffractometer with Cu Kα radiation with the ω incident angle fixed at 0.7°. XRR patterns were collected between 0° and 5° in 2θ using the same instrument. Area detector X-ray diffraction patterns were collected using a Bruker D8 Venture diffractometer equipped with an Incoatec IμS 3.0 Cu Kα radiation source and a Photon III detector with ω incident angle fixed at 18°. For the area detector measurements, MgO powder was adhered to sample surfaces to act as a stress-free height alignment standard. The pyFAI fast azimuthal integration package[212] was utilized for area detector pattern unwarping, and LIPRAS[214] peak fitting software was utilized to fit all area detector line intensity profile and GIXRD patterns. XRR patterns were fit using GSAS-II software.[252] High-temperature XRD (HTXRD) measurements were collected in a Bragg-Brentano geometry between 25 – 600 °C and 26 - 33° in 2θ with 10 °C steps and a continuous 3 °C min^{-1} temperature ramp using a Malvern Panalytical Empyrean diffractometer using Cu Kα radiation, a GaliPIX detector, and a Anton Parr HTK 1200N High-Temperature Oven-Chamber. Wafer flexure measurements were completed following each processing step utilizing a Bruker DektakXT stylus profilometer. Scanning electron microscopy (SEM) measurements were performed with and transmission electron microscopy (TEM) foils were prepared using a Thermo Fisher Scientific dual-beam Helios UC G4 SEM/FIB. Secondary electron micrographs were captured with a 20 kV accelerating voltage and 30 μs dwell time, whereas foil liftouts were completed using a gallium ion beam following platinum deposition to protect the sample surface. High-Angle Annular Dark Field (HAADF) TEM micrographs and energy dispersive X-ray spectra (TEM-EDS) were captured using a Thermo Fisher Scientific Themis Z-STEM operating at 200 kV and equipped with an Ulti-Monochromator. For additional etching experiments to isolate stress from chemical effects, top electrodes were partially and fully removed using a fluorine-based reactive ion etch (RIE) procedure in a PlasmaTherm VersaLine inductively coupled plasma etcher. While etching, the pressure was held at 10 mTorr, while 40 sccm of SF_6 and 10 sccm of argon gases were flowed. A 1200 W, 2 MHz coil power was utilized and a 13.56 MHz substrate bias of 30 W produced an etch rate of 27 nm min^{-1} for TaN with selectivity against HZO.

8.5 Results and Discussion

Comparison of Electrical Properties of Prepared Devices. Nested hysteresis ($P(E)$) loops measured on each pristine device, shown in Figure 8.1(a-c), reveal a strong dependence of polarization responses on the presence of the top electrode. Devices annealed with top electrodes (With-TE, TE-Etched) both exhibit larger polarizations than the No-TE device, which is consistent with results reported by other investigators.[1,151] Regardless of the presence of the top electrode, all polarization responses show saturation, suggesting low leakage current contributions. Comparing both samples processed with top electrodes, the hysteresis loops measured on the With-TE device are more pinched than those measured on the TE-Etched sample, which is suggestive that it contains more antiferroelectric-like tetragonal phase. The remanent polarization values (P_r, extracted from PUND measurements) measured on each of these pristine devices confirm this trend: the lowest P_r of 8.8 μC cm^{-2} was measured on the No-TE device, whereas the highest P_r of 17.5 μC cm^{-2} was measured on the TE-Etched device and a P_r of 14.1 μC cm^{-2} was measured on the With-TE device that demonstrated pinched $P(E)$ behavior. Analogous $P(E)$ measurements performed after 5000 1 kHz, 2.0 MV cm^{-1} square waves, plotted in Figure 8.1(d-f), show that all three devices experienced polarization wake-up. The awoken $P(E)$ responses of devices processed with top electrodes similarly reveal larger polarizations than the response of the sample prepared without one. However, in contrast to the measurement performed on the pristine device, the $P(E)$ response measured on the With-TE device is no longer pinched, and the responses measured on the awoken With-TE and TE-Etched devices are nearly identical. The identical polarization responses are evidence that the films contain essentially equivalent amounts of the orthorhombic phase following wake-up, which occurs in HfO_2-based ferroelectrics via oxygen vacancy redistribution, resulting in domain depinning[172,175] and transformations from the tetragonal to the orthorhombic phase.[154,296]

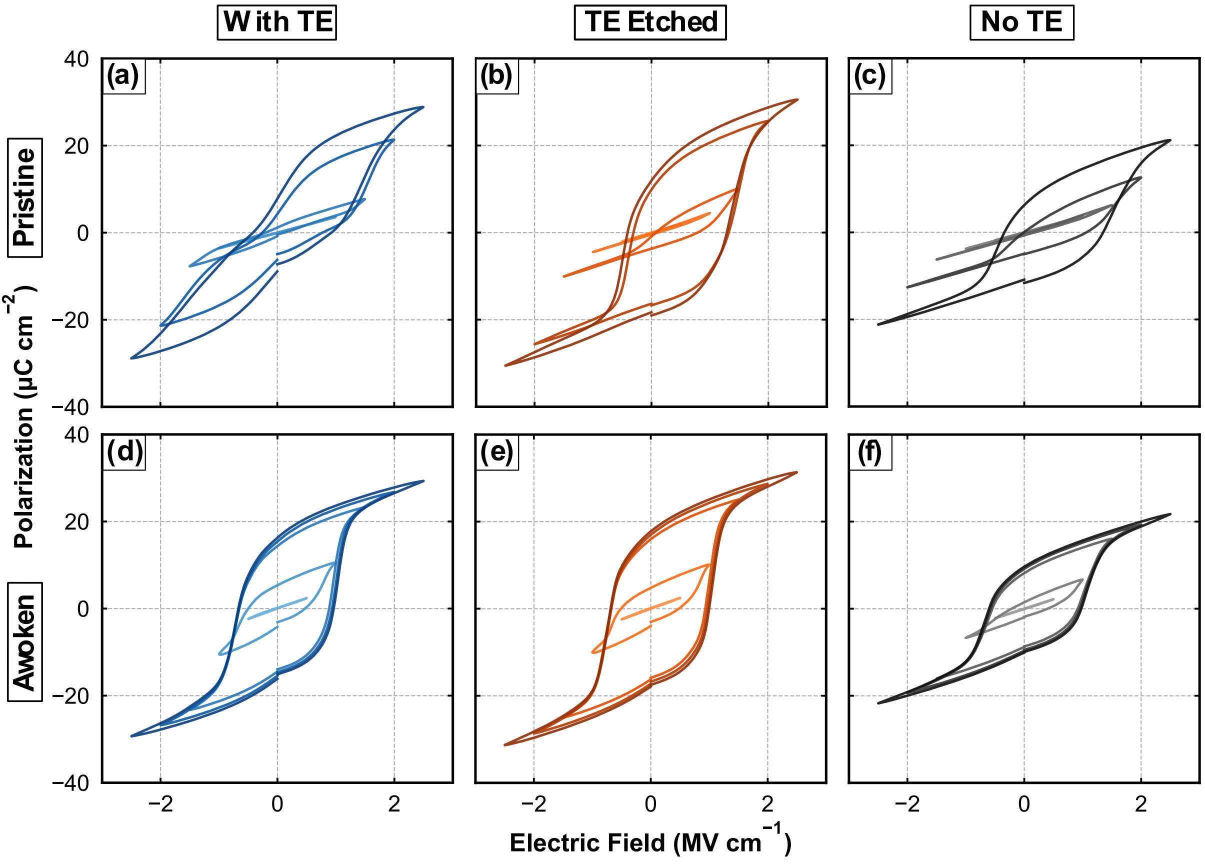

Figure 8.1. Nested $P(E)$ responses measured on pristine (a) With-TE, (b) TE-Etched, and (c) No-TE devices and awoken (d) With-TE, (e) TE-Etched, and (f) No-TE devices.

First order reversal curve (FORC) measurements, which have been utilized to characterize domain dynamics in HfO_2-based ferroelectrics,[178,307] were carried out to further examine the evolution of the switching behavior between the With-TE, TE-Etched, and No-TE devices. Starting at a field of -2.5 MV cm^{-1}, polarization profiles were measured up to a reversal field (α) of 2.5 MV cm^{-1} with a step size of 0.05 MV cm^{-1}. The switching density at each measurement and reversal field, $\rho(\alpha, \beta)$, was then obtained utilizing Equations 8.1 and 8.2:[63]

$$F(\alpha,\beta) = P_{\alpha} - P_{\alpha\rightarrow\beta} \quad 8.1$$

$$\rho(\alpha,\beta) = - \frac{\partial^2 F(\alpha,\beta)}{\partial\alpha\partial\beta} \qquad 8.2$$

Where $F(\alpha,\beta)$ is the difference between the polarization throughout the reversal sweep of the measurement branch ($P_{\alpha\rightarrow\beta}$) and the polarization at the reversal field for the branch (P_{α}), and $\rho(\alpha,\beta)$ is the switching density. For the derivative calculations, the data were binned with a width of 0.05 MV cm^{-1}, which was the step size of the lowest resolution measurement.

Measurements completed on the pristine devices are shown in Figure 8.2(a-c). Once again, the No-TE device yielded the lowest switching density response, as evidenced by the weakest switching peak, while the TE-Etched and With-TE devices yielded stronger switching density responses. However, due to the pinching observed in the $P(E)$ response, the With-TE switching peak is more diffuse than that measured on the TE-Etched device. The switching peak in the pristine With-TE measurement spans 1.0 MV cm^{-1} in α, which is larger than the switching peak in the TE-Etched measurement, which spans 0.5 MV cm^{-1}. Separated switching peaks are evidence of multiple coercive fields, which is a characteristic of an antiferroelectric-like polarization response.[308] Thus, the diffuse switching peak in the With-TE FORC response supports that this film contains more tetragonal phase than the TE-Etched film. Equivalent measurements made following wake-up, shown in Figure 8.2(d-f), once again confirm that the films undergo wake-up with cycling, as evidenced by the sharper, more intense switching density peaks. The With-TE and TE-Etched FORC responses measured on cycled devices appear essentially identical and demonstrate stronger switching responses than the measurement made on the No-TE film, in agreement with hysteresis responses. Thus, electrical responses measured before and after field cycling and wake-up confirm that the presence of the top electrode increases the polarization response of the resulting device. While the etching process appears to reduce hysteresis loop pinching in the pristine state, the awoken With-TE and TE-Etched devices have nearly identical polarization and FORC responses.

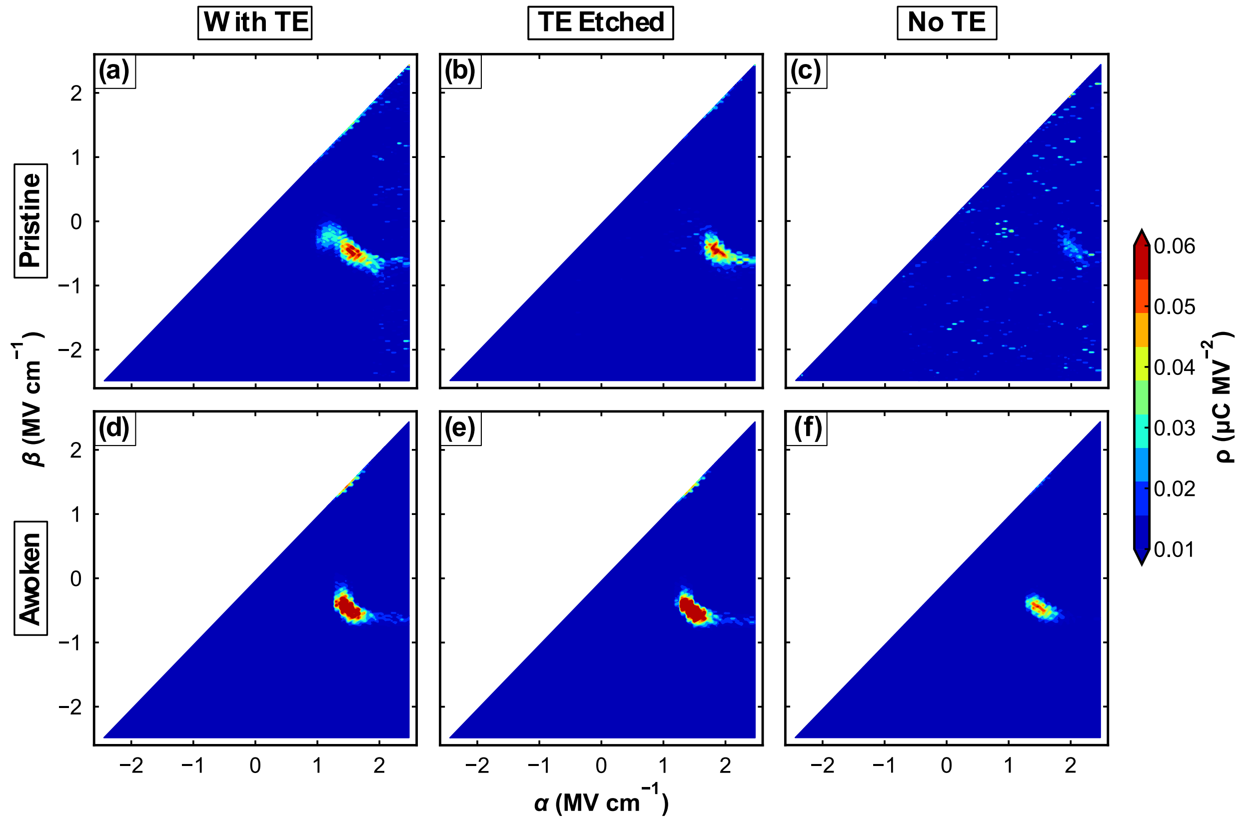

Figure 8.2. FORC measurements made on pristine (a) With-TE, (b) TE-Etched, and (c) No-TE samples and on awoken (a) With-TE, (b) TE-Etched, and (c) No-TE samples.

To further investigate differences in electrical properties between the samples, CV measurements were carried out on the pristine and awoken devices, as plotted in Figure 8.3(a-b), respectively. Permittivities measured on the pristine devices, plotted in Figure 8.3(a), support that all three films all comprise predominantly the tetragonal and orthorhombic phases, as evidenced by the values being larger than the 15 – 24 magnitudes typically reported for HZO films with large monoclinic phase contents.[3,283,309] The With-TE permittivity magnitudes are larger than those measured on the TE-Etched and No-TE films, which is indicative of larger contents of the higher permittivity tetragonal phase.[154] Further, the inhomogeneous switching observed in $P(E)$ loop and FORC measurements due to the partially antiferroelectric-like polarization response in the pristine With-TE film is also displayed in the pinching present vicinity of the positive coercive field in its accompanying CV measurement. Analogous CV measurements made following field cycling, plotted in Figure 8.3(b), show a reduction in permittivity magnitudes, which is consistent with

polarization wake-up.[154,296] Similar to what was observed in the $P(E)$ and FORC polarization measurements made following field cycling, the pinching of the CV response in the vicinity of the positive coercive field in the pristine With-TE sample does not persist following cycling. However, while the $P(E)$ and FORC responses of the With-TE and TE-Etched devices are virtually identical following wake-up, the permittivity magnitudes measured for the awoken With-TE film are 1.5 - 3 higher than the magnitudes measured for the TE-Etched film. The lower permittivity magnitude in the TE-Etched film indicates that this film may contain a greater of the lower permittivity monoclinic phase than the With-TE film.[154]

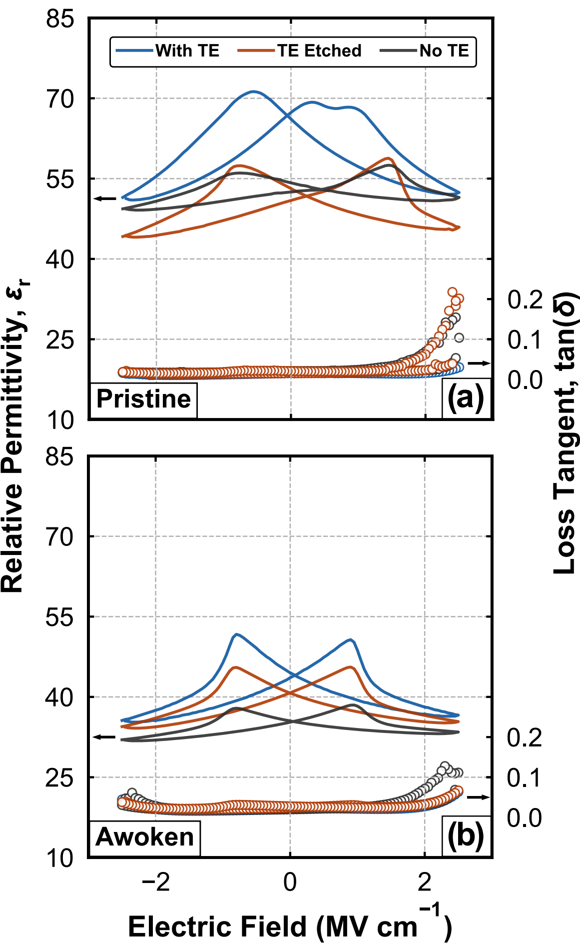

Figure 8.3. CV permittivity (left axis, lines) and loss tangent (right axis, open points) made on (a) pristine and (b) awoken With-TE (blue), TE-Etched (orange), and (c) No-TE (grey) films.

Analysis of Phase Constitutions. GIXRD patterns measured on fully processed With-TE, TE-Etched, and No-TE devices, shown in Figure 8.4, reveal differences in phase constitutions in all three samples. The pattern measured on the No-TE film contains peaks at 28.5°, 30.7°, and 31.7° in 2θ corresponding to the $(\bar{1}11)$ monoclinic (m_1), superimposed (101) tetragonal/(111) orthorhombic (t + o), and (111) monoclinic (m_2) reflections, respectively. The pattern measured on the TE-Etched film exhibited a strong t + o peak, a weak m_2 peak, and a m_1 peak only slightly above the background level. The pattern measured on the With-TE film contained a strong t + o peak and a m_2 peak only slightly above the background level. Integrated intensities for each peak were calculated, through fitting of Pearson VII shapes, and compared to estimate the relative quantities of the t + o phase in each film using Equation 8.3:

$$f_{\mathrm{t+o}} = \frac{I_{\mathrm{t+o}}}{I_{\mathrm{t+o}} + I_{\mathrm{m_1}} + I_{\mathrm{m_2}}} \qquad 8.3$$

Where $I_{\mathrm{t+o}}$, $I_{\mathrm{m_1}}$, and $I_{\mathrm{m_2}}$ are the integrated intensities of the t + o, m_1, and m_2 diffraction peaks, respectively, and $f_{\mathrm{t+o}}$ is the t + o phase fraction. Using this calculation, quantitative t + o phase fractions within each sample can be compared. These fractions were determined to be 0.98 ± 0.01, 0.90 ± 0.01, and 0.62 ± 0.03 for the With-TE, TE-Etched, and No-TE films, respectively. Thus, by comparison, the No-TE film contains less t + o phase than the With-TE and TE-Etched films, which supports the trends observed from polarization measurements. Moreover, the increase in m_1 and m_2 intensity between the With-TE and TE-Etched samples, and corresponding decrease in $f_{\mathrm{t+o}}$, is evidence that the top electrode removal process has increased the amount of monoclinic phase in the TE-Etched film. This increase in the amount of monoclinic phase due to etching would require a corresponding reduction in the amount of the orthorhombic and/or tetragonal phases in this film. The lower permittivities and reduction in hysteresis pinching observed when comparing data from the TE-Etched and With-TE films suggests that the monoclinic phase produced by removing the top electrode is, at least partially, due to a transformation from the tetragonal phase, and the identical polarizations measured on both samples following wake-up is indicative that both contain the similar amounts of orthorhombic phase.

However, changes in permittivity can be attributed to factors besides phase transformations and the wake-up process is known to occur, in part, due to phase transformations from the tetragonal to the orthorhombic phase.[296] Therefore, while changes in permittivity and polarization behavior are consistent with a phase transformation mostly between the tetragonal and monoclinic phases, transformations between the orthorhombic and monoclinic phases cannot be completely dismissed.

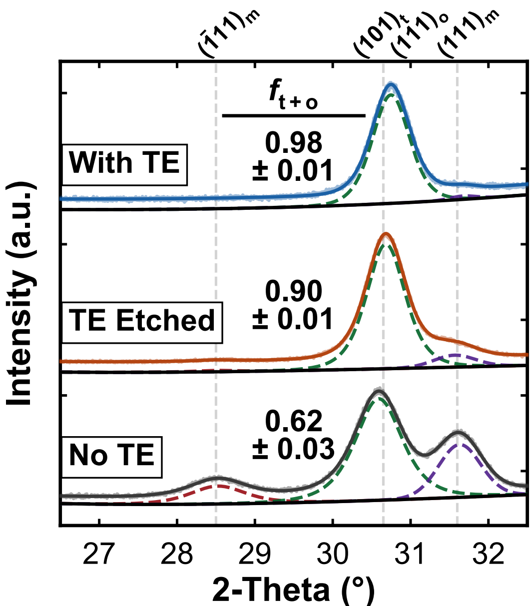

Figure 8.4. GIXRD patterns measured on the No-TE (grey), TE-Etched (orange), and With-TE (blue) films. The fits for each observed ($\bar{1}11$) monoclinic (red dotted line), t + o (green dotted line) and (111) monoclinic (purple dotted line) peak and fit background (black line) are offset below each corresponding pattern. The indexing for each observed peak is indicated by grey vertical dotted line and listed above the panel, and the calculated t + o fraction is indicted to the left of each corresponding pattern.

The presence of more intense monoclinic reflections in the TE-Etched diffraction pattern, lower permittivity, and more homogeneous polarization switching in the pristine TE-Etched film compared to the pattern and responses measured on the With-TE film indicates that the removal of the top electrode affects the phase constitution in the HZO, possibly via a transformation from

the tetragonal to the monoclinic phases. Given that the SC-1 process involves exposure of the film surface to an oxidizing $NH_3OH/HOOH/H_2O$ solution at 60 °C, and that the phase constitution in HfO_2-based thin films is sensitive to oxygen content,[110] it is possible that the top electrode removal affected the HZO chemistry. To examine if the etch was responsible for changing the chemistry of the TE-Etched film, the sample was re-exposed to the SC-1 procedure identical to that utilized to remove the top electrode. The GIXRD patterns measured on the original TE-Etched and re-exposed TE-Etched (Re-exposed) films, compared in Figure 8.5, reveal no difference in phase constitution. The t + o phase fraction for the re-exposed film was calculated to be 0.89 ± 0.01, which is identical to the fraction calculated for the original TE-Etched film. Thus, the extended exposure of the surface of the HZO to the oxidative solution does not appear to be responsible for the change in phase.

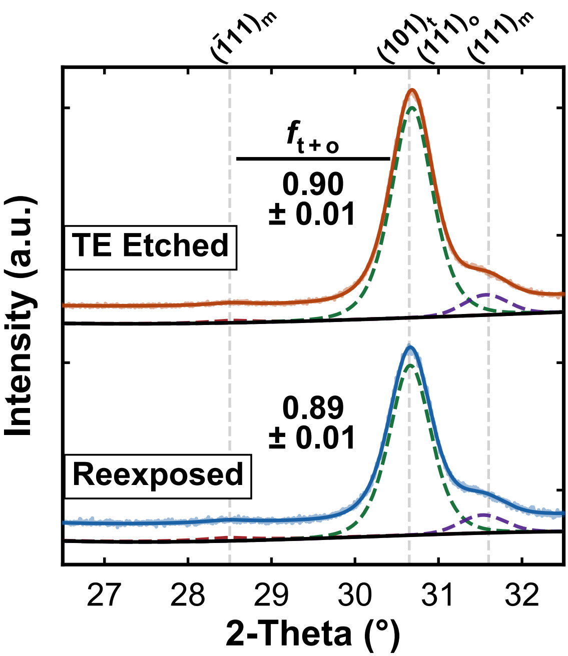

Figure 8.5. GIXRD patterns measured on the TE-Etched (orange) and re-exposed (blue) films. The fits for each observed ($\bar{1}$11) monoclinic (red dotted line), t + o (green dotted line) and (111) monoclinic (purple dotted line) peak and fit background (black line) are offset below each corresponding pattern. The indexing for each observed peak is indicated by grey vertical dotted line and listed above the panel, and the calculated t + o phase fraction is indicted to the left of each corresponding pattern.

For a further investigation of the effects of top electrode removal on the phase constitution in the HZO layers, the With-TE samples were also processed using a RIE to partially and fully remove the top TaN layer. The RIE process presents different oxidative conditions than the SC-1 wet etch procedure, and is capable of selectively and partially removing the 20 nm top electrode layer. In Figure 8.6, the GIXRD patterns measured on the original With-TE, a With-TE film that has had 15 nm of the top TaN electrode removed via RIE (Partial RIE), and a With-TE film that has had the top TaN electrode removed completely via RIE (Full RIE) are compared. The t + o phase fractions calculated following the partial and full removal of the top electrode using the RIE process were 0.94 ± 0.01 and 0.88 ± 0.01, respectively. The fraction calculated for the Full RIE sample is identical to both the TE-Etched and Re-exposed films, and the fraction calculated for the Partial RIE film falls between the With-TE and fully etched films. These different etch procedures

indicate that the increase in monoclinic phase composition occurring during removal of the top electrode is not related to a change in oxygen content in the HZO and is, therefore, related to a change in the mechanical boundary conditions.

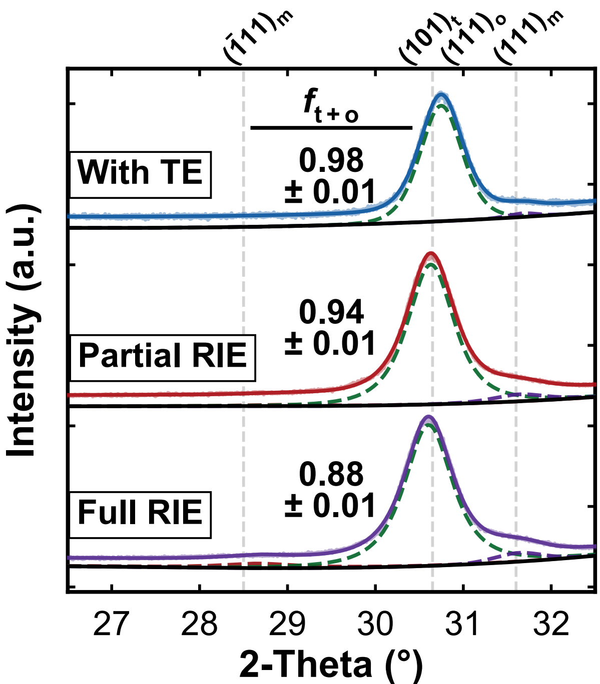

Figure 8.6. GIXRD patterns measured on the With-TE (blue), Partial RIE (red), and Full RIE (purple) films. The fits for each observed $(\bar{1}11)$ monoclinic (red dotted line), t + o (green dotted line) and (111) monoclinic (purple dotted line) peak and fit background (black line) are offset below each corresponding pattern. The indexing for each observed peak is indicated by grey vertical dotted line and listed above the panel, and the calculated t + o phase fraction is indicted to the left of each corresponding pattern.

Comparison of Chemical Properties of Prepared Devices. While changes in oxygen content between the With-TE and TE-Etched samples do not appear to be driving the transformation to the monoclinic phase resulting from electrode etching, such variations related to processing with or without the top electrode could be contributing to the clamping effect. To examine differences in defect concentration and oxygen content due to the presence of the top

electrode during processing, leakage current and transmission electron microscopy – energy dispersive X-ray spectroscopy (TEM-EDS) measurements were carried out. While direct examination of defect concentrations in HfO_2-based thin films is experimentally difficult, leakage current measurements have been employed to provide an estimation of these quantities.[111,295] Leakage current in ferroelectric HfO_2-based thin films has been attributed to the presence of point defects, such as oxygen vacancies[111,122] or trapped electrons,[127,309] which enable the flow of electrons via trap-assisted tunneling where the point defects act as traps.[121,173] Thus, larger leakage currents are indicative of greater defect concentrations.[111] Leakage current measurements of pristine and awoken With-TE, TE-Etched, and No-TE devices, shown in Figure 8.7(a-b), reveal similar leakage current profiles following cycling for all three devices. In the pristine state, different asymmetries are present in the data. These are likely related to the different processing conditions and asymmetric interfaces and prevent direct comparisons. Following field cycling, the leakage current profiles are more similarly asymmetric and are of identical magnitudes. Thus, qualitatively, the presence of the top electrode and its removal does not appear to have a significant impact on the defect concentrations in the samples.

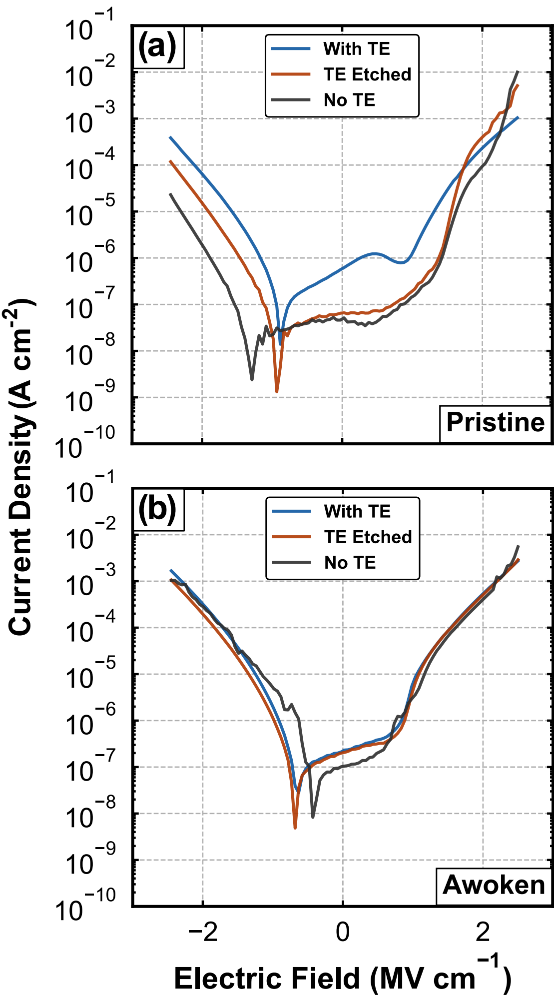

Figure 8.7. IV measurements made on (a) pristine and (b) awoken With-TE (blue), TE-Etched (orange) and No-TE (grey) devices.

The similar defect concentrations, particularly between the With-TE and No-TE samples is indicative that the HZO films have similar oxygen contents regardless of whether the top electrode was in place during processing. To further examine the stoichiometry of these two samples, TEM-EDS profiles were measured across the film thicknesses, as shown in Figure 8.8(a-d). High-Angle Annular Dark Field (HAADF) TEM micrographs captured on the With-TE and No-TE films, shown in Figure 8.8(a-b), were utilized to confirm film thicknesses of 20 nm and reveal the presence of ~1 nm TaO_xN_y interlayers separating the HZO layers and TaN electrodes, which form due to oxygen scavenging during thermal processing.[117,155,295] EDS profiles, shown in Figure 8.8(c-d) for the With-TE and No-TE samples, respectively, were

measured with a width of 10 nm across film thicknesses. By averaging the Hf, Zr, and O atomic fractions within the middle 5 nm of each film, compositions of $Hf_{0.43 \pm 0.07}Zr_{0.56 \pm 0.06}O_{1.34 \pm 0.04}$ and $Hf_{0.40 \pm 0.03}Zr_{0.60 \pm 0.06}O_{1.25 \pm 0.07}$ were determined for the With-TE and No-TE samples, respectively. While EDS measurements cannot reliably quantify oxygen content without a suitable standard, the Hf:Zr ratio for both of the samples is the same within error, which would be expected given that they were prepared with nominally identical deposition conditions, and both films are oxygen deficient, which is consistent with other studies of the oxygen content of HfO_2-based thin films with large contents of the orthorhombic phase.[110,111] Therefore, the film defect concentrations and stoichiometries are similar or identical regardless of the presence of the top electrode during processing insofar as these characteristics can be compared using leakage current measurements and TEM-EDS.

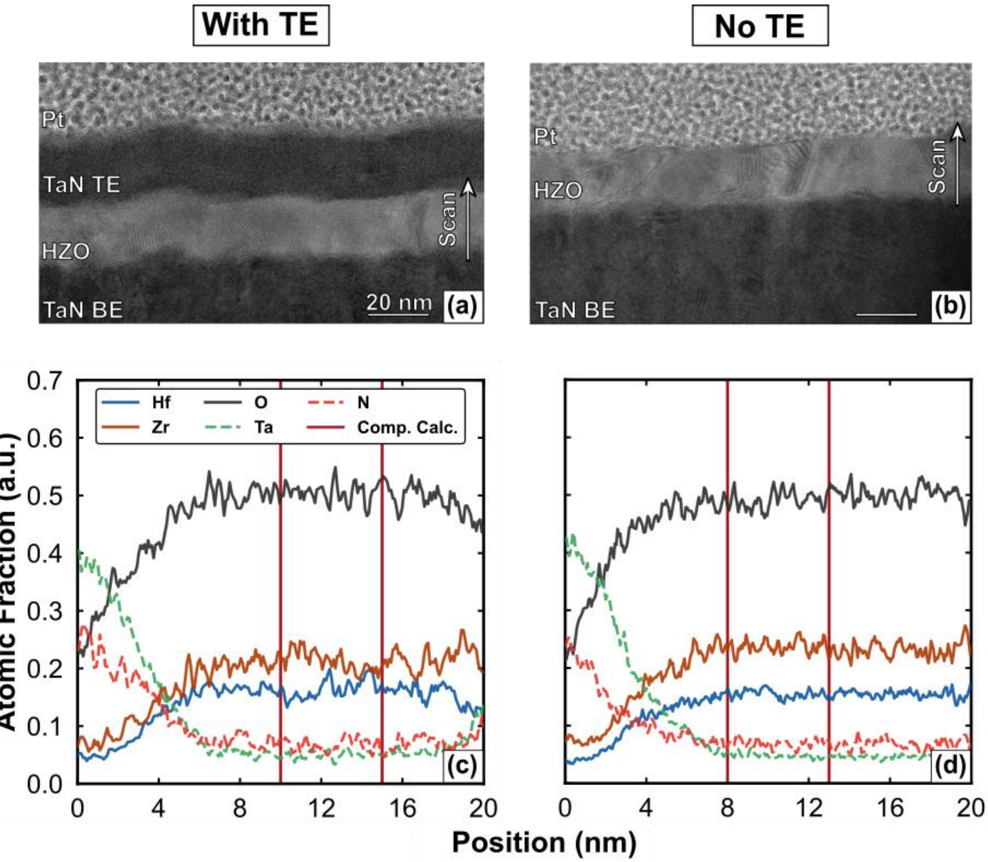

Figure 8.8. TEM micrographs measured on the (a) With-TE and (b) No-TE films. The layer materials are indicated on the left of each micrograph, and the scale bars and scan directions are provided on the right. EDS compositions measured for the Hf (blue line), Zr (red line), O (grey line), Ta (green dotted line), and N (red dotted line) species across the (c) With-TE and (d) No-TE films. The regions averaged to calculate $Hf_xZr_yO_z$ compositions (Comp. Calc.) for both samples are indicated with solid red vertical lines.

Effects of Top Electrode on Film Microstructure. While the presence of the top electrode was not observed to affect the defect concentration and oxygen content of the processed films, it may possibly affect the HZO grain sizes.[306] Such a change could potentially affect the phase constitution given the lower surface energy of the orthorhombic phase compared to the monoclinic,[90,96,97] and thus contribute to the clamping effect. To examine if the presence of the top electrode during thermal processing affects the HZO grain sizes of processed devices, grain intercept analyses were carried out on SEM micrographs captured on the With-TE and No-TE

films. Plan-view micrographs of the TE-Etched and No-TE films, shown in Figure 8.9(a-b) reveal similar grain sizes regardless of top electrode presence. The ASTM standard E112 grain size measurement procedure utilized for this analysis yielded average linear intercepts of 23 ± 1 nm and 22 ± 1 nm for the TE-Etched and No-TE films, respectively. In tandem, inspection of TEM micrographs measured on both of these samples, shown in Figure 8.8(a-b), reveal columnar structures and identical thicknesses (20 nm-thick), supporting that plan-view measurements present valid estimations for grain sizes. Based on the small variance between the two grain sizes, differences in film phase or polarization related to size effects would not be anticipated.[90,101]

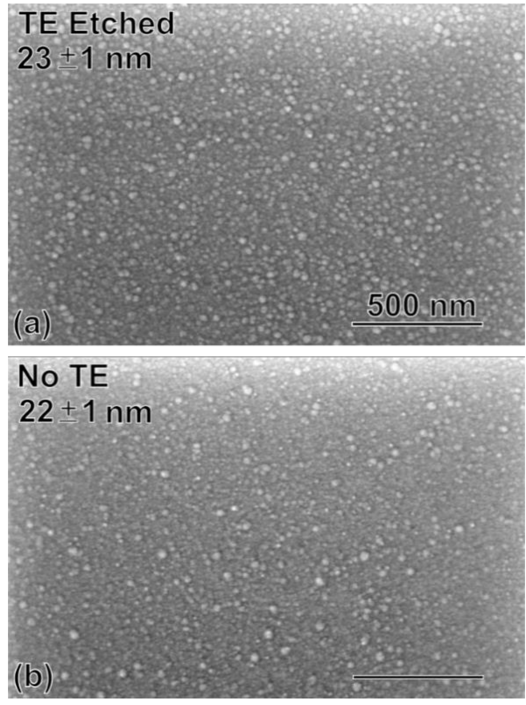

Figure 8.9. Plan-view SEM micrographs taken on (a) TE-Etched and (b) No-TE films. The results of grain size measurement are listed in the upper left of each panel.

Separate from direct examinations of the grain sizes of processed devices, high-temperature X-ray diffraction (HTXRD) patterns were collected on the With-TE and No-TE samples to assess effects of the top electrode on film crystallization temperature. A difference in crystallization temperature dependent on the top electrode presence could contribute to the

clamping effect given that the monoclinic and tetragonal/orthorhombic phases have been reported to crystallize under different thermal budgets.[140] Therefore if the top electrode reduced the crystallization temperature, larger tetragonal and orthorhombic phase compositions would be facilitated. Shown in Figure 8.10(a-b) are HTXRD measurements of the With-TE and No-TE samples. In both patterns, crystallization for the t + o phases was observed to begin at 390°C, regardless of top electrode presence. While the With-TE film demonstrated diffracted intensity corresponding to only the t + o reflection, peaks corresponding to the monoclinic phase were observed starting at 400 °C in the No-TE film. Intensity slightly above the background level is observed in the m_2 peak position in the patterns measured on the With-TE film at 600°C, which is consistent with the room-temperature GIXRD pattern measured on this film following processing. Based upon comparison of these two measurements, the crystallization temperature is unaffected by the presence of the top electrode in the HZO films whereas the nucleating phases are different.

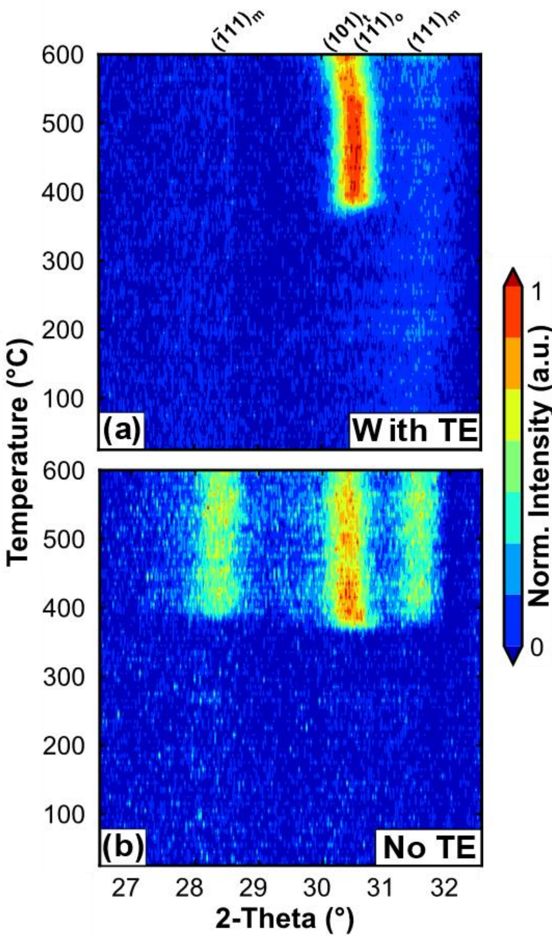

Figure 8.10. HTXRD patterns collected on (a) With-TE and (b) No-TE samples. Indexing for each of the observed peaks is indicated above the plots, and the colors corresponding to the normalized intensities are provided to the right.

Given that crystallization of HZO films from amorphous states occurs with a concomitant increase in film density,[283] and that the difference in crystalline phase volume contributes to the free energy differences between the phases,[87] fitting of X-ray reflectivity (XRR) patterns measured on With-TE, No-TE, and amorphous films was undertaken to determine if the degree of densification during annealing varied due to the presence of the top electrode. Shown in Figure 8.11(a-c) are XRR patterns and associated fits measured on an amorphous TaN/HZO sample (Pre-Anneal), the TE-Etched sample, and the No-TE sample. Utilizing the XRR fits, film densities were extracted. Before annealing, the amorphous HZO film was observed to have a density of

7.05 ± 0.02 g cm^{-3}. Identical densities of 7.35 ± 0.02 g cm^{-3} were fit for both the TE-Etched and No-TE samples following their processing. This difference constitutes a +4.2% densification in the HZO. This densification coincided with a decrease in HZO thickness from 20.4 ± 0.1 nm for the amorphous film, to 19.8 ± 0.1 nm for both of the crystallized films. It should be noted that a densification of +2.0% was also observed in the TaN bottom electrode by separately rapid thermal annealing a 100 nm-thick TaN layer on a silicon substrate, with the measured pattern and associated fit shown in Figure 8.12. While this HZO and TaN densification suggests that the films should be in a tensile stress state, owing to clamping to a rigid single crystal substrate following their thermal processing, it does not clearly show that the presence of the top electrode affects the degree to which the films densify.

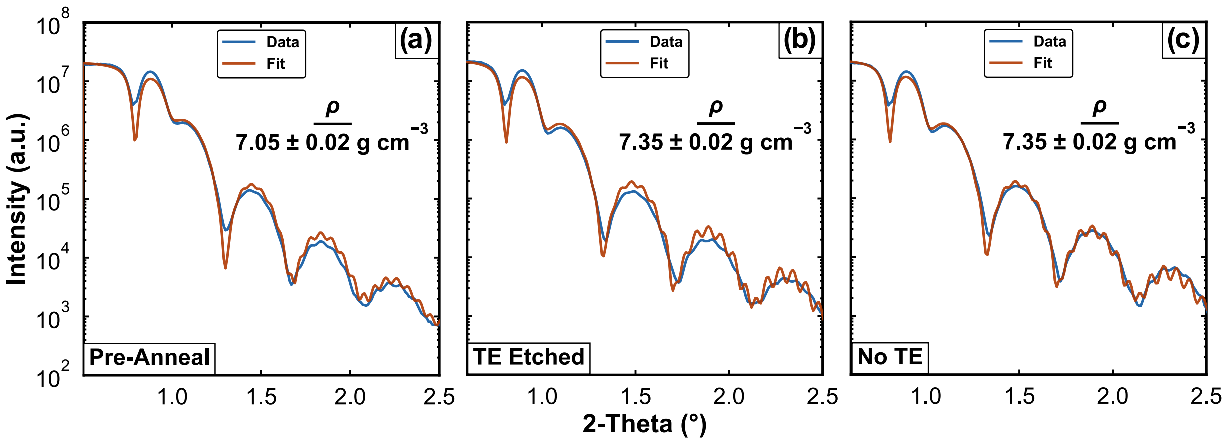

Figure 8.11. XRR patterns (blue lines) and associated fits (orange lines) corresponding to (a) an unannealed TaN/HZO sample, (b) the With-TE sample, and (c) the No-TE sample. The XRR-fit HZO density is indicated in each respective panel.

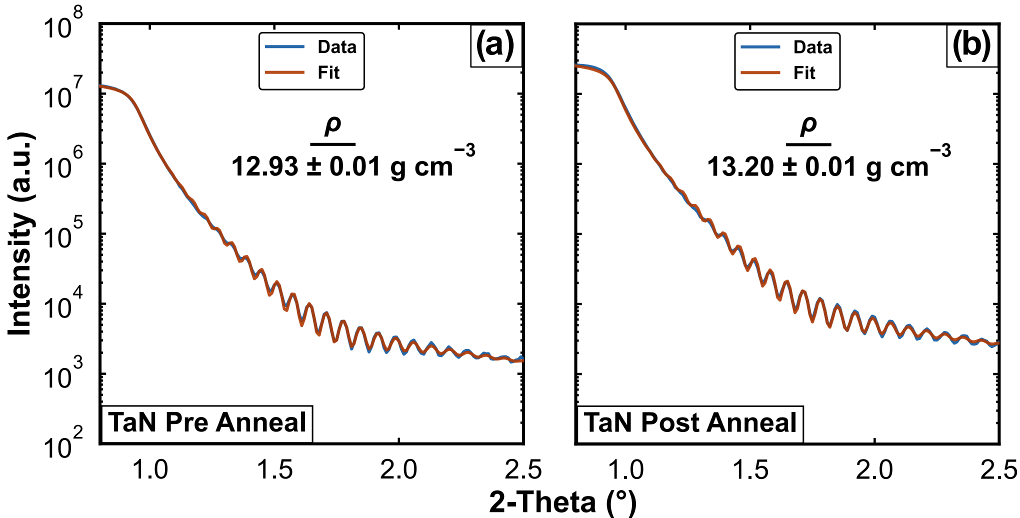

Figure 8.12. XRR patterns (blue lines) and associated fits (orange lines) corresponding to an (a) unannealed and (b) annealed 100 nm-thick TaN layer. The XRR fit density is indicated in each respective panel.

Quantification of Biaxial Stresses. While samples processed with and without top electrodes appear essentially identical when examined using chemical, microstructural, crystallization temperature, and densification measurements, they clearly possess different crystalline phase constitutions, permittivities, and polarization responses. It is evident, based upon densification measurements, that the samples should be in states of tensile stress following processing, which has been shown to affect the orthorhombic phase stabilization and resulting domain structure of the film.[87,115,150] To examine the amount of stress present within the HZO layers following processing due to both the presence and etched removal of the top electrode, $\sin^2(\psi)$ analyses were carried out on area detector diffraction patterns collected on each device structure.[283] The resulting changes in d-spacings with out-of-plane (ψ) angle and calculated biaxial stresses for each of the devices are plotted in Figure 8.13(a-c), with the collected area detector frames and unwarped patterns presented in Figure 8.14(a-f). With the assumption of uniform biaxial stresses in a randomly-oriented, isotropic linear elastic solid, fitting of the variation in d-spacing with ψ angle can be utilized to calculate the biaxial stress following processing using Equations 3.2 and 3.3:[209]

$$\varepsilon_{\psi} = \frac{1+v}{E}\sigma_{\|}\sin^2(\psi) - \frac{2v}{E}\sigma_{\|} \qquad 3.2$$

$$\varepsilon_{\psi} = \frac{d_{\psi} - d_0}{d_0} \qquad 3.3$$

Where d_{ψ} is the d-spacing at each ψ angle, v is the Poisson's ratio of orthorhombic HZO (assumed to be 0.29[261–263] for this analysis), E is Young's modulus of orthorhombic HZO (assumed to be 209 ± 6 GPa for the With-TE and TE-Etched samples and 202 ± 6 GPa for the No-TE sample[283]), $\sigma_{||}$ is the biaxial stress, and d_0 is stress-free d-spacing of orthorhombic HZO, which is calculated to occur at ψ angles at which Equation 3.4 is fulfilled:[209]

$$\sin(\psi^*) = \sqrt{\frac{2v}{1+v}} \qquad 3.4$$

The slopes of the linear fits of the changes in d-spacing with ψ angle, plotted in Figure 8.13(a-c), were all found to be positive, which is indicative that all three samples are under tensile biaxial stress following processing and agrees with the densification behavior observed using XRR. In tandem, the normalized integrated intensities of the t + o diffraction peaks were found to be essentially invariant with ψ angle, which is evidence that the films do not have preferred orientation. The lack of preferred orientation in these films validates the assumption of an isotropic solid. The calculated tensile biaxial stress magnitudes were found to vary approximately between 2 and 4 GPa, which is consistent with other similar investigations of HfO_2-based thin films with binary nitride electrodes.[125,283,295] When the HZO was processed without a top electrode, the resulting biaxial stress was calculated to be 2.10 ± 0.2 GPa, whereas when the film was annealed with a top electrode in place, the resulting biaxal stress was calculated to be 3.56 ± 0.2 GPa. Thus, the biaxial stress in the HZO resultant from the 'clamping effect' for these films is 1.46 ± 0.3 GPa. The TE-Etched film was calculated to have a biaxial stress of 2.74 ± 0.2 GPa following annealing and etching, indicating that the etching process reduced the amount of tensile biaxial stress in the

HZO by -0.82 ± 0.3 GPa. Both the With-TE and TE-Etched samples exhibited larger tensile biaxial stresses and larger polarizations than the No-TE film following processing, which is consistent with computational[87] and experimental investigations[115,116,151] of the effects of stress on ferroelectric HfO_2-based thin films. The different stresses dependent on the top electrode presence present clear differences in these samples to accompany their different phase constitutions and polarization behaviors.

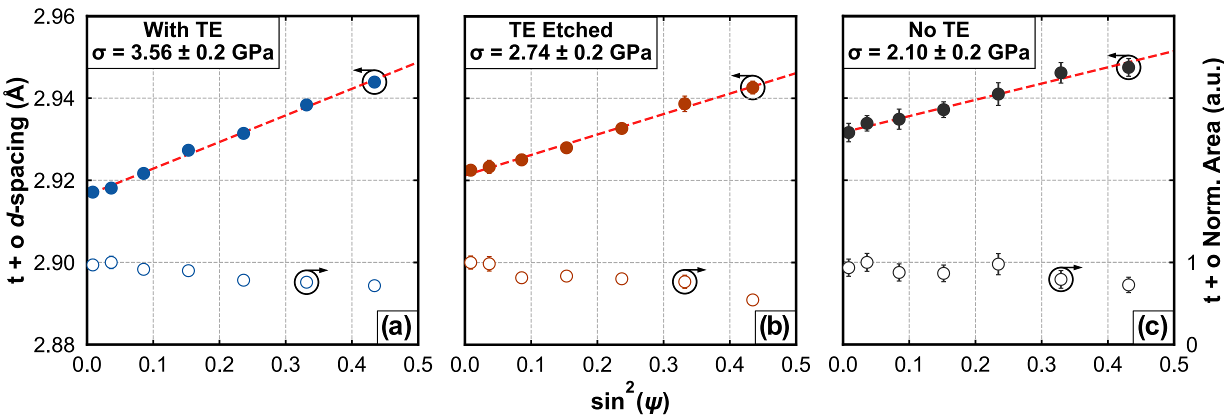

Figure 8.13. Change in t + o *d*-spacing (closed points, left axis) and t + o normalized area (open points, right axis) with ψ angle relative to film normal fit from area detector XRD patterns measured on (a) With-TE, (b) TE-Etched, and (c) No-TE films. The linear fits (red dotted lines) plotted through the *d*-spacing data were utilized to calculate the biaxial stress following processing.

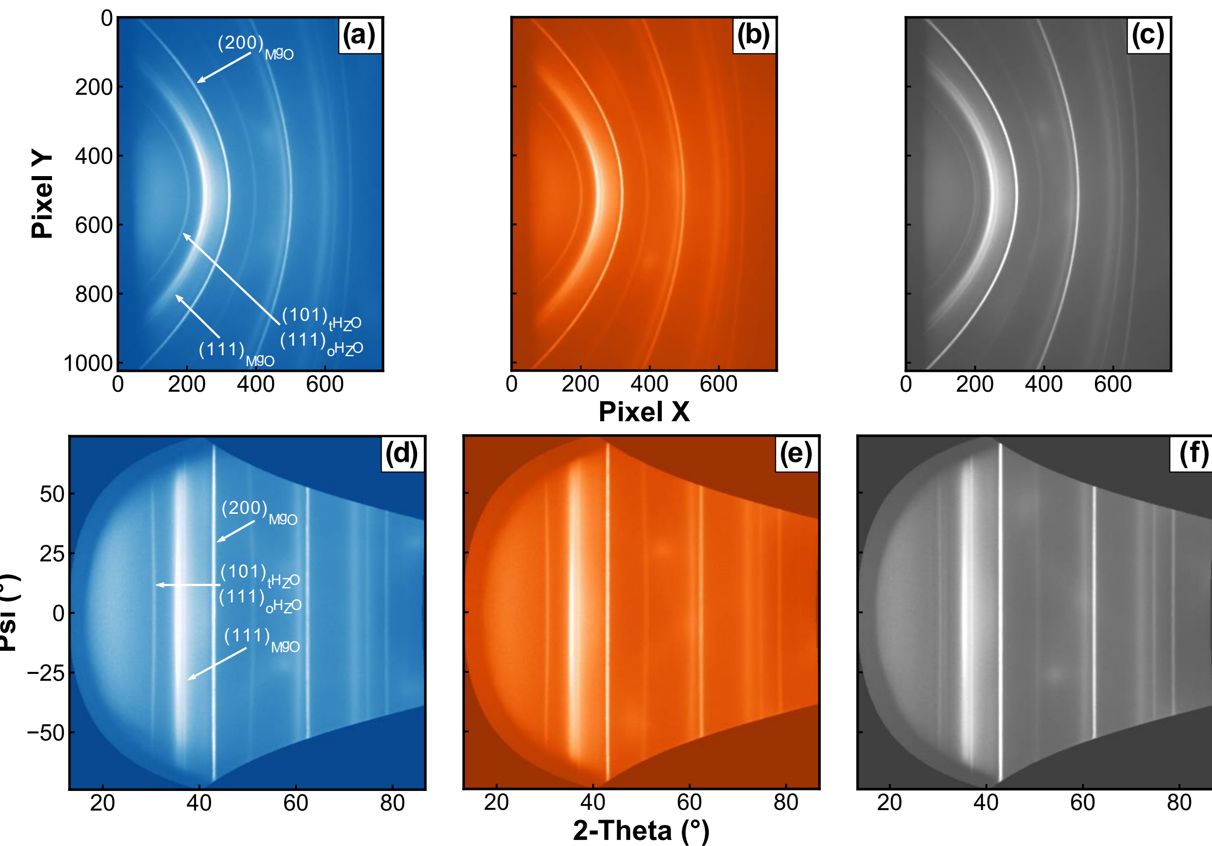

Figure 8.14. Area detector XRD patterns measured on (a) With-TE, (b) TE-Etched, and (c) No-TE samples. Unwarped area detector patterns measured on (d) With-TE, (e) TE-Etched, and (f) No-TE samples. Indexing of MgO and HZO Debye-Scherrer rings utilized for pattern unwarping and $\sin^2(\psi)$ analysis, respectively, are indicated on panels (a) and (d).

While diffraction measurements allow for the quantification of stress due to the clamping effect, and reveal clear differences in biaxial stress that accompany processing HZO thin films with a top electrode in place, they cannot quantify changes in stress that occur throughout the film stack. As a further examination of the evolution in biaxial stress with preparation of each sample, wafer flexure measurements following each deposition, after annealing, and after etching were carried out. Example height profiles for all three samples, measured throughout processing, are shown in Figure 8.15(a-c). Each height profile was fit with a 2d polynomial, which was then utilized in Equation 3.7 to calculate a wafer radius of curvature following each processing step. Then, using radii of curvature fit before and after each step, the resultant biaxial stresses were obtained using Stoney's Equation (Equation 3.6):

$$R_{\mathrm{F},0} = \frac{\left[1+y'(x)_{\mathrm{F},0}^{2}\right]^{\frac{3}{2}}}{\left|y''(x)_{\mathrm{F},0}\right|} \qquad 3.7$$

$$\sigma_{\|} = \frac{E_{\mathrm{s}} h_{\mathrm{s}}^{2}}{6(1\text{-}v_{\mathrm{s}})h_{\mathrm{f}}}\left(\frac{1}{R_{\mathrm{F}}} - \frac{1}{R_{0}}\right) \qquad 3.6$$

Where $R_{\mathrm{F},0}$ is the radius of curvature of the silicon substrate before (0) or following (F) the process step, $y'(x)$ and $y''(x)$ are the first and second derivatives of the polynomial height profile fit, respectively, $\sigma_{||}$ is the biaxial stress resultant from the process step, E_{s} is the elastic modulus of the silicon substrate (130 GPa[310]), h_{s} is the substrate thickness (280 µm), v_{s} is Poisson's ratio of the silicon substrate (0.28[310]), and h_{f} is the film thickness, in the case of deposition and etching steps, or total film stack thickness, in the case of the annealing steps.

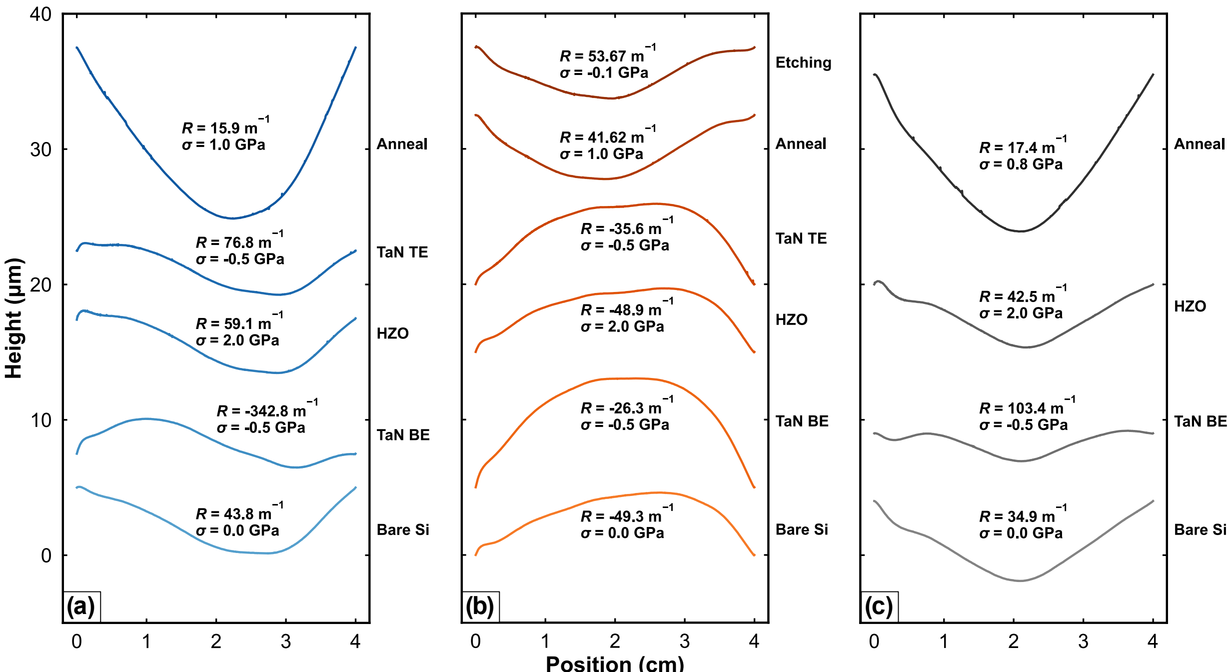

Figure 8.15. Offset height profiles measured on (a) With-TE, (b) TE-Etched, and (c) No-TE samples on the initial substrates and following each processing step. The process steps corresponding to each height profile are listed to the right of each panel. The fit radii of curvature and calculated biaxial stresses are listed on each associated profile.

The biaxial stress magnitudes following each processing step are detailed in Figure 8.16(a-c) for each device structure. All stresses were found to be strongly tensile following complete processing, in agreement with $\sin^2(\psi)$ analyses of the HZO area detector diffraction patterns and XRR densification analyses. Initial deposition of the TaN bottom electrode was measured to result in a compressive biaxial stress of -0.5 GPa in each device. Next, PEALD deposition of the 20 nm HZO layer yielded 2.0 GPa of tensile biaxial stress in the silicon. Deposition of the top electrode on the With-TE and TE-Etched samples resulted in an additional -0.4 GPa of compressive biaxial stress. Following depositions, rapid thermal annealing of the No-TE device was observed to induce an additional 0.7 GPa of tensile biaxial stress, whereas annealing the With-TE and TE-Etched devices resulted in an additional 1.0 GPa of tensile biaxial stress. Thus, 0.3 GPa of tensile biaxial stress was observed in the silicon substrate due to the clamping effect from the TaN top electrode. In tandem, etching of the top electrode following

processing was observed to result in a reduction in tensile biaxial stress of -0.7 GPa. By comparison, the wafer flexure measurements reflect the same signs of the biaxial stresses quantified through $\sin^2(\psi)$ analysis while the magnitudes are smaller for the thermal processing steps and essentially identical for the etching step. Given that flexure measurements can only examine the macroscopic deformation of the silicon substrate, the smaller magnitudes of biaxial stress incurred during thermal processing by this technique are evidence that the biaxial stresses of the TaN electrodes are changing in concert with the HZO during this step. Through 16 separate measurements of TaN bottom electrode layers, it was determined that the confidence interval for each flexure analysis is ± 0.1 GPa, showing that the differences between XRD and wafer flexure-based measurements of stress are real and outside of measurement error.

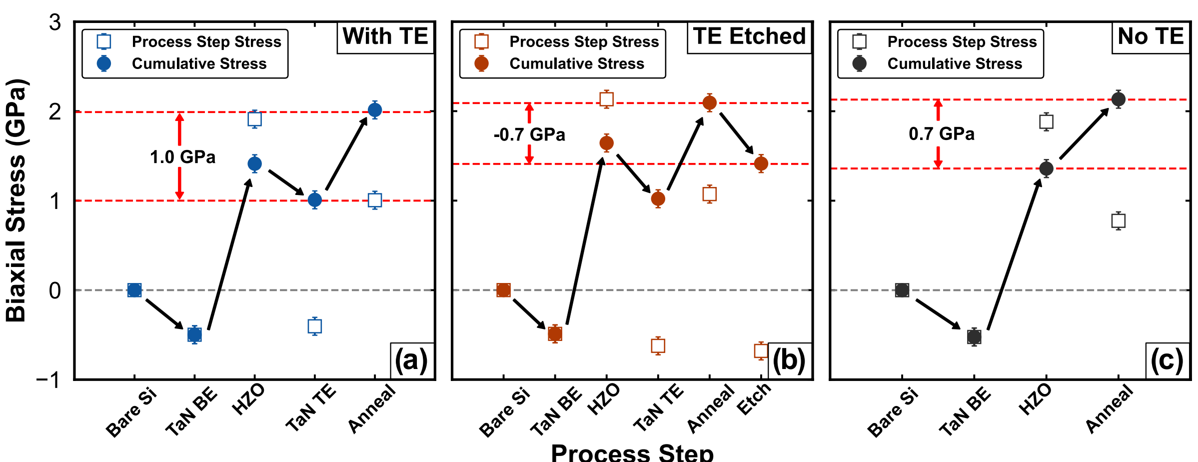

Figure 8.16. Cumulative (closed points) and individual process (open points) biaxial stresses quantified via wafer flexure measurements made on (a) With-TE, (b) TE-Etched, and (c) No-TE samples. The grey dashed line indicates the 0 GPa stress level, whereas the red dashed lines and red arrows indicate the biaxial stresses resultant from annealing with the top electrode, etching of the top electrode following annealing, and annealing without the top electrode in (a), (b), and (c), respectively.

While the combination of HZO crystallization and different densifications of all three layers likely prevents direct comparisons between post processing stresses and strains characterized using diffraction and wafer flexure, the etching process presents a simpler case.

Where diffraction analyses of this step using the t + o peak of the HZO yielded a decrease in tensile biaxial stress of -0.82 ± 0.3 GPa, flexure measurements of the silicon substrate revealed a change of -0.7 ± 0.1 GPa. These measurements are in agreement, which is expected given that this step occurs near room temperature, has negligible contribution from densification changes, and results in a phase transformation of only 8 ± 1% of the 20 nm HZO layer.

The transformation of 8 ± 1% of the HZO film volume from the tetragonal and/or orthorhombic phases to the monoclinic phase occurs with a reduction in the amount of tensile biaxial stress, and can be taken as a reduction in the potential energy of the film. By utilizing the difference in biaxial stress in the HZO layer before and after top electrode removal, the change in the potential energy causing this phase transformation, which is strain energy density in this case, can be calculated using Equation 8.4:

$$\Delta U_{||} = \frac{\Delta\sigma_{||}^2}{2E_{||(\mathrm{HZO})}} \tag{8.4}$$

Where $\Delta U_{||}$ and $\Delta\sigma_{||}$ are the change in biaxial strain energy density and biaxial stress due to the phase transformation, respectively, and $E_{||(\mathrm{HZO})}$ is the biaxial modulus of HZO (assumed to be 278 ± 7 GPa for this analysis[283]). It should be noted that the change in crystallographic strain observed in the HZO due to etching of the top electrode has contributions from substrate deformation. This calculation also assumes a uniform biaxial stress state and randomly oriented isotropic solid, as detailed when utilizing Equations 3.2-3.4 and 3.6, and is reasonable given the invariance of the intensity of the t + o diffraction peak with ψ angle (Figure 8.13(b)). Using these assumptions and the average unit cell volume for the tetragonal and orthorhombic phases[96] (133.7 $Å^3$ per formula unit, $F.U.^{-1}$) results in a strain energy density change of -1.0 ± 0.5 meV $F.U.^{-1}$ during the transformation of 8 ± 1% of the volume of the film from the tetragonal and orthorhombic phases to the monoclinic phase. Based upon these values, it can be estimated that a strain energy density change of -12.5 ± 6.4 meV $F.U.^{-1}$ would be required to completely transform the film to the monoclinic phase. This reduction in potential energy represents the input required to surmount the activation energy barrier separating the orthorhombic

and tetragonal phases from the equilibrium monoclinic phase at near temperature. The total difference between the free energies of the orthorhombic and tetragonal structures and the monoclinic structure, irrespective of the activation energy required for the transformation, have been calculated to be 25 and 70 meV F.U.$^{-1}$ by Materlik *et al*.[96]

Mechanism of the Clamping Effect in Ferroelectric HZO Devices. It is evident, based upon $\sin^2(\psi)$ analyses and wafer flexure measurements, that the clamping effect in HfO_2-based thin films is predominantly driven by biaxial stresses incurred in the ferroelectric layer during processing due to the top electrode. However, wafer flexure and diffraction-based stress measurements cannot directly elucidate the mechanism by which the top electrode influences the stress state and phase of the processed HZO layer. Through chemical and plasma etch removal of the top electrode, increases in the amount of monoclinic phase were observed, whereby full removal of the top electrode resulted in a decrease in $f_{\mathrm{t+o}}$ of 8 ± 1%. This increase in monoclinic phase fraction is accompanied by a decrease in tensile biaxial stress of -0.82 ± 0.3 GPa according to $\sin^2(\psi)$ analyses. Additional $\sin^2(\psi)$ analyses of samples that had the top electrode partially and fully removed via RIE, shown Figure 8.17(a-b), yielded final biaxial stress states of 3.10 ± 0.3 and 3.09 ± 0.3 GPa, respectively, which represent decreases of -0.46 ± 0.1 and -0.47 ± 0.1 GPa. While the analyses are unable to differentiate between the stress states of the Partial and Full RIE samples, it is evident based upon GIXRD patterns and $\sin^2(\psi)$ analyses that the partial removal of the top electrode results in more minor reductions in tensile biaxial stress and transformations to the monoclinic phase than when the top electrode is completely removed.

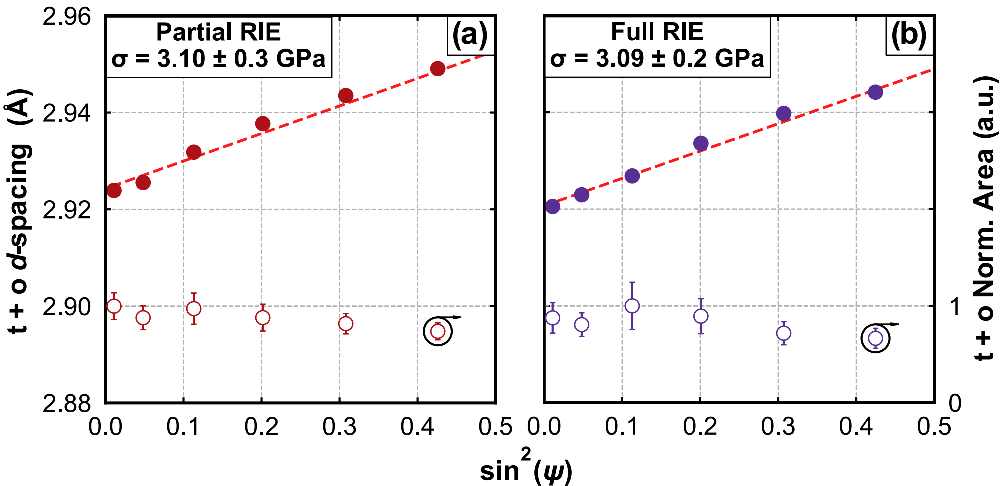

Figure 8.17. Change in t + o *d*-spacing (closed points, left axis) and t + o normalized area (open points, right axis) with ψ angle relative to film normal fit from area detector XRD patterns measured on (a) Partial-RIE and (b) Full-RIE films. The linear fits (red dotted lines) plotted through the *d*-spacing data were utilized to calculate the biaxial stress following processing.

Based upon electrode removal experiments, a decrease in the tensile biaxial stress state of the film results in a transformation to the monoclinic phase. To examine if this phase transformation could be induced via imparting of compressive biaxial stress without removal of the top electrode, GIXRD patterns were measured and $\sin^2(\psi)$ analyses were carried out on a With-TE sample before (Single-TE) and after (Double-TE) sputtering of an additional 20 nm-thick TaN layer to produce additional compressive biaxial stress after thermal processing (i.e. the second TaN layer was deposited after thermal processing was completed), as shown in Figure 8.18(a-c). The $\sin^2(\psi)$ analyses of the Single-TE and Double-TE samples, shown in Figure 8.18(a-b), show a change in tensile biaxial stress of -0.32 ± 0.3 GPa due to the additional layer, from 3.61 ± 0.2 GPa measured on the Single-TE sample to 3.29 ± 0.2 GPa measured on the Double-TE sample. The decrease in tensile biaxial stress is essentially on the order of the compressive biaxial stress imparted on the sample by the sputtering of the second 20 nm-thick TaN layer as characterized by flexure analysis, -0.4 ± 0.1 GPa, and importantly smaller in magnitude than that produced via etch removal of the top electrode. GIXRD patterns measured on the sample before and after the sputtering of the second TaN layer, shown in Figure 8.18(c) reveal similar phase constitutions. f_{t+o} for these samples, calculated using Equation 8.3 and the fits of these two patterns, are the

same within error. However, given the small reduction in tensile biaxial stress due to the additional deposition, it is not clear based upon this measurement if the change in stress state is affecting the phase constitution, especially when it is considered that biaxial strain energy density is proportional to the square of the change in biaxial stress.

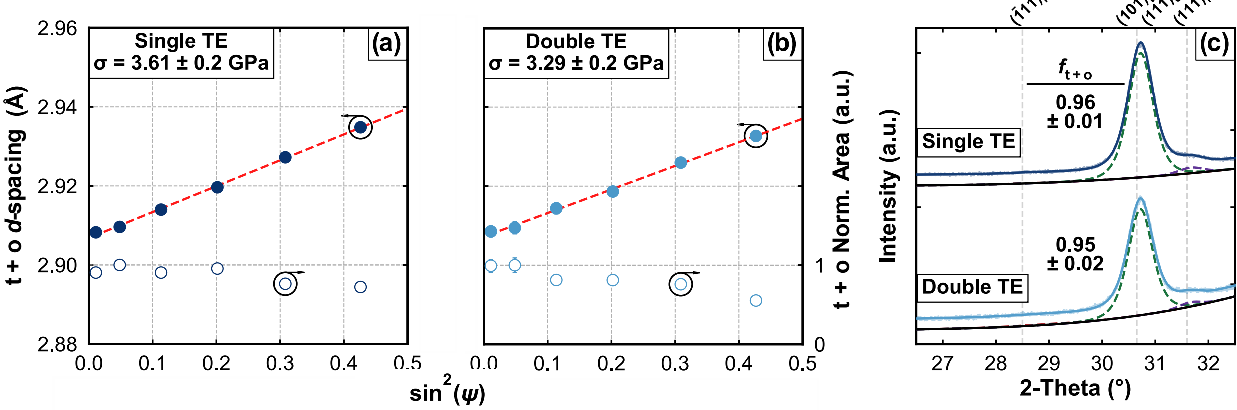

Figure 8.18. Change in t + o *d*-spacing (closed points, left axis) and t + o normalized area (open points, right axis) with ψ angle relative to film normal fit from area detector XRD patterns measured on (a) Single-TE and (b) Double-TE samples. The linear fits (red dotted lines) plotted through the *d*-spacing data were utilized to calculate the biaxial stress following processing. GIXRD patterns measured on the Single-TE (dark blue) and Double-TE (light blue) films. The fits for each observed $(\bar{1}11)$ monoclinic (red dotted line), t + o (green dotted line) and (111) monoclinic (purple dotted line) peak and fit background (black line) are offset below each corresponding pattern. The indexing for each observed peak is indicated by grey vertical dotted line and listed above the panel, and the calculated t + o fraction is indicted to the left of each corresponding pattern.

The transformation from the tetragonal and/or orthorhombic phases to the monoclinic phase upon removal of the top electrode is indicative of the important role that the electrode interfaces play in the stabilization of the orthorhombic phase. TEM micrographs of HfO_2-based thin films between TiN layers captured by Grimley *et al.*[154] show that tetragonal interlayers exist between the electrode and ferroelectric layers, which are produced due to the strain and chemical environment at the interface. Formation of such interlayers at interfaces and grain boundaries has

also been predicted using density functional theory (DFT) by Künneth *et al.*,[90] which explains the small grain size requirements for orthorhombic phase formation. Tetragonal interlayers were not readily observable in TEM micrographs captured within this report, likely due to different foil preparation procedures or measurement conditions. Regardless, the larger free energy and volume differences between the tetragonal and monoclinic phases compared to the orthorhombic and monoclinic phases[87,96] at room temperature support that phase gradients between the equilibrium, high-volume monoclinic phase in the bulk of the film and the high energy, low-volume tetragonal phase stabilized by strain at the interface with the electrode would favor production of the intermediate energy/volume orthorhombic phase. This model is supported by the experiments detailed in this chapter, in which HZO films processed without top electrodes, and only one electrode/ferroelectric interface, exhibit more monoclinic phase and lower magnitudes of tensile biaxial stress. With removal of the top electrode, the amount of tensile biaxial stress within the film is reduced and a partial transformation to the monoclinic phase occurs. It remains unclear if the same phase transformations can be imposed through reduction of tensile biaxial stress magnitude with preservation of the top electrode interface.

8.6 Conclusions

To investigate the clamping effect in HfO_2-based thin films, the effects of processing of TaN/HZO/TaN MIM samples with and without top electrodes have been investigated using electrical, chemical, and structural measurements. It has been shown that processing HZO films with the top electrode in place yields more of the metastable ferroelectric orthorhombic phase than processing with only a bottom electrode layer, which yields films that are a mixture of the tetragonal, orthorhombic, and monoclinic phases. Comparisons between microstructural, leakage current, TEM-EDS, temperature-resolved XRD, and XRR measurements made on samples processed with and without top electrodes did not reveal discernable differences between oxygen content, grain sizes, crystallization temperature, or densification dependent on the top electrode presence. Diffraction-based $\sin^2(\psi)$ stress analyses showed that processing samples with both electrodes in place produced tensile biaxial stresses that were higher than samples that were processed without the top electrode. The substrate flexure-based stresses measured for each processing step, alternatively, revealed an increase in the tensile biaxial stress state of the film

stack due to the clamping effect, but could not completely reconcile the diffraction-based quantification of the stress present in the HZO layer following processing, likely due to a combination of different densification and thermal expansion behaviors of each layer and HZO crystallization. However, the stress changes reported by diffraction and wafer-flexure based measurements that occur due to etching were similar. The nature and mechanism of this stress change was explored further through partial and full etching of the top electrode with wet etch and RIE procedures. It was determined that removal of the top electrode following processing reduces the amount of biaxial stress present in the HZO layer, which is accompanied by a transformation of some volume of the present tetragonal and/or orthorhombic phases to the monoclinic phase. This behavior was shown to not be related to oxidation from the etching procedures, and persisted even if the electrode was only partially removed. Using this change in stress state and phase constitution, the activation energy barrier for the film to completely transform from the tetragonal and orthorhombic phases to the monoclinic phase was determined through calculations of changes in strain energy density. Based upon these measurements, it was concluded that the strain state at the interfaces, which has been shown to produce interlayers of the tetragonal phase,[154] aids in stabilizing the orthorhombic phase as an intermediary separating the interface from the equilibrium monoclinic phase in the bulk of the film. Using these measurements, the following has been revealed about the clamping effect in HfO_2-based ferroelectric thin films:

1. The clamping effect in ferroelectric HfO_2-based thin films occurs due to stress from the top electrode layer at the interface.

2. The presence of the top electrode was not observed to measurably impact the oxygen content, densification, or crystallization temperature of the HZO layer.

3. Samples processed with top electrodes exhibit larger orthorhombic phase contents ($+ 36 \pm 3\%$) and tensile biaxial stress magnitudes ($+ 70 \pm 19\%$) than samples processed with only bottom electrodes.

4. Through removal of the top electrode, the amount of tensile biaxial stress in the HZO layer is reduced by $-23 \pm 6\%$, and $8 \pm 1\%$ of the film volume transforms from the tetragonal and/or orthorhombic phases to the monoclinic.

5. The strain energy density required for complete transformation of the film from the tetragonal and orthorhombic phases to the monoclinic phase is 12.5 ± 6.4 meV $F.U.^{-1}$.

8.7 Acknowledgements

This work is supported, in part, by the Semiconductor Research Corporation's (SRC) Global Research Collaboration Program. Reactive ion etch experiments were supported by the Center for 3D Ferroelectric Microelectronics (3DFeM), an Energy Frontier Research Center funded by the U.S. Department of Energy, Office of Science, Basic Energy Sciences under Award No. DE-SC0021118. This research utilized a PHI VersaProbe III XPS system, which was supported by National Science Foundation Award # 162601. STJ acknowledges support from the National Science Foundation Graduate Research Fellowship Program under award DGE-1842490. PEH appreciates funding from the National Science Foundation, Grant Number DMR EPM 2006231.

Chapter 9: Conclusions

Through varying electrode material, electrode stoichiometry, and examining the stresses associated with processing with electrodes, the effects of the electrode on the ferroelectric properties of HZO films have been explored. It has been shown that the manner in which the electrode and HZO layers exchange oxygen, oxygen vacancies, and electrons is an important factor in the field-cycling behavior of the ferroelectric. When electrodes are incorporated that do not allow oxygen transfer, a buildup of oxygen vacancies at the electrode/ferroelectric interface causes domain pinning and transformations from the tetragonal and orthorhombic phases to the monoclinic phase. When an electrode material is utilized that too-readily allows transfer of oxygen vacancies out of the ferroelectric layer, then charged defects, likely injected electrons, cause domain pinning and polarization fatigue. When electrode materials that allow an intermediate amount of oxygen vacancy transfer are utilized, for example binary nitrides that form oxynitride interlayers, then polarization wake-up and fatigue are observed, which are driven primarily by phase transformations / domain de-pinning and domain pinning, respectively. Separate from material selection, the chemistry of binary nitride electrodes plays an important role in affecting the oxygen content, and resultant phase constitution and polarization of processed HZO devices. Metal-rich electrodes more readily remove oxygen from the HZO layer, which results in larger orthorhombic phase compositions and higher polarizations. These findings address the knowledge gap present in the scientific community's understanding electrode effects on HZO performance, show that careful consideration should be given to incorporated electrode material selection and chemistry, and reveal a means to engineer the ferroelectric and field-cycling properties of HZO using these neighboring layers.

Further, the stresses incurred in the HZO during processing with a top electrode have been investigated. It has been shown that the stress imparted by the top electrode is instrumental in enhancing orthorhombic phase contents in HZO devices. If the top electrode is removed, then a reduction in tensile biaxial stress and a transformation from the tetragonal and/or orthorhombic phases to the monoclinic takes place. While the phase constitution does not appear to change if the amount of tensile biaxial stress is reduced through deposition of an additional layer, without destruction of the top interface, the stress changes employed through experimentation may not

have been large enough to produce observable transformations. Regardless, fully prepared HZO devices with TaN electrodes exhibit tensile biaxial stress, the magnitude of which is larger if processing occurs following top electrode deposition. This tensile biaxial stress enhancement coincides with larger orthorhombic phase fractions and polarization magnitudes, while film oxygen content and crystallization/densification behaviors appear unaffected. These findings confirm that stress from the top electrode drives the orthorhombic phase composition enhancement, while addressing the knowledge gap encompassing the mechanism by which this enhancement occurs.

In total, this dissertation describes experiments undertaken to examine electrode effects on the polarization properties of ferroelectric HZO thin films. Through these experiments, an understanding of the chemical and physical interactions between these layers has been obtained. The knowledge precipitated from these experiments facilitates the incorporation of ferroelectric HZO materials directly into the next generation of silicon-based memory and sensor technology by allowing their polarization and field cycling properties to be tailored through engineering of their neighboring electrode layers.

Chapter 10: Future Work

Throughout completion of the work outlined Chapters 3 - 8, a number of additional research questions arose. Many of these questions are academic, probing deeper into the fundamental changes that occur in the film during processing or field cycling, whereas others are more practical, harnessing findings to specifically engineer electrodes for better performance. Within this section, these questions will be discussed as potential candidates for future or follow-up investigations.

Temperature-Resolved Wafer Flexure Measurement. While the investigation in Chapter 8 harnessed etching experiments to reveal the important nature of the interface between the HZO layer and the top electrode, the complexity of the densification and crystallization processes occurring during annealing prevented direct comparisons between diffraction and wafer-flexure analyses of the tensile biaxial stress associated with the clamping effect. While it is experimentally difficult to design a procedure to allow for decoupling of crystallization and thermal mismatch strains during annealing of TaN/HZO/TaN film stacks, important observations can be made about their contribution to the final stress state through measuring wafer flexure during the annealing process.

Such a measurement is being conducted at Brown University, utilizing a Multi-beam Optical Stress Sensor (MOSS) technique to monitor the stress state of TaN/HZO and TaN/HZO/TaN film stacks throughout annealing. The temperature ramp rate and atmospheric environment for this measurement are designed to be identical to the HTXRD measurements, shown in Figure 8.10, such that the stress can specifically be analyzed in the vicinity of the temperature at which the HZO crystallizes. In tandem, the change in stress with cooling will be monitored such that changes due to densification and different thermal expansion mismatches can be better understood. In total, this measurement will allow for a more complete analysis of the stresses that arise due to annealing of TaN/HZO and TaN/HZO/TaN film stacks, and will provide additional opportunities for analysis of the clamping effect.

Larger Reductions in Tensile Biaxial Stress to Further Investigate the Clamping Effect. While the tensile biaxial stress within the HZO layer was reduced by -0.3 GPa through

deposition of an additional 20 nm-thick TaN layer on top of the With-TE sample in Chapter 8, this change in stress state is small compared to the reduction when the top TaN layer was removed completely via etching, -0.7 GPa. The biaxial stress change of -0.3 GPa did not result in a phase transformation that was observable using GIXRD, however the magnitude of this change is small enough to cause a transformation that may be within the error of the fitting calculation. As a further experiment to confirm that the preservation of the interface with the top electrode is an important aspect of the clamping effect, it is necessary to employ an electrode material or thickness such that the additional deposition on top of the With-TE sample produces a larger reduction in tensile biaxial stress, at least on the order of the reduction observed through etching. To achieve this enhanced tensile biaxial stress reduction without substantially changing the diffraction background, it will be necessary to utilize tungsten instead of TaN, which has low index X-ray reflections that are further from the important reflections in HZO. Further, it will be necessary to determine the thickness of tungsten required to produce the necessary stress change. If this thickness is large enough to appreciably attenuate the diffracted intensity from the underlying HZO, then utilization of a High-Power Impulse Magnetron Sputtering (HiPIMS) deposition process may be necessary. Such processes can produce films of higher biaxial stress due to increased ion bombardment, and will allow for larger biaxial stresses to be imparted using lower film thicknesses.[311]

Stresses Due to Field Cycling of HZO. With the development and adaptation of the $\sin^2(\psi)$ analysis technique detailed throughout this dissertation, investigation of the crystallographic stresses associated with field cycling of HZO has become possible. Such an analysis is made difficult by the stringent X-ray beam footprint requirement to produce sufficient intensity for the $\sin^2(\psi)$ analysis to take place. Owing to this, shadow masks with large contact areas have been obtained so that area detector patterns can be collected with sufficient signal-to-noise on single contacts using laboratory-based single crystal diffractometers.

To perform such an experiment, TaN/HZO/TaN devices could be pre-cycled with specific numbers of square waves, and at each interval, polarization, permittivity, and leakage current measurements could be made. Then, area detector patterns can be captured on contacts cycled at each interval. This procedure can be completed for mild (<2.0 MV cm^{-1}), intermediate (2.0 MV cm^{-1}), and harsh (>2.0 MV cm^{-1}) cycling intensities as an examination of how such

different cycling procedures affect the HZO layer. Further, such a procedure can be carried out using different electrode materials. While such polarization behaviors will likely be different, comparisons between changes in stress may further the scientific community's understanding of the mechanisms governing the differences that arise due to different electrodes and interfaces with HZO.

Engineering of Electrode Stoichiometry in HZO Devices. With findings from the investigation detailed in Chapter 6 and the development of the TaN/HZO/TaN process detailed in Chapter 3 and in the appendix, it is evident that electrode stoichiometry presents and avenue to engineer the phase constitution and field cycling behavior of HfO_2-based devices. While it has been shown in this dissertation that such an optimization can be done, it remains to actually design and conduct such an experiment.

For this experiment, utilization of a DC sputtering process from a sintered TaN target would likely present the most straightforward manner to vary the electrode chemistry. Such an experiment has already shown expected results in small-scale, as detailed in the appendix. Further, the specific stoichiometry of the electrode could be measured using XPS with the procedures detailed in Chapter 6. With different as-prepared polarizations and phases, field cycling experiments could be conducted similar to those detailed in Chapter 7 to examine if the oxygen content of the HZO or different interface gives rise to different mechanisms by which polarization wake-up or fatigue occurs. This experiment would provide the next logical step in harnessing electrode properties to tailor the field cycling and polarization performance of HfO_2-based devices.

Customizable Work Function Asymmetry via Electrode Replacement in HZO. With results presented in Chapter 8, it is evident that the TaN/HZO/TaN process described in Chapter 3 is capable of producing a device which can have the top electrode etch-removed and replaced following processing. Harnessing this procedure, it is possible to incorporate an electrode material that would not normally produce a large content of the orthorhombic phase if thermally processed in contact with HZO by 'replacing' the original TaN top electrode. This provides the opportunity to investigate TaN/HZO/Top electrode devices where the electrodes have different work functions, but identical HZO layers. Such a feature may be useful in devices such as FTJs, which rely on affecting band characteristics via ferroelectric switching.

Such an experiment could be conducted by producing a large quantity of thermally processed TaN/HZO/TaN film stacks, which could have the top electrode etched off and replaced. After, ‘replaced’ top electrode materials could be deposited through a shadow mask directly onto the HZO surface (along with uniform platinum contact layers during the same deposition), and the electrical properties of such devices could be compared. Such an experiment could involve field cycling, to examine how potential different interfaces or asymmetric work functions affects the polarization behavior. In tandem, such a process provides the opportunity to isolate different field cycling behaviors from different as-prepared phase compositions when TaN with different stoichiometries is utilized as the ‘replaced’ electrode. These experiments harness knowledge of electrode effects and procedures developed within this dissertation to enhance the application capabilities of HZO.

Chapter 11: Appendix

Development of an ALD HZO Process. At the outset of development of an ALD process at UVA capable of depositing ferroelectric HZO thin films, it was known that both oxygen content and electrode material were important characteristics to consider. With installation of the FlexAL II ALD system, Oxford Plasma Technologies (the manufacturer of the instrument) provided plasma-based HfO_2 and ZrO_2 recipes that produced films with a high degree of uniformity (1.5% across a 100 mm-diameter wafer), which employed precursor purge lengths of 3 and 6 seconds for HfO_2 and ZrO_2, respectively. Initial process development entailed depositing 20 nm-thick 5:5 HfO_2:ZrO_2 films (combining the two processes) at 295 °C between TiN electrode layers (deposited using a reactive DC process from a pure titanium target at UVA) and examining the electrical properties of processed devices. For all $P(E)$ data plotted in this section, a period of 1 ms was utilized, whereas for all of the cycling, a square wave (100% duty cycle) frequency of 1 kHz and a field of 2.5 MV cm^{-1} was selected. The $P(E)$ response of a device produced via this initial process is shown in Figure 11.1. The pinched response showed a low leakage current contribution, but did not demonstrate a P_r high enough for desired experimentation.

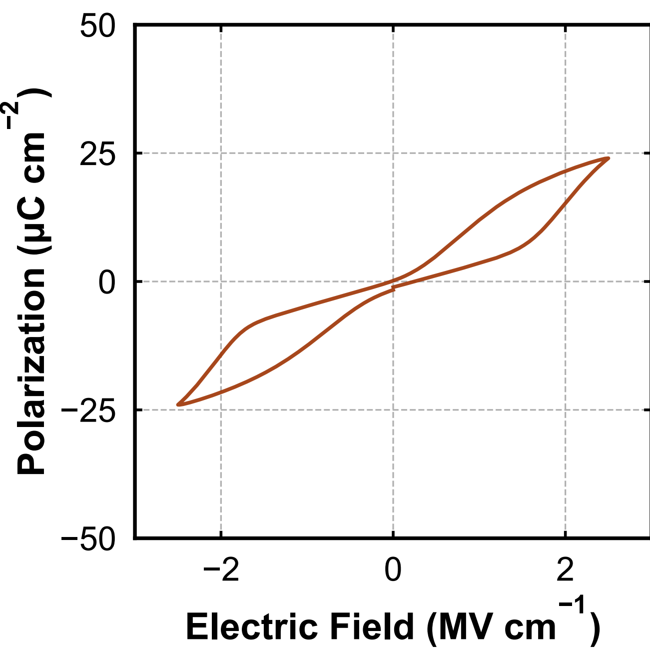

Figure 11.1. Hysteresis response measured on a TiN/HZO/TiN device that employed the Oxford Plasma Technologies HfO_2 and ZrO_2 recipes.

In an attempt to better replicate devices prepared at Sandia National Laboratories, examination of a lower temperature thermal (H_2O) process was then attempted. For this process, the precursor delivery and purge steps from the Oxford process were unchanged, while the plasma oxidation step was replaced with a H_2O exposure with a length between 20 – 60 ms, and the deposition temperature was reduced to 200 °C. Following the H_2O exposure, an 8-second-long purge step length was utilized. The $P(E)$ responses of devices prepared with various water exposure lengths are shown in Figure 11.2. In all cases, leakage current contributions to polarization responses were higher than devices prepared with plasma processes, and responses appeared either heavily pinched or more linear dielectric.

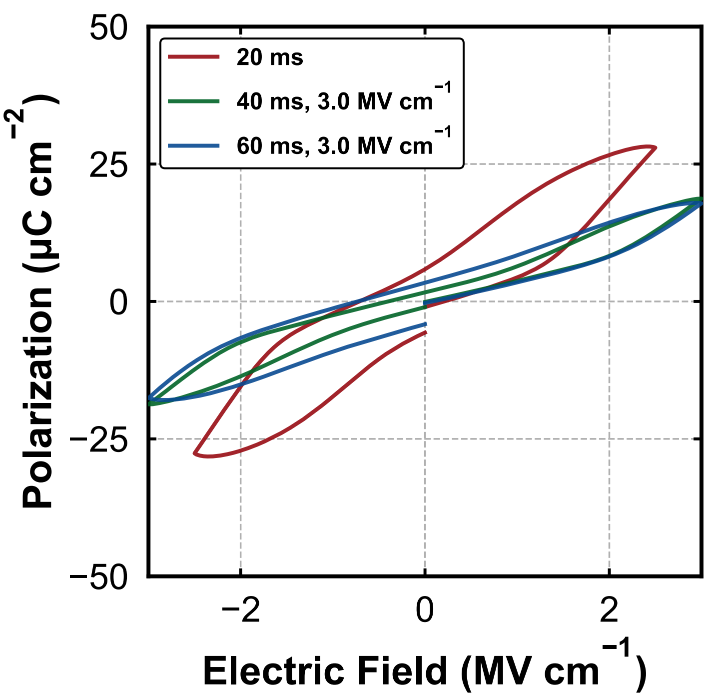

Figure 11.2. Hysteresis responses measured on TiN/HZO/TiN devices prepared with 20 (red), 40 (green), and 60 ms (blue) H_2O pulse lengths. The maximum measurement fields are identified in the legend.

Uniformity and growth rate examinations of HZO films deposited with the 200 °C, H_2O-oxidized process on silicon confirmed that the changes did not adversely affect the film metrics, and that the poor electrical performance was related to either the film or electrode characteristics. To attempt to increase the P_r of the devices, an examination of thermally grown HZO films with TiN electrodes deposited with different N_2-flows was undertaken. The $P(E)$ responses of devices prepared with symmetric TiN electrodes deposited with 17, 19, and 23% N_2 in the flow gas are shown in Figure 11.3. While the increase in N_2 in the processing atmosphere of the TiN electrodes did appear to produce HZO devices with less leakage current, measured P_r for each film remained low.

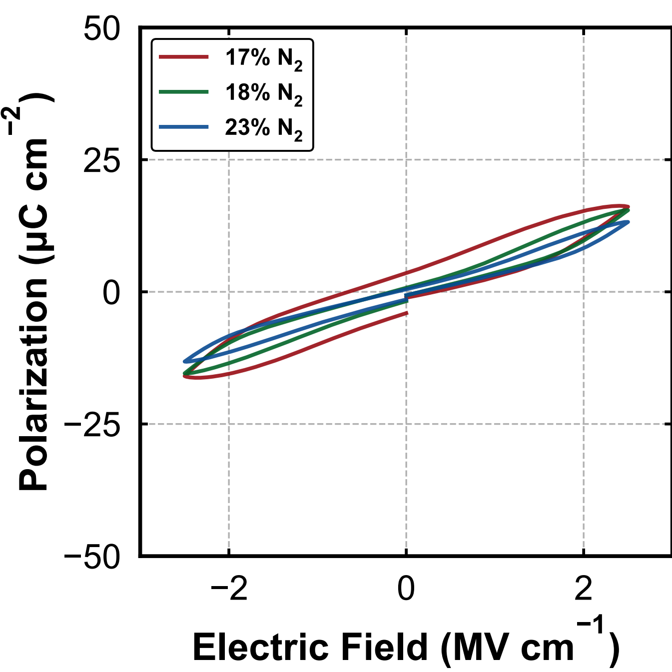

Figure 11.3. Hysteresis responses measured on TiN/HZO/TiN films prepared with TiN electrodes sputter deposited with atmospheres that were 17 (red), 19 (green) and 23% (blue) N_2.

With additional surveying of available literature, it was determined that 260 °C provides a better temperature for deposition using the TEMAH and TEMAZ precursors to reduce carbon impurities.[197] In tandem, it was determined that the precursor purge time is a key processing parameter to consider when these precursors are utilized.[98] As such, thermal HZO was grown between TiN electrodes with increased precursor purge step lengths of 30 and 90 seconds to examine the effects of these changes on the electrical behaviors of the yielded devices, which is shown in Figure 11.4(a-b). The responses were initially leaky, which reduced following cycling, yielding a ferroelectric hysteresis response.

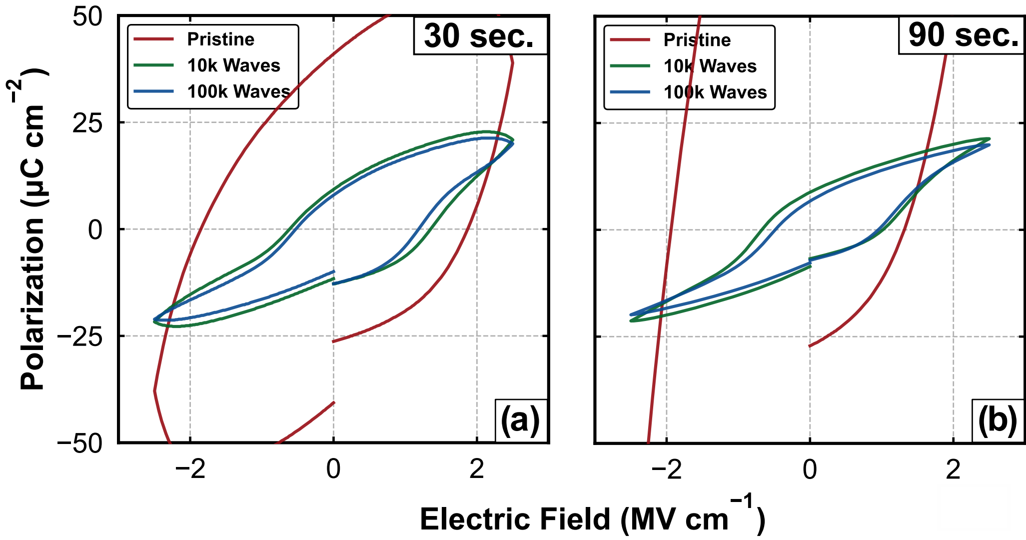

Figure 11.4. Hysteresis responses measured on pristine (red) devices and after 10,000 (green) and 100,000 (blue) square waves. Devices were prepared with HZO recipes that had precursor purge steps that were (a) 30 and (b) 90 seconds long.

Given the abundance of published research which utilized ozone with these precursors, a HZO sample was prepared with this oxidant to examine if the yielded device showed ferroelectric polarization without the large leakage current contribution in the pristine state. For this deposition, the precursor purge step length was returned to 5 seconds to examine if this oxidant allowed deposition of a ~20 nm-thick film in less than 4 hours. Once again, the response, shown in Figure 11.5, was leaky in the initial state. It was thus concluded that this precursor did not alleviate the issues observed for the H_2O-based thermal process.

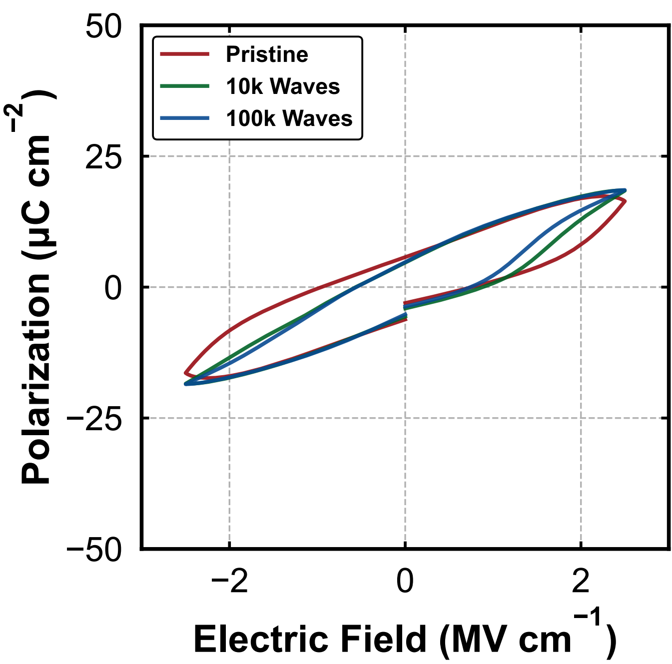

Figure 11.5. Hysteresis responses measured on a TiN/HZO/TiN device in the pristine state (red) and after 10,000 (green), and 100,000 (blue) square wave cycles. The HZO recipe utilized ozone as the oxidant.

In comparing the thermal and plasma processes, it became evident that the lack of apparent leakage current contribution to measured polarization in the pristine measurements of HZO films prepared with plasma-based processes could remedy the issue posed by the longer precursor purge. For this examination, devices were prepared with TiN bottom electrodes in tandem with TaN bottom electrodes prepared at Sandia National Laboratories. The $P(E)$ responses of these devices are shown in Figure 11.6(a-b). While the response of the device with symmetric TiN electrodes was pinched in its pristine state, a strong P_r was measured following field cycling. Further, utilization of a TaN bottom electrode resulted in less pinched pristine $P(E)$ response.

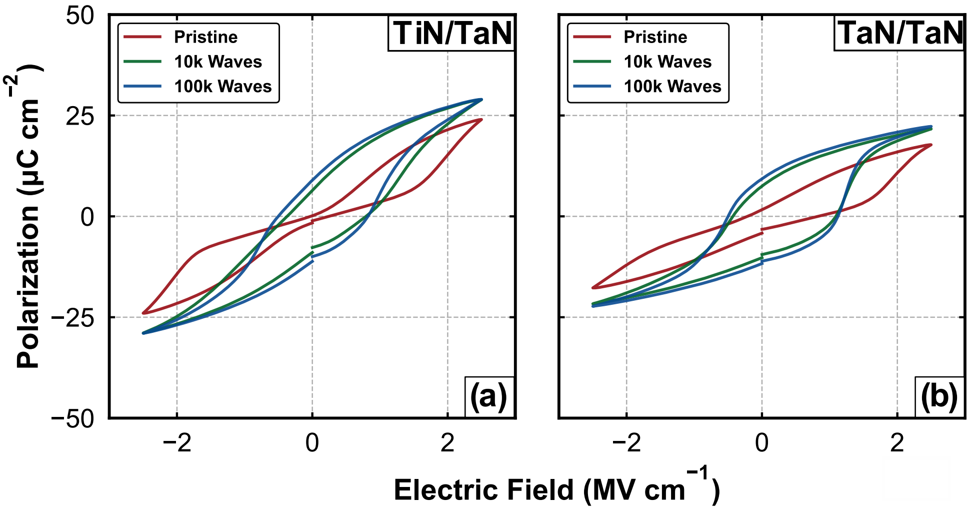

Figure 11.6. Hysteresis responses measured on (a) TiN/HZO/TaN and (b) TaN/HZO/TaN devices in the pristine state (red), and after 10,000 (green) and 100,000 (blue) square wave cycles.

Given the superior polarization response of the device prepared with a TaN bottom electrode, devices were next prepared with TaN layers that were deposited using the DC process described in Chapter 3, however also with the addition of 10 and 20% N_2 flows. The $P(E)$ responses of these devices in the pristine state and after field cycling are shown in Figure 11.7(a-c). When no additional N_2 was added to the sputter atmosphere during deposition of the TaN electrode layers, the best pristine $P(E)$ response was measured. As N_2 was added to the TaN sputtering atmosphere, the pristine $P(E)$ response became more pinched. With field cycling, the polarization response of all devices increased, once again with the largest response measured on the device prepared with the TaN electrodes prepared without any additional N_2 present in the sputtering atmosphere. Thus, the process utilizing the TaN electrodes that were DC sputtered without any additional N_2 in the processing atmosphere and the PEALD HZO with 90-second-long precursor purge steps was settled upon to prepare the final TaN/HZO/TaN devices. Further characterization was conducted on devices prepared with this process to examine the structural and electric properties as a function of HZO film composition and thickness, as detailed in Chapter 3.

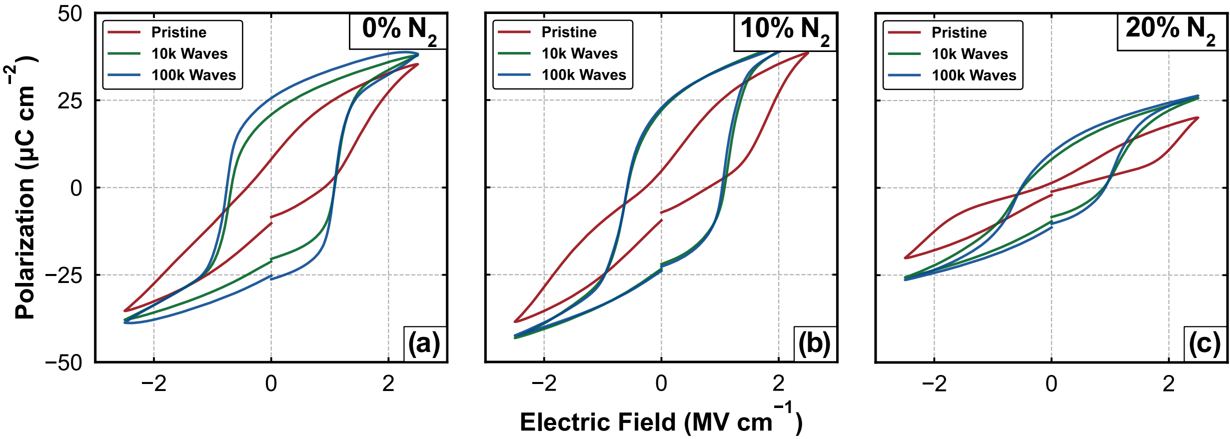

Figure 11.7. Hysteresis responses measured in the pristine state (a) and after 10,000 (b) and 100,000 (c) square wave cycles on TaN/HZO/TaN devices processed with TaN with (a) 0, (b) 10, and (c) 20% N_2 in the sputtering atmosphere.

Repeatability of the sin^2(ψ) Measurement. In order to examine how robust the sin^2(ψ) analysis procedure was against factors such as variable detector distance and sample measurement region, a series of analyses were carried out on TaN/HZO/TaN samples in which such procedural characteristics were intentionally varied. To assess potential height displacement user errors, three measurements were made on a TaN/HZO film that had the top electrode etched off following processing. For these measurements, the sample displacement was manually/intentionally moved above/below the process-specific height which results in the MgO powder dispersed on the surface to become optically focused in the instrument camera. The pyFAI[212] unwarping process identified that these manual displacements resulted in detector distances of 0.069, 0.070 (the distance identified in the procedure), and 0.071 m, as shown in Figure 11.8(a-c).

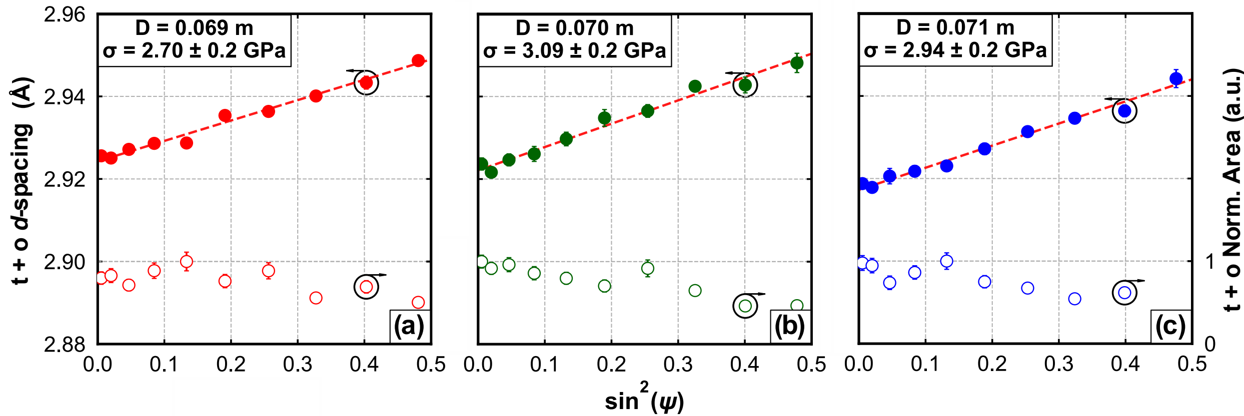

Figure 11.8. Change in t + o *d*-spacing (closed points, left axis) and t + o normalized area (open points, right axis) with ψ angle relative to film normal fit from area detector XRD patterns measured at detector distances of (a) 0.069, (b) 0.070, and (c) 0.071 m. The linear fits (red dotted lines) plotted through the *d*-spacing data were utilized to calculate the biaxial stress following processing.

Based upon these analyses, the unwarping and displacement alignment process, completed with MgO powder dispersed on the surface of the film and the pyFAI integration package,[212] is able to account for ~1 cm displacements in sample height, which may come about due to user error. Next, area detector patterns were collected on a TaN/HZO/TaN film stack that was thermally processed with the electrode in place near the sample edge, and about the center of the sample. The $\sin^2(\psi)$ analyses corresponding to these patterns are shown in Figure 11.9(a-b).

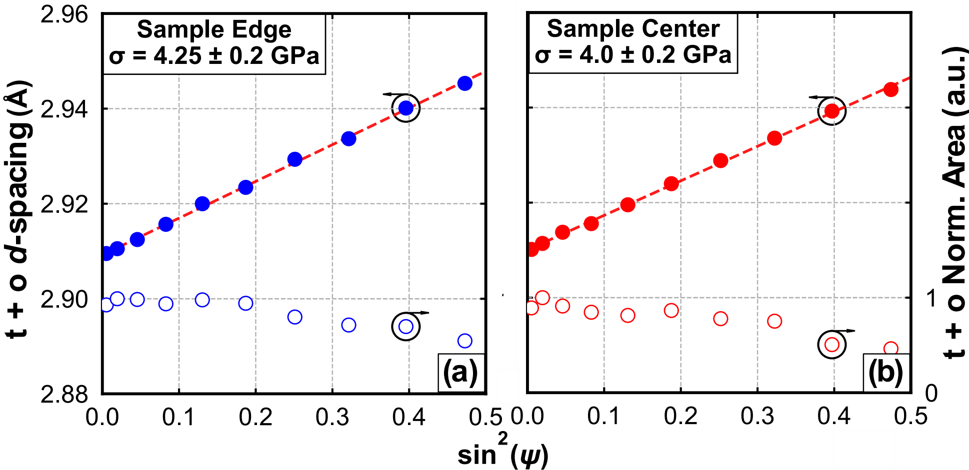

Figure 11.9. Change in t + o *d*-spacing (closed points, left axis) and t + o normalized area (open points, right axis) with ψ angle relative to film normal fit from area detector XRD patterns measured at locations near the (a) sample edge and about the (b) sample center. The linear fits (red dotted lines) plotted through the *d*-spacing data were utilized to calculate the biaxial stress following processing.

Given that both analyses report biaxial stress values that are within error of each other, it was concluded that the measurement procedure does not suffer repeatability issues from common user errors or different measurement regions on the same sample.

Confirmation of a Biaxial Stress State in HZO Films Prepared at UVA. While inspection of area detector patterns measured on processed HZO films allowed for the confirmation of random crystallographic orientation, which validates the assumptions of an isotropic solid, confirmation of a biaxial stress state requires explicit measurements of films at different rotational orientations. Plotted in Figure 11.10(a-c) are $\sin^2(\psi)$ analyses carried out on area detector patterns measured on a processed TaN/HZO/TaN film stack at different φ rotational angles.

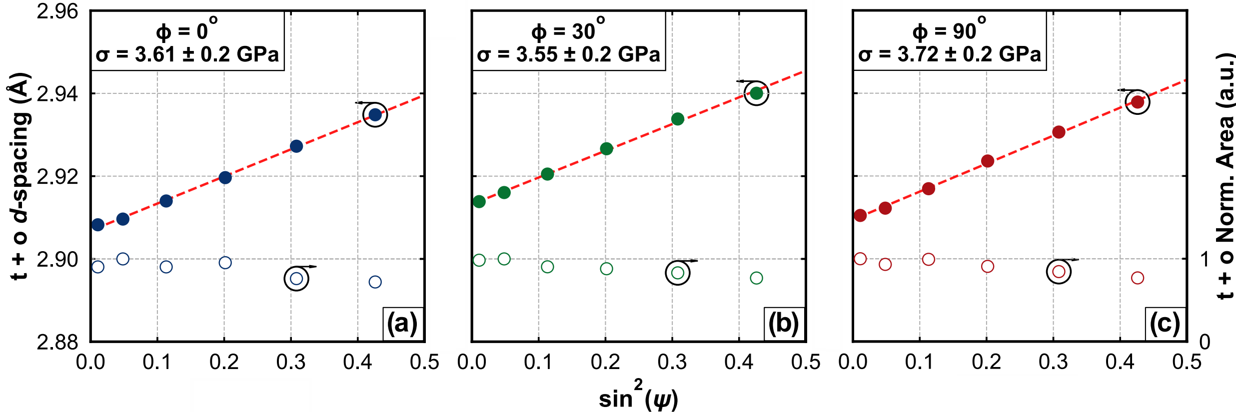

Figure 11.10. Change in t + o *d*-spacing (closed points, left axis) and t + o normalized area (open points, right axis) with ψ angle relative to film normal fit from area detector XRD patterns measured with φ rotational angle set at (a) 0°, (b) 30°, and (c) 90°. The linear fits (red dotted lines) plotted through the *d*-spacing data were utilized to calculate the biaxial stress following processing.

Given that the biaxial stresses calculated at each film rotational angle were the same within error, it was concluded that the assumption of a uniform biaxial stress state within the HZO films prepared for this dissertation was valid, as stated in Equation 3.1.

Error Propagation in $\sin^2(\psi)$ Analyses and Picosecond Acoustic Measurements. With assumptions of a uniform biaxial stress state and an isotropic solid confirmed, and data supporting that the $\sin^2(\psi)$ analysis process was resistant to user error, it remained to determine the best manner to propagate measurement errors. Starting with elastic moduli calculations, it was known that there were error contributions from film density, picosecond acoustic, and film thickness measurements. Film density error estimates were provided by GSAS II[252] fitting software, and were typically on the order of ~0.5% of the fit density value. Picosecond acoustic τ delay time errors were extracted from Gaussian positional fits to each acoustic signature, as detailed in Figure 5.12. For film thickness error contributions, measured spatial uniformity errors of ~1.5 % were propagated in place of XRR fitting error (~0.1 %), in order to provide the most conservative error estimates. The XRR beam footprint is larger than the picosecond acoustic fs laser footprint, making it possible that the picosecond acoustic laser probes a region of film that has a thickness that may not be representative of the global film thickness probed by XRR. Thus, utilization of the known

uniformity (measured by spectroscopic ellipsometry during process development on silicon wafers) provides a more conservative estimate of the error associated with the thickness across the entire film. Equations 11.1 - 11.3, shown below, represent the error propagation procedure for the elastic moduli calculations, assuming uncorrelated errors:[312]

$$\sigma_E = 0.76 \times C_{11} \sqrt{\left(\frac{\sigma_\rho}{\rho}\right)^2 + 2\left(\frac{\sigma_{v_L}}{v_L}\right)^2} \quad (11.1)$$

$$\sigma_{v_L} = 2\, v_L \sqrt{\left(\frac{\sigma_d}{d}\right)^2 + \left(\frac{\sigma_\tau}{\tau}\right)^2} \quad (11.2)$$

$$\sigma_\tau = \sqrt{\left(\sigma_{x_{Al/HZO}}\right)^2 + \left(\sigma_{x_{HZO/TaN}}\right)^2} \quad (11.3)$$

Where σ_E is the propagated error for the elastic modulus (assuming no error in the utilized Poisson's ratio in Equation 5.2), C_{11} is the axial normal component of the strain tensor, σ_ρ is the XRR density fit error, ρ is the XRR fit density, σ_{v_L} is the sound velocity error, v_L is the sound velocity, σ_d is the film thickness error from uniformity measurements, d is the film thickness from XRR, σ_τ is the delay time error, τ is the delay time, and $\sigma_{x_{Al/HZO}}$ and $\sigma_{x_{HZO/TaN}}$ are the positional errors from Gaussian fits of the acoustic peaks associated with the Al/HZO and HZO/TaN interfaces.

These elastic moduli error contributions were then propagated into biaxial stress quantities calculated on the crystallized films. Other contributions to error in biaxial stress calculations included the linear intercept and slope errors from orthogonal distance regression fit of the *d*-spacing vs. $\sin^2(\psi)$ data with associated *d*-spacing error from LIPRAS[214] fitting. Error for the stress-free *d*-spacing (d_0) was calculated using Equation 11.4 with an assumption of no error in Poisson's ratio:

$$\sigma_{d_0} = \sqrt{(\sigma_m)^2+(\sigma_b)^2} \quad 11.4$$

Where σ_m is the slope error and σ_b is the intercept error. Error associated with the biaxial stress calculation was then determined using Equation 11.5:

$$\sigma_{\sigma_{||}} = \sigma_{||}\sqrt{\left(\frac{\sigma_E}{E}\right)^2 + \left(\frac{\sigma_{d_0}}{d_0}\right)^2 + \left(\frac{\sigma_b}{b}\right)^2} \quad 11.5$$

Where $\sigma_{\sigma_{||}}$ and $\sigma_{||}$ are the calculated biaxial stress error and biaxial stress, respectively. Equation 11.5 becomes the relevant error propagation expression when Equations 3.2 and 3.3 are combined and simplified to Equation 11.6:

$$\sigma_{||} = \frac{E}{d_0} * \frac{d_\psi - d_0}{(1+v)\,sin^2(\psi)\,-2v} \approx \frac{E}{d_0} * \left(\frac{\partial d_\psi}{\partial\, sin^2(\psi)}\right) \quad 11.6$$

as described by Prevey.[207] In this expression $\frac{d_\psi - d_0}{(1+v)\,sin^2(\psi)-2v}$ is taken as the slope of the linear fit of the d-spacing vs. $\sin^2(\psi)$ data.

References

[1] T.S. Böscke, J. Müller, D. Bräuhaus, U. Schröder, and U. Böttger, Appl. Phys. Lett. **99**, 102903 (2011).

[2] J. Müller, T.S. Böscke, D. Bräuhaus, U. Schröder, U. Böttger, J. Sundqvist, P. Kücher, T. Mikolajick, and L. Frey, Appl. Phys. Lett. **99**, 112901 (2011).

[3] J. Müller, T.S. Böscke, U. Schröder, S. Mueller, D. Bräuhaus, U. Böttger, L. Frey, and T. Mikolajick, Nano Lett. **12**, 4318 (2012).

[4] J.R. Anderson, Transactions of the American Institute of Electrical Engineers, Part I: Communication and Electronics **71**, 395 (1953).

[5] V. Garcia and M. Bibes, Nat. Commun. **5**, 4289 (2014).

[6] D. Berlincourt and H.H.A. Krueger, J. Appl. Phys. **30**, 1804 (1959).

[7] P.M. Chaplya and G.P. Carman, J. Appl. Phys. **90**, 5278 (2001).

[8] D.L. Polla, Microelectron. Eng. **29**, 51 (1995).

[9] B. Xu, L.E. Cross, and J.J. Bernstein, Thin Solid Films **377–378**, 712 (2000).

[10] N. Setter, D. Damjanovic, L. Eng, G. Fox, S. Gevorgian, S. Hong, A. Kingon, H. Kohlstedt, N.Y. Park, G.B. Stephenson, I. Stolitchnov, A.K. Taganstev, D.V. Taylor, T. Yamada, and S. Streiffer, J. Appl. Phys. **100**, 051606 (2006).

[11] A.I. Khan, K. Chatterjee, B. Wang, S. Drapcho, L. You, C. Serrao, S.R. Bakaul, R. Ramesh, and S. Salahuddin, Nat. Mater. **14**, 182 (2015).

[12] D.W. Chapman, J. Appl. Phys. **40**, 2381 (1969).

[13] M.H. Francombe, Thin Solid Films **13**, 413 (1972).

[14] W.J. Merz, Phys. Rev. **95**, 690 (1954).

[15] T. Mitsui and J. Furuichi, Phys. Rev. **90**, 193 (1953).

[16] B. Jaffe, W.R. Cook, and H. Jaffe, *Piezoelectric Ceramics* (R.A.N. Publishers, Ohio, U. S. A., 1971).

[17] A.J. Moulson and J.M. Herbert, *Electroceramics* (Chapman and Hall, New York, New York, 1990).

[18] S.M. Yang, J.Y. Jo, D.J. Kim, H. Sung, T.W. Noh, H.N. Lee, J.-G. Yoon, and T.K. Song, Appl. Phys. Lett. **92**, 252901 (2008).

[19] K. Kim, Korean. J. Mater. Res. **27**, 484 (2017).

[20] S. Hong, E.L. Colla, E. Kim, D.V. Taylor, A.K. Tagantsev, P. Muralt, K. No, and N. Setter, J. Appl. Phys. **86**, 607 (1999).

[21] A.K. Tagantsev, I. Stolichnov, E.L. Colla, and N. Setter, J. Appl. Phys. **90**, 1387 (2001).

[22] E.L. Colla, I. Stolichnov, P.E. Bradely, and N. Setter, Appl. Phys. Lett. **82**, 1604 (2003).

[23] A.K. Tagantsev, Ferroelectrics **184**, 79 (1996).

[24] S. Ducharme, V.M. Fridkin, A.V. Bune, S.P. Palto, L.M. Blinov, N.N. Petukhova, and S.G. Yudin, Phys. Rev. Lett. **84**, 175 (2000).

[25] J.S. Liu, S.R. Zhang, H.Z. Zeng, C.T. Yang, and Y. Yuan, Phys. Rev. B **72**, 172101 (2005).

[26] Th. Michael, S. Trimper, and J.M. Wesselinowa, Phys. Rev. B **74**, 214113 (2006).

[27] W. Chen and C.S. Lynch, Acta Mater. **46**, 5303 (1998).

[28] T.J. Yang, V. Gopalan, P.J. Swart, and U. Mohideen, Phys. Rev. Lett. **82**, 4106 (1999).

[29] D. Damjanovic, Rep. Prog. Phys. **61**, 1267 (1998).

[30] J.F. Scott, J. Phys.: Condens. Matter **20**, 021001 (2008).

[31] R.A. Moore, J. Benedetto, and B.J. Rod, IEEE Trans. Nucl. Sci. **40**, 1591 (1993).

[32] J.F. Scott, L.D. McMillan, and C.A. Araujo, Ferroelectrics **93**, 31 (1989).

[33] J.A. Rodriguez, K. Remack, K. Boku, K.R. Udayakumar, S. Aggarwal, S.R. Summerfelt, F.G. Celii, S. Martin, L. Hall, K. Taylor, T. Moise, H. McAdams, J. McPherson, R. Bailey, G. Fox, and M. Depner, IEEE T. Dev. Mat. Re. **4**, 436 (2004).

[34] E.L. Colla, A.L. Kholkin, D. Taylor, A.K. Tagantsev, K.G. Brooks, and N. Setter, Microelectron. Eng. **29**, 4 (1995).

[35] I.K. Yoo and S.B. Desu, Phys. Status Solidi-A **133**, 565 (1992).

[36] D.P. Vijay and S.B. Desu, J. Electrochem. Soc. **140**, 7 (1993).

[37] I.K. Yoo and S.B. Desu, Mater. Sci. Eng. B **13**, 319 (1992).

[38] J.F. Scott, C.A. Araujo, B.M. Melnick, L.D. McMillan, and R. Zuleeg, J. Appl. Phys. **70**, 382 (1991).

[39] W.L. Warren, D. Dimos, B.A. Tuttle, and D.M. Smyth, J. Am. Ceram. Soc. **77**, 2753 (1994).

[40] W.L. Warren, D. Dimos, B.A. Tuttle, R.D. Nasby, and G.E. Pike, Appl. Phys. Lett. **65**, 1018 (1994).

[41] J. Lee, S. Esayan, A. Safari, and R. Ramesh, Appl. Phys. Lett. **65**, 254 (1994).

[42] E.L. Colla, A.K. Tagantsev, D.V. Taylor, and A.L. Kholkin, Integr. Ferroelectr. **18**, 19 (1997).

[43] T. Nakamura, Y. Nakao, A. Kamisawa, and H. Takasu, Jpn. J. Appl. Phys. **33**, 5207 (1994).

[44] I. Stolichnov, A. Tagantsev, N. Setter, J.S. Cross, and M. Tsukada, Appl. Phys. Lett. **74**, 3552 (1999).

[45] L. Chen, V. Nagarajan, R. Ramesh, and A.L. Roytburd, J. Appl. Phys. **94**, 5147 (2003).

[46] K. Lefki and G.J.M. Dormans, J. Appl. Phys. **76**, 1764 (1994).

[47] N. Bassiri-Gharb, I. Fujii, E. Hong, S. Trolier-McKinstry, D.V. Taylor, and D. Damjanovic, J. Electroceram. **19**, 49 (2007).

[48] H. Kishi, Y. Mizuno, and H. Chazono, Jpn. J. Appl. Phys. **42**, 1 (2003).

[49] V. Buscaglia and C.A. Randall, J. Eur. Ceram. Soc. **40**, 3744 (2020).

[50] F.D. Morrison, D.C. Sinclair, J.M.S. Skakle, and A.R. West, J. Am. Ceram. Soc. **81**, 1957 (2005).

[51] C.R. Bowen, H.A. Kim, P.M. Weaver, and S. Dunn, Energy Environ. Sci. **7**, 25 (2014).

[52] R. Bruchhaus, D. Pitzer, M. Schreiter, and W. Wersing, J. Electroceram. **3**, 12 (1999).

[53] G. Sebald, D. Guyomar, and A. Agbossou, Smart Mater. Struct. **18**, 125006 (2009).

[54] M.-M. Zhang, Z. Jia, and T.-L. Ren, Solid-State Electron. **53**, 473 (2009).

[55] L. Goux, G. Russo, N. Menou, J.G. Lisoni, M. Schwitters, V. Paraschiv, D. Maes, C. Artoni, G. Corallo, L. Haspeslagh, D.J. Wouters, R. Zambrano, and C. Muller, IEEE Trans. Electron Dev. **52**, 447 (2005).

[56] V. Garcia, S. Fusil, K. Bouzehouane, S. Enouz-Vedrenne, N.D. Mathur, A. Barthélémy, and M. Bibes, Nature **460**, 81 (2009).

[57] D. Pantel, H. Lu, S. Goetze, P. Werner, D. Jik Kim, A. Gruverman, D. Hesse, and M. Alexe, Appl. Phys. Lett. **100**, 232902 (2012).

[58] J.F. Ihlefeld, D.T. Harris, R. Keech, J.L. Jones, J.-P. Maria, and S. Trolier-McKinstry, J. Am. Ceram. Soc. **99**, 2537 (2016).

[59] M.D. Dennis and R.C. Bradt, J. Appl. Phys. **45**, 1931 (1974).

[60] F. Saurenbach and B.D. Terris, Appl. Phys. Lett. **56**, 1703 (1990).

[61] C.A. Randall, D.J. Barber, and R.W. Whatmore, J. Mater. Sci. **22**, 925 (1987).

[62] A.Yu. Emelyanov and N.A. Pertsev, Phys. Rev. B **68**, 214103 (2003).

[63] J.T. Graham, G.L. Brennecka, P. Ferreira, L. Small, D. Duquette, C. Apblett, S. Landsberger, and J.F. Ihlefeld, J. Appl. Phys. **113**, 124104 (2013).

[64] D.M. Marincel, H.R. Zhang, J. Britson, A. Belianinov, S. Jesse, S.V. Kalinin, L.Q. Chen, W.M. Rainforth, I.M. Reaney, C.A. Randall, and S. Trolier-McKinstry, Phys. Rev. B **91**, 134113 (2015).

[65] D. Zhao, T. Lenz, G.H. Gelinck, P. Groen, D. Damjanovic, D.M. de Leeuw, and I. Katsouras, Nat. Commun. **10**, 2547 (2019).

[66] R.R. Mehta, B.D. Silverman, and J.T. Jacobs, J. Appl. Phys. **44**, 3379 (1973).

[67] P. Wurfel, I.P. Batra, and J.T. Jacobs, Phys. Rev. Lett. **30**, 1218 (1973).

[68] F. Griggio, S. Jesse, A. Kumar, O. Ovchinnikov, H. Kim, T.N. Jackson, D. Damjanovic, S.V. Kalinin, and S. Trolier-McKinstry, Phys. Rev. Lett. **108**, 157604 (2012).

[69] T.M. Shaw, S. Trolier-McKinstry, and P.C. McIntyre, Annu. Rev. Mater. Sci. **30**, 263 (2000).

[70] Y.S. Kim, D.H. Kim, J.D. Kim, Y.J. Chang, T.W. Noh, J.H. Kong, K. Char, Y.D. Park, and S.D. Bu, Appl. Phys. Lett. **86**, 4 (2005).

[71] V. Nagarajan, J. Junquera, J.Q. He, C.L. Jia, R. Waser, K. Lee, Y.K. Kim, S. Baik, T. Zhao, R. Ramesh, Ph. Ghosez, and K.M. Rabe, J. Appl. Phys. **100**, 051609 (2006).

[72] V. Nagarajan, C.L. Jia, H. Kohlstedt, R. Waser, I.B. Misirlioglu, S.P. Alpay, and R. Ramesh, Appl. Phys. Lett. **86**, 192910 (2005).

[73] G.E. Moore, Electronics **38**, 114 (1965).

[74] S.E. Thompson and S. Parthasarathy, Mater. Today **9**, 20 (2006).

[75] K.J. Hubbard and D.G. Schlom, J. Mater. Res. **11**, 2757 (1996).

[76] K. Mistry, R. Chau, C.-H. Choi, G. Ding, K. Fischer, T. Ghani, R. Grover, W. Han, D. Hanken, M. Hattendorf, J. He, C. Allen, J. Hicks, R. Huessner, D. Ingerly, P. Jain, R. James, L. Jong, S. Joshi, C. Kenyon, K. Kuhn, K. Lee, C. Auth, H. Liu, J. Maiz, B. McIntyre, P. Moon, J. Neirynck, S. Pae, C. Parker, D. Parsons, C. Prasad, L. Pipes, B. Beattie, M. Prince, P. Ranade, T. Reynolds, J. Sandford, L. Shifren, J. Sebastian, J. Seiple, D. Simon, S. Sivakumar, P. Smith, D. Bergstrom, C. Thomas, T. Troeger, P. Vandervoorn, S. Williams, K. Zawadzki, M. Bost, M. Brazier, M. Buehler, and A. Cappellani, in *2007 IEEE International Electron Devices Meeting* (IEEE, Washington, DC, 2007), pp. 247–250.

[77] D.G. Schlom, S. Guha, and S. Datta, MRS Bull. **33**, 1017 (2008).

[78] A. Delabie, M. Caymax, B. Brijs, D.P. Brunco, T. Conard, E. Sleeckx, S. Van Elshocht, L.-Å. Ragnarsson, S. De Gendt, and M.M. Heyns, J. Electrochem. Soc. **153**, F180 (2006).

[79] M.H. Park, Y.H. Lee, T. Mikolajick, U. Schroeder, and C.S. Hwang, MRS Comm. **8**, 795 (2018).

[80] B. Max, M. Hoffmann, S. Slesazeck, and T. Mikolajick, in *2018 48th European Solid-State Device Research Conference (ESSDERC)* (2018), pp. 142–145.

[81] C. Mart, A. Viegas, S. Esslinger, M. Czernohorsky, W. Weinreich, D. Mutschall, A. Kaiser, N. Neumann, T. Grossmann, K. Hiller, and L.M. Eng, in *2020 Joint Conference of the IEEE International Frequency Control Symposium and International Symposium on Applications of Ferroelectrics (IFCS-ISAF)* (IEEE, Keystone, CO, USA, 2020), pp. 1–3.

[82] J.F. Ihlefeld, T.S. Luk, S.W. Smith, S.S. Fields, S.T. Jaszewski, W.T. Riffe, S. Bender, C. Constantin, M.V. Ayyasamy, P.V. Balachandran, P. Lu, M.D. Henry, and P.S. Davids, J. Appl. Phys. **128**, 034101 (2020).

[83] Y. Watanabe, H. Ota, S. Migita, Y. Kamimuta, K. Iwamoto, M. Takahashi, A. Ogawa, H. Ito, T. Nabatame, and A. Toriumi, ECS Trans. **11**, 35 (2007).

[84] X. Zhao and D. Vanderbilt, Phys. Rev. B **65**, 233106 (2002).

[85] J. Adam and M.D. Rogers, Acta Cryst. **12**, 951 (1959).

[86] R.E. Hann, P.R. Suitch, and J.L. Pentecost, J. Am. Ceram. Soc. **68**, C (1985).

[87] R. Batra, T.D. Huan, J.L. Jones, G. Rossetti, and R. Ramprasad, J. Phys. Chem. C **121**, 4139 (2017).

[88] O. Ohtaka, H. Fukui, T. Kunisada, T. Fujisawa, K. Funakoshi, W. Utsumi, T. Irifune, K. Kuroda, and T. Kikegawa, J. Am. Ceram. Soc. **84**, 1369 (2004).

[89] C. Adelmann, H. Tielens, D. Dewulf, A. Hardy, D. Pierreux, J. Swerts, E. Rosseel, X. Shi, and S.V. Elshocht, J. Electrochem. Soc. 7 (n.d.).

[90] C. Künneth, R. Materlik, and A. Kersch, J. Appl. Phys. **121**, 205304 (2017).

[91] D. Martin, J. Müller, T. Schenk, T.M. Arruda, A. Kumar, E. Strelcov, E. Yurchuk, S. Müller, D. Pohl, U. Schröder, S.V. Kalinin, and T. Mikolajick, Adv. Mater. **26**, 8198 (2014).

[92] X. Sang, E.D. Grimley, T. Schenk, U. Schroeder, and J.M. LeBeau, Appl. Phys. Lett. **106**, 162905 (2015).

[93] T.D. Huan, V. Sharma, G.A. Rossetti, and R. Ramprasad, Phys. Rev. B **90**, (2014).

[94] S. Clima, D.J. Wouters, C. Adelmann, T. Schenk, U. Schroeder, M. Jurczak, and G. Pourtois, Appl. Phys. Lett. 5 (2014).

[95] W. Ding, Y. Zhang, L. Tao, Q. Yang, and Y. Zhou, Acta Mater. **196**, 556 (2020).

[96] R. Materlik, C. Künneth, and A. Kersch, J. Appl. Phys. **117**, 134109 (2015).

[97] M.H. Park, Y.H. Lee, H.J. Kim, T. Schenk, W. Lee, K.D. Kim, F.P.G. Fengler, T. Mikolajick, U. Schroeder, and C.S. Hwang, Nanoscale **9**, 9973 (2017).

[98] T. Mittmann, F.P.G. Fengler, C. Richter, M.H. Park, T. Mikolajick, and U. Schroeder, Microelectron. Eng. **178**, 48 (2017).

[99] H.J. Kim, M.H. Park, Y.J. Kim, Y.H. Lee, W. Jeon, T. Gwon, T. Moon, K.D. Kim, and C.S. Hwang, Appl. Phys. Lett. **105**, 192903 (2014).

[100] P. Polakowski and J. Müller, Appl. Phys. Lett. **106**, 232905 (2015).

[101] M. Lederer, T. Kämpfe, R. Olivo, D. Lehninger, C. Mart, S. Kirbach, T. Ali, P. Polakowski, L. Roy, and K. Seidel, Appl. Phys. Lett. **115**, 222902 (2019).

[102] H.-J. Lee, M. Lee, K. Lee, J. Jo, H. Yang, Y. Kim, S.C. Chae, U. Waghmare, and J.H. Lee, Science **369**, 1343 (2020).

[103] Y.H. Lee, H.J. Kim, T. Moon, K.D. Kim, S.D. Hyun, H.W. Park, Y.B. Lee, M.H. Park, and C.S. Hwang, Nanotechnology **28**, 305703 (2017).

[104] M. Hyuk Park, H. Joon Kim, Y. Jin Kim, W. Lee, T. Moon, and C. Seong Hwang, Appl. Phys. Lett. **102**, 242905 (2013).

[105] S.S. Cheema, D. Kwon, N. Shanker, R. dos Reis, S.-L. Hsu, J. Xiao, H. Zhang, R. Wagner, A. Datar, M.R. McCarter, C.R. Serrao, A.K. Yadav, G. Karbasian, C.-H. Hsu, A.J. Tan, L.-C. Wang, V. Thakare, X. Zhang, A. Mehta, E. Karapetrova, R.V. Chopdekar, P. Shafer, E. Arenholz, C. Hu, R. Proksch, R. Ramesh, J. Ciston, and S. Salahuddin, Nature **580**, 478 (2020).

[106] D. Martin, E. Yurchuk, S. Müller, J. Müller, J. Paul, J. Sundquist, S. Slesazeck, T. Schlösser, R. van Bentum, M. Trentzsch, U. Schröder, and T. Mikolajick, Solid-State Electron. **88**, 65 (2013).

[107] M. Hoffmann, M. Pešić, K. Chatterjee, A.I. Khan, S. Salahuddin, S. Slesazeck, U. Schroeder, and T. Mikolajick, Adv. Funct. Mater. **26**, 8643 (2016).

[108] M. Pešić, U. Schroeder, S. Slesazeck, and T. Mikolajick, IEEE T. Device Mat. Re. **18**, 154 (2018).

[109] S.J. Kim, J. Mohan, C.D. Young, L. Colombo, J. Kim, S.R. Summerfelt, and T. San, in *2018 IEEE International Memory Workshop (IMW)* (2018), pp. 1–4.

[110] T. Mittmann, M. Materano, P.D. Lomenzo, M.H. Park, I. Stolichnov, M. Cavalieri, C. Zhou, C.-C. Chung, J.L. Jones, T. Szyjka, M. Müller, A. Kersch, T. Mikolajick, and U. Schroeder, Adv. Mater. Interfaces **6**, 1900042 (2019).

[111] A. Pal, V.K. Narasimhan, S. Weeks, K. Littau, D. Pramanik, and T. Chiang, Appl. Phys. Lett. **110**, 022903 (2017).

[112] L. Xu, T. Nishimura, S. Shibayama, T. Yajima, S. Migita, and A. Toriumi, J. Appl. Phys. **122**, 124104 (2017).

[113] M.H. Park, T. Schenk, C.M. Fancher, E.D. Grimley, C. Zhou, C. Richter, J.M. LeBeau, J.L. Jones, T. Mikolajick, and U. Schroeder, J. Mater. Chem. C **5**, 4677 (2017).

[114] R. Batra, T.D. Huan, G.A. Rossetti, and R. Ramprasad, Chem. Mater. **29**, 9102 (2017).

[115] T. Shiraishi, K. Katayama, T. Yokouchi, T. Shimizu, T. Oikawa, O. Sakata, H. Uchida, Y. Imai, T. Kiguchi, T.J. Konno, and H. Funakubo, Appl. Phys. Lett. **108**, 262904 (2016).

[116] T. Shiraishi, K. Katayama, T. Yokouchi, T. Shimizu, T. Oikawa, O. Sakata, H. Uchida, Y. Imai, T. Kiguchi, T.J. Konno, and H. Funakubo, Mat. Sci. Semicon. Proc. **70**, 239 (2017).

[117] M. Hoffmann, U. Schroeder, T. Schenk, T. Shimizu, H. Funakubo, O. Sakata, D. Pohl, M. Drescher, C. Adelmann, R. Materlik, A. Kersch, and T. Mikolajick, J. Appl. Phys. **118**, 072006 (2015).

[118] J.-D. Luo, H.-X. Zhang, Z.-Y. Wang, S.-S. Gu, Y.-T. Yeh, H.-T. Chung, K.-C. Chuang, C.-Y. Liao, W.-S. Li, Y.-S. Li, K.-S. Li, M.-H. Lee, and H.-C. Cheng, Jpn. J. Appl. Phys. **58**, SDDE07 (2019).

[119] L. Baumgarten, T. Szyjka, T. Mittmann, M. Materano, Y. Matveyev, C. Schlueter, T. Mikolajick, U. Schroeder, and M. Müller, Appl. Phys. Lett. **118**, 032903 (2021).

[120] M. Materano, T. Mittmann, P.D. Lomenzo, C. Zhou, J.L. Jones, M. Falkowski, A. Kersch, T. Mikolajick, and U. Schroeder, ACS Appl. Electron. Mater. **2**, 3618 (2020).

[121] D.R. Islamov, T.V. Perevalov, V.A. Gritsenko, C.H. Cheng, and A. Chin, Appl. Phys. Lett. **106**, 102906 (2015).

[122] D.R. Islamov, T.M. Zalyalov, O.M. Orlov, V.A. Gritsenko, and G.Ya. Krasnikov, Appl. Phys. Lett. **117**, 162901 (2020).

[123] S. Mueller, C. Adelmann, A. Singh, S.V. Elshocht, U. Schroeder, and T. Mikolajick, ECS J. Solid State Sci. Technol. **1**, N123 (2012).

[124] U. Schroeder, C. Richter, M.H. Park, T. Schenk, M. Pešić, M. Hoffmann, F.P.G. Fengler, D. Pohl, B. Rellinghaus, C. Zhou, C.-C. Chung, J.L. Jones, and T. Mikolajick, Inorg. Chem. **57**, 2752 (2018).

[125] T. Schenk, C.M. Fancher, M.H. Park, C. Richter, C. Künneth, A. Kersch, J.L. Jones, T. Mikolajick, and U. Schroeder, Adv. Electron. Mater. **5**, 1900303 (2019).

[126] J. Müller, U. Schröder, T.S. Böscke, I. Müller, U. Böttger, L. Wilde, J. Sundqvist, M. Lemberger, P. Kücher, T. Mikolajick, and L. Frey, J. Appl. Phys. **110**, 114113 (2011).

[127] F. Huang, X. Chen, X. Liang, J. Qin, Y. Zhang, T. Huang, Z. Wang, B. Peng, P. Zhou, H. Lu, L. Zhang, L. Deng, M. Liu, Q. Liu, H. Tian, and L. Bi, Phys. Chem. Chem. Phys. **19**, 3486 (2017).

[128] S. Mueller, J. Mueller, A. Singh, S. Riedel, J. Sundqvist, U. Schroeder, and T. Mikolajick, Adv. Funct. Mater. **22**, 2412 (2012).

[129] H. Ryu, K. Xu, J. Kim, S. Kang, J. Guo, and W. Zhu, IEEE T. Electron. Dev. **66**, 2359 (2019).

[130] M.H. Park, H.J. Kim, Y.J. Kim, Y.H. Lee, T. Moon, K.D. Kim, S.D. Hyun, F. Fengler, U. Schroeder, and C.S. Hwang, ACS Appl. Mater. Inter. **8**, 15466 (2016).

[131] M.H. Park, Y.H. Lee, H.J. Kim, Y.J. Kim, T. Moon, K.D. Kim, J. Müller, A. Kersch, U. Schroeder, T. Mikolajick, and C.S. Hwang, Adv. Mater. **27**, 1811 (2015).

[132] U. Schroeder, E. Yurchuk, J. Müller, D. Martin, T. Schenk, P. Polakowski, C. Adelmann, M.I. Popovici, S.V. Kalinin, and T. Mikolajick, Jpn. J. Appl. Phys. **53**, 08LE02 (2014).

[133] T. Mimura, T. Shimizu, H. Uchida, O. Sakata, and H. Funakubo, Appl. Phys. Lett. **113**, 102901 (2018).

[134] C. Richter, T. Schenk, M.H. Park, F.A. Tscharntke, E.D. Grimley, J.M. LeBeau, C. Zhou, C.M. Fancher, J.L. Jones, T. Mikolajick, and U. Schroeder, Adv. Electron. Mater. **3**, 1700131 (2017).

[135] M.G. Kozodaev, A.G. Chernikova, E.V. Korostylev, M.H. Park, R.R. Khakimov, C.S. Hwang, and A.M. Markeev, J. Appl. Phys. **125**, 034101 (2019).

[136] P.D. Lomenzo, Q. Takmeel, C. Zhou, C.-C. Chung, S. Moghaddam, J.L. Jones, and T. Nishida, Appl. Phys. Lett. **107**, 242903 (2015).

[137] T. Mittmann, M. Materano, S.-C. Chang, I. Karpov, T. Mikolajick, and U. Schroeder, in *2020 IEEE International Electron Devices Meeting (IEDM)* (2020), p. 18.4.1-18.4.4.

[138] S. Migita, H. Ota, K. Shibuya, H. Yamada, A. Sawa, T. Matsukawa, and A. Toriumi, Jpn. J. Appl. Phys. **58**, SBBA07 (2019).

[139] J. Schmitz, Surf. and Coat. Tech. **343**, 83 (2018).

[140] M.H. Park, C.-C. Chung, T. Schenk, C. Richter, K. Opsomer, C. Detavernier, C. Adelmann, J.L. Jones, T. Mikolajick, and U. Schroeder, Adv. Electron. Mater. **4**, 1800091 (2018).

[141] D. Lehninger, R. Olivo, T. Ali, M. Lederer, T. Kämpfe, C. Mart, K. Biedermann, K. Kühnel, L. Roy, M. Kalkani, and K. Seidel, Phys. Status Solidi A **217**, 1900840 (2020).

[142] H.A. Hsain, Y. Lee, G. Parsons, and J.L. Jones, Appl. Phys. Lett. **116**, 192901 (2020).

[143] A.E.O. Persson, R. Athle, P. Littow, K.-M. Persson, J. Svensson, M. Borg, and L.-E. Wernersson, Appl. Phys. Lett. **116**, 062902 (2020).

[144] T. Mimura, T. Shimizu, H. Uchida, and H. Funakubo, Appl. Phys. Lett. **116**, 062901 (2020).

[145] R. Ruh, H.J. Garrett, R.F. Domagala, and N.M. Tallan, J. Am. Ceram. Soc. **51**, 23 (1968).

[146] R. Ruh and P.W.R. Corfield, J. Am. Ceram. Soc. **53**, 126 (1970).

[147] R.C. Garvie, J. Phys. Chem. **69**, 1238 (1965).

[148] R.I. Hegde, D.H. Triyoso, S.B. Samavedam, and B.E. White, J. Appl. Phys. **101**, 074113 (2007).

[149] S.W. Smith, A.R. Kitahara, M.A. Rodriguez, M.D. Henry, M.T. Brumbach, and J.F. Ihlefeld, Appl. Phys. Lett. **110**, 072901 (2017).

[150] S.-T. Fan, Y.-W. Chen, and C.W. Liu, J. Phys. D: Appl. Phys. **53**, 23LT01 (2020).

[151] S.J. Kim, D. Narayan, J.-G. Lee, J. Mohan, J.S. Lee, J. Lee, H.S. Kim, Y.-C. Byun, A.T. Lucero, C.D. Young, S.R. Summerfelt, T. San, L. Colombo, and J. Kim, Appl. Phys. Lett. **111**, 242901 (2017).

[152] T. Schenk, A. Bencan, G. Drazic, O. Condurache, N. Valle, B.E. Adib, N. Aruchamy, T. Granzow, E. Defay, and S. Glinsek, Appl. Phys. Lett. **118**, 162902 (2021).

[153] M. Hyuk Park, H. Joon Kim, Y. Jin Kim, T. Moon, and C. Seong Hwang, Appl. Phys. Lett. **104**, 072901 (2014).

[154] E.D. Grimley, T. Schenk, X. Sang, M. Pešić, U. Schroeder, T. Mikolajick, and J.M. LeBeau, Adv. Electron. Mater. **2**, 1600173 (2016).

[155] W. Hamouda, A. Pancotti, C. Lubin, L. Tortech, C. Richter, T. Mikolajick, U. Schroeder, and N. Barrett, J. Appl. Phys. **127**, 064105 (2020).

[156] W. Hamouda, C. Lubin, S. Ueda, Y. Yamashita, O. Renault, F. Mehmood, T. Mikolajick, U. Schroeder, R. Negrea, and N. Barrett, Appl. Phys. Lett. **116**, 252903 (2020).

[157] P.D. Lomenzo, P. Zhao, Q. Takmeel, S. Moghaddam, T. Nishida, M. Nelson, C.M. Fancher, E.D. Grimley, X. Sang, J.M. LeBeau, and J.L. Jones, J. Vac. Sci. Technol. B **32**, 03D123 (2014).

[158] P.D. Lomenzo, Q. Takmeel, C. Zhou, C.M. Fancher, E. Lambers, N.G. Rudawski, J.L. Jones, S. Moghaddam, and T. Nishida, J. Appl. Phys. **117**, 134105 (2015).

[159] Y. Li, R. Liang, B. Xiong, H. Liu, R. Zhao, J. Li, T. Liu, Y. Pang, H. Tian, Y. Yang, and T.-L. Ren, Appl. Phys. Lett. **114**, 052902 (2019).

[160] T. Szyjka, L. Baumgarten, T. Mittmann, Y. Matveyev, C. Schlueter, T. Mikolajick, U. Schroeder, and M. Müller, Phys. Status Solidi-R **15**, 2100027 (2021).

[161] T. Mittmann, T. Szyjka, H. Alex, M.C. Istrate, P.D. Lomenzo, L. Baumgarten, M. Müller, J.L. Jones, L. Pintilie, T. Mikolajick, and U. Schroeder, Phys. Status Solidi-R **15**, 2100012 (2021).

[162] Y. Goh, S.H. Cho, S.-H.K. Park, and S. Jeon, Nanoscale **12**, 9024 (2020).

[163] S. Starschich, D. Griesche, T. Schneller, R. Waser, and U. Böttger, Appl. Phys. Lett. **104**, 202903 (2014).

[164] S. Starschich, S. Menzel, and U. Böttger, Appl. Phys. Lett. **108**, 032903 (2016).

[165] S. Starschich, S. Menzel, and U. Böttger, J. Appl. Phys. **121**, 154102 (2017).

[166] T. Shimizu, T. Yokouchi, T. Oikawa, T. Shiraishi, T. Kiguchi, A. Akama, T.J. Konno, A. Gruverman, and H. Funakubo, Appl. Phys. Lett. **106**, 112904 (2015).

[167] Y.-C. Lin, F. McGuire, and A.D. Franklin, J. Vac. Sci. Technol. B **36**, 011204 (2018).

[168] K. Ni, J. Smith, H. Ye, B. Grisafe, G.B. Rayner, A. Kummel, and S. Datta, in *2019 IEEE International Electron Devices Meeting (IEDM)* (IEEE, San Francisco, CA, USA, 2019), p. 28.8.1-28.8.4.

[169] K. Ni, J.A. Smith, B. Grisafe, T. Rakshit, B. Obradovic, J.A. Kittl, M. Rodder, and S. Datta, in *2018 IEEE International Electron Devices Meeting (IEDM)* (IEEE, San Francisco, CA, 2018), p. 13.2.1-13.2.4.

[170] T.S. Böscke, St. Teichert, D. Bräuhaus, J. Müller, U. Schröder, U. Böttger, and T. Mikolajick, Appl. Phys. Lett. **99**, 112904 (2011).

[171] M. Pešić, F.P.G. Fengler, L. Larcher, A. Padovani, T. Schenk, E.D. Grimley, X. Sang, J.M. LeBeau, S. Slesazeck, U. Schroeder, and T. Mikolajick, Adv. Funct. Mater. **26**, 4601 (2016).

[172] F.P.G. Fengler, M. Pešić, S. Starschich, T. Schneller, C. Künneth, U. Böttger, H. Mulaosmanovic, T. Schenk, M.H. Park, R. Nigon, P. Muralt, T. Mikolajick, and U. Schroeder, Adv. Electron. Mater. **3**, 1600505 (2017).

[173] D.R. Islamov, V.A. Gritsenko, T.V. Perevalov, V.A. Pustovarov, O.M. Orlov, A.G. Chernikova, A.M. Markeev, S. Slesazeck, U. Schroeder, T. Mikolajick, and G.Y. Krasnikov, Acta Mater. **166**, 47 (2019).

[174] T. Schenk, U. Schroeder, M. Pešić, M. Popovici, Y.V. Pershin, and T. Mikolajick, ACS Appl. Mater. Inter. **6**, 19744 (2014).

[175] A. Chouprik, M. Spiridonov, S. Zarubin, R. Kirtaev, V. Mikheev, Y. Lebedinskii, S. Zakharchenko, and D. Negrov, ACS Appl. Electron. Mater. **1**, 275 (2019).

[176] T. Shimizu, T. Mimura, T. Kiguchi, T. Shiraishi, T. Konno, Y. Katsuya, O. Sakata, and H. Funakubo, Appl. Phys. Lett. **113**, 212901 (2018).

[177] P.D. Lomenzo, S. Slesazeck, M. Hoffmann, T. Mikolajick, U. Schroeder, B. Max, and T. Mikolajick, in *2019 19th Non-Volatile Memory Technology Symposium (NVMTS)* (IEEE, Durham, NC, USA, 2019), pp. 1–8.

[178] T. Schenk, M. Hoffmann, J. Ocker, M. Pešić, T. Mikolajick, and U. Schroeder, ACS Appl. Mater. Inter. **7**, 20224 (2015).

[179] D. Zhou, J. Xu, Q. Li, Y. Guan, F. Cao, X. Dong, J. Müller, T. Schenk, and U. Schröder, Appl. Phys. Lett. **103**, 192904 (2013).

[180] S. Li, D. Zhou, Z. Shi, M. Hoffmann, T. Mikolajick, and U. Schroeder, Adv. Electron. Mater. 2000264 (2020).

[181] F.P.G. Fengler, M. Hoffmann, S. Slesazeck, T. Mikolajick, and U. Schroeder, J. Appl. Phys. **123**, 204101 (2018).

[182] A.K. Tagantsev and I.A. Stolichnov, Appl. Phys. Lett. **74**, 1326 (1999).

[183] E. Bouyssou, P. Leduc, G. Guégan, and R. Jérisian, J. Phys.: Conf. Ser. **10**, 317 (2005).

[184] S.R. Bradley, K.P. McKenna, and A.L. Shluger, Microelectron. Eng. **109**, 346 (2013).

[185] S.W. Smith, M.D. Henry, M.T. Brumbach, M.A. Rodriguez, and J.F. Ihlefeld, Appl. Phys. Lett. **113**, 182904 (2018).

[186] R.L. Puurunen, J. Appl. Phys. **97**, 121301 (2005).

[187] J.W. Elam, M.D. Groner, and S.M. George, Rev. Sci. Instrum. **73**, 2981 (2002).

[188] M. Ritala, M. Leskelä, J.-P. Dekker, C. Mutsaers, P.J. Soininen, and J. Skarp, Chem. Vapor. Depos. **5**, 7 (1999).

[189] L. Reijnen, B. Meester, F. de Lange, J. Schoonman, and A. Goossens, Chem. Mater. **17**, 2724 (2005).

[190] S.K. Kim and C.S. Hwang, Electrochem. Solid-State Lett. **11**, G9 (2008).

[191] M. Materano, C. Richter, T. Mikolajick, and U. Schroeder, J. of Vac. Sci. Technol. A **38**, 022402 (2020).

[192] J. Hur, N. Tasneem, G. Choe, P. Wang, Z. Wang, A.I. Khan, and S. Yu, Nanotechnology **31**, 505707 (2020).

[193] S.L. Weeks, A. Pal, V.K. Narasimhan, K.A. Littau, and T. Chiang, ACS Appl. Mater. Inter. **9**, 13440 (2017).

[194] D.M. Hausmann, E. Kim, J. Becker, and R.G. Gordon, Chem. Mater. **14**, 4350 (2002).

[195] E.A. Scott, S.W. Smith, M.D. Henry, C.M. Rost, A. Giri, J.T. Gaskins, S.S. Fields, S.T. Jaszewski, J.F. Ihlefeld, and P.E. Hopkins, Appl. Phys. Lett. **113**, 192901 (2018).

[196] C. Mart, K. Kühnel, T. Kämpfe, M. Czernohorsky, M. Wiatr, S. Kolodinski, and W. Weinreich, ACS Appl. Electron. Mater. **1**, 2612 (2019).

[197] K.D. Kim, Y.H. Lee, T. Gwon, Y.J. Kim, H.J. Kim, T. Moon, S.D. Hyun, H.W. Park, M.H. Park, and C.S. Hwang, Nano Energy **39**, 390 (2017).

[198] K.D. Kim, M.H. Park, H.J. Kim, Y.J. Kim, T. Moon, Y.H. Lee, S.D. Hyun, T. Gwon, and C.S. Hwang, J. Mater. Chem. C **4**, 6864 (2016).

[199] T. Onaya, T. Nabatame, N. Sawamoto, A. Ohi, N. Ikeda, T. Nagata, and A. Ogura, Microelectron. Eng. **215**, 111013 (2019).

[200] J. Hur, P. Wang, N. Tasneem, Z. Wang, A.I. Khan, and S. Yu, J. Mater. Res. **36**, 1206 (2021).

[201] T. Onaya, T. Nabatame, Y.C. Jung, H. Hernandez-Arriaga, J. Mohan, H.S. Kim, N. Sawamoto, C.-Y. Nam, E.H.R. Tsai, T. Nagata, J. Kim, and A. Ogura, APL Mater. **9**, 031111 (2021).

[202] V.K. Narasimhan, M.E. McBriarty, D. Passarello, V. Adinolfi, M.F. Toney, A. Mehta, and K.A. Littau, Phys. Status Solidi-R 2000598 (2021).

[203] J.F. Shepard, S. Trolier-McKinstry, M.A. Hendrickson, and R. Zeto, in *ISAF '96. Proceedings of the Tenth IEEE International Symposium on Applications of Ferroelectrics* (1996), pp. 161–165 vol.1.

[204] G.L. Brennecka, W. Huebner, B.A. Tuttle, and P.G. Clem, J. Am. Ceram. Soc. **87**, 1459 (2004).

[205] E.D. Specht, H.-M. Christen, D.P. Norton, and L.A. Boatner, Phys. Rev. Lett. **80**, 4317 (1998).

[206] K.J. Choi, Science **306**, 1005 (2004).

[207] P.S. Prevey, ASM Handbook: Materials Characterization **10**, (1986).

[208] J. Keckes, J. Appl. Crystallogr. **38**, 311 (2005).

[209] M. Birkholz, *Thin Film Analysis by X-Ray Scattering* (Wiley - VCH, KGaA, Weinheim, 2006).

[210] G. Abadias, E. Chason, J. Keckes, M. Sebastiani, G.B. Thompson, E. Barthel, G.L. Doll, C.E. Murray, C.H. Stoessel, and L. Martinu, J. Vac. Sci. Technol. A **36**, 020801 (2018).

[211] Q. Zeng, A.R. Oganov, A.O. Lyakhov, C. Xie, X. Zhang, J. Zhang, Q. Zhu, B. Wei, I. Grigorenko, L. Zhang, and L. Cheng, Acta Crystallogr. C Struct. Chem. **70**, 76 (2014).

[212] J. Kieffer, V. Valls, N. Blanc, and C. Hennig, J. Synchrotron Radiat. **27**, 558 (2020).

[213] B. He, *Two-Dimensional X-Ray Diffraction*, 2nd ed. (John Wiley & Sons Inc., Hoboken, NJ, 2018).

[214] G. Esteves, K. Ramos, C.M. Fancher, and J.L. Jones, *LIPRAS: Line-Profile Analysis Software* (10.13140/RG.2.2.29970.25282/3).

[215] P.A. Flinn, D.S. Gardner, and W.D. Nix, IEEE T. Electron. Dev. **34**, 689 (1987).

[216] G.C.A.M. Janssen, M.M. Abdalla, F. van Keulen, B.R. Pujada, and B. van Venrooy, Thin Solid Films **517**, 1858 (2009).

[217] G. Stoney, P. R. Soc. London **82**, (1909).

[218] S. Shiri, P. Ashtijoo, A. Odeshi, and Q. Yang, Surf. and Coat. Tech. **308**, 98 (2016).

[219] B. Freund and S. Suresh, *Thin Film Materials; Stress, Defect Formation, and Surface Evolution* (Cambridge University Press, New York, 2006).

[220] L.E. Garn and E.J. Sharp, J. Appl. Phys. **53**, 8974 (1982).

[221] M. Hoffmann, U. Schroeder, C. Künneth, A. Kersch, S. Starschich, Ulrich Böttger, and T. Mikolajick, Nano Energy **18**, 154 (2015).

[222] S. Pandya, G. Velarde, L. Zhang, and L.W. Martin, Phys. Rev. Mater. **2**, 124405 (2018).

[223] C. Mart, M. Czernohorsky, S. Zybell, T. Kämpfe, and W. Weinreich, Appl. Phys. Lett. **113**, 122901 (2018).

[224] B. Hanrahan, Y. Espinal, C. Neville, R. Rudy, M. Rivas, A. Smith, M.T. Kesim, and S.P. Alpay, J. Appl. Phys. **123**, 124104 (2018).

[225] C. Mart, K. Kühnel, T. Kämpfe, S. Zybell, and W. Weinreich, Appl. Phys. Lett. **114**, 102903 (2019).

[226] E.J. Sharp and L.E. Garn, J. Appl. Phys. **53**, 8980 (1982).

[227] S. Jachalke, T. Schenk, M.H. Park, U. Schroeder, T. Mikolajick, H. Stöcker, E. Mehner, and D.C. Meyer, Appl. Phys. Lett. **112**, 142901 (2018).

[228] P.D. Lomenzo, R. Alcala, C. Richter, S. Li, T. Mikolajick, and U. Schroeder, Appl. Phys. Lett. **119**, 112903 (2021).

[229] S. Mueller, S.R. Summerfelt, J. Muller, U. Schroeder, and T. Mikolajick, IEEE Electr. Device L. **33**, 1300 (2012).

[230] M. Hoffmann, F.P.G. Fengler, M. Herzig, T. Mittmann, B. Max, U. Schroeder, R. Negrea, P. Lucian, S. Slesazeck, and T. Mikolajick, Nature **565**, 464 (2019).

[231] F. Ambriz-Vargas, G. Kolhatkar, R. Thomas, R. Nouar, A. Sarkissian, C. Gomez-Yáñez, M.A. Gauthier, and A. Ruediger, Appl. Phys. Lett. **110**, 093106 (2017).

[232] Y. Goh and S. Jeon, Nanotechnology **29**, 335201 (2018).

[233] X. Tian, S. Shibayama, T. Nishimura, T. Yajima, S. Migita, and A. Toriumi, Appl. Phys. Lett. **112**, 102902 (2018).

[234] S.S. Cheema, D. Kwon, N. Shanker, R. dos Reis, S.-L. Hsu, J. Xiao, H. Zhang, R. Wagner, A. Datar, M.R. McCarter, C.R. Serrao, A.K. Yadav, G. Karbasian, C.-H. Hsu, A.J. Tan, L.-C. Wang, V. Thakare, X. Zhang, A. Mehta, E. Karapetrova, R.V. Chopdekar, P. Shafer, E. Arenholz, C. Hu, R. Proksch, R. Ramesh, J. Ciston, and S. Salahuddin, Nature **580**, 478 (2020).

[235] H.J. Kim, M.H. Park, Y.J. Kim, Y.H. Lee, T. Moon, K.D. Kim, S.D. Hyun, and C.S. Hwang, Nanoscale **8**, 1383 (2016).

[236] P. Buragohain, C. Richter, T. Schenk, H. Lu, T. Mikolajick, U. Schroeder, and A. Gruverman, Appl. Phys. Lett. **112**, 222901 (2018).

[237] R. Ramesh, H. Gilchrist, T. Sands, V.G. Keramidas, R. Haakenaasen, and D.K. Fork, Appl. Phys. Lett. **63**, 3592 (1993).

[238] R. Dat, D.J. Lichtenwalner, O. Auciello, and A.I. Kingon, Appl. Phys. Lett. **64**, 2673 (1994).

[239] H.N. Al-Shareef, A.I. Kingon, X. Chen, K.R. Bellur, and O. Auciello, J. Mater. Res. **9**, 2968 (1994).

[240] M.H. Park, H.J. Kim, Y.J. Kim, W. Jeon, T. Moon, and C.S. Hwang, Phys. Status Solidi-R **8**, 532 (2014).

[241] Y. Ding, Y. Chen, K.C. Pradel, M. Liu, and Z. Lin Wang, J. Appl. Phys. **120**, 214302 (2016).

[242] D.V. Taylor and D. Damjanovic, J. Appl. Phys. **82**, 1973 (1997).

[243] A.K. Tagantsev, M. Landivar, E. Colla, and N. Setter, J. Appl. Phys. **78**, 2623 (1995).

[244] J.P. Bonnet, J. Nowotny, M. Onillon, and I. Sikora, Oxid. Met. **13**, 273 (1979).

[245] L. Chen, T.-Y. Wang, Y.-W. Dai, M.-Y. Cha, H. Zhu, Q.-Q. Sun, S.-J. Ding, P. Zhou, L. Chua, and D.W. Zhang, Nanoscale **10**, 15826 (2018).

[246] S. Kirbach, K. Kühnel, and W. Weinreich, in *2018 IEEE 18th International Conference on Nanotechnology (IEEE-NANO)* (2018), pp. 1–4.

[247] M. Hoffmann, B. Max, T. Mittmann, U. Schroeder, S. Slesazeck, and T. Mikolajick, in *2018 IEEE International Electron Devices Meeting (IEDM)* (2018), p. 31.6.1-31.6.4.

[248] S. Starschich and U. Boettger, J. Mater. Chem. C **5**, 333 (2017).

[249] H. Yu, C.-C. Chung, N. Shewmon, S. Ho, J.H. Carpenter, R. Larrabee, T. Sun, J.L. Jones, H. Ade, B.T. O'Connor, and F. So, Adv. Funct. Mater. **27**, 1700461 (2017).

[250] M. Ghatge, G. Walters, T. Nishida, and R. Tabrizian, Appl. Phys. Lett. **116**, 043501 (2020).

[251] F. Hakim, M. Ghatge, and R. Tabrizian, Appl. Phys. Lett. **117**, 063502 (2020).

[252] B.H. Toby and R.B. Von Dreele, J. Appl. Crystallogr. **46**, 544 (2013).

[253] J.L. Braun, S.W. King, A. Giri, J.T. Gaskins, M. Sato, T. Fujiseki, H. Fujiwara, and P.E. Hopkins, Appl. Phys. Lett. **109**, 191905 (2016).

[254] C. Thomsen, H.J. Maris, and J. Tauc, Thin Solid Films **154**, 217 (1987).

[255] H. -N. Lin, R.J. Stoner, H.J. Maris, and J. Tauc, J. Appl. Phys. **69**, 3816 (1991).

[256] K. Kang, Y.K. Koh, C. Chiritescu, X. Zheng, and D.G. Cahill, Rev. Sci. Instrum. **79**, 114901 (2008).

[257] D.H. Olson, J.T. Gaskins, J.A. Tomko, E.J. Opila, R.A. Golden, G.J.K. Harrington, A.L. Chamberlain, and P.E. Hopkins, Scripta Mater. **177**, 214 (2020).

[258] R. Newnham, *Properties of Materials: Anisotropy, Symmetry, Structure* (Oxford University Press, 2005).

[259] G. Mavko, T. Mukerji, and J. Dvorkin, *The Rock Physics Handbook: Tools for Seismic Analysis in Porous Media* (Cambridge University Press, Cambridge ; New York, 1998).

[260] C. Lane, *The Development of a 2D Ultrasonic Array Inspection for Single Crystal Turbine Blades* (Springer International Publishing, Cham, 2014).

[261] S.L. Dole, O. Hunter, and C.J. Wooge, J. Am. Ceram. Soc. **60**, 488 (1977).

[262] X.-S. Zhao, S.-L. Shang, Z.-K. Liu, and J.-Y. Shen, J. Nucl. Mater. **415**, 13 (2011).

[263] A. SelCuk and A. Atkinson, J. Eur. Ceram. Soc. **17**, 1523 (1997).

[264] Y. Al-Khatatbeh, K.K.M. Lee, and B. Kiefer, Phys. Rev. B **82**, 144106 (2010).

[265] L. Bolotov, N. Uchida, and S. Migita, AIP Adv. **11**, 015216 (2021).

[266] R.P. Haggerty, P. Sarin, Z.D. Apostolov, P.E. Driemeyer, and W.M. Kriven, J. Am. Ceram. Soc. **97**, 2213 (2014).

[267] B.M. Hudak, S.W. Depner, G.R. Waetzig, A. Talapatra, R. Arroyave, S. Banerjee, and B.S. Guiton, Nat. Commun. **8**, 15316 (2017).

[268] T. Shiraishi, S. Choi, T. Kiguchi, T. Shimizu, H. Funakubo, and T.J. Konno, Appl. Phys. Lett. **114**, 232902 (2019).

[269] J. Qin, F. Huang, X. Li, L. Deng, T. Kang, A. Markov, F. Yue, Y. Chen, X. Wen, S. Liu, Q. Xiong, S. Semin, T. Rasing, D. Modotto, R. Morandotti, J. Xu, H. Duan, and L. Bi, ACS Nano **13**, 1213 (2019).

[270] C.-K. Lee, E. Cho, H.-S. Lee, C.S. Hwang, and S. Han, Phys. Rev. B **78**, 012102 (2008).

[271] Z. Wang, O. Yaegashi, H. Sakaue, T. Takahagi, and S. Shingubara, J. Appl. Phys. **94**, 4697 (2003).

[272] S. Logothetidis, E.I. Meletis, G. Stergioudis, and A.A. Adjaottor, Thin Solid Films **338**, 304 (1999).

[273] N.D. Cuong, D.-J. Kim, B.-D. Kang, C.S. Kim, K.-M. Yu, and S.-G. Yoon, J. Electrochem. Soc. **153**, G164 (2006).

[274] G. Lemperière and J.M. Poitevin, Thin Solid Films **111**, 339 (1984).

[275] S. Zafar, H. Jagannathan, L.F. Edge, and D. Gupta, Appl. Phys. Lett. **98**, 152903 (2011).

[276] K. Park and D.R. Olander, J. Electrochem. Soc. **138**, (1991).

[277] T. Szyjka, L. Baumgarten, T. Mittmann, Y. Matveyev, C. Schlueter, T. Mikolajick, U. Schroeder, and M. Müller, ACS Appl. Electron. Mater. **2**, 3152 (2020).

[278] Y.G. Shen, Mat. Sci. Eng. A **359**, 158 (2003).

[279] T. Brat, J. Vac. Sci. Technol. B **5**, 1741 (1987).

[280] S.E. Reyes-Lillo, K.F. Garrity, and K.M. Rabe, Phys. Rev. B **90**, (2014).

[281] K.M. Freedy, P.M. Litwin, and S.J. McDonnell, ECS Trans. **77**, 11 (2017).

[282] M.Y. Liao, Y. Gotoh, H. Tsuji, and J. Ishikawa, J. Vac. Sci. Technol. A **22**, 214 (2004).

[283] S.S. Fields, D.H. Olson, S.T. Jaszewski, C.M. Fancher, S.W. Smith, D.A. Dickie, G. Esteves, M.D. Henry, P.S. Davids, P.E. Hopkins, and J.F. Ihlefeld, Appl. Phys. Lett. **118**, 102901 (2021).

[284] P. Lamour, P. Fioux, A. Ponche, M. Nardin, M.-F. Vallat, P. Dugay, J.-P. Brun, N. Moreaud, and J.-M. Pinvidic, Surf. Interface Anal. **40**, 1430 (2008).

[285] R.G. Vitchev, J.J. Pireaux, T. Conard, H. Bender, J. Wolstenholme, and Chr. Defranoux, Appl. Surf. Sci. **235**, 21 (2004).

[286] C.J. Powell and A. Jablonski, J. Surf. Anal. **9**, 322 (2002).

[287] P.J. Cumpson and M.P. Seah, Surf. Interface Anal. **18**, 345 (1992).

[288] K. Harrison and L.B. Hazell, Surf. Interface Anal. **18**, 368 (1992).

[289] X. Zhong, I. Rungger, P. Zapol, H. Nakamura, Y. Asai, and O. Heinonen, Phys. Chem. Chem. Phys. **18**, 7502 (2016).

[290] S.J. Kim, J. Mohan, H.S. Kim, J. Lee, C.D. Young, L. Colombo, S.R. Summerfelt, T. San, and J. Kim, Appl. Phys. Lett. **113**, 182903 (2018).

[291] M.H. Park, H.J. Kim, Y.J. Kim, T. Moon, K.D. Kim, and C.S. Hwang, Nano Energy **12**, 131 (2015).

[292] H. Mulaosmanovic, J. Ocker, S. Müller, U. Schroeder, J. Müller, P. Polakowski, S. Flachowsky, R. van Bentum, T. Mikolajick, and S. Slesazeck, ACS Appl. Mater. Inter. **9**, 3792 (2017).

[293] T.S. Boscke, J. Muller, D. Brauhaus, U. Schroder, and U. Bottger, in *2011 International Electron Devices Meeting* (IEEE, Washington, DC, USA, 2011), p. 24.5.1-24.5.4.

[294] Y. Lee, H. Alex Hsain, S.S. Fields, S.T. Jaszewski, M.D. Horgan, P.G. Edgington, J.F. Ihlefeld, G.N. Parsons, and J.L. Jones, Appl. Phys. Lett. **118**, 012903 (2021).

[295] S.S. Fields, S.W. Smith, C.M. Fancher, M.D. Henry, S.L. Wolfley, M.G. Sales, S.T. Jaszewski, M.A. Rodriguez, G. Esteves, P.S. Davids, S.J. McDonnell, and J.F. Ihlefeld, Adv. Mater. Interfaces **8**, 2100018 (2021).

[296] S.S. Fields, S.W. Smith, P.J. Ryan, S.T. Jaszewski, I.A. Brummel, A. Salanova, G. Esteves, S.L. Wolfley, M.D. Henry, P.S. Davids, and J.F. Ihlefeld, ACS Appl. Mater. Inter. **12**, 26577 (2020).

[297] Y. Goh, S.H. Cho, S.-H.K. Park, and S. Jeon, IEEE T. Electron. Dev. **67**, 3431 (2020).

[298] D. Damjanovic, Phys. Rev. B **55**, R649 (1997).

[299] T. Rojac, M. Kosec, B. Budic, N. Setter, and D. Damjanovic, J. Appl. Phys. **108**, 074107 (2010).

[300] J. Seidel, L.W. Martin, Q. He, Q. Zhan, Y.-H. Chu, A. Rother, M.E. Hawkridge, P. Maksymovych, P. Yu, M. Gajek, N. Balke, S.V. Kalinin, S. Gemming, F. Wang, G. Catalan, J.F. Scott, N.A. Spaldin, J. Orenstein, and R. Ramesh, Nature Mater. **8**, 229 (2009).

[301] T. Rojac, A. Bencan, G. Drazic, N. Sakamoto, H. Ursic, B. Jancar, G. Tavcar, M. Makarovic, J. Walker, B. Malic, and D. Damjanovic, Nature Mater. **16**, 322 (2017).

[302] A.K. Saha, K. Ni, S. Dutta, S. Datta, and S. Gupta, Appl. Phys. Lett. **114**, 202903 (2019).

[303] J. Müller, U. Schröder, T.S. Böscke, I. Müller, U. Böttger, L. Wilde, J. Sundqvist, M. Lemberger, P. Kücher, T. Mikolajick, and L. Frey, J. Appl. Phys. **110**, 114113 (2011).

[304] S. Starschich, D. Griesche, T. Schneller, and U. Böttger, ECS J. Solid State Sci. Technol. **4**, P419 (2015).

[305] C.E. Murray, P.R. Besser, C. Witt, and J.L. Jordan-Sweet, J. Mater. Res. **25**, 622 (2010).

[306] D.H. Triyoso, P.J. Tobin, B.E. White, R. Gregory, and X.D. Wang, Appl. Phys. Lett. **89**, 132903 (2006).

[307] Y. Goh and S. Jeon, J. Vac. Sci. Technol. B **36**, 052204 (2018).

[308] M. Hoffmann, T. Schenk, M. Pešić, U. Schroeder, and T. Mikolajick, Appl. Phys. Lett. **111**, 182902 (2017).

[309] S.S. Fields, S.W. Smith, S.T. Jaszewski, T. Mimura, D.A. Dickie, G. Esteves, M. David Henry, S.L. Wolfley, P.S. Davids, and J.F. Ihlefeld, J. Appl. Phys. **130**, 134101 (2021).

[310] J.J. Wortman and R.A. Evans, J. Appl. Phys. **36**, 153 (1965).

[311] T. Shimizu, K. Takahashi, R. Boyd, R.P. Viloan, J. Keraudy, D. Lundin, M. Yang, and U. Helmersson, J. Appl. Phys. **129**, 155305 (2021).

[312] S. Meyer, *Data Analysis for Scientists and Engineers* (John Wiley & Sons Inc., 1975).